Experimental and Numerical Analysis of Deformation and Fracture of Cortical Bone Tissue

by

Adel Abdel-Ghaffar Mohamed Abdel-Wahab

A doctoral thesis submitted in partial fulfilment of the requirements for the award of doctor of philosophy of Loughborough University

Wolfson School of Mechanical and Manufacturing Engineering

August 2011

Certificate of Originality

This is to declare my responsibility of the work submitted in this thesis. All the original work is my own except as stated in the acknowledgment. Neither the thesis nor the original work included has been submitted to this or any other institution for a degree.

Signed.....

Data.....

Dedicated to my parents and my wife (Rania)

Abstract

Bones are the principal structural components of a skeleton; they provide the body with unique roles, such as its shape maintenance, protection of internal organs and transmission of muscle forces among body segments. Their structural integrity is vital for the quality of life. Unfortunately, bones can only sustain loads until a certain limit, beyond which it fails. Usually, the reasons for bone fracture are traumatic falls, sports injuries, and engagement in transport or industrial accidents. The stresses imposed on a bone in such activities can be far higher than those produced during normal daily activities and lead to fracture. Understanding deformation and fracture behaviours of bone is necessary for prevention and diagnosis of traumas. Even though, in principle, studying bone's deformation and fracture behaviour is of immense benefit, it is not possible to engage volunteers in *in-vivo* investigations. Therefore, by developing adequate numerical models to predict and describe its deformation and fracture behaviours, a detailed study of reasons for, and ways to prevent or treat bone fracture could be implemented. Those models cannot be formulated without a set of experimental material data. To date, a full set of bone's material data is not implemented in the material data-base of commercial finite-element (FE) software. Additionally, no complete set of data for the same bone can be found in the literature. Hence, a set of cortical bone's material data was experimentally measured, and then introduced into the finite-element software.

A programme of experiments was conducted to characterise mechanical properties of the cortical bone tissue and to gain a basic understanding of the spatial variability of those properties and their link to the underlying microstructure. So, several types of experiments were performed in order to quantify mechanical properties of the studied bone tissue at macro- and microscales under quasi-static and dynamic loading regimes for different cortex positions called *anterior*, *posterior*, *medial* and *lateral*. Those experiments included: (1) uniaxial tension and creep tests to obtain its elastic, plastic and viscoelastic properties; (2) nanoindentation tests to characterise its microstructural elastic-plastic properties; (3) Izod tests to investigate its fracture properties under impact bending loading; (4) tensile-impact tests to characterise its impact strength and fracture force when exposed to a longitudinal

loading regime. All the experiments were performed for different cortex positions and different directions (along the bone axis and perpendicular to it) when possible. Based on the results of those experiments, a number of finite-element models were developed in order to analyse its deformation and fracture using the extended finite-element method (X-FEM) at different length scales and under various loading conditions. Those models included: (1) two-dimensional (2D) FE models to simulate its fracture and deformation at microscale level under quasi-static tensile loading. Additionally, the effect of the underlying microstructure on crack propagation paths was investigated; (2) 2D and three-dimensional (3D) FE models to simulate its fracture and deformation at macroscale level for the Izod impact test setup. In addition, the applicability of different constitutive material models was examined; (3) 3D FE models to simulate its fracture and deformation at macroscale level for tensile-impact loading conditions. The developed models provided high-quality results, and most importantly, they adequately reflected the experimental data.

The main outcome of this thesis is a comprehensive experimental analysis and numerical simulations of the deformation and fracture of the cortical bone tissue at different length scales in response to quasi-static and dynamic loading. Recommendations on further research developments are also suggested.

Keywords: cortical bone tissue; fracture; nanoindentation; viscoelastic; impact; Izod test; tensile-impact; finite-element; X-FEM.

Acknowledgment

I would like to thank my supervisor Prof. Vadim Silberschmidt for his invaluable guidance, support, encouragement, knowledge, and patience throughout the different levels of this project. His understanding, suggestions and constructive criticism helped me to sail throughout the hard times. Honestly, He played all the roles, the supervisor, the fair judge, the fan, and when needed the friend. I really appreciate and will never ever forget that great teacher.

I would also like to take the opportunity to thank Dr. Angelo Maligno for his help, assistance, and inputs at various stages of the research.

I also acknowledge with a great appreciation the role of the academic and technical staff of the Wolfson School of Mechanical and Manufacturing Engineering. Special thanks to Mr. Andy Sandavar for this help with specimen preparation and experimental work.

I'm thankful to my office colleagues Dr. Aamir Mubashar, Dr. Khursid Alam and Dr. Kazim Altaf for their invaluable help in understanding many complicated tasks in both the experimental and finite-element analysis. Once again, thanks to Dr. Aamir Mubashar, his help was one of the key roles for the succession of this report.

Finally, this thesis is dedicated to my parents and my lovely wife for their love, encouragement, support and prayers.

Date: 27/07/2011

Adel Abdel-Ghaffar

Loughborough/Leicester

UK

Publications

Journal Publications

1. **Adel A. Abdel-Wahab**, Khurshid Alam, Vadim V. Silberschmidt, “Analysis of anisotropic viscoelastoplastic properties of cortical bone tissues”, Journal of the Mechanical Behavior of Biomedical Materials, 2011, Vol. 4, No. 5, pp. 807-820.
2. **Adel A. Abdel-Wahab**, Angelo R. Maligno, and Vadim V. Silberschmidt, “Microscale modelling of bovine cortical bone fracture: Analysis of crack propagation and micro-structure using X-FEM”, Computational Materials Science, 2011 (**In Press**). doi:10.1016/j.commatsci.2011.01.021.
3. **Adel A. Abdel-Wahab**, Angelo R. Maligno, and Vadim V. Silberschmidt, “Dynamic Properties of Cortical Bone Tissue: Izod Tests and Numerical Study”, Computers, Materials & Continua, 2010, Vol. 19, No. 3, pp. 217-238.
4. **Adel A. Abdel-Wahab**, and Vadim V. Silberschmidt, “Numerical Modelling of Impact Fracture of Cortical Bone Tissue Using X-FEM”, Journal of Theoretical and Applied Mechanics, 2011, Vol. 49, No. 3, pp. 599-619.

Conference Publications

1. **Adel A. Abdel-Wahab**, Angelo R. Maligno and Vadim V. Silberschmidt, ''Micro-scale numerical model of bovine cortical bone: analysis of plasticity localization'', Proceedings of the ASME 10th Biennial Conference on Engineering Systems Design and Analysis (ESDA2010), Istanbul, Turkey, 1^{st} – 9^{th} July 2010, ISBN 978-0-7918-3877-8.
2. **Adel A. Abdel-Wahab** and Vadim V. Silberschmidt, “Dynamic Properties of Cortical Bone Tissue: Impact Tests and Numerical Study”, Proceeding of the 2011 International Conference on Advances in Experimental Mechanics: Integrating Simulation and Experimentation for Validation (ISEV), the British Society for Strain Measurement (BSSM) and the Society for Experimental Mechanics, USA (SEM), 7^{th}-9^{th} September 2011, The Royal College of Physicians, Edinburgh. (**Accepted for Publication**).

Conference Contributions

1. **Adel A. Abdel-Wahab**, and Vadim V. Silberschmidt, BSSM workshop on Experimental Mechanics in Biological Tissues, Loughborough University, UK, 23rd June 2009.
2. **Adel A. Abdel-Wahab**, Khurshid Alam, Vadim V. Silberschmidt, Third International Conference on Mechanics of Biomaterials and Tissues, Florida (USA), 13th – 17th December, 2009.
3. **Adel A. Abdel-Wahab**, Angelo R. Maligno, and Vadim V. Silberschmidt, International Conference on Computational & Experimental Engineering and Sciences, Las Vages (USA), 28th March – 1st April, 2010.
4. **Adel A. Abdel-Wahab**, Angelo R. Maligno and Vadim V. Silberschmidt, ASME 2010, 10th Biennial Conference on Engineering Systems Design and Analysis, Istanbul (Turkey), 12th – 14th April, 2010.
5. **Adel A. Abdel-Wahab**, Angelo R. Maligno and Vadim V. Silberschmidt, The 20th International Workshop on Computational Mechanics of Materials (IWCMM 20), Loughborough University, UK, 8th – 10th September, 2010.
6. **Adel A. Abdel-Wahab** and Vadim V. Silberschmidt, International Conference on Computational and Experimental Engineering & Sciences (ICCES'11), Nanjing, China, 18th – 21st April 2011.

Contents

List of Figures

List of Tables

Symbols

Symbol	Meaning and Units
a	Contact circle radius, μm
a_c	Crack size, m
$\mathrm{a_I}$	Crack-surface nodal enriched degrees of freedom vector
a_r	True contact circle radius, μm
A	Projected contact area of the indenter, nm^2
A_m	Area fraction of interstitial matrix
A_o	Area fraction of osteons
$\mathrm{b_I^{\alpha}}$	Crack-tip nodal enriched degrees of freedom vector
B	Specimen thickness, m
C	Compliance, 1/Pa
d	Specimen displacement, m
e_i	Shear relaxation modulus ratio
$e_R\,(t)$	Dimensionless relaxation modulus, Pa
E	Elastic modulus, GPa
E_0	Instantaneous modulus, Pa
E_1	Longitudinal elastic modulus, GPa
E_2	Transverse elastic modulus, GPa
E_3	Radial elastic modulus, GPa
E_c	Effective macroscopic elastic modulus, Pa

E_i	Elastic modulus of the indenter, Pa
E_m	Microscopic elastic moduli for interstitial matrix, Pa
E_o	Microscopic elastic moduli for osteons, Pa
E_r	Reduced modulus of nanoindentation's specimen, Pa
E_s	Elastic modulus of nanoindentation's specimen, Pa
$E_R(t)$	Relaxation modulus, Pa
$\overline{E}$	Absorbed energy, J
$E^{'}$	Storage modulus, Pa
$E^{''}$	Loss modulus, Pa
E^{*}	Complex modulus, Pa
f	Volume fraction
f_i	Volume fraction of a composite component, i = 1, 2, ...
F	Impact force, N
$\mathrm{F}_{\alpha}(\mathrm{x})$	Asymptotic crack-tip functions
g	Gravitational acceleration, m/s^2
G	Shear modulus, GPa
G_c	Critical strain energy release rate, J/m^2
h	Indentation depth, nm
h_e	Elastic-depth component of the indentation, nm
h_p	Plastic-depth component of the indentation, nm
h_r	Residual impression depth, nm
h_s	Partially recovered depth, nm

h_t	Total penetration depth, nm
H	Hardness, Pa
$\mathrm{H(x)}$	Heaviside function
K_c	Critical stress intensity factor, Pa$\sqrt{\mathrm{m}}$
k_i	Bulk relaxation modulus ratio
$K_{(\mathrm{I,II,III})}$	Mode I, II and III stress intensity factor, Pa$\sqrt{\mathrm{m}}$
l	Length of the hammer, m
$\mathrm{L_{cr}}$	Crack's length, m
$\mathrm{L_{notch}}$	Notch depth, m
m	Mass of the hammer, kg
$\mathbf{m}^+$	Positive normal to the crack front
n	Indentation cycles
n	Outward unit normal
$\mathbf{n}^+$	Positive normal to the crack surface
$\mathrm{N_I(x)}$	Nodal shape functions
P	Applied load, N
P_c	Composite property
P_i	Property of a composite component, i = 1, 2, ...
P_m	Mean pressure, Pa
P_{max}	Maximum indentation load, mN
P_s	Reduced load, mN
P_t	Total penetration load, mN

Q	Dimensionless constant
(r, θ)	Polar coordinates system
R	Stress ratio
R_s	Radius of the sphere, μm
t	Time, s
V	Hammer velocity, m/s
V_s	Sound velocity, m/s
W	Specimen width, m
W_f	Work of fracture, J/m^2
$(\mathrm{W} - \mathrm{L_{notch}})$	Un-notched specimen's width, m
$\mathrm{u_I}$	Nodal displacement vector, m
x	Sample (Gauss) point
Y	Yield stress, Pa
ν	Poisson's ratio
ν_i	Poisson's ratio of the indenter
ν_{ij}	Poisson's ratio that corresponds to a contraction in the direction j when an extension is applied in direction i
ν_s	Poisson's ratio of nanoindentation's specimen
ν_{12}	Ratio of strain in transverse direction, 2, to strain in longitudinal direction, 1
ν_{13}	Ratio of strain in radial direction, 3, to strain in longitudinal direction, 1
ν_{21}	Ratio of strain in longitudinal direction,1, to strain in transverse

	direction, 2
ν_{23}	Ratio of strain in radial direction, 3, to strain in transverse direction, 2
ρ	Density, kg/m^3
ε	Strain
$\dot{\varepsilon}$	Rate of deformation or Strain rate, 1/s
ε_r	Flow strain
σ	Stress, Pa
σ_{app}	Applied stress, Pa
σ_r	Flow stress, Pa
δ	Phase lag angle between stress and strain
tan δ	Loss factor
$k;\alpha$	Continuous shape parameters of the probability density function Dagum (4P)
α_o	Starting angle, rad
α_r	Angle of rise, rad
τ_i	Relaxation time
Δt	Time difference, s
η	Viscosity, Pa s
γ	Continuous location parameters of the Dagum (4P) probability density function
μ	Continuous scale parameter of the hypersecant probability density function
ϑ	Continuous location parameter of the hypersecant probability density function

β	Empirical shape factor
$\emptyset$	Angle between the indenter and sample surfaces, rad
ψ	Continuous scale parameters of the Dagum (4P) probability density function

Acronyms

Abbreviation	Meaning
2D	Two-dimensional
3D	Three-dimensional
3-PT	Three-point bending
µXCT	X-ray micro-computed tomography
ANOVA	Analysis of variance
BEV	Bone elementary volume
BMC	Bone mineral content
CT	Compact tension
CZM	Cohesive zone model
DCB	Double-cantilever beam
DMA	Dynamic mechanical analysis
DMTA	Dynamic mechanical thermal analysis
DSC	Differential scanning calorimeter
DSI	Depth-sensing indentation
FE	Finite-element
FEM	Finite-element modelling
HA	Hydroxyapatite
KWW	Kohlraush-Williams-Watts
LEFM	Linear elastic fracture mechanics
R-Curve	Resistance curve
SD	Standard deviation
SEM	Scanning electron microscopy
SEN	Single-edge notched bend
SHPB	Split-Hopkinson pressure bar
SIF	Stress intensity factor(s)
VCCT	Virtual crack-closure technique
VMIB	Virtual multi-dimensional internal bonds
X-FEM	Extended finite-element method

1. Chapter 1

Introduction

1.1. Background

Research in the area of biological materials and tissues is developing fast. One of the most important issues in this area is characterisation and modelling of hard and soft tissues to develop realistic models of the human body and its parts. Once such models are available, various problems such as effects of car crash and sports injuries as well as falling fractures could be studied in detail. As the skeletal system is the main building block for these models, the need to obtain an adequate description of its mechanical behaviour and properties is crucial. The skeletal system is made up of individual bones, and the connective tissue that joins them. Bone is the principal structural component of a skeleton: it assists the load-bearing framework of a living body. So, bone fractures have significant health, economic and social consequences. Both healthy and unhealthy bones are susceptible to fracture due to low- or high-energy trauma. High-energy traumas are usually a result of car or cycling accidents, while low-energy traumas often occur in contact sports. In both cases they are caused by dynamic loading.

When loads are applied to whole bones they exhibit structural behaviour. Factors such as mass material properties and geometry of bones as well as the magnitude and orientation of applied loads affect their response to such loading. Bones are fractured when they are exposed to severe loads, generating stresses exceeding their ultimate strength. Thus, a fracture event occurs initially at the material level that eventually affects the load carrying capacity of the whole bone at its structural level [22]. To investigate numerically the deformation and fracture of bone at the material level, a set of parameters that indicates its mechanical behaviour is required. To date these parameters are not implemented in material data-bases of the most common commercial finite-element software; in addition, there is no complete set of mechanical data for the same bone in the literature.

Accordingly, a set of data for the same bone has to be measured experimentally, and then input in finite-element software. It is worth mentioning here that bone is a viscoelastic material and its properties can change spatially even for the same bone, for instance, for various cortex positions of a femur. Therefore, such variability had to be considered in the experimental part of this work. Consequently, in the first part of this study, a robust experimental foundation was built through characterization of bone's mechanical properties to underpin numerical models developed to simulate bone's deformation and fracture at different time and length scales under quasi-static and dynamic loading. It included characterization of cortical bone's elastic-plastic, viscoelastic, and dynamic properties at macroscale. Additionally, its elastic-plastic properties and topological data at the microscopic level were investigated.

By developing adequate numerical models capable of predicting and describing bone's deformation and fracture behaviours, a detailed study of reasons for, and ways to prevent, bone fracture could be implemented. To plan prevention therapies and treatment strategies, scientific knowledge of bone fracture mechanisms is needed. More effective prevention treatments including physical therapies, protectors, and medications is expected to be improved, if a comprehensive, more realistic, and reliable finite-element simulations of bone deformation and fracture are introduced. Accordingly, in the second part of this study, finite-element simulations for deformation and fracture of a cortical bone tissue under different loading regimes, for different time and length scales were established.

1.2. Aim and Objectives

Aim:

The aim of this study is to acquire a robust experimental-based material data using a bovine cortical bone tissue to enable adequate numerical modelling of its deformation and fracture behaviours at various time and length scales. The obtained data is used to develop models and simulation tools with the capability to investigate these behaviours under quasi-static and dynamic loading at micro- and macro-structural levels. Accordingly, the experimental part of this study focuses on acquiring the related set of data including the elastic-plastic, viscoelastic, and

fracture behaviours. Whereas, in the simulations part, extended finite-element method (X-FEM) is used to investigate cortical bone's failure microscopically and macroscopically under quasi-static and dynamic loading, respectively.

Objectives:

In order to achieve the aim of this study, several areas were covered through experimental and numerical studies of the bovine cortical bone tissue as follows:

- Characterising elastic-plastic behaviour along a bone axis (parallel to osteons) and normal to it (perpendicular to osteons) at different cortex positions called anterior, posterior, medial and lateral.
- Acquiring viscoelastic material properties using creep tests for specimens from different cortex positions.
- Quantifying elastic-plastic behaviour at microscopic level along the bone axis using nanoindentation technique.
- Measuring the bending fracture load and impact strength using Izod tests for different cortex positions.
- Evaluating the tensile fracture load and impact strength using tensile-impact tests for different cortex positions.
- Formulating finite-element models of a real microstructure to investigate fracture evolution in cortical bone using X-FEM.
- Developing finite-element models to simulate cortical bone's deformation and fracture under bending impact loading using X-FEM.
- Formulating finite-element models to simulate cortical bone's deformation and fracture under tensile-impact loading using X-FEM.

1.3. Thesis Layout and Research Methodology

A schematic of the overall layout of this thesis including the research methodology is given in Fig. 1.1. The thesis covers five main areas: introduction, literature review, experimentation, simulations, and conclusions and future work. Apart from introduction and conclusions and future work, each area is presented in more than one chapter. A brief description of the chapters will be given in the following section. The rest of this section will be focusing on the interaction between the elements of

research methodology. In fact, it is comprised of two main parts: experimentation and simulations. Experimentation was carried out to characterise various behaviours of cortical bone tissue at different time and length scales. Therefore, experimentation part is divided into microscale and macroscale experiments. In the part on microscale experiments, bone topology was captured using optical microscopy for osteonal bone, and the elastic-plastic behaviour of their constituents was quantified using the nanoindentation technique. Employing the rule of mixture, used generally for composite materials, their homogenized properties were calculated and compared to those measured in the part covering macroscale experiments. In the latter, elastic-plastic, viscoelastic and dynamic behaviours of cortical bone tissue were investigated. The elastic-plastic behaviour was characterized using uniaxial tension tests for specimens cut along and perpendicular to the bone's axis, whereas creep tests were used to quantify its viscoelastic behaviour. In addition, its dynamic behaviour was investigated using two different loading configurations: bending- and tensile-impact loading. The former was implemented using Izod tests whereas the latter using tensile-impact tests. The experimental results were used in development and validation of simulations.

In order to predict the deformation and fracture of cortical bone tissue at macroscale and microscale, novel finite-element models were developed. At the beginning, to understand the crack evolution at microscopic scale, finite-element models with direct introduction of microstructure were developed to investigate the effect of cement lines on the crack propagation path and the global macroscopic quasi-static behaviour. Then, as cortical bones predominantly break under impact loading – whether they are young or old – two different loading regimes were modelled: bending- and tensile-impact. In order to predict failure and damage of the cortical bone tissue under those loads, the extended finite-element method (X-FEM) was used to predict the crack paths. The modelling results were validated by comparison with experiment data.

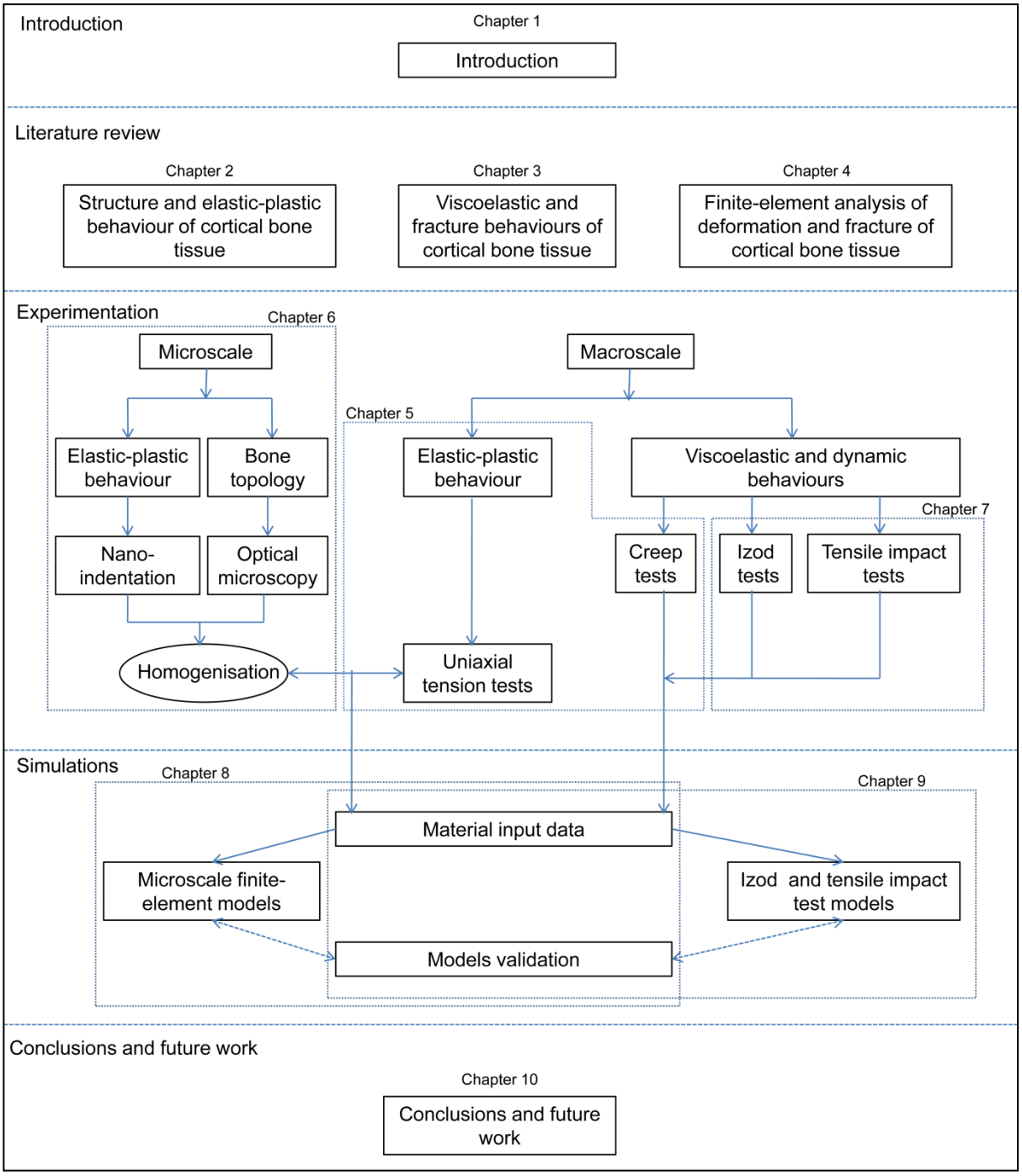

Figure 1.1: Overall thesis layout and research methodology

1.4. Thesis structure

A brief description of the remaining Chapters of this thesis is given below:

Chapter 2 Structure and Elastic-Plastic Behaviour of Cortical Bone Tissue

This chapter is divided into two main parts. In the first part, a description of composition, macroscale and microscale structure and functions of cortical bone tissue are introduced, whereas, in the second part, the literature on experimental techniques used to determine its mechanical properties is reviewed.

Chapter 3 Viscoelastic and Fracture Behaviours of Cortical Bone Tissue

A review of literature on experimental techniques for determining viscoelastic and fracture properties of cortical bone is summarized in this chapter. Creep, relaxation and Dynamic Mechanical Analysis (DMA) of the tissue are described in the lights of available literature.

Chapter 4 Finite-Element Analysis of Deformation and Fracture of Cortical Bone Tissue

A general description of the Extended Finite-Element Method (X-FEM) is presented followed by the literature review of the developments in finite-element models (FEM) of deformation and fracture of cortical bone tissue.

Chapter 5 Characterisation of Macroscale Mechanical Properties of Cortical Bone Tissue

The experimental methods used for acquiring the macroscopic mechanical properties are given in this chapter. These include uniaxial tension tests as well as creep tests. Furthermore, the experimental results and their discussion are also included.

Chapter 6 Characterisation of Microscale Mechanical Properties of Cortical Bone Tissue

This chapter focuses on characterising the elastic-plastic behaviour of the microscopic constituents of the cortical bone tissue using the nanoindentation technique. In addition, topological and statistical studies of microstructure of

osteonal bone are introduced. Hence, a comparison of nanoindentation elastic moduli with macroscopic ones using the rule of mixture is considered. This chapter is closed with the results and discussion of the experimental data.

Chapter 7 Characterisation of Dynamic Properties of Cortical Bone Tissue

Two-experimental setups for acquiring the dynamic properties of cortical bone are described in this chapter: Izod and tensile-impact tests. The experimental methods used for both tests are presented. Then, the experimental results and their discussions are provided.

Chapter 8 Microscale Finite-Element Modelling of Cortical Bone Tissue

In this chapter, the details of general features and development of the microscale finite-element models are given. Implementing a statistical realization of the real osteonal bone microstructure as well as the material properties and the effect of the cement line on the crack propagation path are introduced. Results and discussion of the simulations are given.

Chapter 9 Finite-Element Analysis of Impact Loading of Cortical Bone Tissue

Two different sets of models are used to analyse the dynamic behaviour of cortical bone tissue: Izod and tensile-impact test models. Details of the development and analysis of those models are described. Results of simulations with their discussion are introduced at the end of this chapter.

Chapter 10 Conclusions and Future Work

The outcomes and the conclusions drawn from the research are presented in this chapter. Also, proposals and recommendations for the possible future research are introduced.

2. Chapter 2

Structure and Elastic-Plastic Behaviour of Cortical Bone Tissue

2.1. Introduction

The skeletal system is important to the body both biomechanically and metabolically. It is comprised of bones and a connective tissue that joins them. Bones differ from other connective tissues by their hardness and rigidity. They gain these characteristics from their complex composition; they consist of collagen fibres, various noncollagenous proteins and mineral crystals. Bones' rigidity and hardness provide the body with unique roles, such as maintenance of body shape, protection of internal organs and transmission of muscle forces from one part to another. In addition, they serve as a reservoir of calcium and contribute in the regulation of extracellular fluid composition. Moreover, unlike structural materials, bone is a self-repairing structural material and can adapt its mass, shape and properties to variations in mechanical loading [23].

It is important to understand in detail the composition, function and complex structure of bone in order to comprehend occurrence of complex process of bone fracture when it is exposed to loads exceeding its strength and/or fracture toughness. Furthermore, it is only by understanding the structure and mechanical properties of bone, its adequate models predicting the response to loads could be introduced. The best bone models are naturally those based on biomechanical and biological properties directly linked to those of real bones.

2.2. Bone Composition

Bone is a natural composite material that consists of mineral crystals deposited in an organic matrix. Generally, a mineral, an organic matrix, water and small amounts of proteoglycans and noncollagenous proteins are the main constituents of bone.

The mechanical properties of bone are determined by fractions and arrangement of these three phases as follows [1]:

Mineral: Calcium phosphate, calcium carbonate with sodium, magnesium and fluoride are the basic constituents of bone mineral. Mainly, the mineral constituent of the bone takes the form of hydroxyapatite crystals and comprises approximately 65% of the total mass of bone. An electron microscopic study reported that the mineral crystals are plate-shaped with average dimensions of 50 nm x 25 nm x 3 nm [24]. Basically, strength and stiffness of bone are provided by the mineral phase.

Organic Matrix: Approximately 30% of the total mass of bone is its organic phase. It is composed of 90% of collagen fibres with remaining 10% containing a mixture of non-collageneous proteins [25, 26]. Nucleation and growth of mineral crystals take place among collagen fibrils with diameter of 80-100 nm. Therefore, one of the main determinants of mechanical properties of bone is the arrangement of collagen fibrils. In terms of fibres arrangements, there are two main forms of bone: woven and lamellar. Woven bone has a randomly oriented pattern of collagen fibres; these fibres form quickly after fracture. On the contrary, in lamellar bone collagen fibres are organised and result in a higher modulus and strength than those of woven bone. In lamellar bone, collagen fibres are aligned parallel to each other but fibre orientations change between layers. Woven bone is formed initially after the fracture and over the time it is replaced by lamellar bone. The mineral phase is much stiffer than the collagen one; stiffness of collagen fibres is 1.5 GPa, much lower than that of the mineral phase. However, ductility and fracture toughness for bone are provided by collagen fibres that act as reinforcement for the mineral constituents [27, 28].

Water: The remaining some 5% of the total mass of bone is occupied by water that is located within collagen fibres, in the pores, and bound in the mineral phase. Water has an important role in determining the mechanical properties of bone. For example, it was shown that dehydration of bone samples has a significant effect on strength, stiffness, and ductility of bone: dehydrated samples have increased strength and stiffness but decreased ductility [29].

2.3. Functions of Bone

Bone does not only serve as a mechanical support for the body; it also provides other functions that are of great importance in physiological processes occurring throughout the body [29]. Bone has three different functions; they can be summarized as following:

- **Mineral Homeostasis**: Bone is the body's storage of calcium, phosphate, sodium and magnesium. Approximately 99% of such ions are stored in bone. These ions are essential for regulating physiological processes such as blood clotting, nerve impulse transmission and chemical signalling.
- **Hematopoiesis**: Red blood cells are formulated and developed by the marrow found in the intermedullary canal (the void in the centre of long bones).
- **Mechanical**: Bone constitutes the primary framework of the human body: it is the primary structural material of the human body. It has a complex architecture to protect vital internal organs such as heart, lungs, and brain. Furthermore, it provides the structural levers that allow transmitting the force between segments to provide mobility [1].

Bone as a material has essential features different from those of engineering materials. On the one hand, it is a living tissue that has the ability to adapt its structure to changes in the mechanical and physical environment. On the other hand, through a controlled process of regeneration and repair, its mechanical function can be retrieved after fracture. In the physiological range of strain between 50-200 $\mu\varepsilon$ and 1500-2500 $\mu\varepsilon$, bone mass is maintained, see Fig. 2.1 [1]. Obviously, some cases like disuse of bone, i.e. when the range of strain is below the physiological range of 50-200 $\mu\varepsilon$, lead to bone mass loss. Also, when bone experiences pathological overload through excessive exercise, bone mass is increased [30-32]. These features are essential to maintain the structural integrity of the skeleton to meet mechanical demands.

There are two main processes associated with bone; the first one is throughout the life and it is associated with a growth and reforming in childhood and youth, called bone *modelling*. The second one is a lifelong process with a skeletal tissue being continuously resorbed and replaced in order to maintain skeletal integrity, called *remodelling*. The interaction between osteoblasts (bone forming cells), osteoclasts (bone eating cells) and the components of the bone matrix to keep balanced processes of bone resorption and formation enables the maintenance of a normal and healthy bone [33].

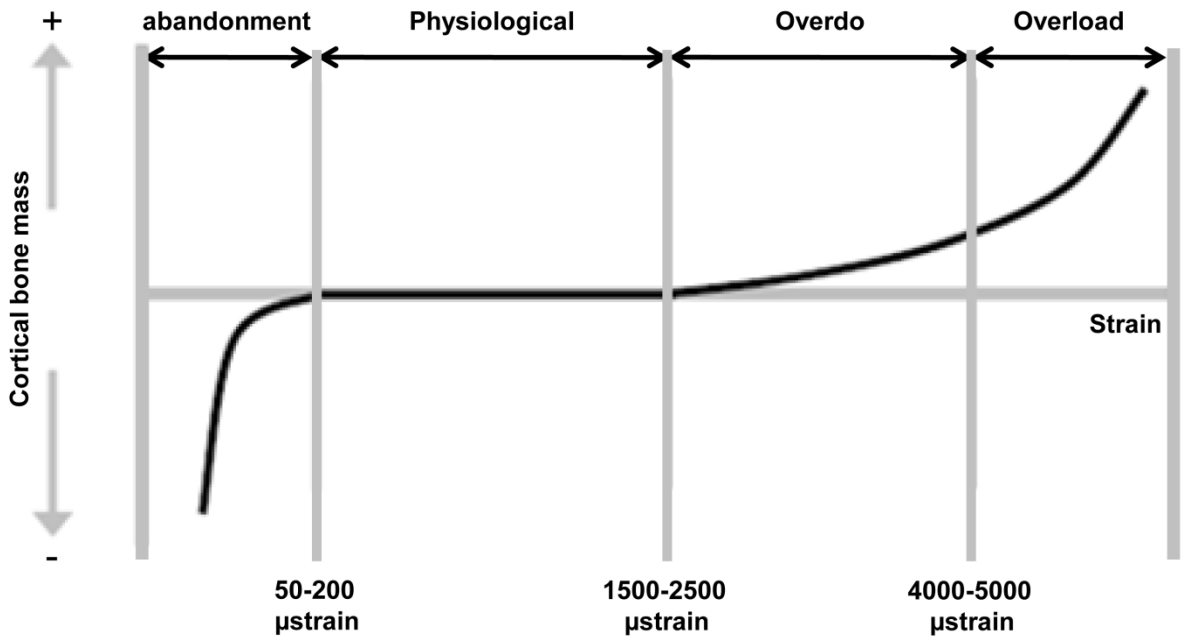

Figure 2.1: Frost's mechanostat theory; adaptation of bone to mechanical stimuli (after [1])

2.4. Macroscopic Structure of Bone

Bone has a structure with different hierarchical levels, where the mechanical properties at every level are influenced by the constituents of its sub-level [23]. The macroscopic level, greater than 5 cm, is that of whole bones such as radius, ulna, tibia, and femur. Since these long bones are slightly curved, they experience both axial compression and bending during loading. Figure 2.2 shows a section through a long bone revealing the two basic types of bone: cortical bone and trabecular bone [1].

Cortical bone is mainly found in the cylindrical shaft of the long bones, called *diaphysis*. It also forms a *cortex* or a shell around vertebral bodies and other cancellous bones [18].

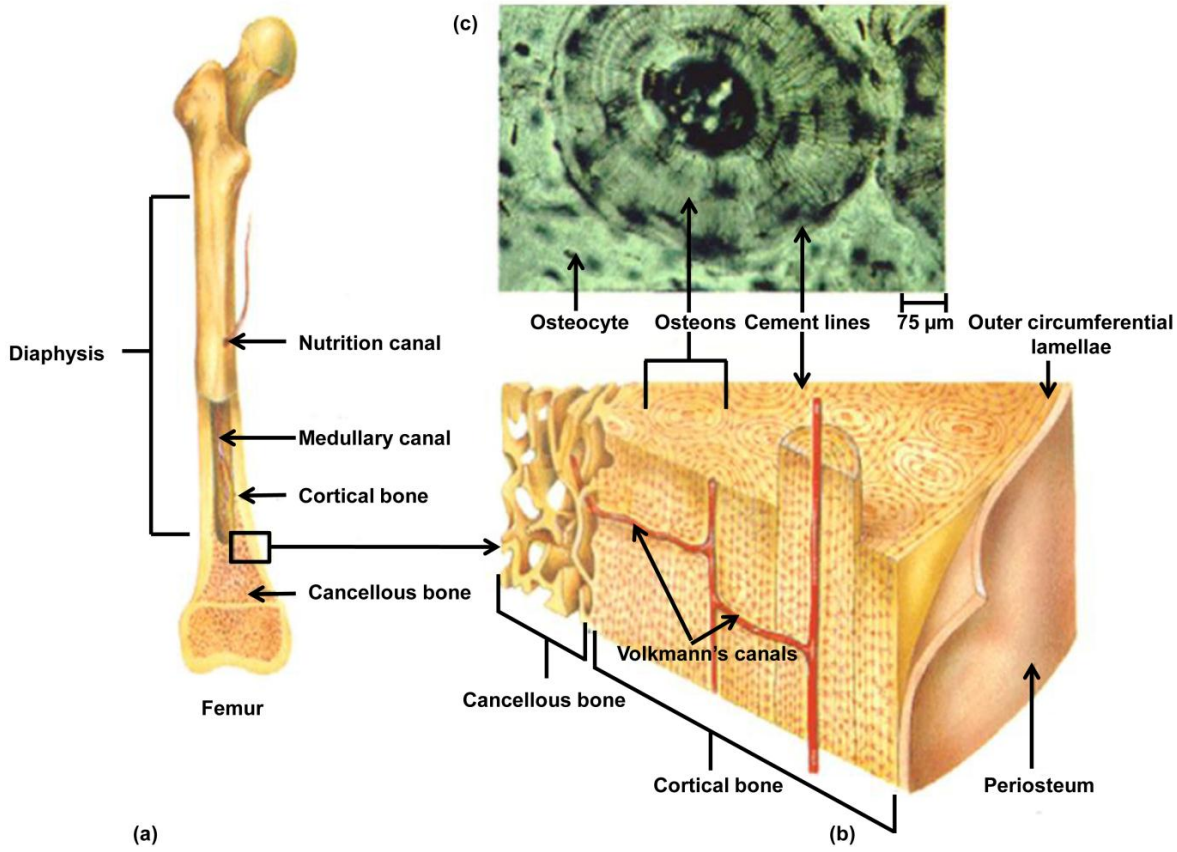

Figure 2.2: Basic structures of human thighbone: (a) femur; (b) compact bone, cancellous bone, and periosteum outer layer; (c) haversian-system (after [2])

Cortical bone has tubular structure that provides a high moment of inertia that in turn resists bending; it is mainly responsible for the function of supporting the skeleton. In addition, tubular structure has relatively low weight. The porosity of cortical bone is approximately between 5%-10%.

On the other hand, trabecular bone (also called cancellous or spongy) is a porous bone with porosity in the range of 75%-95%. It can be found in the cuboidal bones (such as vertebrae), the flat bones and the end of long bones. The structure of trabecular bone is a complex three-dimensional network of interconnecting plates and rods, called *trabeculae*, less than 200 µm in thickness [34]. It has a variable trabeculae arrangement. The microstructural level of trabecular bone is trabeculae

that are similar to osteons in cortical bone. These trabeculae consist of sheets of non-concentric lamellae.

2.5. Microstructure of Cortical Bone

Cortical bone has a hierarchal structure with varied arrangement of material structures at several length scales, which work in harmony to perform different mechanical, biological and chemical functions. At the microstructural level (approximately 200 μm), cortical bone has a repeating structural units called *osteons*. An osteon is a set of concentric lamellae. Each osteon is surrounded by a thin layer of mineralized matrix called *cement line*. The spaces between osteons are occupied with interstitial matrix, as shown in Figure 2.3. At the lamellar level (approximately 10 μm), osteons are relatively large hollow fibres composed of concentric lamellae and pores. The lamellae are built of fibres that contain fibrils [33]. At the ultrastructural level (nanoscale) the fibres are a composite of mineral Hydroxyapatite (HA) and protein collagen (Figure 2.4).

There are distinct bone forms as the hierarchical order increases from the nanoscale [4, 35]:

1. Woven, lamellar and parallel-fibred bone;
2. Haversian-system (with primary and secondary osteons);
3. Compact (cortical) and cancellous bone [36].

Woven bone is primarily produced in two main situations: in a foetus and after the fracture with fine and randomly oriented collagen fibres. On the contrary, lamellar bone is more organized than woven bone. It consists of 5 μm-thick sheets of lamellae with collagen, oriented almost perpendicular to the short axis of each lamellae [37, 38], and generally is less mineralized than woven bone. On the other hand, parallel-fibred bone is the intermediate configuration between woven and lamellar bone [39, 40].

There are two types of Haversian-system osteons: primary and secondary. By deposition of concentric lamellae, primary osteons are formed around the Haversian canals. Over the time, the primary osteons are replaced by secondary osteons

through the removal process by osteoclasts cells and re-deposition by osteoblast cells. Cement lines are formed around the secondary osteons as a result of the remodelling process. It is reported that secondary osteons are formed to repair damaged (microcracked) bone [41].

Bone cells need ways and media to be able to get nutrition as well as dispose their waste products. Therefore, bone fluid can perform this by flowing through various microstructural spaces. A network, consisting of Haversian and Volkman canals together with the lacunae-canalicular, serves as a network of channels for fluid transport [4].

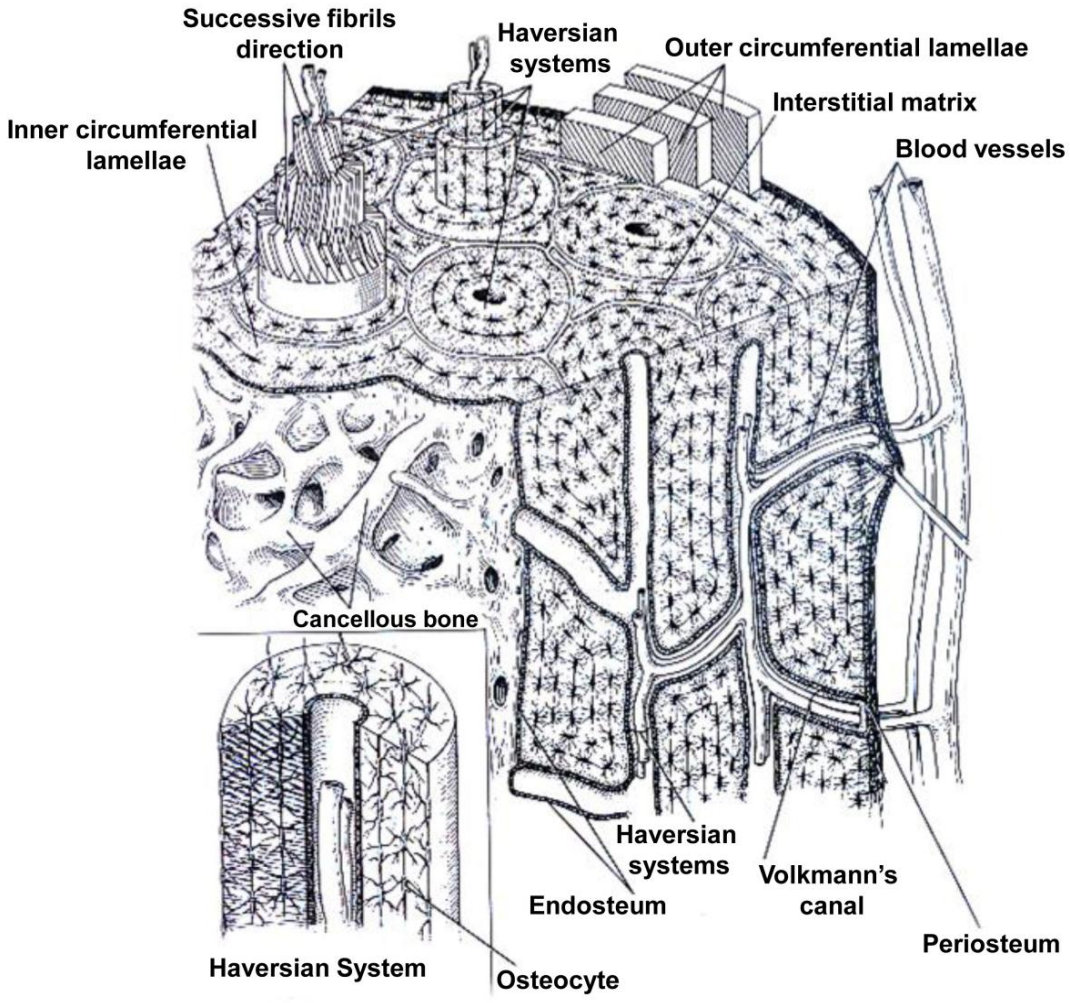

Figure 2.3: Schematic diagram of cortical bone structure (after [3])

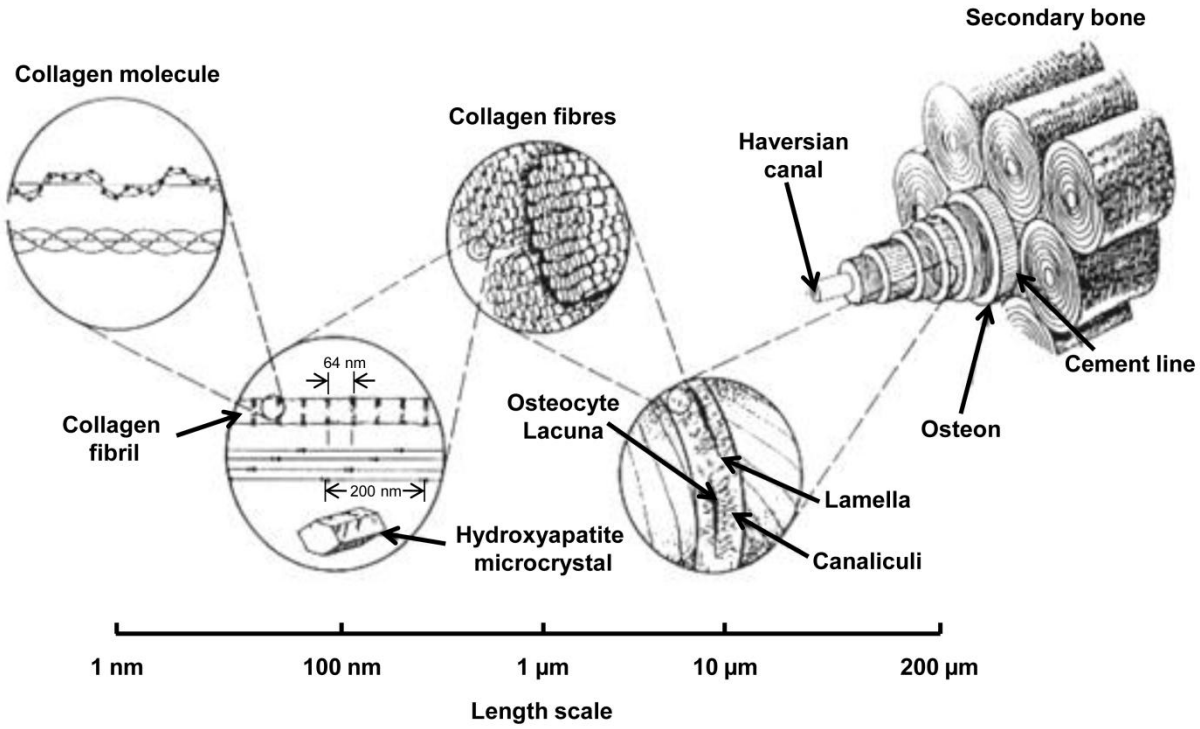

Figure 2.4: Hierarchy of structure of cortical bone (after [4])

2.6. Bone as a Natural Composite Material

Bone is an anisotropic material; its properties vary with orientation with respect to its natural axes. Details of its microstructure as well as its constitutive behaviour are required to predict its anisotropy. Commonly, bone is assumed to have either transversely isotropic or orthotropic material properties. Several authors modelled bones as standard fibre-, rod- or platelet-reinforced materials [42-44]. Hierarchical models involving ultrastructural and microstructural levels were used by other authors [45-47]. On the one hand, at the ultrastructural level, the lamellar bone tissue can be treated as a fibre-reinforced composite of collagen fibrils and mineral crystals. At the microstructural level, secondary osteons of the Havesian bone tissue can be treated as a collection of longitudinally arrayed fibres embedded in a matrix composed of interstitial lamellae but separated from it by a ductile interface – cement line. A wide range of results from the hierarchical approach are yielded because there are very little information about the elastic properties of individual lamellae and cement lines in bone and, without this information hierarchical, models rely on assumptions.

2.7. Mechanical Properties of Cortical Bone Tissue

To the best author's knowledge, there are no standardised tests to determine the mechanical properties of bone. It has been attested that the experimentally determined properties of bone tissue can be used to support, or contradict to, various hypotheses as a result of the absence of standardisation or unification of experimental methods, approaches and goals [20]. The common test types to determine the mechanical properties of bone include mechanical (three-point bending, buckling, tension, compression and torsion) and ultrasonic tests. The type of the test used can affect the value of the material properties obtained. Also, variations in the material properties can occur within a specific test type linked to the specimen's origin (the anatomical location from which the specimens were obtained), specimen's geometry, structure and orientation as well as age, degree of mineralisation, test protocol, strain rate, specimen preparation, storage temperature and conditions, physical characteristics (such as porosity and density) and consideration of end effects during the test.

2.8. Structural and Material Properties of Bone

It is important to distinguish between the structural properties and the material properties of bone. The structural properties of the bone refer to the whole-bone properties, while the material properties refer to specific bone segments, for instance, in the case of cortical bone, a machined section of the cortex and in the case of cancellous bone, isolated trabeculae. Structural properties are important for the cases of global stress analysis, while material properties are important for characterising various bone pathologies, micro-level stress analysis, and bone adaptation around implants [35]. An investigation into the susceptibility of fracture of bones for old and young animals was introduced [48] to explain the hierarchical nature of bone properties. In that study, it was suggested that, initially, investigation of structure of the whole-bone can ascertain that the load required to cause fracture of the old bone is lower than that of the young one. Though the fracture load is known, an important parameter still remains unknown – quality of bone specimens. Hence, the reasons for variations in the fracture load should be further investigated; this can initially be carried out by examining specimen's geometry. Intuitively, the geometry of the older bone might possess lower wall thickness of cortical bone. If

the reason for variation in properties of test specimens is not determined then testing of samples taken from each specimen would be needed.

The material properties of bone could be considered anisotropic and heterogeneous; however, it was observed that few studies investigated the degree of anisotropy, nor they attempted to determine the elastic properties of the bone as a function of anatomical position [49]. The suggested reason for this is the fact that traditional mechanical tests employed for engineering materials are not applicable for the bone. For instance, the bone's heterogeneity requires the specimen to be small in order to obtain properties of a "physical point", i.e. rather a small volume. Also, there are natural constraints for the bone specimen's size, especially, in the radial and transverse directions of long bones such as femur. It is also mentioned that at most three elastic coefficients can be extracted from a single specimen of bone: the elastic modulus and the Poisson's ratio can be obtained from a tensile test, and, with a specimen with a circular cross-section, the shear modulus can be determined using the torsion test, and this is presumably for cortical bone only [49]. Since, there are 9 elastic coefficients for an orthotropic material, so at least three specimens should be used to characterise the bone material. This raises the issue that it is not feasible to obtain three specimens of bone that contain the same mechanical properties, on account of the fact that the three specimens cannot be obtained from the same position in a bone. This makes it is challenging to measure the anisotropic material properties of bone at a point using traditional engineering testing methods. Other methods are available that can be used to determine the mechanical properties of bone without relying on a mechanical testing such as ultrasound testing. In the current study, a programme of experiments will be considered to examine the elastic-plastic behaviour as well as anisotropy of the cortical bone tissue for different cortex positions along bone axis and perpendicular to it using uniaxial tension tests.

2.9. Material Properties of Cortical Bone

A linear relationship between induced stresses and the resulting strain for a particular material can be expressed in terms of proportionality constant that is termed an *elastic constant*. The elastic properties of any given material might differ with respect to the direction of performed testing. If the properties are different for all

the directions of testing, the material is said to be anisotropic, and twenty-one elastic constants are needed to fully describe the behaviour of such a material. However, if there is one plane, for which the elastic properties are direction-independent, the material is called *transversely isotropic*, and only five elastic constants have to be defined to describe its behaviour. Finally, if there is no direction dependence of the elastic properties, complete symmetry, the material is called *isotropic* and has only two elastic constants, the elastic modulus and Poisson's ratio in the engineering terminology [20].

The Elastic modulus (E) known also as *stiffness*, is the ratio of the stress to the strain obtained from the uniaxial test performed within the limits of elasticity. The Poisson's ratio (ν) is defined as the negative of the ratio of a transverse strain and a longitudinal one in the direction of uniaxial loading. It is a measure of the material's ability to keep volume when loaded.

Another elastic constant is the shear modulus (G), which is defined as the ratio of the induced shear stress to the resulting shear strain. So, it relates the angular distortion (shear strain) to the shear stress in the material. If the material is isotropic, the shear modulus is dependent on the elastic modulus and Poisson's ratio and is often determined from torsion test [20].

2.9.1. Anisotropy of Mechanical Properties of Cortical Bone

Cortical bone possesses highly ordered arrangements of collagen fibres and mineral crystals. Both collagen fibres and mineral crystals are oriented along a bone axis, leading to a higher elastic modulus and strength along the long axis compared to transverse and radial directions [50, 51]. Figure 2.5 shows a femur bone, its cortex positions and specimens in longitudinal and transverse directions. In previous studies, it was shown that the mineral phase is responsible for stiffness of the bone, whereas collagen plays a significant role in both a post-yield behaviour and fracture properties [52, 53]. The difference in mechanical properties between longitudinal, transverse and radial directions was recognized long ago [54]. For primary bone histology, transverse and radial directions are distinguishable; however, heavily modelled bone appears to a naked eye to be transversely isotropic [18]. Table 2.1 summarized data based on work by Reilly and Burstein [20]. They measured the elastic moduli of Haversian and primary bovine femur bones in

different directions and compared them to those of human Haversian bone. It was noticed that human and bovine Haversian bones have similar elastic moduli in the transverse direction; whereas bovine bone seems to give higher values in the longitudinal direction [18]. In bovine bone, the anisotropy, the ratio of the elastic modulus in the longitudinal and transverse directions, is similar in tension and compression for Haversian and primary bone. Due to the fact that human bone is less stiff in the longitudinal direction, it has smaller anisotropy compared to bovine Haversian and primary bones [18].

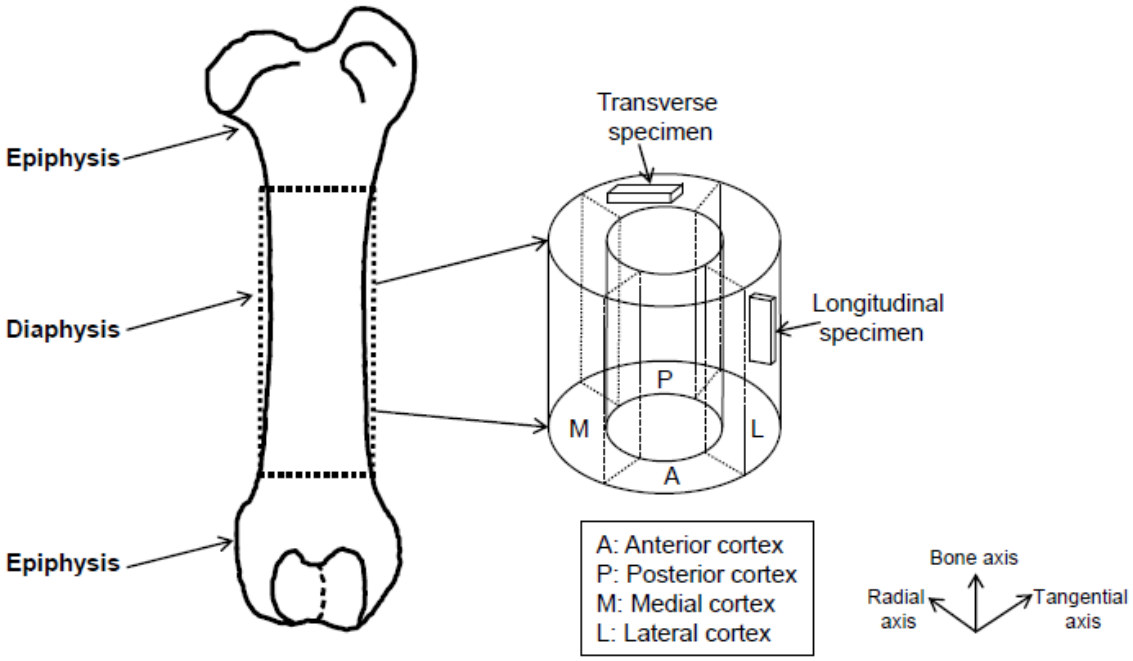

Figure 2.5: Femur cortical bone axes, cortex positions, and specimens for longitudinal and transverse direction

Table 2.1 Elastic Moduli Anisotropy of Bovine and Human Bone (after [18])

Loading Mode	Bone Species	Bone Histology	Elastic Modulus (GPa)		Anisotropy
			Longitudinal	Transverse	
Tension	Human	Haversian	17.9 ± 0.9	10.1 ± 2.4	1.77
	Bovine	Haversian	23.1 ± 3.2	10.4 ± 1.6	2.22
		Primary	26.5 ± 5.4	11.0 ± 0.2	2.4
Compression	Human	Haversian	18.2 ± 0.9	11.7 ± 1.0	1.55
	Bovine	Haversian	22.3 ± 4.6	10.1 ± 0.9	2.21

Regarding the ultimate strength, bovine bone is stronger when loaded in compression than in tension for both longitudinal and transverse directions, see Table 2.2. On the other hand, human bone is stronger in compression than in tension only when it is loaded in the transverse direction, but it is weaker in compression when it is loaded along the main bone axis [18]. It is also noticed here that anisotropy of ultimate stress is more pronounced in tension than in compression giving a higher ratio for bovine bone. Therefore, Haversian bovine bone can be used as a reasonable model for human cortical bone; the former is expected to be more anisotropic due to the higher stiffness and strength along bone axis. Based on Reilly and Burstein's data, osteon bone's remodelling, the process of removing portion of the old bone and replacing it with new bone to repair microscopic damage and prevents its accumulation, has two significant effects on anisotropy of bone's properties. On the one hand, reduction in secondary osteons' tensile strength and stiffness is more pronounced along bone axis than in transverse direction, which suggests that, the difference between bovine and human Haversian bone data originates from the excessive intracortical remodelling

of human bone. On the other hand, the osteonal remodelling process tends to transform bone from orthotropic into transversely isotropic material [18].

Table 2.2: Ultimate strength anisotropy of bovine and human bone (after [18])

Loading Mode	Bone Species	Bone Histology	Ultimate strength (MPa)		Anisotropy
			Longitudinal	Transverse	
Tension	Human	Haversian	135 ± 16	53 ± 11	2.55
	Bovine	Haversian	150 ± 11	49 ± 7	3.1
		Primary	167 ± 9	55 ± 9	3.0
Compression	Human	Haversian	105 ± 17	131 ± 21	0.8
	Bovine	Haversian	272 ± 3	146 ± 32	1.86

2.9.2. Elastic Modulus of Cortical Bone

The elastic modulus is one of two independent constants, required to define an isotropic material and is the ratio between normal stress to normal strain produced during a simple tension or compression test. Table 2.3 gives some literature values for the elastic modulus (E_1) for a cortical bone tissue considering only longitudinal direction (along the bone axis). All of those data are for machined specimens measured along the long axis of the cortical bone and subjected to a uniaxial stress field; Table 2.3 does not contain values obtained for whole bones. Obtaining the values of elastic modulus for a whole-bone usually entails a bending test with the compounded problem of the complex cross section and structure, both of which must be accounted for in normalization of results. Hence, values obtained from whole-bone tests are of little use in discussing material characteristics but may be used for comparative studies [55]. Bending tests have also been interpreted with the assumption that the material behaviour is linear elastic and that the strain can be

calculated from the deflection of the beam midpoint. These assumptions hold only if the stress in the material is kept below the yield point or the initial slope of the bending moment-deflection curve is used.

The use of elastic assumption beyond the yield point can produce errors at least as great as the value determined. While the values in longitudinal and transverse directions for the elastic moduli obtained with bending tests may be used to compare the magnitudes of the elastic constants (considering the above reservations), those obtained for specimens excited from a whole-bone at different angles between the extremes of the longitudinal and transverse directions are of limited use unless an anisotropic beam theory is used.

Due to discussed problems, not all the experimental methods used to determine the values for the elastic modulus presented in Table 2.3 were satisfactory. Some of the drawbacks associated with the values are listed in the column “Comments”. The most difficult problem was the measurement of the actual strain (elongation or shortening) in the gauge section of the specimen rather than the travel of the grips or the testing machine’s cross-head.

Kimura [56] attempted to minimize the errors in strain determination by using optical measurements for the changing distance between two wires attached to the test section of the specimen. In other investigations strain gauges were attached to the surface of the specimen, but the use of the strain gauges necessitate drying of the bone surface and hence yields values of questionable biological significance. One of interesting investigations was performed in [57], in which equal elastic moduli in both tension and compression were found. For small deformations there are no theoretical reasons for the Elastic modulus to be different for the two loading conditions. Comparison of the values for the modulus in tension and compression obtained by McElhaney *et al*. [58, 59], is impossible, since in their compression test long thin specimens were used (prone to buckling behaviour), supported laterally. However, if the values of the moduli for similar strain rates obtained in tension [58] and in compression [59] are compared, a ratio between 3 and 4 can be found. The values reported by Simikin and Robin [60] and by Kimura [56] for the modulus in compression are unexpectedly low, and it might be influenced by compliance of the used testing machine.

Table 2.3: Elastic modulus of bovine cortical bone (parallel to bone axis) (after [20])

Reference	Type of Loading	Elastic Modulus, GPa	Comments
[56]	**Tension, low strain rate**	24.5	Specimens were excised from femur; strain was measured by optical lighting.
	Compression, low strain rate	8.5	Specimens were excised from femur; crosshead movement was measured with a dial indicator.
[58, 59]	**Tension, strain rate: 3 s^{-1}**	20.5	Specimens were excised from femur; strain was measured from distance between platens.
	Compression of cubes Strain rate: 0.1 s^{-1}	24.1	Specimens were excised from femur; strain was measured from distance between platens.
	Strain rate: 1 s^{-1}	27.6	
[57]	**Tension, no strain rate reported**	17.2	Specimens were excised from femur; specimens were stored in 50% alcohol before machining.
	Compression, no strain rate reported	16.5	Strain was measured from crosshead motion.
[61]	**Tension, strain rate:0.1 s^{-1}**	24.5 ± 5.1	Specimens were excised from femur; strain was measured using extensometer.
[60]	**Tension, low strain rate**	23.8 ± 2.21	Specimens were excised from tibia; strain was measured using extensometer.
	Compression, low strain rate	7.1 ± 1.05	Specimens were excised from tibia, strain was measured using cross-head; same strain rates for tension and compression; tests took as long as five minutes.

2.9.3. Strength of Cortical Bone

The strength of bone specimen is usually defined as the maximum stress that can be sustained by it without fracture in some loading configurations, such as, tension, compression, bending, or torsion. This level of the maximum stress can be affected by the shape of the used specimen. As cortical bone is most likely to fracture in tension than in compression so our study is mainly focus on its tension properties. Table 2.4 shows a comparison of the ultimate strength values of the cortical bone by different investigators and for bovine and human cortical bone.

Table 2.4: Tensile strength for cortical bone (after [20])

Bone Species	Ultimate Stress, MPa	Load Direction	Comments	References
Bovine	112	Longitudinal	Femur, plexiform; very low strain rate, 2 minutes to fracture	[62]
	129	Longitudinal	Femur stored in alcohol, histology not reported; no information on strain rate	[57]
	172 ± 22.0	Longitudinal	Femur, plexiform; strain rate 0.1 s^{-1}	[61]
	52 ± 8.0	Transverse		
	112-120.4	Longitudinal	Femur, low strain rate	[40]
Human	134	Longitudinal	Femur, low strain rate	[63]
	90.6-116	Longitudinal	Femur, low strain rate	[40]
	151	Longitudinal	Femur, strain rate 0.1 s^{-1}	[61]

2.9.4. Poisson's Ratio of Cortical Bone

For an isotropic material, the Poisson's ratio (ν) is the second of the two independent constants describing its elastic behaviour. Some of the reported values are shown in Table 2.5. A direct comparison of these values is not possible due to different factors including species, moisture, and strain rate. The value of Poisson's ratio, reported by Ko [63], varied as the level of the load was changed and reached the lower value just prior to fracture of the specimen. No strain measurements method was described in this study. In a study by McElhaney *et al*. [58] study, a strain gauge glued to the specimen surface for strain measurements was used,

therefore, dried specimen were used. On the other hand, Lang [64] used ultrasonic technique with wet bovine bone at the extreme of the physiological strain rate. No values for Poisson's ratio for human bone deformed at physiological strain rates have been published so far.

Table 2.5: Poisson's ratio for cortical bone (after [20])

Bone Species	Type of Loading	Value*	Comments	Reference
Bovine	Ultrasonic determination	ν_{12} = 0.482 ν_{23} = 0.397	Phalanx, unknown histological type.	[64]
Bovine	Compression; strain rate= 0.1 s^{-1}	ν_{23} = 0.28	Femur, unknown histological type, dried.	[58]
Human	Tension; low strain rates	ν_{23} = 0.08-0.45	Femur; ν_{23} varied with load level; unknown strain measurement technique.	[63]
Bovine	Ultrasound	ν_{12} = 0.30 ν_{23} = 0.11	Ultrasound technique.	[65]
Human		ν_{12} = 0.58 ν_{23} = 0.31		

*ν_{12}= axially loaded longitudinal specimen; ratio of strain in transverse direction, 2 to strain in longitudinal direction, 1. ν_{23} = axially loaded transverse specimen; ratio of strain in radial direction, 3 to strain in transverse direction, 2.

2.9.5. Shear Modulus of Cortical Bone

The shear modulus is the ratio of the applied shear stress to the resulting shear strain. Assuming isotropy, the shear modulus was determined by Ko [63] for human bone tissue as 0.31 GPa, using a slow rate torsion test. On the other hand, the independent shear modulus within the framework of a transversely isotropic

material model was found by Lang [64] as 0.54 GPa for bovine phalanx but the histological type of the used specimen of bone was not specified. In a more recent study, the reported shear modulus for cortical human bone is 3.3 GPa [66]. Using ultrasound technique, the shear moduli were reported for human and bovine cortical bone in longitudinal direction as 3.6 GPa and 5.3 GPa, respectively. In the transverse direction the shear moduli were as 3.3 GPa and 6.3 GPa for human and bovine bone respectively [65].

2.10. Utrasound Method for Elastic Moduli of Cortical Bone

Conventional methods for characterising the elastic properties of bones are mechanical tests (tensile, compressive, bending, and torsion). One of the drawbacks of these tests is damage of the specimen, which makes it difficult to test it again for other measurements or in other directions. Ultrasound is an alternative technique that uses the speed of a high-frequency wave to determine the elastic moduli of materials. The theory of elastic waves is essential because it relates elastic moduli of the material to the velocity of propagation of these waves along arbitrary directions in the material. The ultrasound technique possesses the advantage that smaller sample sizes with simple geometries are acceptable [34]. Limitations of this technique include the influence of the structural properties on the material properties obtained and the length that the wave travels is not actually known [67].

Sound travels with different speeds in different media. The rate at which sound travels is function of the elastic properties and density of media as follows [68]:

$$V_s = (E/\rho)^{\frac{1}{2}}, \qquad (2-1)$$

where, V_s is the velocity of sound travelling in the solid, E is the elastic modulus and ρ is the density. Elastic properties of a solid can be found using this relation if both of the sound velocity and the density of the solid are known. Sound velocity can be calculated by measuring the time required for the sound to travel through the specimen, and then divide the specimen's width by this time. Table 2.6 gives elastic moduli for cortical bone using ultrasonic testing, where E_1, E_2 and E_3 are elastic moduli in longitudinal, transverse, and radial directions, respectively.

Table 2.6: Elastic moduli of cortical bone tissue using ultrasonic testing (after [20])

Bone Species	E_1 (GPa)	E_2 (GPa)	E_3 (GPa)	Comments	References
Human	21.2	12.9	12.6	Orthotropic	[69]
Bovine	26.2	-	20	Transversely isotropic	[70]
	30.2	23.4	20.6	Orthotropic	

2.11. Summary

- In order to comprehend the complex process of deformation and fracture of a cortical bone tissue, it is important to study its composition, function, macroscopic and microscopic structure.
- Bone has a structure with different hierarchical levels, where the mechanical properties of each level are influenced by the constituents of its sublevel.
- Bone is an anisotropic material; commonly, it can be represented as orthotropic or transversely isotropic according to its histology, primary or Haversian-system, respectively.
- No standardised test methodology to determine the mechanical properties of bone was developed so far.
- Haversian bovine bone can be used as a reasonable model of human cortical bone with bovine bone being more anisotropic.

3. Chapter 3

Viscoelastic and Fracture Behaviours of Cortical Bone Tissue

3.1. Introduction

In order to understand fracture in traumatic accidents or falls, it is important to evaluate viscoelastic and fracture behaviours of bone under dynamic loading. Therefore, in this chapter, a brief description of viscoelastic phenomena and fracture mechanics is introduced; in addition, a review of literature for their applications to the cortical bone tissue is covered, with bone viscoelasticity followed by fracture mechanics.

In fact, viscosity is a measure of the fluid resistance to shear stress, for instance, someone can feel the difference in the fluid resistance when he immerses his finger in water or honey. The viscoelastic properties of most biological materials are significant for understanding of distribution and redistribution of deformation fields with time under loading. The values of viscoelastic constants that required to adequately describing the cortical bone for modelling are not fully defined. These constants are dependent on parameters such as age and intensity of loading, as well as on the period of time that loading acts. The viscoelstic properties of the cortical bone help in understanding issues such as the effect of damping properties of the bone and the dissipated energy during bone fracture.

The mechanical behaviour of bone has a viscoelastic character; so it exhibits a time-dependent response. New materials that are used in biomedical applications should have a time-dependent behaviour similar to that of the bone, i.e. viscoelastic biocompatibility. Therefore, evaluating and understanding the bone viscoelastic properties and the underlying mechanism responsible for its damping features are crucial. There is also another reason for the importance of bone viscoelasticity: most of bone fractures occur under dynamic loading conditions, under which the viscoelasticity of bone might have a pronounced effect [71, 72]. Hence, it is necessary to understand viscoelasticity of bone tissue and its mechanism; this would contribute to further development of orthopaedic research of bone substitutes and contribute to understanding of the underlying mechanisms responsible for bone

fracture. The significant importance of implementing the viscoelastic properties in adequate numerical modelling of the cortical bone fracture, and the absence of such models up to date ensure the need for such developments. In order to numerically model the fracture of cortical bone tissues caused by an impact it is important to obtain parameters characterising its viscoelastoplastic behaviour. These parameters should be measured for various cortex positions due to bone's properties variability linked to its microstructure.

A significant number of viscoelastic experimental researches have been introduced including creep, relaxation, and DMA tests. The findings and the methodologies of these researches will be discussed in the following sections of this chapter.

3.2. Viscoelastic Material Phenomena

Solid materials are often described, for small strains, by the Hooke's law of linear elasticity: stress σ is proportional to strain ε. In one dimension, the Hooke's law is written as $\sigma = E\varepsilon$ with E as the elastic modulus. Real materials deviate from the Hooke's law, one form of deviation is viscoelasticity. In viscoelastic materials, the relationship between stress and strain depends on time or upon frequency in oscillatory loading. Anelasticity is a special case of viscoelasticity, in which full recovery ultimately occurs after removal of a transient load. Phenomena in viscoelastic materials include the following:

1. If the stress is held constant, the strain increases with time (creep);
2. If the strain is held constant, the stress decreases with time (relaxation);
3. If cyclic loading is applied, a hysteresis (a phase lag angle δ between stress and strain) occurs, representing a dissipation of mechanical energy [73].

3.3. Viscoelasticity Models

The expression "viscoelastic" signifies the dual nature of a material: on the one hand, it behaves in a viscous way, as a liquid, on the other hand, elastically, as a solid. Besides the elastic modulus E other quantities also play a role, such as the shear modulus, G in a shearing deformation or torsion, which is related to the elastic

modulus E. For simplicity, E shall be mainly used as a representative quantity for the elastic stiffness in any geometry of loading.

As a model for an elastic body we take a helical spring with stiffness E. The response of such a spring to a stress is strain ε as schematically indicated in Figure 3.1; the response is instantaneous, without any time dependency, and the recovery after a release of the stress at $t = t_r$ is also instantaneous and complete [5].

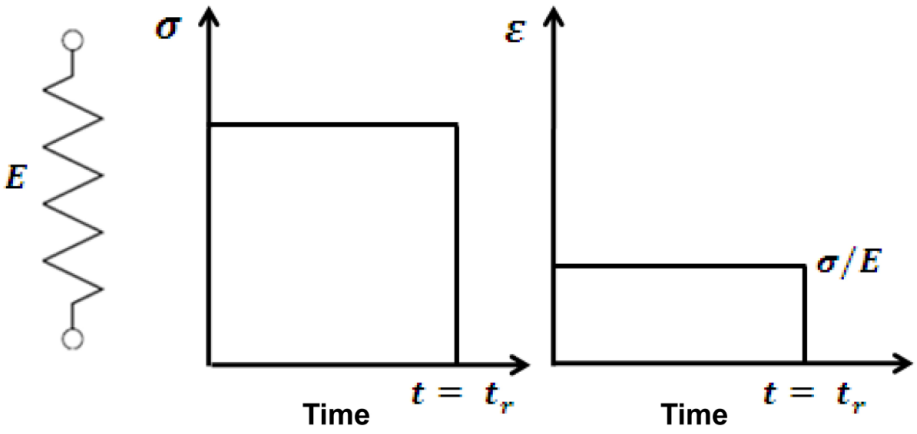

Figure 3.1: Response of an ideal spring (after [5])

For an ideal liquid, the Newton's law holds: the stress σ is proportional to the rate of deformation $d\varepsilon/dt = \dot{\varepsilon}$; the proportionality constant is the viscosity η, so $\sigma = \eta\dot{\varepsilon}$. As a model for such behaviour we choose a dashpot; within a cylinder filled with a fluid a piston with some clearance can move. Figure 3.2 shows its behaviour: There is no instantaneous response; the deformation is proportional to time, and no recovery takes place. The dashpot is characterized by η.

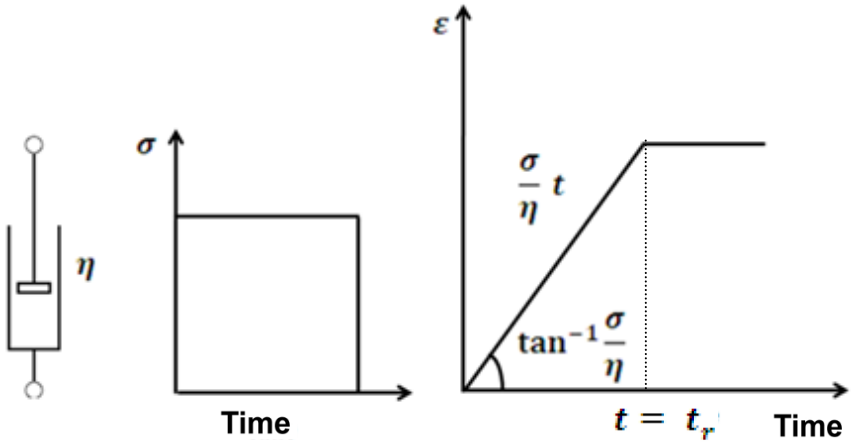

Figure 3.2: Response of an ideal liquid (after [5])

The behaviour of viscoelastic materials can be represented mathematically by combinations of spring and dashpot elements connected together. In these mathematical models springs and dashpots are used to simulate the elastic and viscous components of the constitutive material response. Despite models consisting of combinations of springs and dashpots do not correspond directly to discrete molecular structure; they enhance our understanding of the material's response to stress/strain variations. Generally, the more sophisticated the model, the better it will fit to experiment, but the greater the number of experimental constants required. Examples of simple models include the Maxwell model, the Kelvin-Voigt model, the standard linear solid model, and generalized Maxwell model. The latter is the most general form to represent linear viscoelasticity. It assumes that relaxation does not occur at a single time; instead it occurs at a distribution of times. Molecular segments have different lengths with shorter ones contributing less than longer ones; this leads to varying time distribution. This can be represented by having as many spring-dashpot Maxwell elements as are necessary to accurately represent the distribution. Figure 3.3 shows a representation of the generalized Maxwell model [6].

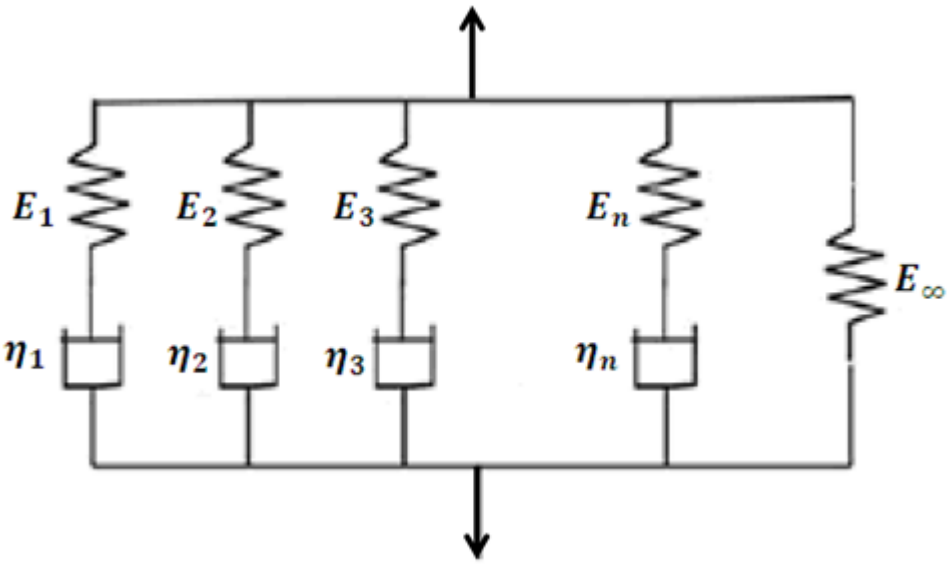

Figure 3.3: Generalized Maxwell model (after [6])

From creep or relaxation experimental results, see Figs. 3.4 and 3.5, it is possible to determine the time-dependent constitutive equations based on the stress and strain history as well as the loading rate and time of load application. A common form for

these constitutive equations employs a Prony series; the viscoelastic material model is defined as follows using that technique:

For a small-strain tension test with a constant tension strain ε applied to the material, the stress response $\sigma(t)$ can be defined by the viscoelastic material model [9]:

$$\sigma(t) = E_R(t)\varepsilon, \text{ for } t > 0, \qquad (3-1)$$

where $E_R(t)$ is a relaxation modulus. The viscoelastic material has an asymptotic constant stress level for t→ ∞, in other words, $E_R(t) \to E_\infty$.

The relaxation modulus can be written in dimensionless form as:

$$e_R(t) = E_R(t)/E_0, \qquad (3-2)$$

where $E_0 = E_R(t)$ is the instantaneous modulus, so the expression of the stress takes the form:

$$\sigma(t) = E_0 e_R(t)\varepsilon, \qquad (3-3)$$

The dimensionless relaxation function has the limits of $e_R(0) = 1$ and

$$e_R(\infty) = E_\infty/E_0. \qquad (3-4)$$

The viscoelastic material is defined by a Prony series expansion of the dimensionless relaxation modulus in the following way:

$$e_R(t) = 1 - \sum_{i=1}^{N} e_i\left(1 - e^{-t/\tau_i}\right), \qquad (3-5)$$

where e_i and τ_i are material constants, i =1,2,…, N.

These material constants can be obtained by fitting creep or relaxation experimental data to the dimensionless relaxation modulus, Eq. 3-5, as it will be discussed in chapter 5.

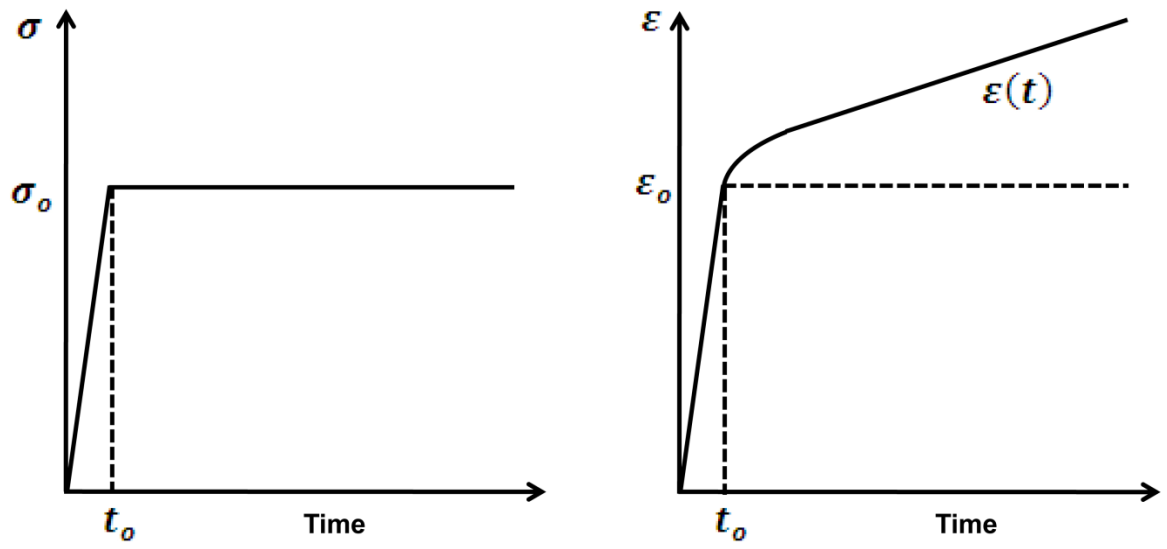

Figure 3.4: Viscoelastic material characterization: creep test

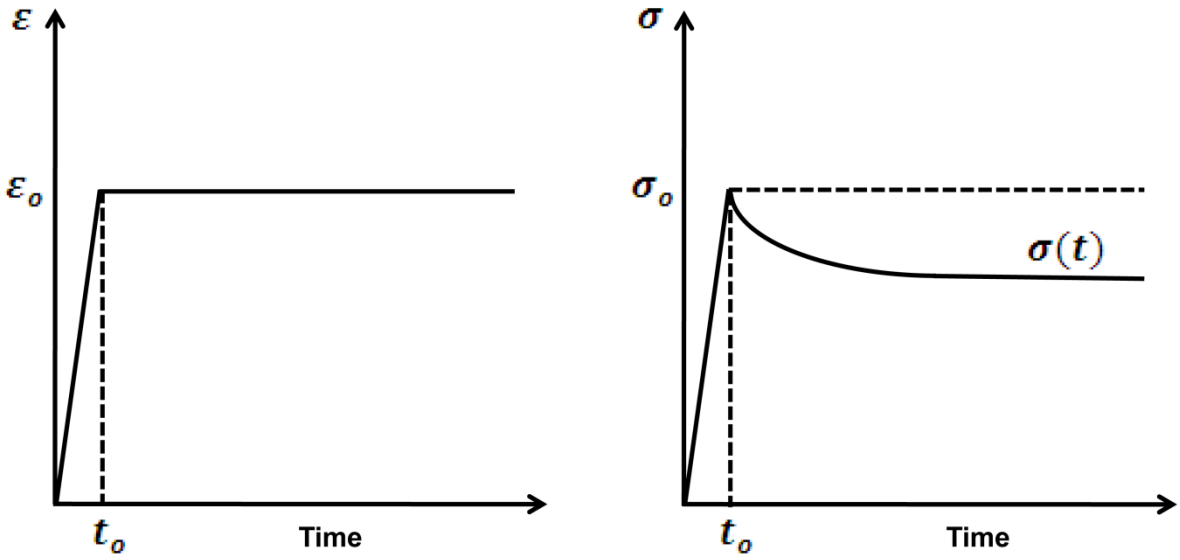

Figure 3.5: Viscoelastic material characterization: relaxation test

3.4. Creep and Relaxation Tests of Cortical Bone Tissue

Bone like all biological materials possesses time-dependent viscoelastic properties. Thus, different paths of load-elongation curves for each test cycle are yielded when a specimen is subjected to cyclic uniaxial tension, forming hysteresis loops. The hysteresis loops represent the energy dissipated as a result of non-conservative or dissipative process. There are three classic experimental tests for characterising the viscoelastic properties; stress relaxation, creep tests, and dynamic mechanical

analysis (DMA) [74]. The following sections describe some viscoelastic experimental tests available in the literature. Rauber [75] was the first to investigate bone viscoelasticity by studying its creep, anisotropy and strength. Later studies investigated a bone's viscoelastic behaviour, for instance, Smith and Keiper [76], Sedlin [77], Knets and Vilks [78]. Lakes and Katz [79] converted the results obtained by various authors in tension/compression to a common representation and compared them; a significant disagreement was found among axial deformation results. They applied the Boltzman superposition integral to describe the viscoelastic behaviour of bone in compression and came to the conclusion that it cannot be applied for the entire frequency range. This was followed by a series of papers for torsional and biaxial loading conditions [80-82]. Now, more data are available; some are covered below.

3.4.1. Effect of Water Content, Demineralization and Stress-Induced Fluid Flow on Viscoelasticity

The major constituents of bone are a stiff hydroxyapatite mineral phase and collagen matrix. It is considered that the interaction between these two phases determines mechanical properties of a bone element. Still, as yet there have been no models, describing the mechanical structure responsible for the interaction between mineral phase and collagen matrix in bone. It was known that the mechanical properties of fibril collagen are affected by the water content [83], while those of the mineral phase are believed to be unaffected. There have been many observations of the effects of water content on mechanical properties of bone tissues [84]. Drying increases the modulus of elasticity, increases the tensile and bending strength and makes bone much more brittle and less tough. Bone is not a perfectly elastic material; it is non-elastic. The importance of molecular motion in the collagen phase of bone in determining bone's non-elastic properties was demonstrated in [85]. Accordingly, it has been thought that the relaxation phenomenon in bone may be changed by water content of the bone specimen. This was found to be true [85]. Such changes in the relaxation properties due to water content might provide a clear interpretation for relaxation mechanisms in bone [86]. In an attempt to determine the phase (collagen or hydroxyapatite) responsible for creep behaviour in cortical bone, Bowman *et al*. [87] investigated demineralised bone. The study results suggested that collagen is the phase responsible for creep.

The same conclusion was drawn by another study using a thermally-stimulated creep method [88]. Another study investigated the effect of stress, temperature and microstructure on creep of bovine compact bone; a positive significant association between the estimated mean steady-state creep rate, the volume fraction of the secondary Haversian bone, applied stress and temperature was found [89]. Also, the effect of structural anisotropy on the relaxation modulus of cortical bone was presented by Iyo *et al*. [90]. In that study, stress relaxation of cortical bone was expressed by a combination of two relaxation processes according to Kohlraush-Williams-Watts (KWW) functions: a fast process with relaxation time less than 100 s, and a slow process with a relaxation time in the order of 10^6 s. The study results indicated that for the fast process the relaxation modulus for specimens cut parallel and perpendicular to bone axis was almost the same, and the relaxation process is attributed to a mechanically isotropic component – collagen. However, the slow relaxation process was related to a higher order structure that is responsible for the anisotropic mechanical properties of bone – a mixed phase of collagen matrix and mineral particles.

3.4.2. Experimental Studies of Creep Deformation

Only a small number of experimental studies of creep are available for investigation of cortical bone tissues. Fondrk *et al*. [91] performed multiple cycle tensile creep tests on human and bovine cortical bone specimens. The results of that study suggested the existence of a stress threshold, above which time-dependent effects dominate the material response and below which the behaviour is primarily linear-viscoelastic, with time effects playing only a secondary role. There were two regimes of behaviour in the experimental results a regime associated with lower stresses and a regime associated with higher stresses. In the former, strains were completely recoverable and approached a limit when the load was held constant. In the later, permanent strains developed and a constant creep rate was produced by a constant load. In that study, 10 s^{-1} creep rate criterion was proposed to distinguish between the two types of behaviour, i.e. the stress that produces a steady-state creep rate of 10 s^{-1} was considered to be the boundary between the two regimes. A constant steady-state creep rate is produced by a constant stress above the threshold. By relating the steady-state creep rate to the hold stress, the creep threshold was obtained. The creep rate thresholds were 73($\pm$5) MPa for human

bone and 117($\pm$10) MPa for bovine bone. Even after defining these stress levels, there is a possibility of various creep mechanisms at lower stress levels that still has to be considered in the future research.

The steady-state creep rate was plotted as a function of stress, and the magnitude of the creep rate was an exponential function of the stress magnitude. In that study, it was found that the creep rate remained relatively constant over 50 minutes until rupture occurred at a final strain of 3.5%. Moreover, it was found that a major part of inelastic strain was recovered on unloading and that accumulation of creep strain increased the material's compliance on subsequent loading below the threshold. Those two factors suggested that a damage mechanism was responsible for the nonlinear behaviour of the material.

Cotton *et al*. [92] observed an accumulated permanent strain in fatigue tests with creep behaviour, but the primary and tertiary portions of curve were not examined. The primary portion included plasticity and the tertiary portion included fracture and reduction of stressed. It demonstrated that creep was not the only mechanism in loading responsible for accumulation of the "permanent strain". Some effects such as viscoelasticity or plasticity may still occur in the non-linear material response of cortical bone to fatigue. Another study, that reported the result of tensile fatigue tests, was introduced in [93] using specimens from femoral cortex. The specimens were tested in zero tension fatigue (stress ratio $R = 0$) until failure. In that study, creep rates were reported as well as the rate of stiffness loss over the middle part (between 10% and 90%) of the specimen's life time for various levels of stress and numbers of cycles. In that work, authors examined associations of the evolution of damage (drop in modulus per cycle) with the stress level (or through the undamaged tangent modulus) and with the creep rate.

A method for identification of viscoelastic characteristics of the bone using transient-response information arising from a Split-Hopkinson Pressure-Bar (SHPB) test was developed by Tanabe *et al*. [94]. Impact compression experiments of bovine femoral compact bone (plexiform bone) were performed using SHPB. Interesting results regarding the cortical bone internal friction loss and its rigidity along different axes were also found: both parameters are greatest along the bone's axial direction. In

other words, the function of a shock absorber, along the bone axis direction is superior to that in the other directions.

Damage in bone can be manifested not only as a stiffness or strength loss but also in its viscous properties as measured by changes in both the rate and magnitude of relaxation. It was found that these properties are more sensitive to damage than the modulus [95]. Won *et al*. [96] investigated the effect of hold condition and recovery time on viscoelastic measures of tensile damage in cortical bone. In that study, longitudinal bone specimens were subjected to tensile test consisting of three loading cycles: pre-damage loading cycle, damage loading cycle, and post-damage cycle. Controlled variables were the recovery time (1, 10 and 100 min) and hold condition (zero-load or zero-strain) after the damage cycle. The damage measures were calculated as the ratio of each post-damage cycle to the pre-damage value for the loading modulus, secant modulus, unloading modulus, stress relaxation and strain (stress) recovery at 1 min post-diagnostic time. It was concluded in that work that the damage cycle caused reduction in all measures. Also, there was apparent modulus degradation for both hold conditions with recovery time. On the contrary, stress relaxation was unaffected by recovery time for both hold conditions. On the other hand, zero-strain hold conditions resulted in lower values for degradation of the modulus and change in relaxation. Finally, it was found that stress or strain recovery after the damage cycle was evident even after 100 min, but 90% of the recovery occurred within 10 min. Accordingly, the results of that study suggests that a choice of the test conditions can influence the apparent magnitude of the damage effects. Also, it was suggested that 10 min recovery was sufficient to stabilize most measures of the damage state.

3.5. Dynamic Mechanical Analysis (DMA)

The first one who attempted to measure a material elasticity was Poynting in 1909. Following this, attempts started to develop experimental techniques using oscillatory deformations to study metals, which were reviewed by Nijenhuis in 1978. Then, DMA started to be an important tool to deal with materials such as polymers, metals, etc. Dynamic Mechanical Analysis (DMA) provides a unique insight into both mechanical and thermal properties of materials. It also gives information about the modulus and damping behaviour of a material with respect to frequency and/or

temperature [97]. In DMA the specimen is deformed and released in sinusoidal fashion. Using the amplitudes of the force and motion, the modulus is calculated. Whereas, using the time delay between the applied force and the resulting motion, damping is measured. In the following sections, some of the available results for DMA-based experimental work with cortical bone specimens are introduced.

For decades, researchers have been trying to characterize viscoelastic properties of bone tissues. Some literature works about viscoelastic properties of bone tissue, particularly cortical bone, will be summarized here. Wang and Feng [98] explored the effect of mineral content on the dynamic mechanical thermal behaviour of cortical bone with the use of dynamic mechanical thermal analysis (DMTA). In addition, the effect of reducing the bone mineral content (BMC) on the microstructure of the collagen fibres and the denaturation temperatures of bone was investigated. In that experimental study, three specimens from each group were tested in a single cantilever mode, using a dynamic mechanical analyzer. Temperature was scanned from 20°C to 300°C at the scanning rate of 2°C/min and a loading frequency of 1 Hz. During temperature scanning the equipment was able to monitor the complex modulus, E^* and the loss factor, tan δ.

The results from DMTA analysis indicated that the storage modulus (E') and loss modulus (E'') of bone specimens decreased systematically upon decreasing BMC, whereas the loss factor (tan δ) increased. A tan δ peak broadened and split into two peaks with the decreasing BMC. In assessments with a differential scanning calorimeter (DSC), a shift of denaturation temperature to a lower region with decreasing BMC was observed, and the denaturation temperature was nearly the same at which E' decreased significantly with the temperature increase. The DSC analysis revealed the protection role of mineral crystals; they function more effectively to prevent collagen from denaturing and decomposing when BMC is higher. In conclusion, the results of that study suggested that the decrease of bone mineral content not only resulted in the decrease of stiffness of bone, but also, in the increased of risk of bone fracture in fall due to the decrease of E''.

In terms of the physiological range of strain, Schaller *et al*. [99] summarised that within, i.e. (10^{-4} and 10^{-3}), bone behaves essentially as poroviscoelastic material with linear elasticity, weakly non-linear viscosity and multiscale porosity. Bone

behaves in a time-dependent manner beyond the physiological range in the form of irreversible deformations and reduction in its elastic properties. The author stated that since the mineral crystals behaved in a linear elastic fashion, so the organic phase was associated with a viscous behaviour of bone. Therefore, the reversible viscoelastic properties of bone could be used as a diagnostic tool for an organic phase status and also provide relevant clinical information for post-yield properties. By using mechanical spectroscopy, the viscoelastic behaviour of bovine cortical bone in terms of temperature and frequency was investigated. In that study, a continuous increase in the damping associated with a continuous decrease in the shear modulus with a temperature range from 300 to 350 K and a frequency range from 5 Hz to 5 mHz was observed for bovine compact bone. It was also found that an irreversible change of viscoelastic properties when subjecting the specimen to thermal cycling up to 420 K can be interpreted as degradation of the organic phase.

From another point of view, in measuring viscoelastic properties of bone tissue, Yener *et al*. [100] studied whether the presence of a flaw would have an influence on the apparent viscoelastic properties of bone. That work examined the effect of flaw orientation on apparent viscoelastic properties and studied utilization of Dynamic Mechanical Analysis as a non-destructive means for detection of damage. Using a DMA machine, a storage modulus (E') and loss factor ($\tan\delta$) were measured, for loads in two different orientations. In that experiment, cortical bone beams were subjected to three-point-bending DMA analysis in two orientations. They were vibrated both in the craniocaudal (i.e. starting from anterior of cortical bone and ending at posterior) and in the mediolateral direction (i.e. starting from the middle of the cortical bone and ending at one side). A through-thickness notch was cut at the centre of the beams on the caudal surface, and the DMA analyses were repeated in the same orientations as pre-notch measurements (W = 2 mm, a/W= 0.5, and d = 150 μm) [100]. In that study, viscoelastic measurements were performed in 0.9% saline solution at 37°C using a three-point bending configuration for a frequency range of 1–10 Hz. The craniocaudal/mediolateral ratio was calculated for $\tan\delta$ and E' and considered as a measure of anisotropy.

Regression analysis and analysis of covariance for results of experiments were used in that work to examine a relationship between viscoelastic parameters and

frequency. The results showed that tan δ and E' were not different for craniocaudal and mediolateral measurements before the flaw was introduced. In the presence of the flaw, tan δ significantly increased whereas E' reduced significantly for craniocaudal measurements. Accordingly, tan δ and E' were nearly isotropic in the tested directions before the introduction of a flaw into the bone tissue. By introduction of a flaw an increase in the anisotropy of tan δ and E' was observed. Presence of a notch resulted in a significant increase in tan δ anisotropy with increasing frequency. In conclusion, that work demonstrated that cortical bone tissue exhibited different apparent viscoelastic behaviour in the presence of flaw and depending on the flaw's orientation.

3.6. Fracture Models of Cortical Bone

Bone is a vital connective tissue, which reflects the balance between two major functions: provision of mechanical integrity for locomotion and protection of vital internal organs, and sustains calcium homeostasis [101]. One of the primary functions of bone is to support applied loads and moments generated during life activities; these loads and moments result in mechanical strains in the bone tissue. Therefore, the mechanical performance of bone is of significant importance for the quality of life. Bone as a material has its maximum capacity for supporting loads, beyond which it can fracture. There is more than one reason for bone fracture; on the one hand, bone can fracture under loads exceeding certain threshold levels of its capacity, for instance, in cases of traumatic falls and involvement in a car crash. On the other hand, other fractures are caused as a result of disease, surgical intervention and pharmaceutical treatments [102]. Following bone fracture, implants for bone reconstruction, such as internal fixation screws can be used [103].

In the current study, the major aim is development of a numerical model of cortical bone's fracture under impacts arising from sudden events, for instance, traumatic falls and car accidents. Hence, one of the main factors that would help to formulate the model, capable to reproduce adequately cortical bone fracture, is defining bone's fracture properties and implementing them in the model. Therefore, in the following sections a description of the use of mechanics, along with various characterization techniques, used to develop a framework for the study of failure

behaviour of cortical bone in addition to quantifying its fracture properties, is introduced.

3.6.1. Fracture Toughness

The susceptibility of bone to fracture can be assessed using an important parameter called *fracture toughness*. Fracture toughness measures the ability of a material to resist crack growth. Therefore, bone with low fracture toughness is more likely to fail compared to that with high toughness. Commonly, there are three main approaches to assess fracture toughness: the critical stress intensity factor, K_c the critical strain energy release rate, G_c and the work of fracture W_f. By computing the area under the stress-strain curve, the work of fracture can be characterised. A stress field near a crack tip can be described by the critical stress intensity factor(s), and the energy required to extend a pre-existing crack is linked to the critical strain energy release rate [104]. The critical stress intensity factor and critical strain energy release rate depend on loading conditions, geometry of the crack, and mode of fracture. Any fracture can be described using one or combination of three basic modes; Mode I (tension mode), Mode II (shear mode), and Mode III (tearing mode), Figure 3.6.

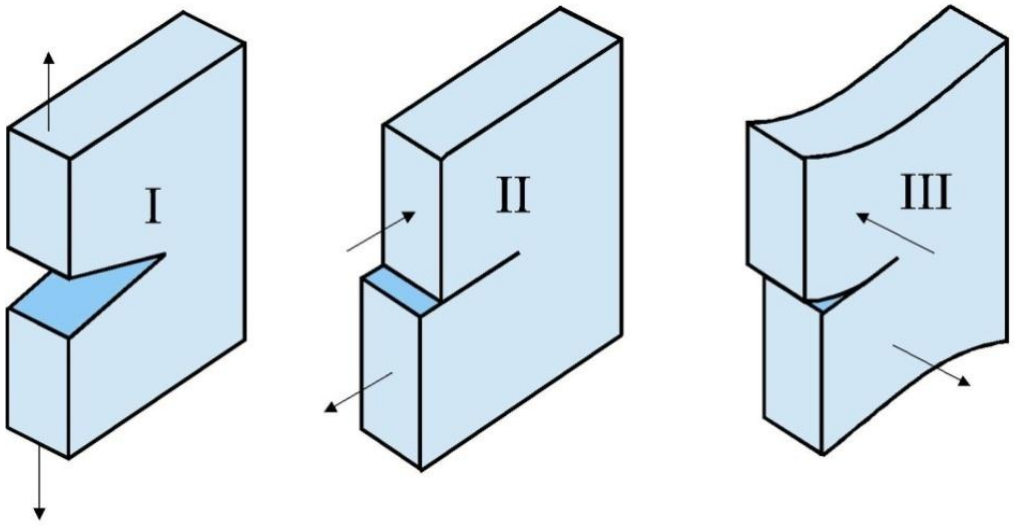

Figure 3.6: Schematic illustrations of different modes of fracture (after [7])

Small flaws in bone could lead to catastrophic failure due to crack propagation; this means that bone is notch-sensitive [105]. In addition, bone in nature is anisotropic and heterogeneous; therefore, fracture toughness of bone depends on crack

orientation (longitudinal or transverse) [106]. Several techniques are being used to assess fracture toughness of bone, such as compact tension, single-edge notched tension and three-point bending tests. Some of these techniques as well as some factors affecting bone fracture are described in the following sections.

3.6.2. Work of Fracture

One approach that has been used to characterise the toughness of cortical bone is the work-of-fracture method [107, 108]. The work of fracture W_f is the area under a load-displacement curve measured at failure of a flaw-free specimen divided by twice nominal crack-surface area. The dependence of the results of both the specimen size and geometry is a major drawback of this method [7]. Thus, comparison of different study results using this method is not valuable [7]. Accordingly, it is better to use linear elastic fracture mechanics (LEFM) to characterise such a tissue. Hence, the stress and displacement fields near a pre-existing crack can be described by stress intensity factor(s). Alternatively, bone's toughness can be expressed in terms of strain energy release rate as discussed in the next section.

3.6.3. Measurements of Fracture Toughness K_{IC} and G_{IC}

In order to characterise bone as a material, understanding its failure characterisation is required. Since the fracture of cortical bone is a complex process, it has received considerable attention in the past few decades. Using traditional strength of materials approach, some investigations of the ultimate strength of bone revealed that the gained information did not fully characterize the actual process of bone fracture. This conclusion led to the utilization of the LEFM for better understanding of the fracture of the bone in terms of its fracture toughness. This means determination of the critical stress intensity factor K_c and critical strain energy release rate, G_c [33].

On the one hand, the stress intensity factor $K_{(\mathrm{I,II,III})}$ can be defined for Mode I (tension mode), Mode II (shear mode), and Mode III (tearing mode) in terms of applied stress σ_{app}, crack geometry, and crack size a_c, as follows [109]:

$$K_{(I,II,III)} = Q\ \sigma_{app}\ (\pi a_c)^{\frac{1}{2}}, \qquad (3-6)$$

where Q is a dimensionless constant dependent on sample geometry and loading mode (i.e. Mode I, II and III). Then, the critical stress intensity factor can be determined for a particular mode of failure at the onset of the unstable fracture, which is the resistance to fracture, or the fracture toughness.

On the other hand, critical strain energy release rate G_c can also be used to describe the resistance to fracture. It can be defined as the change in the potential energy per unit increase in a crack area at fracture; this can be expressed as follows [109]:

$$G_c = \frac{P^2}{2B}\frac{dC}{da_c}, \qquad (3-7)$$

where P is the applied load, B the specimen thickness and dC/da_c is the change in sample compliance with crack extension (the compliance C is the slope of the displacement-load curve).

Some results for fracture toughness reported by various investigators are given in Table 3.1.

Table 3.1: Fracture toughness of bovine femur for longitudinal cracks for SEN (single-edge notched bend), 3-PT (three-point bending) and CT (compact tension) (after [21])

Direction	Specimen type	K_c (MPa$\sqrt{\text{m}}$)	G_c (J/m^2)	Type of Crack Propagation	Reference
Longitudinal	SEN	3.21±0.43	1383-2557	Slow	[110]
	CT	3.62±0.73	-	Slow	[111]
	CT	3.4	1260	Slow	[112]
	CT	4.01± 0.31	-	Slow	[113]
Transverse	SEN	5.58±0.52	3135 - 5534	Slow	[110]
	3-PT	5.1±1.4	7960	Slow	[114]
	SEN	2.2 - 4.6	-	Slow	[115]
	CT	5.1	-	Slow	[116]

3.6.4. Dependence of Cortical Bone's Fracture Toughness on Orientation and Loading Conditions

Long bones that have an irregular shape and anisotropic mechanical properties are usually under combined loading during daily life or spontaneous activities. Accordingly, bones rarely experience pure tensile loading, but rather a combination of the three basic fracture modes [117]. A recent study was devoted to finding out the dependence of fracture toughness on the orientation and loading condition [117]. Using bovine femora, G_{IIc}/G_{Ic} and G_{IIIc}/G_{Ic} ratios between critical energy for fractures of Modes I, II and III were found to be 3.8 and 2.6, for longitudinal fracture and 3.4 and 2.9 for transverse fracture, respectively. Though such results suggest that Mode-III fracture might be easier than Mode-II, it is unclear whether this will be true for all species, locations, orientations and other variables [7].

3.7. Indentation Fracture Technique

Indentation fracture was first proposed by Palmqvist [118] and developed by Evans *et al*. [119] for measurement of microstructural toughness in ceramics. Biological materials like dentin and enamel that often considered as analogies to the bone tissue because of their structure and anisotropy have also been considered the subject of indentation fracture [120]. In this technique, a sharp indenter is employed to grow cracks at the microstructural level in the materials. Then, toughness of the material can be calculated using the length of these cracks and empirical relation, Figure 3.7. Indentation fracture has some advantages over the traditional toughness- testing methods:

1. The ability to measure the toughness at the microscale level.
2. No need for preparing/machining micro-specimens.
3. Extremely efficient technique, allowing many measurements on a small quantity of material.

In the case of bone, the developed cracks are of the same length scale as those observed *in-vivo*, therefore, it might provide a more relevant insight into the nature of damage in bone [8].

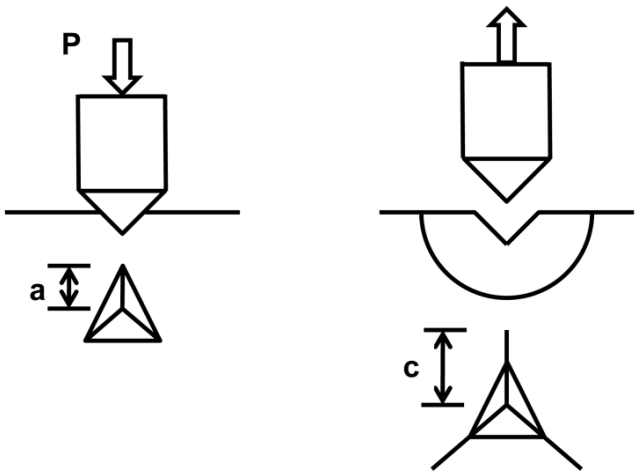

Figure 3.7: Indentation fracture schematic diagram: (a) growth of a Palmqvist-radial cracks upon loading of length, a which is observed along the impression of the interface of the indenter tip; (b) median cracks that emanate from indentation corners, producing an overall crack length c (after[8])

When bone experiences daily activities, microcracks are generated. To understand their growth as well as fracture of bones, various methods to measure bones' fracture toughness have been proposed. However, those studies measured only fracture toughness at macroscopic level, and not at microscopic level [8]. Mullins *et al.* [8] proposed a technique for measuring fracture toughness of cortical bone at microstructural level. Since it allows the investigator to observe mechanisms and measure toughness at a length scale, at which *in-vivo* damage is known to exist.

Fracture toughness K_c can be related to the crack length c using the following equation (Evans *et al*. [119]):

$$K_c = \alpha(E/H)^{\frac{1}{2}}(P/c)^{\frac{3}{2}}, \qquad (3-8)$$

where P is the maximum indentation load, E and H are the modulus and hardness of the material, respectively, and α is an empirical constant, which depends on the geometry of the indenter (α=0.040 for a cube-corner tip). Since the cortical bone is anisotropic and the equation derived by Evans *et al*. [119] assumes isotropy, so an average modulus and hardness values were used to compute fracture toughness K_c. It was found that only the cube-corner indenter tip produces cracks. Also,

toughness increases when a crack length increases. At the maximum applied load of 3 N, the maximum toughness was measured at about 2.3 MPa$\sqrt{m}$, and produced an average crack length of 56 μm. This value is at the lower end of the range observed in other studies, in which macroscopic toughness of bone was measured [121]. The observed scatter in the data was explained as a result of a heterogeneous nature of cortical bone and differences between the tested samples. Later, by the same group and the approach, the difference in crack resistance of a microstructural bone tissue, such as osteons, interstitial matrix and trabecular bone was investigated [122]. It was found that at the same load, cracks produced in trabecular bone are longer than those in interstitial and osteonal cortical bone. Similarly, within individual constituents, cracks produced in interstitial bone are longer than those in osteonal cortical bone.

A novel microindentation testing method was designed to force pre-existing naturally occurring linear microcracks to open [123]. In that study, a 3 cm mid diaphyseal part of left humerus of a dog (age 15 years) was excised and bulk-stained in 1% basic fuchsin in a graded series of alcohols (80%, 90%, and 100%) under a vacuum of 20 mmHg for the total of 18 days. After the sample was embedded in methylmethacrylate, a microtome was used to produce a smooth surface for microindentation testing. A CSEM microindenter (Peseux, Switzerland) was used to conduct all the indentation testing. Based on the optical microscopic observations, linear cracks with approximate length of 100-150 μm were selected. A Vickers indenter tip was used in all the tests. The edges of the indenter were aligned with the crack orientation before measurement. Initially, a 5N load was placed near the centre of the microcrack. This load caused the existing crack to open, but did not cause its growth. Additional indentations were made at progressively higher loads (up to 9 N) until crack growth was discernable. The fracture toughness was calculated based on Equation (3-8).

Obviously, quantifying deformation and fracture behaviours of the cortical bone tissue analytically is cumbersome, especially, for impact loading. Therefore, in the current study, finite-element methods will be employed, and finite-element models available in the literature will be introduced in the next chapter.

3.8. Summary

- The mechanical behaviour of bone, as most biological materials, has a viscoelastic character; it exhibits a time-dependent response to external loads.
- The viscoelastic properties can help in understanding the effect of dissipated energy during bone fracture.
- The behaviour of viscoelastic material can be mathematically represented by combinations of spring and dashpot elements connected together, such as in the generalized Maxwell model.
- A relaxation phenomenon response in bone is affected by its water content.
- Collagen is the phase responsible for bone's creep behaviour.
- Bone can fracture when it is loaded beyond its capacity in cases such as traumatic falls, involvement in car crash, etc.
- There are three main approaches to assess fracture toughness of bone at macroscopic level: the stress intensity factor, the strain energy release rate and the work of fracture.
- Fracture toughness of bone at microscopic level can be quantified using the indentation fracture technique.

4. Chapter 4

Finite-Element Analysis of Deformation and Fracture of Cortical Bone Tissue

4.1. Introduction

Finite-element analysis is a branch of computational mechanics, in which an approximate numerical solution is obtained to the equations of calculus, to predict a response of a physical system to external loading conditions. In this method, the continuous structure (or continuum) is divided into regions called *elements*. The collection of elements is called a *mesh*. Both the material properties and the governing equations are assumed over these elements and expressed mathematically in terms of unknown values at specific points in the element called *nodes*. Individual elements are assembled together to represent the whole structure. A set of algebraic equations is obtained when the loads and the boundary conditions are imposed. Solution of these equations gives an approximate solution of the behaviour of the structure.

With the recent developments in the computer science (hardware and software), finite-element analysis is being applied to a variety of engineering problems including biomechanics, for instance, in structural and material analysis of bone. A research interest in this area was arisen focusing on the use of the finite-element method to understand the mechanism of bone fracture [124]. However, most of the research studies in the literature analysed distributions of stresses and strains, and did not show the fracture process including crack initiation, propagation and complete failure. One reason behind this was the limitations of the standard finite-element method. Due to the mesh-based interpolation, distorted or low quality meshes, as a result of crack propagation, lead to higher errors, necessitate remeshing, a time-consuming and laborious task. In addition, this method is not suitable for treating problems with discontinuity that do not align with the element edges. Therefore, alternative approaches were recently tried to overcome scheme drawbacks of the standard finite-element when dealing with problem, such as

fracture; one of them is so called *extended finite-element method* (X-FEM), which will be introduced in the next section.

This chapter is divided into three main sections: a brief introduction to the extended finite-element method (X-FEM), literature review of finite-element models of cortical bone at macro- and microscopic levels.

4.2. Extended Finite-Element Method for Crack Propagation (X-FEM)

Modelling crack growth using the standard finite-element method is cumbersome due to the need for the mesh to conform to the continuous geometry. This becomes even more difficult when dealing with problems with evolving discontinuities where the mesh has to be regenerated at each step. Another challenge is representation of the crack-tip singularity [125]. Due to the fact that standard finite-element method is based on piecewise differentiable polynomial approximation, it is not suitable for discontinuous or singular solution problems. It entails considerable refinements of the mesh or meshes that conform to the geometry of the discontinuity to get accurate results [126]. Apparently, X-FEM was developed in response to the deficiency of the standard finite-element method to tackle these drawbacks.

The extended finite-element method (X-FEM) is a numerical method used to simulate discontinuities included in a continuum, such as holes, inclusions or cracks, without entailing the mesh to conform to these discontinuities. It enables analysis of crack propagation without remeshing a cracked specimen in accordance with the newly created crack faces. It employs a local enrichment of the approximation areas. The method can be useful for evolving processes with non-smooth characteristics in small parts of a computational domain, e.g. near discontinuity or singularity regions, as in the case of cracks, for which standard finite-element method is not accurate. The X-FEM was first introduced by Belytschko and Black [127]. Enrichment is realized based on a partition-of-unity concept developed by Melenk and Babuska [128]; it allows incorporation of local enrichment functions into a finite-element approximation domain. Spatial discontinuous enrichment functions with additional degrees of freedom to the finite-element approximation ensure account for discontinuities [9].

The basic components of the mesh-independent crack modelling in the finite-element software, Abaqus 6.10, used in this thesis, are as following:

1- A way to incorporate the geometry of discontinuity and the discontinuous solution field into finite-element standard functions;
2- A way to quantify the magnitude of the discontinuity – the displacement jump across the crack faces;
3- A method to locate the discontinuity;
4- Definition of crack initiation and propagation criteria [9].

These four elements are introduced briefly below.

4.2.1. Geometry of Discontinuity

For the purpose of fracture analysis, the geometry of discontinuity is ensured by special enriched functions in conjunction with additional degrees of freedom. These enrichment functions are near-tip asymptotic functions and discontinuous functions that can represent the crack-tip singularity and the jump in displacement across the crack surfaces, respectively. The displacement interpolation function is as following [9]:

$$u^h(x) = \sum_{I \epsilon N} N_I(x) \left[u_I + H(x) a_I + \sum_{\alpha=I}^{4} F_\alpha(x) b_I^\alpha \right], \qquad (4-1)$$

where $N_I(x)$ are the usual nodal shape functions; the first term in the square bracket of Eq. (4-1), u_I, is the nodal displacement vector related to the continuous part of the finite-element solution; the second term is the product of the nodal enriched degrees of freedom vector, a_I, linked to the discontinuous jump function across the surfaces of the crack, $H(x)$; the last term is the sum of products of the nodal enriched degrees of freedom vector, b_I^α, and the associated elastic asymptotic crack-tip functions, $F_\alpha(x)$. It is worth mentioning that the first term is applicable to the entire model's nodes; the second term is only valid for nodes of elements cut by the crack interior; and the third term is used only for nodes of elements cut by the crack tip [9].

Figure 4.1 shows the discontinuous jump function, called the Heaviside function $H(x)$, across the crack faces that is given by

$$H(x) = \begin{cases} 1 \text{ if } (x - x^*) \cdot \mathbf{n} \geq 0, \\ -1 \quad \text{otherwise,} \end{cases} \qquad (4-2)$$

where x is a sample (Gauss) point, x^* is the closest point on the crack to x and $\mathbf{n}$ is the outward unit normal to the crack at x^*. Also, it shows coordinates of the asymptotic crack-tip function $F_\alpha(x)$ in an isotropic elastic material, which is given by

$$F_\alpha(x) = \left[\sqrt{r}\,\sin\frac{\theta}{2}, \sqrt{r}\,\cos\frac{\theta}{2}, \sqrt{r}\,\sin\theta\sin\frac{\theta}{2}, \sqrt{r}\,\sin\theta\cos\frac{\theta}{2}\right], \qquad (4-3)$$

where (r, θ) are the polar coordinates system with its origin at the crack tip and $\theta = 0$ represents the tangent to the crack tip. Other asymptotic crack-tip functions can also be used to represent crack along a bimaterial interface, impinged on the bimaterial interface or in an elastic-plastic power law hardening material [9]. However, these functions depend on the crack location and the extent of inelastic material deformation [9]. To accurately model the crack-tip singularity, a constant track of crack propagation is required, which cannot be easily achieved, especially in a non-isotropic material. Therefore, asymptotic singularity functions can only be considered in the case of stationary cracks, whereas in the case of propagating cracks, they can be modelled using one of the two methods discussed in the next section.

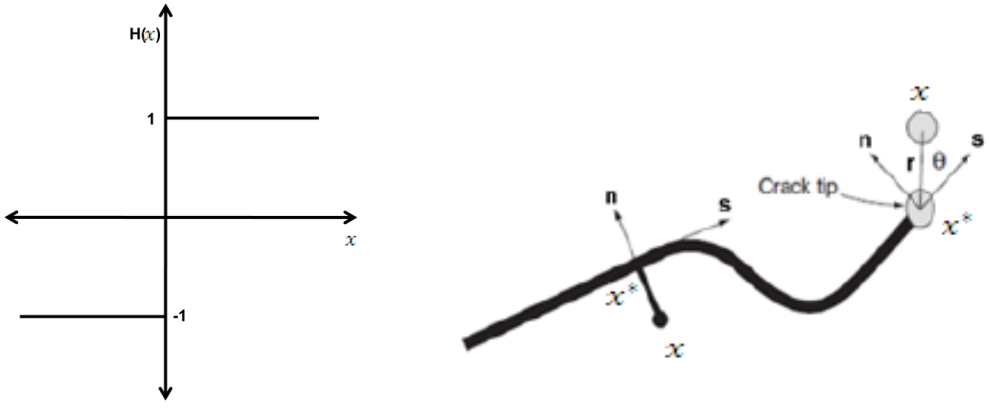

(a) (b)

Figure 4.1: (a) Heaviside function; (b) schematic illustration of normal and tangential coordinates for a smooth crack [9]

4.2.2. Magnitude of Discontinuity

In a case of propagating cracks, a displacement jump across crack faces can be quantified using two different methods: a cohesive zone model (CZM), and a virtual crack-closure technique (VCCT). The former is based on traction-separation cohesive behaviour, and the latter is based on the principals of linear elastic fracture mechanics (LEFM). The first approach, X-FEM-based cohesive segments method, can be employed to simulate the crack initiation and propagation along an arbitrary, solution-dependent path in a continuous material as the crack does not have to conform to the mesh boundaries. It is appropriate for both brittle and ductile materials. Furthermore, only the displacement jump across the cracked element is considered, since the crack has to propagate across the entire element at a time to avoid stress singularity modelling [9]. The second approach, X-FEM-based LEFM, is more suitable to model brittle fracture. Similar to the first approach, the crack-tip asymptotic singularity is not considered, and only the displacement jump across the cracked element is modelled. The modified virtual crack closure technique (VCCT) is used to quantify the strain energy release rate that in its turn is used to model a propagating crack along an arbitrary, solution-dependent path in the continuum without pre-existing cracks [9].

To represent the discontinuity of the cracked element in both cases, phantom nodes, superimposed on the real ones, are used. A discontinuous element with Heaviside enrichment is treated as a single element with real and phantom nodes that get split into two parts (see Fig. 4.2). Real and phantom nodes are completely constrained in an intact element, whereas when the element is cut by a crack, it splits into two, and each part has both nodes.

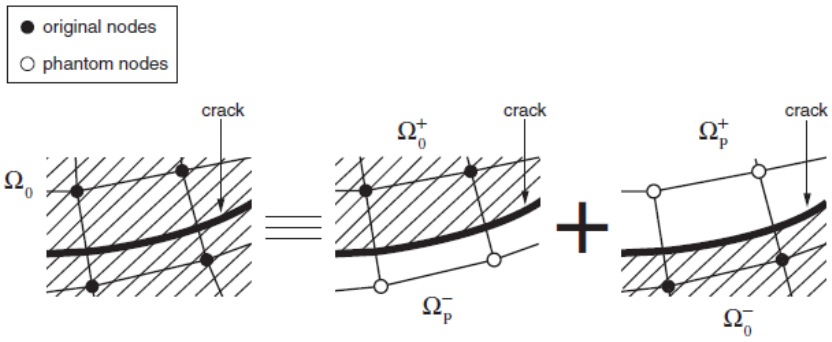

Figure 4.2: Phantom node method [9]

4.2.3. Location of Discontinuity

A crack can be located using a level set method. It is a powerful numerical technique for analyzing and computing interface motion. This method facilitates modelling of arbitrary crack propagation without remeshing. The crack geometry is defined by two approximately orthogonal signed distance functions (level sets) as shown in Fig. 4.3. The crack surface is described by the function ϕ, while the second function ψ generates an orthogonal surface. The intersection of the two surfaces gives the crack front. The positive normal to the crack surface is referred to as $\mathbf{n}^+$, and that of the crack front is referred to as $\mathbf{m}^+$. To describe the crack geometry, two signed distance functions per node are required [9].

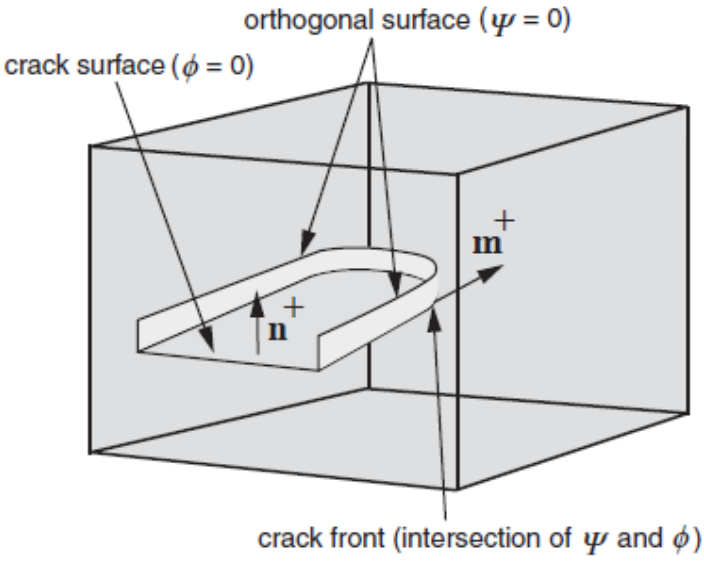

Figure 4.3: Three-dimensional non-planar crack represented by two singed distance functions ϕ and ψ [9]

4.2.4. Crack Initiation and Propagation Criteria

In the current study, only the cohesive behaviour that describes and governs the X-FEM-based cohesive behaviour will be introduced, since it will be used in the numerical part of this study. The X-FEM-based cohesive behaviour is modelled using the traction-separation law that consists of linear-elastic traction-separation model, damage initiation and damage evolution criteria. The traction-separation law in Abaqus presumes initially linear elastic behaviour followed by damage initiation and evolution. The elastic behaviour is represented in terms of elastic constitutive

matrix that relates the normal and shear stresses to their respective normal and shear separation of a cracked element [9]. Parameters of the elastic constitutive matrix are calculated based on elastic properties of an enriched element. Once the stress/strain level is high enough to introduce damage, degradation of the cohesive response begins at the enriched element; it is the crack-initiation symptom. There are several criteria for damage initiation, such as maximum principal stress, maximum principal strain, maximum nominal stress, maximum nominal strain, quadratic traction-interaction, and quadratic separation-interaction. Once the damage initiation criterion is met, a damage evolution law starts to be activated; it describes the rate at which the cohesive stiffness is degraded. Damage evolution can occur according to displacement-based damage evolution or energy-based damage evolution models. In the former model, the softening portion of the traction-separation has to be defined, such as linear, exponential or user-defined (see Fig. 4.4), in addition to the displacement at failure. In the latter model, the strain energy release rate of the enriched area's material can define damage evolution. More details regarding the mathematical representation of these criteria can be found in the Abaqus theoretical manual [9].

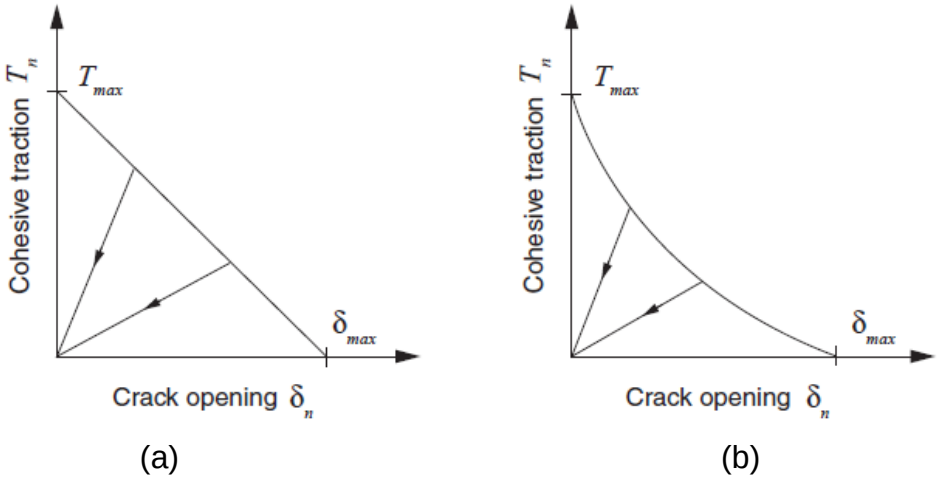

Figure 4.4: Typical traction-separation response: linear (a) and non-linear (b) [9]

4.3. Macroscopic Finite-Element Models of Cortical Bone Tissue

In the recent time, structural analysis of bone has been actively performed using the finite-element method in order to understand its fracture mechanisms. With an increasing number of bone fractures due to factors related to ageing, diseases or

dynamic events and taking into account complexity of the bone's mechanical behaviour, it becomes more and more important to understand and predict this behaviour using numerical models. Though most previous studies focused predominantly on distributions of stresses or strains, and did not demonstrate initiation and propagation of fracture in a cortical bone tissue, some studies developed simple bone fracture models as discussed below.

4.3.1. Modelling of Mechanical Behaviour

Several finite-element models were developed in the automobile industry to investigate the mechanical response of the human body under impact loading [129, 130]; but bones included in the model always considered as a linear-elastic material. In addition, the output of the model was predominantly force-deformation behaviour. Though some of those models considered the whole body model including bones, they dealt with bone from a structural rather than a material point of view.

From a point of view of mechanics of materials, some previous numerical models were developed using the homogenization theory to predict a macroscopic behaviour of the cortical bone tissue. For instance, Crolet *et al*. [43] introduced a mathematical developments based on the theory of homogenization to simulate the macroscopic behaviour based on microscopic mechanical characteristics. In their model, the compact bone was considered as a composite with a three structural levels material. At each level, the effective elastic tensor was obtained using homogenization based on the basic periodic cell. Approximations were made for modelling of lamellae and osteons: they were divided into cylindrical sectors; each sector was approximated with a parallelepiped having a periodic structure. The first level simulated the lamella characteristics, where the basic periodic cell was approximated by a cubic sector, and composed of collagen fibres and hydroxyapatite, which were considered isotropic. At the second level, the osteons were considered as cylinders with equal-thickness lamellae. In the last level, the Haversian's-system characteristics were simulated. In that model, in their endeavour to simplify the anisotropy of compact bone, they accounted only for geometric symmetry rather than the elastic one. Later, Aoubiza [131] developed another mathematical model to simulate the behaviour of compact bone using

homogenization method but without the approximations made for lamellae and osteons in the model developed by Crolet *et al*. [43]. Obviously, those mathematical models dealt with the elastic macroscopic behaviour of compact bone based on its microscopic properties, but they don't resolve the spatial distribution of local strain nor account for time-dependent properties.

4.3.2. Modelling of Fracture Behaviour

Since *in-vivo* fractures are often initiated and/or promoted by cracks, fracture mechanics is considered an important tool in assessing bone tissue's quality. Therefore, it can be used to enhance the diagnoses and treatment of bone fractures [132]. A limited number of numerical models were reported in literature studying initiation and propagation of cracks in cortical bone. For instance, Ural and Vashishth [10] developed a cohesive-zone-element model in order to capture an experimentally observed rising crack growth behaviour and age-related loss of bone toughness. The developed model was based on a traction-crack opening displacement relationship that can represent the propagating crack fracture process, see Fig. 4.5. The work showed a good agreement between the model and experimental results.

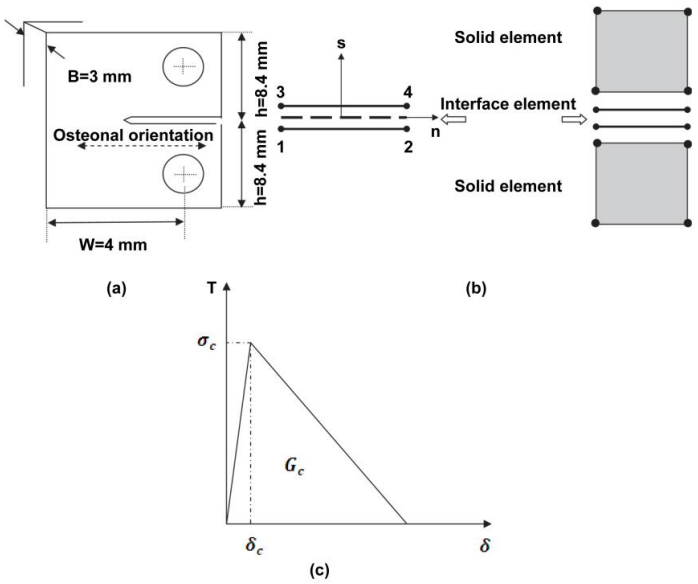

Figure 4.5: (a) CT specimen for fracture toughness testing; (b) schematics of 2D, 4-noded cohesive element and (c) traction-displacement relationship of cohesive-zone model (after [10])

Later, the same authors used their previous model to investigate the effects of age-related changes and orientation of crack growth on a toughening behaviour of human cortical bone. In addition, the model was used to investigate changes in the anisotropy of toughening mechanisms with age. The simulation results showed that, for a given age, initiation fracture toughness values were higher for a transverse crack growth than for a longitudinal one. On the contrary, during crack growth for a given age, the resistance in the longitudinal direction was higher than for the transverse crack growth. In addition, toughness anisotropy was higher for propagation than for initiation with almost no change with age (less than 1% for age from 50 to 90 yrs). On the contrary, anisotropy of initiation toughness decreased with increasing age by 6%/decade [133]. The used approach - cohesive-zone elements - still has a primary drawback: the crack extension path must be predefined. Obviously, this is not the case in the real fracture, where a real crack path is hard to predict.

Recently Morais *et al*. [11] demonstrated the adequacy of a Double-Cantilever Beam (DCB) test for determining fracture toughness under pure mode I loading of cortical bone by implementing a new data-reduction scheme based on specimen compliance and equivalent crack concept, see Fig. 4.6. The used method assisted to overcome the crack-monitoring difficulty during growth. In that study, a cohesive-zone model was used to simulate damage initiation and propagation, thus assessing the used methodology. The obtained results demonstrated the efficacy of both the DCB test and the proposed data reduction scheme on characterization of bone fracture under mode-I loading. Still, the model considered only quasi-static loading condition with a linear elastic material model of the cortical bone tissue.

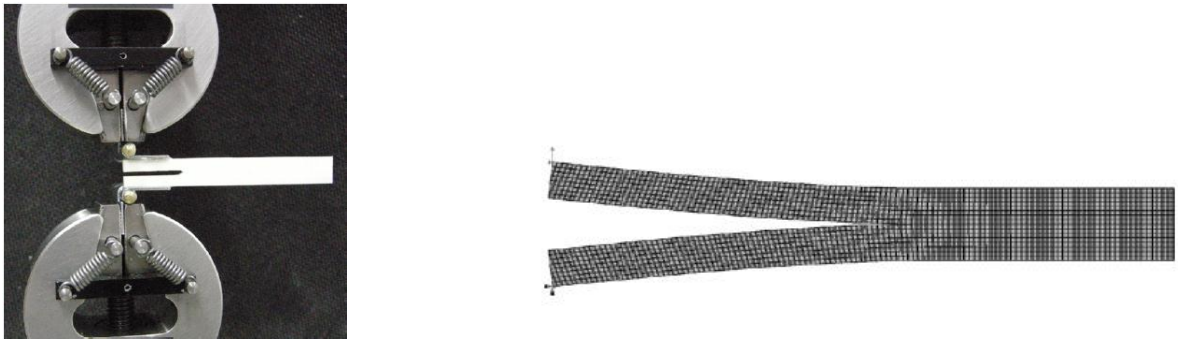

(a) (b)

Figure 4.6: DCB specimen: (a) during test and (b) mesh used in simulations [11]

In another study, a combination of experimental and numerical approaches was used to investigate crack-propagation mechanisms contributing to toughness of cortical bone [134]. Compact-bone specimens were prepared to study crack propagation in both longitudinal and transverse directions. The fracture response was simulated using virtual multi-dimensional internal bonds (VMIB) modelling. Using this numerical method, macroscopic constitutive relationship that describes the material's behaviour in terms of a tangent modulus can be expressed with parameters related to the microstructure. In that study, cortical bone was modelled as a material consisting of numerous bone unites/particles, with virtual bonds existing between adjacent bone particles. A constitutive relationship was derived and implemented into finite-element software (Abaqus 6.7) as a FORTRAN subroutine. Experimental and numerical results of the study exhibited rising resistance curves and anisotropy for crack growth in both longitudinal and transverse directions. Still, they neither accounted for dynamic loading nor viscoelasticity of cortical bone.

More recently, Ural *et al*. [135] used cohesive finite-element modelling to evaluate the effect of strain rate on both initiation and propagation toughness for human cortical bone. In addition, three-dimensional models of micro-computed tomography-based compact tension specimens were used to assess the effect of strain rate and porosity. The simulation results demonstrated that the values of crack growth toughness decreased with the increased strain rate until 1 s^{-1} then attained almost constant value for strain rates greater than 1 s^{-1}, whereas initiation fracture toughness showed more gradual decrease throughout the range of strain rates (0.08-18 s^{-1}). In addition, the amount of porosity affected only the behaviour of propagation fracture toughness that decreased with the increasing strain rate. The conclusion drawn from that study was that during high-strain conditions associated with traumatic fracture, there was a sharp decrease and/or absence of toughening mechanisms in cortical bone. Though the authors tried to model the fracture behaviour of the cortical bone tissue, still their models were based on the cohesive-element approach with its drawbacks mentioned earlier, and a linear elastic material model used for bone.

A small number of papers studied fracture of bone at the macroscopic level using X-FEM, for instance, Liu *et al*. [12] demonstrated how X-FEM can be used to predict

proximal femur fracture due to impact. The geometry of an intact human femur was imported into Abaqus/CAE and meshed using linear tetrahedron elements. The bone material was assumed to be linear elastic with elastic modulus as a cubic function of bone density. In addition, damage initiation and propagation parameters were assumed as a function of bone density. The simulation results exhibited the crack initiation at the femur neck and propagated towards the femur head, see Fig. 4.7. It was reported that no physical testing was performed to validate the simulation results. Though the model is based on impact loading, it is over simplified and there is no account for the viscoelasticity of the bone tissue.

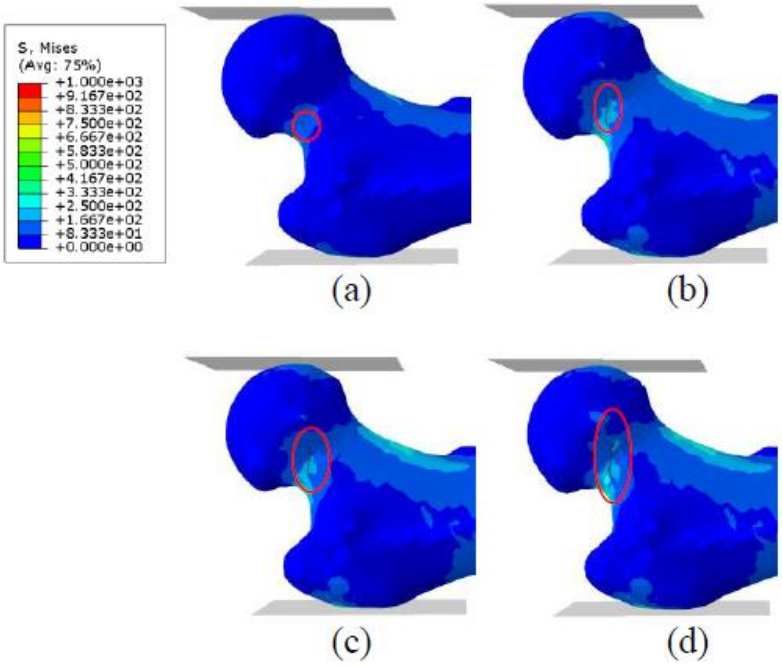

Figure 4.7: Femur head crack path: (a) crack initiation (b, c and d) crack growth [12]

Another study introduced a probabilistic X-FEM model and applied it to the prediction of femur's head fracture [136]. In that model, the random load amplitude variable with mean of 3040 N and standard deviation of 100 N was applied to a 2D mesh of the mid plane of the bone. An initial crack length of 1 mm was assumed at the maximum principal stress location. Stress intensity factors in Mode I and Mode II and the propagation angle were calculated based on the probabilistic extended finite-element method. This was a first-order approximation and other random variables, such as crack length or geometry still need to be considered. Also, more

experimentation is still needed to obtain fracture bone properties and define more realistic damage criteria.

Obviously, the reported X-FEM models, including those that tried to simulated fracture under impact, modelled cortical bone as a linear-elastic material with no account for its viscoelastic properties. Therefore, in this study, the extended finite-element method (X-FEM) will be used to develop models to simulate the fracture of a cortical bone tissue under impact loading that enables arbitrary, solution-dependent path of the crack without the requirement of remeshing. Furthermore, several material constitutive models, such as linear-elastic, elastic-plastic and viscoelastic will be tried. Such models can be used as a basis for development of more advanced numerical tools capable to predict the behaviour of other bone tissues under arbitrary loading conditions as well as for diseased and osteoporotic bones. To the best of the author's knowledge, no work covers modelling of a cortical bone tissue at the material level using X-FEM under impact loading event.

4.4. Microscopic Finite-Element Models of Cortical Bone Tissue

Bone-fracture susceptibility is increased by factors such as bone loss, microstructure changes and variations in material properties. Therefore, investigation of the effect of cortical bone's microstructure and its material properties on a crack propagation path and its global behaviour at macroscale is important. A non-uniform distribution of osteons in a cortical bone tissue results in a localization of deformation processes. Such localization can affect bone's performance under external loads and initiate fracture or assist its propagation. Once the fracture initiates, that distribution can play an important role in the crack propagation process at microscale; subsequently, the global response at macroscale could also be affected.

4.4.1. Modelling of Mechanical Behaviour

A few finite-element (FE) models have been developed to investigate the effect of microstructural constituents on the deformation behaviour of a cortical bone tissue. For instance, Prendergast *et al*. [137] modelled numerically a single osteon to investigate the relationship between damage formation and local strain to ascertain that microdamage changes local strain fields in the bone microstructure. Using that

model, it was predicted that microdamage alters the local deformation behaviour around lacunae, and these changes increase as microdamage accumulates. Hence, accumulation of microdamage can be linked to a change in strain at microstructural level. Still, that model did not account for the interaction between several osteons and their interstitial matrix. In another study, Dong *et al*. [138] used a generalized self-consistent method to estimate the effective elastic moduli of a fibre-reinforced composite material with multiple transversely isotropic inclusions. It was proposed that the method can be useful in establishing micromechanical models of natural biological composite materials such as cortical bone to examine the dependence of the elastic properties of cortical bone on its porosity.

Considering a Haversian cortical bone tissue as a fibre-reinforced composite, Hogan [13] developed and studied a micromechanical finite-element model presenting osteons as a fibre component and interstitial bone as the matrix material, see Fig. 4.8. A cement line was included as an "interphase" component along the fibre/matrix interface. The distribution of osteons was assumed to be regularly spaced and repeatable which does not capture its real form. Porosity was also introduced by considering hollow fibres. Results were obtained based on the application of uniform macroscopic stresses at the unit cell boundary conditions. Measuring the elastic modulus as a function of porosity, the simulation results exhibited a reasonable agreement with experimental ones, but it depended on the constituents' properties that were not fully established. The model is still not based on real microstructural distributions of osteons and interstitial matrix.

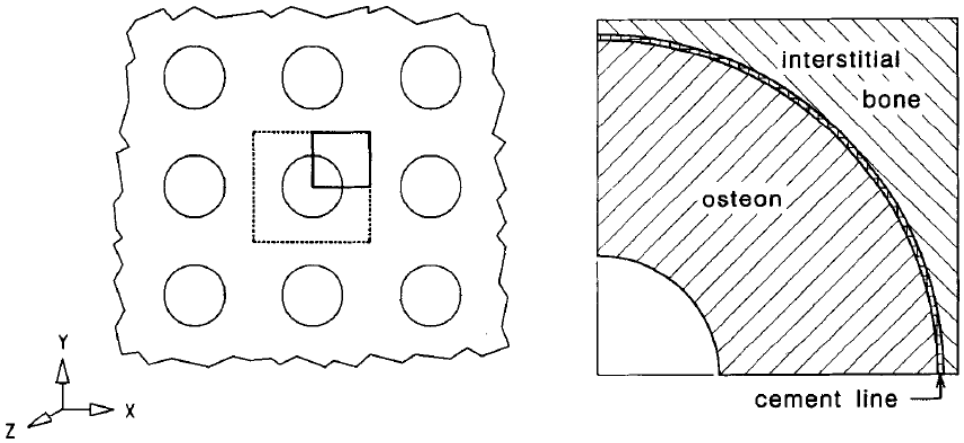

Figure 4.8: (a) Transverse section of fibre-reinforced composite; (b) quarter-fibre micromechanical model [13]

Also at the microstructural level, Mullins *et al*. [139] developed a micromechanical model of a porous fibre-composite, to investigate the effect of microstructural morphology on the macroscopic properties of cortical bone. It was used to study the effect of lacunar and vascular porosities, percentage of osteonal bone and orientation of the Haversian-system on the macroscopic elastic moduli and Poisson's ratios. Simulation results showed that both porosity and orientation of Haversian system had a significant effect on the macroscopic properties of cortical bone and should not be neglected. Also, simulation results showed that microstructural features affected distributions of local stresses and strains and caused a strain magnification effect. Again, the microstructure is not based on real microstructure distributions of components of the cortical bone tissue.

4.4.2. Modelling of Fracture Behaviour

Because of the complexity of cortical bone architecture and the lack of adequate tools, a few numerical models are found in the literature [140]. For instance, a microscale finite-element model of the osteonal cortical bone tissue was developed by Raeisi Najafi *et al*. [141] to evaluate the interaction between osteons and microcracks. The model considered osteons as fibres, interstitial bone as the matrix and the cement line as interface tissue. LEFM theory was used to evaluate the interaction between the osteons and microcracks; a stress intensity factor (SIF) was calculated at the vicinity of the microcrack tips. The simulation results demonstrated a significant effect of microstructural heterogeneity on fracture parameters. Also, both microstructural morphology and loading conditions affected a microcrack's growth trajectory. In another study, Huang *et al*. [142] developed a cortical bone-like composite material model using circular inclusions as osteons, introducing also cement lines. The crack location, inclusion size and property-variation effect on propagation of an initial crack was investigated using a two-inclusion model. Simulations were performed to calculate stress distributions and strain energy release rate. Mode I was dominant in the two-inclusion model, and the stress intensity factor, K_I, was used to determine the crack instability. Then, the model was expanded into a four-inclusion one that was optimized to arrest any crack initiated in the interstitial matrix. The results exhibited that soft inclusions tended to attract the crack whereas hard inclusions tended to repel it. Also, the size and properties of the inclusion affected the crack-propagation direction.

Budyn *et al*. [14] introduced a multi-scale method for modelling a growth of multiple crack in a cortical bone tissue under tension using X-FEM. Cortical bone was considered as a four-phase composite; comprising Haversian canals, osteons, interstitial matrix and cement lines. To emulate the nature of cortical bone tissue, both geometric and mechanical parameters were introduced at microscopic scale based on random distributions. Cracks were initiated at the microscopic level where a critical elastic-damage strain-driven criterion was met, the grown occurred when a critical stress intensity factor criterion was reached until complete failure of the modelled unit cell. Cracks were located randomly in the microstructure as shown in Fig. 4.9. It was concluded that cement lines appeared to be a critical element protecting bone against fracture; they are relevant structural elements to study their evolution in osteoporosis.

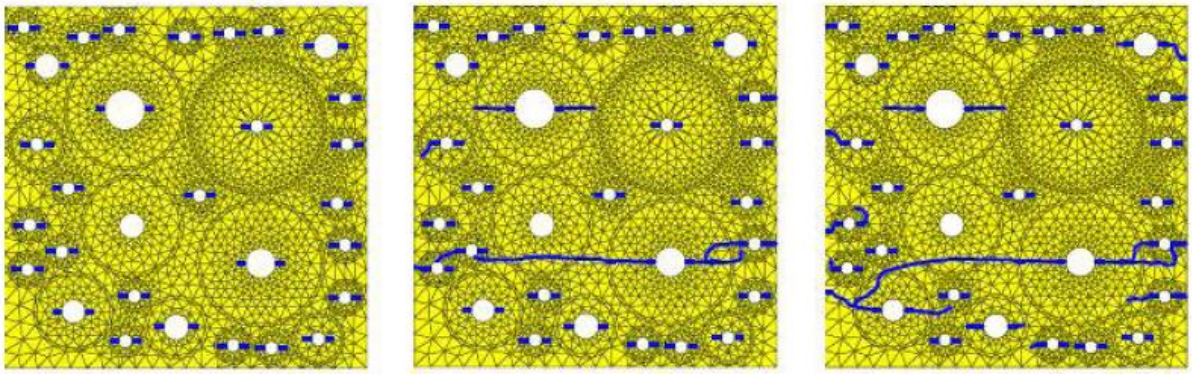

(a) (b) (c)

Figure 4.9: (a) Initial cracks; (b) final crack paths, SIF ratio between stress and Interstitial matrix is 3 and (c) final crack paths, SIF ratio between stress and Interstitial matrix is 6 [14]

Later, Budyn and Hoc [143] investigated the effect of aging on structural and mechanical properties of human cortical bone using a 3D FEM unit cell. At the macroscopic scale, the 3D model was able to provide elastic moduli and describe the anisotropy of regular remodelling and osteoporosis of a cortical bone tissue. Also, using their X-FEM model discussed previously, failure mechanisms and propagation of cracks in cortical bone under tension were studied. Distributions of microscopic strain fields showed that cement lines have an important role in isolating the osteons from the matrix. This could explain why cement lines were correlated with energy in fracture processes in the deflection of propagation of

cracks by slowing them down. Though the model accounted for real microstructural distributions it did not employ an experimentally based fracture parameters.

Recently, some researchers attempted to develop multi-scale models of a cortical bone tissue; for instance, Hamed *et al*. [144] predicted analytically the effective elastic constants of cortical bone by modelling its elastic response at scales spaning from a nanostructural level to a mesostructural one. Micromechanics and composite laminate theories were used. Also, Racila and Crolet [140] proposed a multi-scale approach to model numerically the properties of cortical bone as a five-level hierarchical structure: Bone Elementary Volume (BEV), osteon, lamella, fibre and fibril. In that model, physical properties were computed at each level using the mathematical homogenization theory. Some assumptions of the model have no physiologic foundation, such as the spatial distribution of the hydroxyapatite mineral crystal.

Though significant studies were reported in the literature dealing with bone at its microstructural level, still there are some unresolved issues related to modelling of cortical bone at this level. Among them are a lack of direct introduction of experimental fracture properties, non account for real microstructural distributions and absence of models that relate the effect of microstructural distributions to homogeneous media. In this study, filling these gaps will be attempted.

4.5. Summary

- An X-FEM method was developed in response to the deficiency of the standard finite-element method to simulate a crack initiation and propagation.
- X-FEM does not require the mesh to match the geometry of discontinuity.
- X-FEM can be used to simulate crack initiation and propagation along an arbitrary, solution-depended path without remeshing.
- Developed FE models in the automobile industry consider bone as a structural component rather than a material and usually employ a linear-elastic material model.
- Mathematical homogenization models of cortical bone behaviour do not resolve the spatial distribution of local strain nor account for time-dependent properties.

- Modelling cortical bone using cohesive zone models still has the primary drawback that a crack path must be pre-defined.
- Microstructural modelling of cortical bone still lacks implementation of real experimental data and real microstructure distributions.

5. Chapter 5

Characterisation of Macroscale Mechanical Properties of Cortical Bone Tissue

---

5.1. Introduction

The structure and properties of mineralized biological tissues such as bone have attracted much interest over the past few decades, particularly, a link between their properties and fracture. Characterisation of bone properties is of great importance not only for the biomedical community but also for engineering science. A contribution of each level of structural elements organized hieratically determines the overall mechanical properties of bone [35, 145]. In-depth understanding of bone's mechanical properties is necessary to develop biocompatible bone substitutes with load-bearing capacity close to that of a real bone. In addition, these properties are necessary to develop numerical models to analyse deformation and fracture of cortical bone at different structural levels. Compared to other structural materials, bone has complex microstructure and conveys unique properties like self-repair and adaptation to mechanical loading changes [41]. A significant amount of information has been acquired on mechanical properties of a cortical bone tissue in the literature concerning its stiffness, strength, and toughness, and it has been shown that they are affected by its components at different hierarchal levels. However, acquiring an exact set of data for a specific type of bone is necessary for finite-element models of cortical bone in our study.

This chapter presents the technique and results of direct measurements of cortical bone's mechanical properties. First, uniaxial tension tests were performed to characterise the elastic-plastic behaviour of bovine cortical bone tissue. Second, the Poisson's ratios were quantified using uniaxial tension tests and a digital camera. Finally, creep tests were performed to measure bone's viscoelastic properties. Tested specimens were cut along different directions with regard to the bone's axis - longitudinal (parallel to the bone axis) and transversal (perpendicular to it) - and at different cortex positions known as anterior, posterior, medial and lateral (Fig. 2.5).

5.2. Uniaxial Tension Tests

Uniaxial tension tests provide the material data input for predictive models to simulate deformation and fracture of a cortical bone tissue. In our study, development of numerical finite-element models was the motivation to conduct those tests. Bone is a material that has various hierarchical levels with different structural components. This hierarchically organized structure with its optimized arrangement and different component orientations makes bone a heterogeneous and anisotropic material [35]. Therefore, conducting those tests in different directions as well as for different anatomical positions was pursued. Characterising the mechanical properties of cortical bone tissue necessitates conducting uniaxial tension tests for specimens cut along three mutually orthogonal axes: longitudinal, transversal, and radial. However, due to the natural geometrical constraints of the cortical bone's thickness that is approx. 8-9 mm, acquiring mechanical data in the radial direction using uniaxial tension test was not feasible. Based on the assumption that cortical bone can be modelled as a transversely isotropic material [146, 147], the uniaxial tension tests were conducted only along the longitudinal and transversal axes.

5.2.1. Experimental Equipment

Properties of the cortical bone tissue were obtained under tensile-test conditions. Unlike traditional structural materials there are restrictions for the specimen size when dealing with cortical bone. So, to make the mechanical properties of both longitudinal and transverse directions comparable, the same specimen size must be used. As the specimen length in the transverse direction is limited to approx. 28 mm, a high-precision tensile testing machine capable of handling small specimens is required. The Instron 5848 MicroTester material testing machine provides a solution to the challenge of testing specimens at the microscale level (Fig. 5-1). A high-precision displacement measurement together with a load frame that maintains both alignment and high stiffness throughout its loading range are required for accurate testing. These requirements invalidate the use of standard universal testing machine because it lacks the required precision needed for small-deformation measurements, since the expected deformation in the specimen is at the micron level. The MicroTester testing machine has a very stiff loading frame

with submicron accuracy displacement measurement to ensure required performance in the range of tests with micro-specimens. It is suitable for tests requiring less than 2 kN load. It is offered with Instron's 5500 series controller and Bluehill 2 software used for monotonic and simple cyclic applications. Two precision-aligned columns fixed to a rigid support base together with movable crosshead are the features of the MicroTester loading frame, high stiffness of which results in accurate and repeatable deformation information and displacement control. Instron guarantees displacement accuracy better than 0.5 µm over short distances and resolution better than 20 nm by utilizing a precision digital encoder mounted directly to the loading actuator. Load-measurement transducers provide accurate load measurements with accuracy of 0.5% of the load reading down to 1/250 of the capacity of the load cell.

As stated earlier, Bluehill 2 software is used for operating the machine, in addition to it is interfaced with the data acquisition system to generate essential data such as load, displacement, etc. in the form of ASCII file format for further uses [15].

Figure 5.1: Instron's Model 5848 MicroTester [15]

5.2.2. Specimen Preparation

One of the most accurate methods to measuring cortical bone's properties is tensile testing. Specimens for this test must be relatively large and carefully cut from the region of interest. The specimens in our tests were cut from fresh bovine femora bones (aged 1.5-2 years). The mid-part of three femurs (diaphysis) was extracted using a handsaw. Specimens were cut from four anatomical positions along and perpendicular to, the bone axis using a milling machine (Fig. 5.2). After cutting, the specimens were ground using a series of grinding papers Standard ANSI grit: 240, 600, and 1200 to make sure that the surface is clean, without any scratches or irregularities. After being prepared, the test specimens were put in a 0.9% physiological saline solution for 24 hr; it is well-known from literature that dry bone specimens exhibit higher mechanical properties than wet ones [148]. This procedure is used to reproduce the living conditions as far as possible. It was pointed out in the literature that while dry bone behaves approximately elastic, wet bone creeps [62]. Evans and Lebow [149] stated that wet bone's absorbing energy capacity is approximately proportional to the total strain; it plays an important role in traumatic fractures, most of which arises from impacts. Specimen dimensions were the same for both directions and at all anatomical positions as 10 mm × 5 mm × 3 mm (gauge length × width × thickness). The total length was different for longitudinal and transverse directions - 35 mm and 25 mm, respectively - due to natural geometry restrictions in the transverse directions. Figure 2.5 (chapter 2) shows cortical bone axes and anatomical positions, with Figure 5.2 demonstrating a stage of the specimen's preparation process and the final shape of the specimen. A specimen's cross-secional area used in most of the previous studies was in the range between four to twenty square millimetres; these dimensions contain at least several Haversian-systems that make them of satisfactory size [20]. Since bone histologically displays the symmetry of a transversely isotropic material, transversely isotropic model can be a good representation [20].

It is worth mentioning here that all the specimens used in this study were excised from the diaphysis part of bovine femur cortical bone and prepared using the same protocol stated in this section.

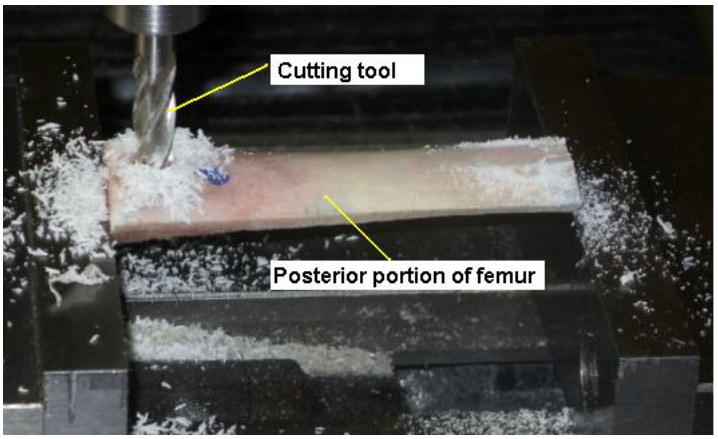

(a)

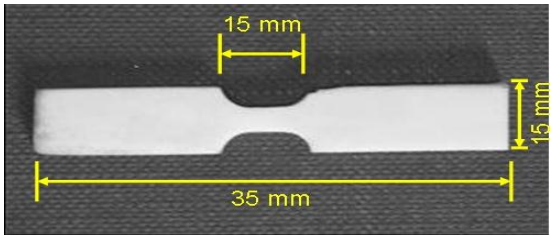

(b)

Figure 5.2: (a) Exciting bovine cortical bone using milling machine and (b) cortical bone specimen

5.2.3. Experimental Procedure

This part of the study focused on quantification of elastic-plastic behaviour under uniaxial tension for specimens cut along different directions and from different anatomical positions. Specimens were prepared mainly for the axial direction of the long bones that is parallel to the osteons and in the transverse direction that is perpendicular to the osteons. The tests were performed using Instron MicroTester 5848 machine that allowed testing relatively small specimens (Fig. 5.3). Monotonic loading was applied to each specimen until failure. The tests were performed in the displacement-control regime. The specimens were tested at a strain rate of 10^{-3} s^{-1} and at room temperature of 20°C. An extensometer with a gauge length of 10 mm was used to measure the displacement. During the test a 0.9% saline solution was sprayed on the external surface of the specimen with short time intervals to avoid specimens drying up.

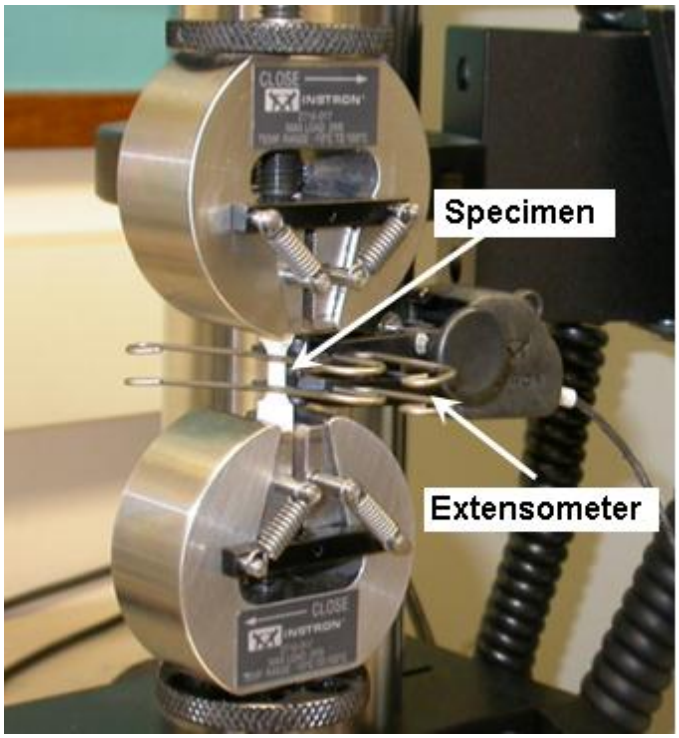

Figure 5.3: Specimen in Instron MicroTester 5848

5.3. Poisson's Ratio Tests

Solid materials tend to retain their total volume when deformed. In the tensile-test case, as two ends of a long rod are pulled apart, its sides move closer. In other words, the elongation produced in the longitudinal direction is accompanied by contraction in the transverse directions. The strain in the longitudinal direction is called *axial strain* while the one in the transverse direction is called *lateral strain*. The Poisson's ratio is the absolute value of the ratio of lateral strain to the axial strain. For an isotropic material, deformation of a material in the direction of one axis will produce a deformation along the other two axes with the Poisson's ratio being the same for all the directions. In an orthotropic material it is different in each direction; however, the symmetry of the stress and strain tensors implies that not all the six Poisson's ratios are independent [150]. There are only nine independent material properties; three elastic moduli, three shear moduli, and three Poisson's ratios, so the remaining three Poisson's ratios can be obtained using relationships:

$$\nu_{ij} = \frac{E_i}{E_j}\nu_{ji}\,, \qquad (5-1)$$

where ν_{ij} is the Poisson's ratio that corresponds to a contraction in the direction j when an extension is applied in direction i ; E_i is the Young's modulus along axis i.

In the case of transversely isotropic materials, the number of independent material constants is reduced to five: two elastic moduli, shear moduli, and two Poisson's ratios.

5.3.1. Specimen Preparation

The specimen preparation and storage protocol are the same as those for uniaxial tension test discussed earlier in Section 5.2.2. Specimens were cut in two orthogonal directions: longitudinal and transverse, and from different anatomical positions: anterior, posterior, medial, and lateral from the mid-diaphysis of bovine femur. Three specimens were cut for each direction and anatomical position. Specimens' dimensions were 10 mm × 5 mm × 3 mm (gauge length × width × thickness). The total length was different for longitudinal and transverse directions - 35 mm and 25 mm, respectively - due to natural geometry restrictions in the transverse directions.

5.3.2. Experimental Procedure

The Poisson's ratios of a cortical bone tissue can be determined by direct observations of surface displacements in two perpendicular planes simultaneously considering it as a transversely isotropic material. The well-polished specimens were marked with four marks on their face and side, where the face represents the longitudinal-transverse plane and the side represents the longitudinal-radial plane as shown in Fig. 5.4. Two high resolution digital cameras (10 MPixel) were fixed on tripod and focused on the marks before applying the tensile load through the grips of the MicroTester machine. Optical zoom was used to get reasonable images. All the pictures were taken from the same place and using the same optical zoom value. A metal part with known dimensions was put in the field of the camera focus to be used for image analysis and calibration. For each surface, four points gave two values of the Poisson's ratio and the average value was used for the analysis.

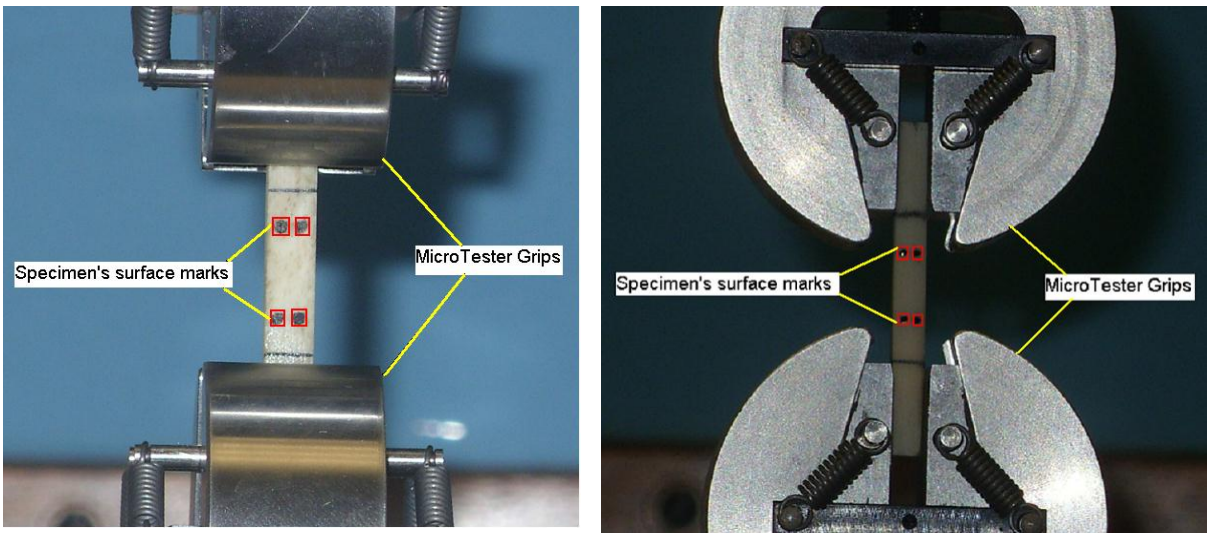

(a) (b)

Figure 5.4: Specimen's face marks (a) and side marks (b)

One specimen for each direction and anatomical position was first tested using MicroTester 5848 until fracture to determine a load value to be applied that ensured elastic behaviour during Poisson's ratio determination tests. A value of 250 N was found optimal for all directions and positions. Before applying the load, one camera shot from each side was taken, and then the load was applied to increase monotonically from zero to 250 N and then remains constant, again another camera shot was taken for both sides. The previous procedure was applied for all the specimens tested in both directions and anatomical positions.

5.4. Creep Behaviour Tests

5.4.1. Experimental Equipment

MicroTester 5848, described in detail in Section 5.2.1 and shown in Fig. 5.1, was used to carry out creep tests. The machine allowed the use of specimens of relatively small dimensions due to the natural geometrical constraints of the cortical bone tissue. The method file used to control the test's parameters was adjusted to fulfil creep tests, such as specimen dimensions, the total testing time, rise time, end-of-test criterion, loading rate during the rise time period, and the final load level.

5.4.2. Specimen Preparation

The specimen preparation and storage protocol are the same as those for uniaxial tension test discussed in Section 5.2.2. Twelve identical specimens with dimensions of 10 mm × 5 mm × 3 mm (gauge length × width × thickness) were cut in the longitudinal direction of each anatomical position comprising a total of 48 specimens. All the specimens were cut with the same geometry and dimensions from the mid position of a femur and as close to each other as possible to minimize variability of local material properties.

5.4.3. Experimental Procedure

This part of the experimental study covered creep properties of bovine femoral cortical bone. The method file for Instron MicroTester was prepared with the stress ramping from zero to a defined stress level in 60 s and remaining afterwards constant for 3000 s. Four stress levels were applied with values 45 MPa, 50 MPa, 55 MPa and 60 MPa. Three specimens for each position and stress level were assigned for creep test. During the test a 0.9% saline solution was sprayed on the external surface of the specimen with short time intervals to avoid specimens' drying up. The creep behaviour will be used to obtain coefficients of the Prony series, as discussed in Section 3.3.

5.5. Results and Discussion

5.5.1. Uniaxial Tension Test

Non-linear elastic-plastic behaviour with strain hardening was observed for both longitudinal and transverse directions and all the examined cortex positions. Typical curves obtained at moderate strains are shown in Figs. 5.5 and 5.6. Also, the obtained elastic moduli, stresses and strains at failure are provided in Table 5.1 for bovine femoral cortical bone tissues in longitudinal and transverse directions for four cortex positions. The values of the elastic modulus were obtained using a tangent for the initial portion of stress-strain curves of uniaxial tension tests. Along the bone axis, comparison of those values demonstrates small differences among specimens cut from anterior, medial or lateral cortex positions, whereas those cut from posterior position exhibit the smallest values. These results are in line with another

study that demonstrated a variation in the properties around the human femoral shaft; bone from posterior quadrant is more porous and weaker than other quadrants [151]. This weakness is associated with the presence of Haversian-systems (secondary osteons), and this can appear in two different ways: first, reduction in the amount of bone, and, secondly, reduction in the amount of calcium [62]. Figure 5.7 shows the differences of microscopic features among cortex positions.

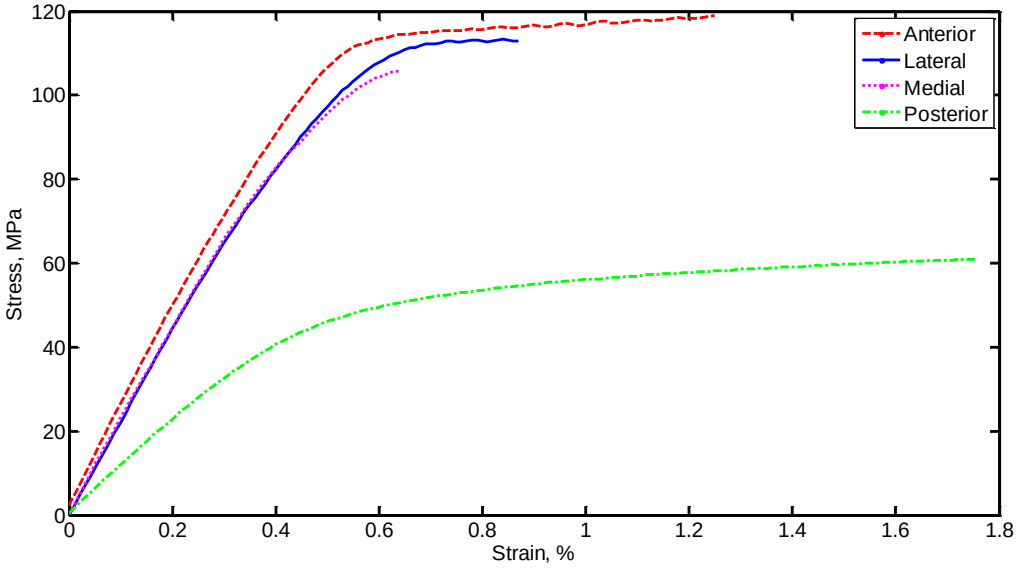

Figure 5.5: Typical elastic-plastic behaviours for longitudinal direction for different anatomical positions of bovine femoral cortical bone tissue

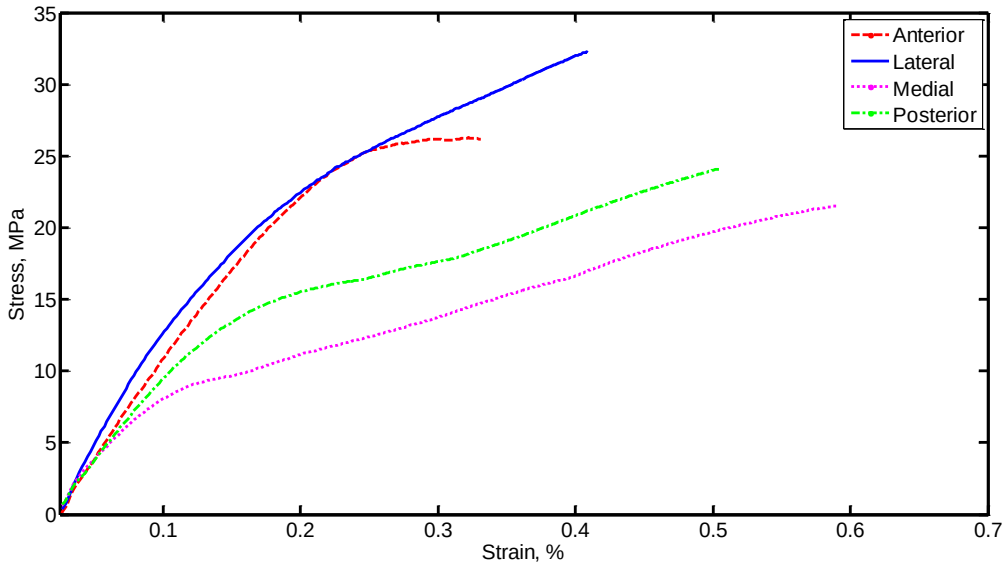

Figure 5.6: Typical elastic-plastic behaviour for transverse direction for different anatomical positions of bovine femoral cortical bone tissue

Table 5.1: Elastic moduli, ultimate strength and ultimate strain of bovine femoral cortical bone tissue in longitudinal and transverse directions for different cortex positions

Dir.	Cortex Position	Elastic modulus (GPa)	Ultimate strength (MPa)	Ultimate Strain %
Longitudinal	Anterior	21.27 (±2.22)	124.90 (±5.16)	0.86 (±0.034)
	Posterior	12.53 (±1.86)	62.13 (±1.06)	1.18 (±0.051)
	Medial	21.40 (±1.73)	110.6 (±13.15)	0.65 (±0.016)
	Lateral	21.57 (±1.29)	107.13 (±7.86)	1.04 (±0.038)
Transverse	Anterior	11.07 (±2.02)	27.95 (±6.53)	0.78 (±0.041)
	Posterior	10.41 (±1.64)	29.91(±3.99)	0.78 (±0.048)
	Medial	14.23 (±4.19)	25.19 (±3.13)	0.71 (±0.055)
	Lateral	11.08 (±1.88)	29.90 (±3.99)	0.77 (±0.047)

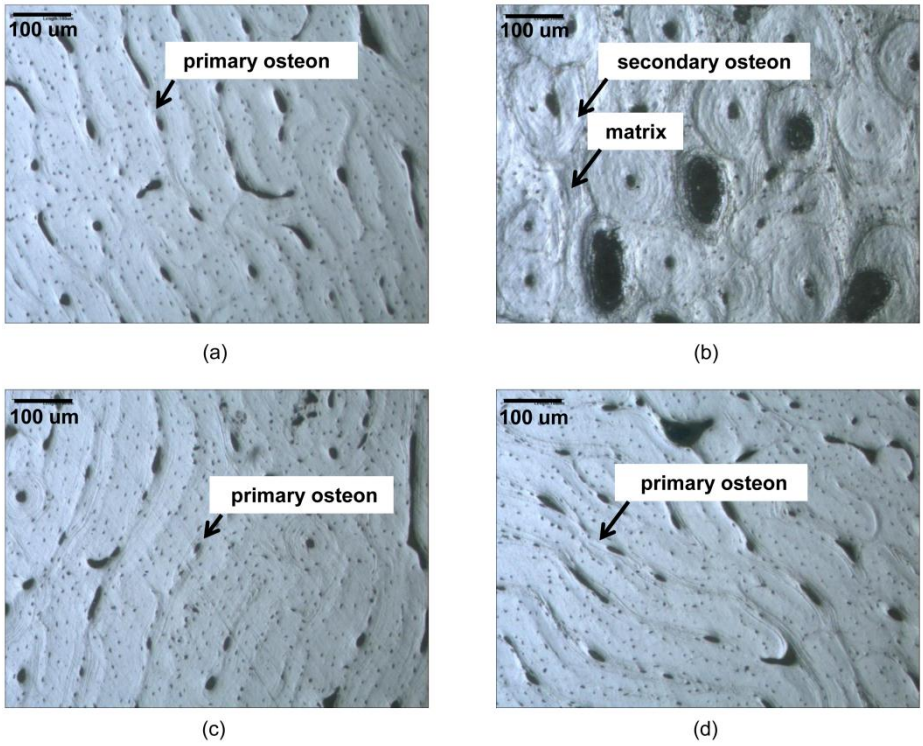

Figure 5.7: Typical microscopic images of microstructural features of different cortex positions: (a) anterior; (b) posterior; (c) medial and (d) lateral. Images were captured at different cortex positions of a transverse-radial plane across the mid-diaphysis of bovine cortical bone femur using a NIKON-OPTIPHOT microscope

It was found for tests along the bone axis that lateral specimens have the highest elastic moduli, while posterior ones were the weakest, see Fig. 5.8. The average values of the elastic modulus for all cortex positions measured along the bone axis were in the range of 12–21 GPa. On the other hand, for specimens cut perpendicular to the bone axis, the medial ones had the highest elastic moduli with posterior specimens the lowest. The average values of the elastic modulus measured perpendicular to the bone axis were in the range of 10–14 GPa for all cortex positions [152]. All the obtained data are within the range for cortical bone tissue's moduli, accepted in the literature, suggested as 6–24 GPa in [61, 153] depending on parameters such as mineralization, porosity, and the method employed. Also, they agree with more recent data reported in the literature; for instance, Edward [154] provided values of 20.4 GPa and 11.7 GPa for longitudinal and transverse directions of bovine cortical bone specimens, respectively. Using other experimental technique – ultrasonics – elastic moduli of 20.7 GPa and 12 GPa in longitudinal and transverse directions for cortical bone micro-specimens were reported in [49]. In addition, Martin *et al*. [18] reported elastic modulus values of 23.1±3.2 GPa and 26.5±5.4 GPa for specimens cut along the bone axis from Haversian and primary bones, respectively. In the transverse direction, the elastic moduli were 10.41±1.6 GPa and 11.0±0.2 GPa for Haversian and primary specimens, respectively.

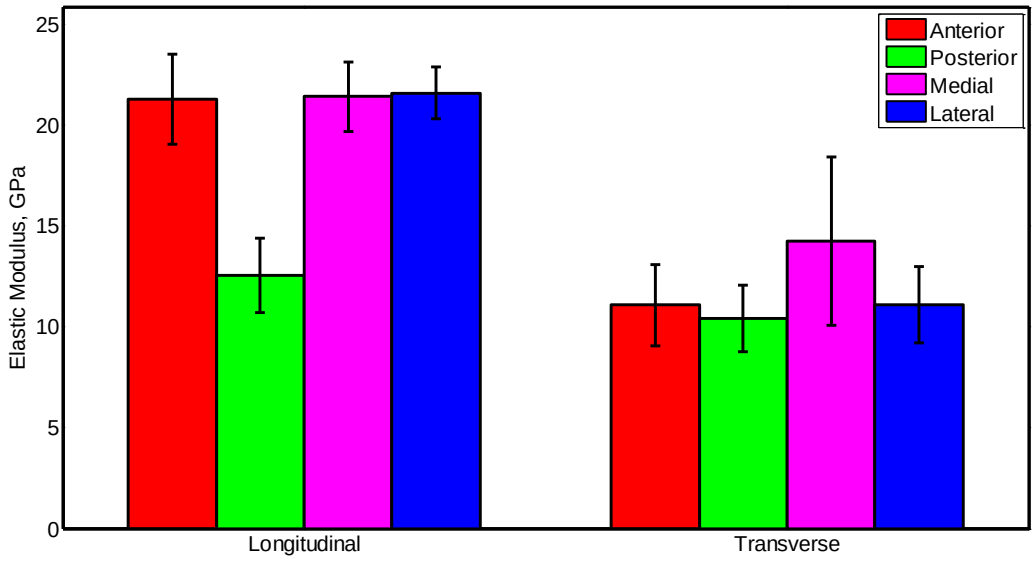

Figure 5.8: Comparison of elastic moduli in longitudinal and transverse directions for different cortex positions of bovine femoral cortical bone tissue

Anisotropy in this study was calculated as the ratio of elastic modulus magnitudes for longitudinal and transverse directions. Specimens cut from the posterior cortex demonstrated the lowest anisotropy ratio, close to 1.2, whereas those cut from the lateral cortex exhibited the highest, close to 2. Based on these results, specimens from a posterior cortex position can be approximated as isotropic material, whereas those from other cortices have a low level of anisotropy. Anterior specimens have the ratios close to those of lateral ones, while the medial position is closer to the posterior in this respect. The literature data give the range for anisotropy ratios between 1.5 and 2 [18, 155, 156].

In terms of ultimate strength, for longitudinal specimens, the highest average level of 124.90 MPa was found for anterior specimens, whereas the lowest (62.13 MPa) was found for posterior ones. Both medial and lateral specimens revealed approximately the same average ultimate stress values. For transversal specimens, the variation in the ultimate strength value among different cortex specimens was rather small. In general, the ultimate strength was higher for the longitudinal direction. This is in agreement with the literature data; for instance, Currey [62] reported the level of 112 MPa for the longitudinal direction of bovine femur, while Sweeney *et al*. 129 MPa [57]. For the transversal directions, Burstein *et al*. [61] gives a value of 52$\pm$8 MPa. No specific information on the anatomical position of specimens was given in those works. It is obvious here that the ultimate strength values for the transverse direction were lower than those in the literature; still the measured values depend on many parameters, such as variation in the mineral content, microstructure or the used method [61]. Therefore, the specimens used in the current study might have been collected from an animal that is of different age, diet or have different activities from those in the literature. Hence, specimens of different nature can give slightly different results. In fact, this is one of the main motivators to measure and use, when possible, a consistent set of data using the same source for specimens.

The last element to compare was the fracture strain. It was in the range from 0.65% to 1.18% in the longitudinal direction for all the anatomical positions, and in the transverse direction was between 0.71% and 0.78%. In the current study, some of the specimens exhibited ductile failure (i.e. snapped in two halves), and some broke just near the machine grips. In literature, large variations of stress at failure, from

100 to 200 MPa, and strain at failure, from 0.4% to 4%, were found for bovine cortical bone tissue [157]. The variations in the failure stress and strain among specimens can be due to the distribution of defects in the specimens, and the largest defect in the structure could be the one that led to the final failure [157].

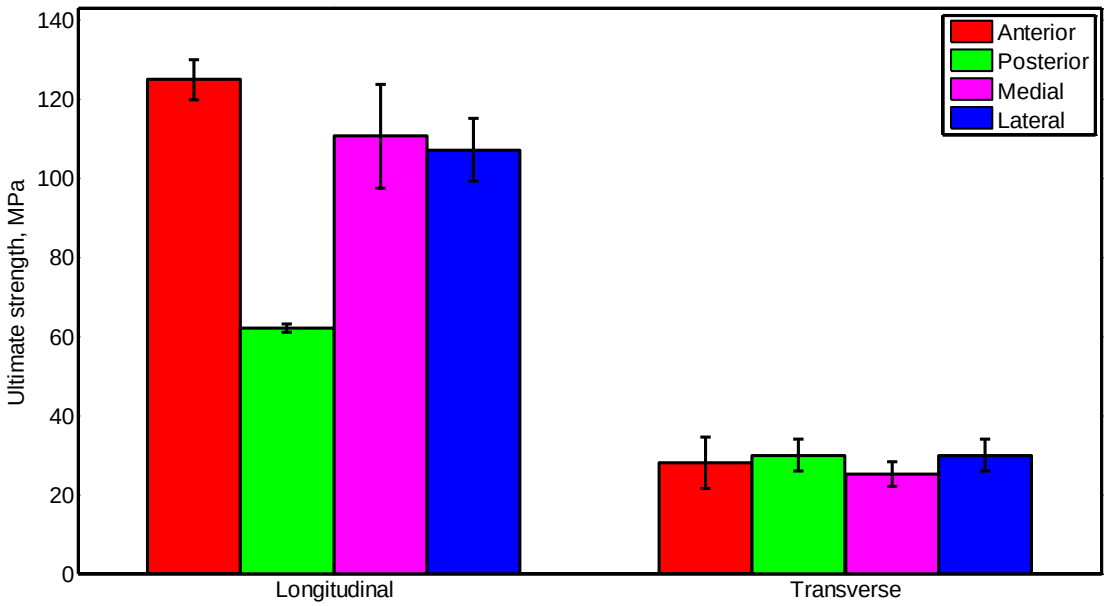

Figure 5.9: Comparison of ultimate strength in longitudinal and transverse directions for different cortex positions of bovine femoral cortical bone tissue

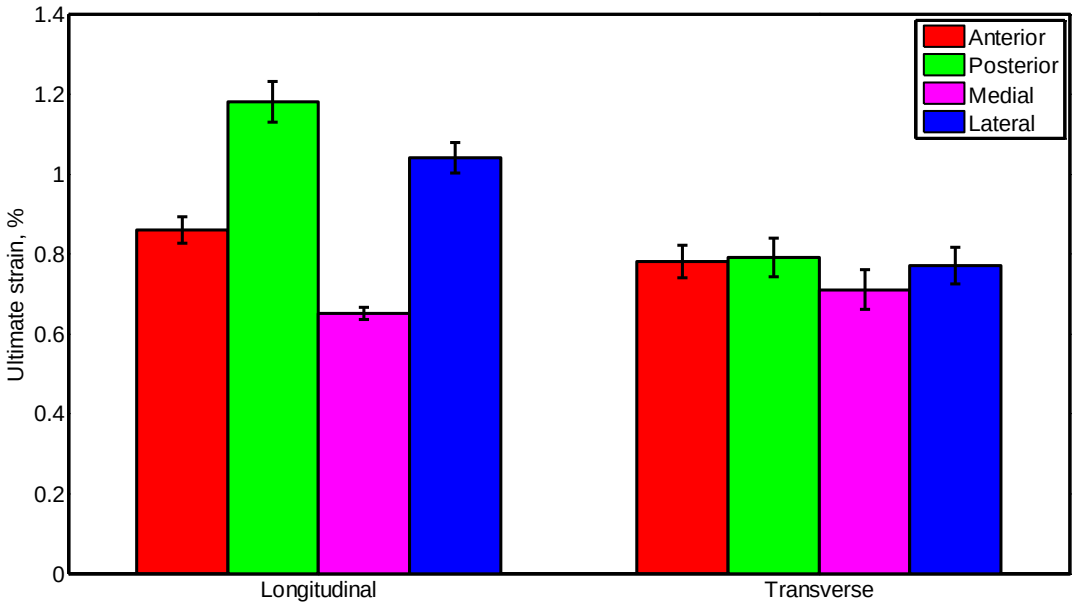

Figure 5.10: Comparison of ultimate strain in longitudinal and transverse directions for different cortex positions of bovine femoral cortical bone tissue

Our experimental study demonstrated that anisotropy and position-sensitivity of mechanical properties and behaviours of the bovine femoral cortical bone tissue are relatively moderate with a lower contrast compared, e.g., to many structural composites. Based on elastic properties, it is obvious from its position-sensitivity that changes in the mechanical properties are linked to changes in composition and/or microstructure, Fig. 5.7. The reason for different mechanical properties at different cortex positions stems from the non-uniform *in-vivo* loading experienced by bone due to body weight and muscle forces; and, according to the Wolf's Law [158], it adapts itself to be stiffer and stronger in positions subjected to higher loads. Our results elucidated that for longitudinal specimens cut from the anterior, medial and lateral parts of the femur were subjected to the highest longitudinal loading while posterior to the lowest. The character for the transversal specimens is different; the medial part is the stiffest and the posterior is weakest.

5.5.2. Poisson's Ratio Tests

Using a high-resolution digital camera and surface marks, the Poisson's ratios of the bovine femoral cortical bone tissue in two orthogonal directions were successfully measured. By measuring the surface's vertical and horizontal distances before and after loading the specimen in the elastic region, the Poisson's ratios were calculated. Having measured two vertical and two horizontal distances using four surface marks, two Poisson's ratio at a time can be calculated. The average values of those Poisson's ratios are given in Table 5.2. The subscripts 1, 2, and 3 refer to longitudinal, transverse and radial directions, respectively. The results showed considerable difference between the Poisson's ratios ν_{12} for different cortex positions in longitudinal direction; the posterior position has the highest value of 0.55 while the lateral position has the lowest of 0.38. The difference was around 45%. Still, the difference of ν_{12} values among specimens cut from anterior, medial, and lateral is not high. Also, a slight difference was found for ν_{13} values for different cortex positions. The medial position has the highest value of 0.37, where the lateral has the lowest of 0.32. Still, the difference is not too high – 13.5%. The difference in Poisson's ratio values for different cortex positions is linked to their distinct microstructure that was seen under the light microscope, see Fig. 5.7. The microscopic images showed that anterior, medial and lateral microstructures are

similar – they are primary bone with few small osteons. The posterior microstructure, on the other hand, reveals many secondary osteons. On the other hand, when applying the load in the transverse direction no significant difference was found for ν_{23} for all the cortex positions and directions studied, giving a value of around 0.40. Moreover, the same situation was observed for ν_{21}, where a value of 0.27 was found for all the directions and positions. Few studies determined experimentally Poisson's ratios for cortical bone; for instance, Reilly and Burstein [153] assumed a cortical bone tissue as transversely isotropic material and measured deformation by using extensometers in two orthogonal planes concurrently. They reported the Poisson's ratio ranging between 0.29 and 0.63. Using the ultrasonic continuous-wave technique, Ashman *et al*. [49] considered cortical bone as an orthotropic material and measured its Poisson's ratios that were found ranging between 0.27 and 0.45. The obtained results from our study are within the range of the literature data.

Table 5.2 Poisson's ratios of bovine femoral cortical bone specimens for different cortex positions

Dir.	Anatomical Position	Symbol *	Poisson's Ratio
Longitudinal	Medial	ν_{12}	0.39 (±0.009)
		ν_{13}	0.37 (±0.010)
	Lateral	ν_{12}	0.38 (±0.007)
		ν_{13}	0.32 (±0.008)
	Anterior	ν_{12}	0.44 (±0.009)
		ν_{13}	0.34 (±0.006)
	Posterior	ν_{12}	0.55 (±0.006)
		ν_{13}	0.33 (±0.007)
Transverse	Medial	ν_{23}	0.41 (±0.006)
		ν_{21}	0.27 (±0.007)
	Lateral	ν_{23}	0.39 (±0.006)
		ν_{21}	0.27 (±0.005)
	Anterior	ν_{23}	0.40 (±0.008)
		ν_{21}	0.27 (±0.009)
	Posterior	ν_{23}	0.42 (±0.007)
		ν_{21}	0.26 (±0.009)

*1, 2 and 3 refers to longitudinal, transversal and radial directions

5.5.3. Creep Behaviour Tests

Bovine cortical bone exhibits a time-dependent behaviour. In creep tests, the strain induced when a constant load is applied is a function of time. Several stress levels were attempted during an initial study to obtain the lower stress threshold, at which bone specimens start to creep – the initial value was 30 MPa. The results of the initial study showed that stress levels greater than 45 MPa produced a creep response, with no response for lower stress levels. Having obtained the minimum threshold of the stress level, other, higher stress values – 50 MPa, 55 MPa and 60 MPa – were applied during the creep tests. When bone specimens from different cortex positions were subjected to those constant stress levels, they deformed continuously. For instance, typical creep response curves of different cortex positions in longitudinal direction at stress levels of 45 MPa and 50 MPa are shown in Figs. 5.11 and 5.12. Applied stress values of 55 MPa and 60 MPa demonstrated similar creep response for all cortex positions, except for higher strain values. For all stress levels and cortex positions, it is observed that as the stress ramped from zero to the defined values in 60 seconds, the strain also ramped in an elastic manner followed by inelastic strain behaviour (Figs. 5.11 and 5.12).

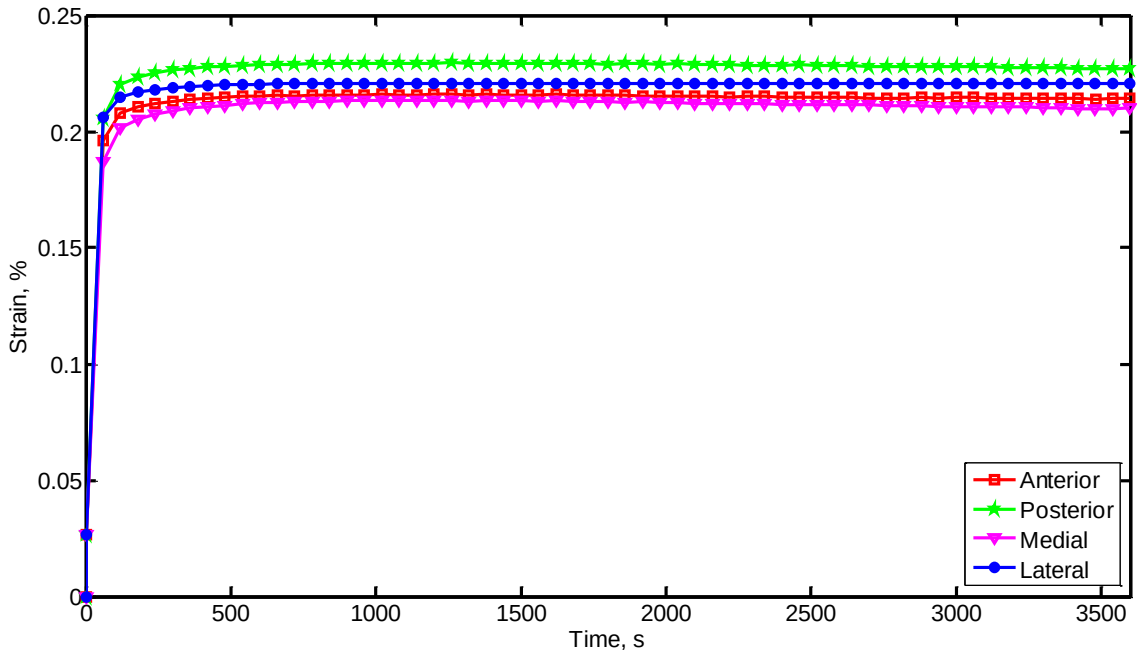

Figure 5.11: Typical creep responses in longitudinal direction for different cortex positions of bovine femoral cortical bone tissue (σ = 45 MPa)

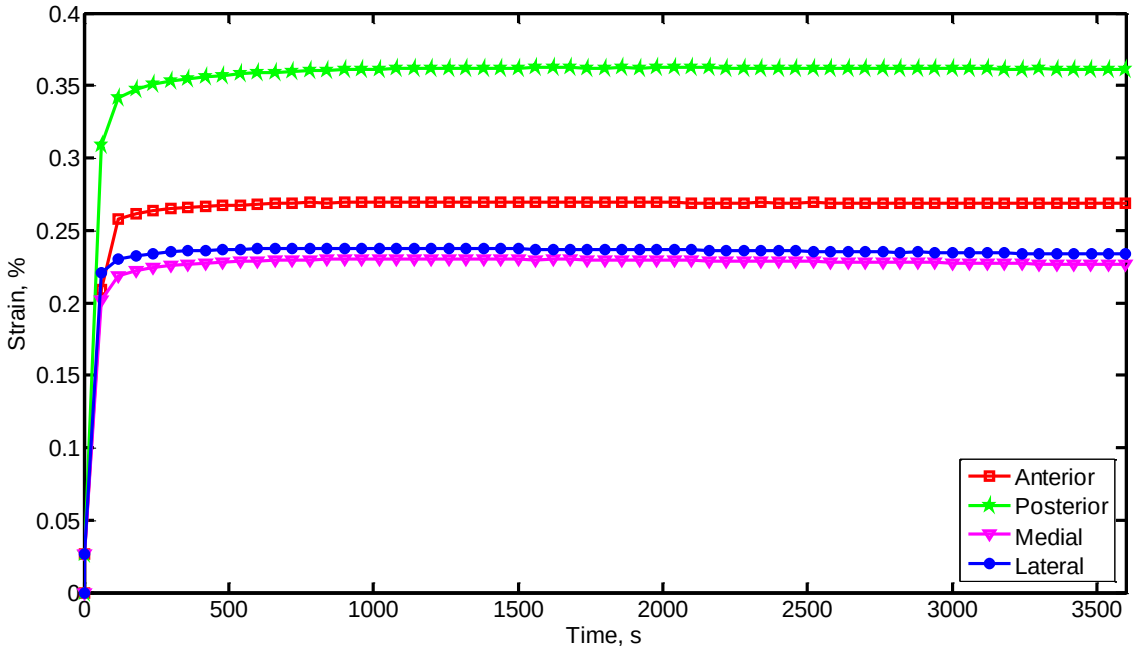

Figure 5.12: Typical creep responses in longitudinal direction for different cortex positions of bovine femoral cortical bone tissue (σ = 50 MPa)

Creep results demonstrated a small difference between elastic and inelastic strain values when the stress value of 45 MPa was applied to specimens from the different cortex positions. However, the difference was higher for higher stress levels. Obviously, different cortex positions have different microstructures (Fig. 5.7). The microstructural features of cortical bone are believed to contribute to the viscoelastic behaviour of cortical bone tissue. For instance, Martin and Burr [18] identified the presence of cement lines, varying amounts of osteoids, and the fluid flow through Haversian canals, canaliculi and interstitial spaces as a possible source of bone viscoelasticity. Also, macroscale bone viscoelasticity causes dissipation of energy that can be linked to such mechanisms. Since bone has a hierarchical structure, viscolelasticity can arise from various processes at different scales. Some authors reported such mechanisms in the literature, for instance, at the molecular level; the collagen phase can incur significant viscoelasticity [159]. At the microstructural level, many interfaces such as cement lines and boundaries between lamellae within osteons dissipate some energy [160]. A viscous motion of the cement line also contributes to viscoelasticity, in particular in cases of long-time loading [161]. Another mechanism that can cause damping is thermoelastic coupling [162]. Fluid flow in porous media can also contribute to viscoelasticity in hard tissues like bone [85, 95]. Although the basis for viscoelastic effects of cortical

bone have been explored by several other studies, but the source of viscoelastic effect still remains a topic of considerable study.

To successfully predict the deformation and fracture behaviours of the cortical bone tissue under dynamic loading, an adequate material model is required. It is well-known from literature that cortical bone is a viscoelastic material, yet it is necessary to define whether it is linear- or nonlinear-viscoelastic material to develop such a model. This can be achieved using isochronous creep curves. A material is called *linear-viscoelastic* if the relationship between strain rate and applied stress is linear at particular time, and called *non-linear viscoelastic* if their relation is non-linear. Results of this study of creep tests showed linear-viscoelastic behaviour of bovine cortical bone in the stress range between 45 MPa and 60 MPa. The applied stress – strain rate behaviour was identical at different times, 500 s, 1500 s, 3000 s, and 3600 s. Therefore, only the obtained behaviour at 3600 s was presented (Fig. 5.13). First-order polynomial curve fitting was employed to fit the isochronous data points. When grouping the isochronous curves for different cortex positions, a slight difference between them was found. At this moderate level of applied stresses, bovine cortical bone can be considered linear-viscoelastic material, and its response can be represented by mechanical models consisting of varying numbers of springs and dashpots, which in turn can be represented mathematically by Prony series.

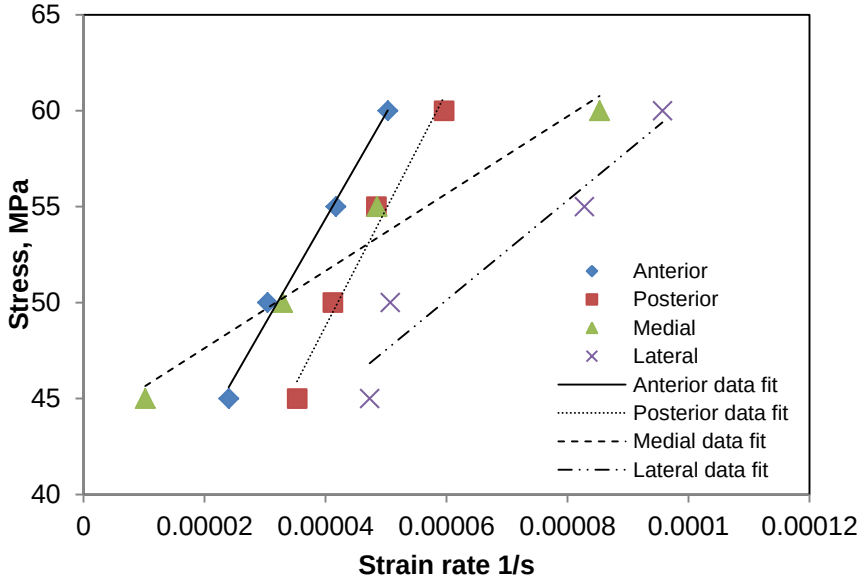

Figure 5.13: Stress-strain rate curves for different cortex positions of bovine femoral cortical bone tissue in longitudinal direction

Previous authors concluded that the assumption of linear-viscoelasticity of cortical bone is valid provided that the loading remained below a particular threshold. At stress levels above the threshold stress, the behaviour is non-linear and indicative of a time-dependent damage accumulation process [91, 163]. Hence, the obtained results indicate that the bovine cortical bone tissue is a linear-viscoelastic material in a stress range between 45 MPa and 60 MPa.

From the obtained experimental results on creep it was possible to determine the time-dependent constitutive equations for cortical bone based on the stress and strain history as well as the loading rate and time of load application to the specimen. A common form for those constitutive equations employs a Prony series that were calculated with the material evaluation technique provided by the Abaqus finite-element software [9], as discussed in Section 3.3. The calculated constants of the series are provided in Table 5.3 for stress levels of 45 MPa, 50 MPa, 55 MPa and 60 MPa for different cortex positions.

Prony-series representation of linear-viscoelastic models offers a simple fitting approach to experimental data. Both experimental and calculated results for the dimensionless relaxation modulus are in a good agreement. Apparently, even a series truncated to one or two terms provides a good approximation for experimental data, while it offers exact numerical conversion to other linear-viscoelastic material functions.

Now, a consistent set of macroscale properties of the cortical bone tissue is obtained; these parameters will be used later as input for numerical models to simulate bone's deformation and fracture. Those models will be presented in chapter 9 of this thesis.

Table 5.3: Material constants for Prony-series for different cortex positions of bovine cortical bone specimens in longitudinal direction

Cortex position	Applied stress (MPa)	i	e_i	k_i	τ_i
Anterior	45	1	0.0616	0	89.65
	50	1	0.0880	0	71.99
	55	1	0.1489	0	52.12
	60	1	0.1346	0	117.85
Posterior	45	1	0.0999	0	67.30
	50	1	0.0655	0	93.01
	55	1	0.1444	0	79.75
	60	1	0.0904	0	41.68
		2	0.0927	0	834.78
Medial	45	1	0.1170	0	81.85
	50	1	0.1179	0	73.98
	55	1	0.1465	0	80.78
	60	1	0.0612	0	130.12
Lateral	45	1	0.0655	0	82.43
	50	1	0.0659	0	70.74
	55	1	0.0875	0	169.75
	60	1	0.2455	0	29.68
		2	0.0727	0	1211.80

5.6. Conclusion

One of the most important requirements for adequate modelling of fracture of, and deformation in, the cortical bone tissue is comprehensive characterisation of its mechanical properties. This was the motivation behind our study to measure experimentally its main mechanical properties. The obtained experimental data cover a wide range of loading conditions and respective deformation mechanisms to provide a basis for future numerical simulations. The undertaken experimental studies include the characterisation of elastic–plastic behaviour as well as

viscoelastic properties using creep tests considering different cortex positions to account for position-sensitivity and data variability.

The experimental work performed can be summarized as following:

- Microscopic features of cortical bone tissue play an important role in its elastic-plastic behaviour. In general, bone specimens with lamellar microstructure (anterior, medial and lateral specimens) maintained higher properties compared to those containing secondary osteons (posterior specimens).
- Low anisotropy ratios were observed for the longitudinal and transverse directions of bovine cortical bone tissue with magnitudes ranging between 1.2 and 2; the anterior specimens have the ratios close to those of lateral ones, while the medial position is closer to the posterior one in this respect.
- Specimens cut from anterior, medial and lateral demonstrate similar pre- and post-yield properties, such as elastic modulus, stress at fracture and strain at fracture, while posterior specimens are weaker. The distribution of voids and defects in specimens, such as Haversian canals, canaliculi, resorption cavities lead to variation in both stress and strain values at failure.
- Different values of the Poisson's ratios obtained for different cortex positions are linked to their underlying microstructure. The difference between Poisson's ratios for specimens cut from anterior, medial and lateral in the longitudinal direction is small, while it is negligible for the transverse direction.
- The bovine cortical bone tissue in the longitudinal directions starts to creep when a stress level greater than 45 MPa is applied. Mechanisms, such as viscous motion of cement lines, boundaries between lamellae and osteons, and fluid flow in porous media can contribute to cortical bone's viscoelasticity. In the stress range of 45 MPa to 60 MPa, the cortical bone tissue demonstrates linear-viscoelastic behaviour; therefore, its response can be represented by mechanical models that include a number of springs and dashpots. These mechanical models can be represented mathematically by the Prony-series. When comparing the isochronous curves and Prony-series parameters for different cortex positions, only insignificant differences were found.

6. Chapter 6

Characterisation of Microscale Mechanical Properties of Cortical Bone Tissue

6.1. Introduction

Bone has several arrangements of material structures at many length scales that work together to serve as a structural support, organ protection and ion mineral homeostasis [35]. It is a multi-scale composite material made of type-I collagen matrix and apatite mineral phase [164]. Bone's structural units (osteons and interstitial matrix) are produced thanks to remodelling activities; they represent an elementary level of hierarchy. Hence, the scale is important when studying cortical bone tissue. Different techniques for assessing bone's architecture and properties have their own resolution; therefore, a combination of techniques is required to measure bone's properties at several length scales [35]. Accordingly, mechanical properties and fracture mechanisms of bone material can be better understood. In this sense, in the current study two length scales are considered to quantify bone's mechanical properties: macro- and microscopic. In the previous chapter, mechanical properties of the cortical bone tissue at macroscopic length scale were measured and analyzed; here, its mechanical properties at microscopic scale are presented. Measuring those properties at both length scales is necessary to develop macro- and microscale finite-element models to simulate bone's deformation and fracture as it is discussed in the next chapters.

Also, characterisation of mechanical properties of cortical bone's microstructural constituents is essential to understand mechanical and fracture behaviours of the whole bone. Thanks to the micro- and nano-indentation techniques it is possible to measure mechanical properties in a region as small as 1 μm [165]. Depth-sensing nanoindentation together with theoretical methods can be used for extracting the elastic modulus from load-displacement data [16, 166]. Over the last two decades, the nanoindentation technique has achieved very high resolution for both load and displacement as well as a submicron spatial resolution, e.g., load resolution of 0.3

μN and displacement resolution of 0.16 nm [16, 166]. In this technique, mechanical properties of the microstructural features of interest can be derived from the analysis of high-resolution load-displacement data obtained as the indenter is driven into and withdrawn from the specimen leaving a residual imprint on its surface [16]. For instance, the elastic modulus values of those features can be determined from the slope of the unloading portion of the measured load-displacement curve, whereas their hardness can be calculated from the measured peak load and the residual indentation area. Hardness measurement conveys data about the quality and degree of bone mineralization [165]. This technique has been shown to be a successful tool for quantifying the material properties of bone's microstructural constituents, such as osteons and trabeculae [167]. Since many of the cortical bone tissue's features of interest are at the microscale level, nanoindentation technique is capable of probing directly its intrinsic mechanical properties at that level. Other methods were also used to measure bone's microscopic properties: microhardenss, microtesting and ultrasonic techniques [168, 169]. However, it was difficult to deduce directly bone's elastic properties such as elastic modulus from hardness measurements, because of the fact that microhardness of mammalian mineralized tissues is correlated to both elastic and yield stress [170]. Recently, an increased number of studies were performed to measure the elastic modulus and hardness of cortical bone using different indenters [171, 172]. For instance, Hoffler *et al*. [170] investigated the effect of different nanoindentation's experimental parameters on the measurements of the microstructural mechanical properties of a human cortical bone tissue. The studied parameters included the specimen preparation conditions, indentation depth, repetitive loading, time delay, and displacement rate. It was concluded that consistent values of the elastic modulus can be obtained from a 500 nm-deep indent. Also, it was found that the modulus and the hardness values of the dry specimens were significantly higher than those of the wet specimens - 22.6% and 56.9%, respectively. In addition, there were differences in the elastic moduli obtained at different loading rates; values at 5 nm/s were smaller than those obtained at 10 nm/s and 20 nm/s while there was no significant difference in data obtained at those higher rates. Different studies revealed a significant difference between the mechanical properties of osteons and interstitial matrix [167, 173]. These differences could be due to several factors, such as degree of mineralization,

collagen fibre orientation, and arrangement of these materials [167, 173]. Although literature data demonstrate that mechanical properties of microstructural features of bones such as elastic modulus and hardness were captured by various teams, yet complete constitutive equations, i.e., stress-strain curves at that length scale are still not available. Among all the mechanical properties of cortical bone's microstructural constituents, their stress-strain behaviour is one of the most important because it provides us with their deformation response. Relaying on that behaviour, phenomena such as plasticity localization, crack initiation and propagation as well as crack interaction with cortical bone's microstructural features can be assessed, using advanced modelling techniques.

In this study, in addition to measuring the elastic modulus and hardness values of cortical bone constituents, the flow stress-flow strain relationships for osteons and interstitial matrix are measured – to the author's knowledge – for the first time using a spherical indenter tip at different loading rates, maximum load level and dwell times. Before carrying out nanoindentation tests it was important to investigate the microstructure of cortical bone using optical microscopy. An optical microscopy images were captured for a transversal-radial section of a bovine femoral cortical bone tissue. Bone morphology captured in those images was implemented in the finite-element models and was also used to analyze some geometrical data such as porosity, volume fraction of osteons, and interstitial matrix. Moreover, it was used to investigate the presence of the secondary osteonal bone structure for the nanoindentation tests.

6.2. Optical Microscopy of Osteonal Cortical Bone Tissue

The cortical bone tissue at the microstructural level is composed of secondary osteons and interstitial bone. Osteons could be considered as fibre reinforcements in the composite structure and interstitial bone as a matrix [174]. To model cortical bone at the microstructural level using finite-element modelling, an optical microscopy images are needed to study its microstructural topology. Also, to quantify the mechanical properties of its constituents at microscale level, nanoindentation tests can be used. Therefore, investigation of the tested section to insure the presence of osteonal bone is important before carrying out nanoindentation tests. Different images were captured using an optical microscope

NIKON-OPTIPHOT (Banner Scientific limited; Coventry, England) with a GXCAM-5 digital camera, see Fig. 6.1. The microscope delivered sharp, clear images with good contrast and resolution that facilitate spotting defects and small microscopic features. The microscope was connected to a PC and employed TSView software for image analysis. Five image eyepiece tubes, including tilting models were available; 5X, 10X, 20X, 40X and 100X. A coarse- and fine-focusing control was provided through the microscope stand. Also, a rectangular mechanical stage was fitted with a coaxial control. The GXCAM-5 digital camera used for microscopy with 5.17 Megapixel has sensitivity of 0.8v/Lux-sec at 550 nm. A microscopic image of an osteonal transverse-radial section of cortical bone used for nanindentation testing as well as an input to the Abaqus finite-element software is shown in Fig. 6.2.

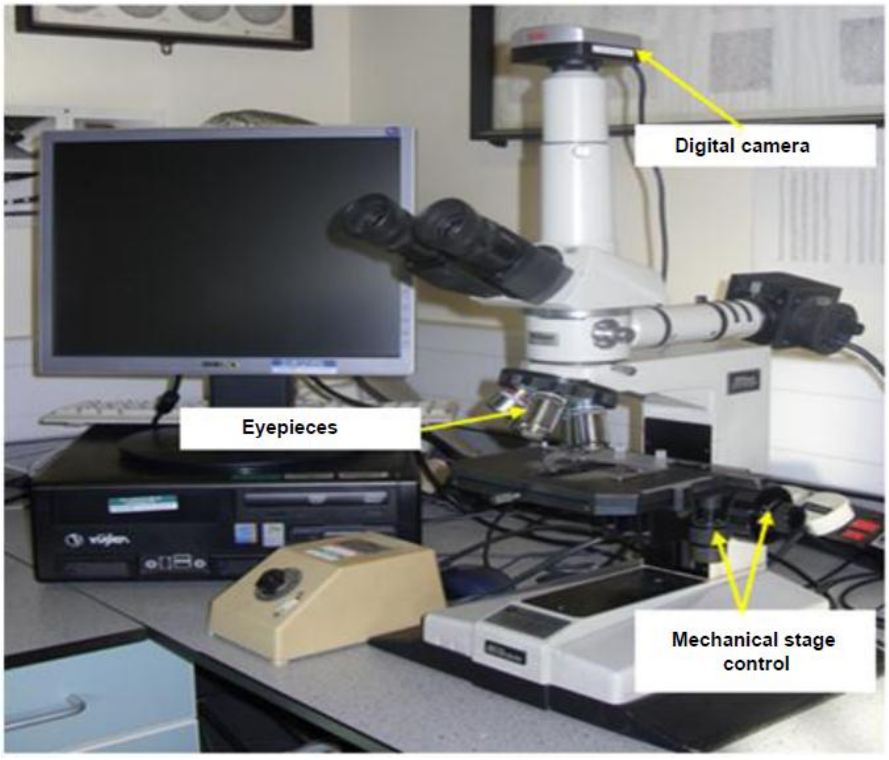

Figure 6.1: NIKON-OPTIPHOT microscope

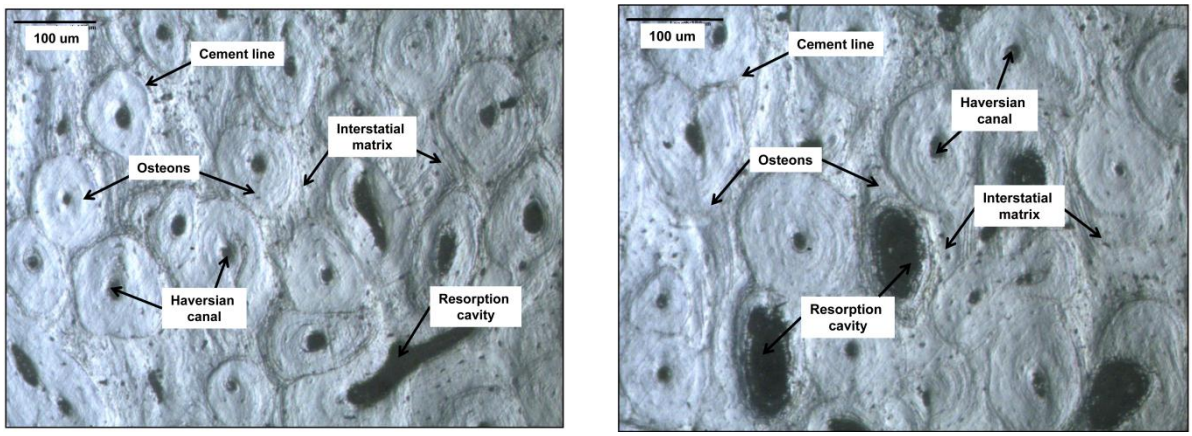

(a) (b)

Figure 6.2: Different samples of optical microscopic images for bovine femoral cortical bone tissue

6.3. Nanoindentation

Nanoindentation has been widely used by the material science community; for instance, it is employed for probing surface properties of thin films, small volumes, and microstructural features [16]. A schematic Illustration of a nanoindentation load-displacement curve is shown in Fig. 6.3.

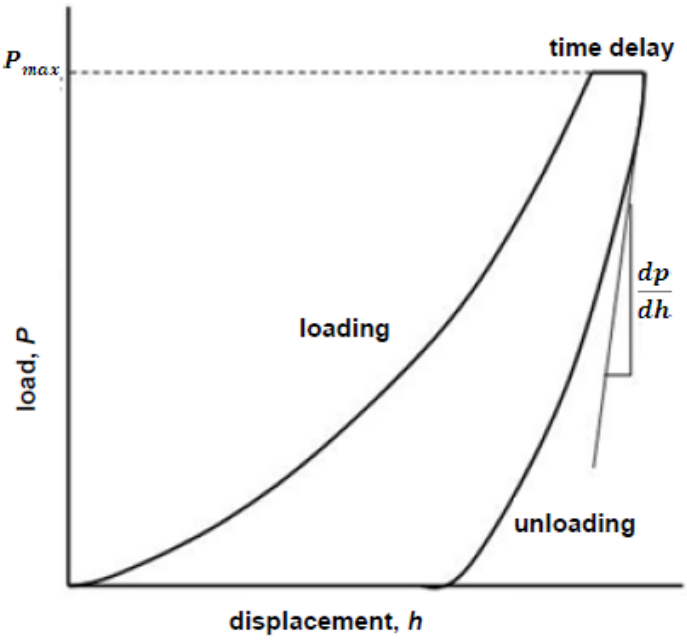

Figure 6.3: Schematic illustration of nanoindentation load-displacement curve during loading, time delay and unloading (after [16])

6.3.1. Theoretical Method

The theoretical basis of nanoindentation method relies on the solution of the problem of indentation of an elastic half-space with a rigid axis-symmetrical indenter derived by Sneddon [175]. The mathematical solution was adjusted by Oliver and Pharr [16]. Measurements of load-displacement curves from nanoindentation experiments are utilized to determine the contact stiffness, from which the indentation modulus can be calculated.

The relationship between elastic properties of a sample and contact stiffness is as follows:

$$S = \frac{dP}{dh} = \beta \frac{2}{\sqrt{\pi}} E_r \sqrt{A}\,, \qquad (6-1)$$

where P is the applied load, h is the indentation depth, A is the projected contact area of the indenter and function of depth h, and β is an empirical shape factor. To account for a non-rigid indenter used, a reduced modulus E_r is implemented and determined as follows:

$$\frac{1}{E_r} = \frac{(1-v_s^2)}{E_s} + \frac{(1-v_i^2)}{E_i}, \qquad (6-2)$$

where E_s and v_s are the elastic modulus and Poisson's ratio of the specimen, respectively, and E_i and v_i are the respective parameters of the indenter. In Eq. (6-2) the specimen is considered as an isotropic material, and the Poisson's ratio value has to be known. For a diamond indenter tip an elastic modulus is 1141 GPa and a Poisson's ratio is 0.07 [16]. The shape factor β=1 for a spherical diamond indent, which was used in our study.

Hardness of the cortical bone tissue's constituents can be calculated as follows:

$$H = \frac{P_{max}}{A}, \qquad (6-3)$$

where P_{max} is the maximum indentation load and A is the corresponding projected area.

In general, nanoindentation reveals a wealth of information about the mechanics and mechanisms of thin films or small volumes of the studied material. This information includes levels of the elastic modulus, hardness, surface adhesion, creep, and stress relaxation behaviours. Moreover, it can also be used to obtain the flow stress-flow strain behaviour; the respective methodology is described elsewhere in [176].

6.3.2. Spherical Indentation Theory

Sharp-tipped indenters don't allow a smooth transition between elastic and plastic behaviour of the material because they produce a constant strain impression [16]. On the other hand, spherical indenters provide a smooth transition and evaluation of the elastic-plastic behaviour of the material because an increasing contact stress is developed with the increasing indentation load [19]. The model used to investigate the effects of geometry on local elastic deformation properties was first considered Heinrich Hertz in 1882 [20]. In Hertizian contact, the circular contact area of two contacting spheres is related to the elastic deformation properties of the materials. The radius of that area predicted by Hertizian analysis is given as follows [21]:

$$a = \left(\frac{3PR_s}{4E_r}\right)^{1/3}, \qquad (6-4)$$

where P is the applied load, R_s is the radius of the sphere, and E_r is the reduced modulus given in Eq. 6-2.

For static Hertizian contact, the maximum shear stress is situated at a distance of approx. half the contact radius measured from the point of contact. On the other hand, yielding first takes place below the surface when

$$P_m = 1.1\,Y \qquad (6-5)$$

where P_m is the mean pressure and Y is the yield stress. The contact remains elastic if the mean pressure is less than this value.

An indentation process may produce one of three possible deformations: (i) reversible, elastic; (ii) permanent, plastic; or (iii) both elastic and plastic. The ratio between the actual strain and the yield strain of the material determines its behaviour during indentation process. The elastic behaviour can be obtained for low

ratios (less than 2), and the behaviour can be considered purely plastic for high ratios (higher than 50). The value of the actual strain is given by $\tan\emptyset$, where $\emptyset$ is the angle between the indenter and sample surfaces; it is obvious that a spherical and pyramid indenter will behave differently. In the case of a Vickers pyramid, for instance, $\emptyset$ is constant and the strain is therefore constant (8%), regardless of depth. On the other hand, for a spherical indenter, $\emptyset$ and, therefore, strain increases with indentation depth. Consequently, a series of spherical indentations with an increasing maximum load can produce results ranging from purely elastic to elastic-plastic deformation in addition to stress-strain curves [17].

By performing multiple loading-unloading cycles with increasing maximum loads at a single point using a spherical indenter with a known radius, the contact area, hardness, elastic modulus as well as stress and strain can be calculated.

6.3.3. Spherical Indentation Analysis Procedure

For a given indentation experiment consisting of n indentation cycles, the related total penetration depth is h_t at a load P_t and a partially recovered depth h_s at a reduced load of P_s. The depth h_r of the residual impression relative to the specimen original surface for a fully unloaded indenter can be calculated as follows [17]:

$$h_r = \frac{rh_s - h_t}{r - 1}, \qquad (6-6)$$

where

$$r = \left(\frac{P_t}{P_s}\right)^{\frac{2}{3}}. \qquad (6-7)$$

The elastic component h_e and the plastic component h_p of the indentation at each cycle can be calculated as follows:

$$h_e = h_t - h_r, \qquad (6-8)$$

$$h_p = \frac{h_t + h_r}{2}. \qquad (6-9)$$

The contact circle radius a in the original surface plane at each indentation cycle can be calculated as follows:

$$a = \sqrt{(2R_s h_p - h_p^2)}, \qquad (6-10)$$

where R_s is the spherical indenter's radius.

Hardness H, reduced modulus E_r, flow stress σ_r and corresponding flow strain ε_r at each indentation cycle i can be calculated as follows:

$$H_i = \frac{P_{t_i}}{\pi a_i^2}, \qquad (6-11)$$

$$E_{r_i} = \frac{3}{4}\frac{P_{t_i}}{a_i h_{e_i}}, \qquad (6-12)$$

$$\sigma_{r_i} = \frac{H_i}{3}, \qquad (6-13)$$

$$\varepsilon_{r_i} = 0.2\ \frac{a_i}{R}, \qquad (6-14)$$

where $i = 1\ to\ N$.

To account for the piling-up or sinking-in possibilities around the spherical indenter contact, the true contact circle radius a_r is related to a determined above by the following function:

$$a_r = ca. \qquad (6-15)$$

The value of the constant c can be determined as follows: first from plotting a double logarithmic curve between P_{t_i} and a_i, the Meyer's index $(2 + 1/n)$ is calculated as the slope of the curve, and then c can be calculated as

$$c^2 = \frac{5}{2}\frac{2n-1}{4n+1}. \qquad (6-16)$$

Thus, a correction factors $1/c^2$ and $1/c$ should be applied to hardness H and the reduced modulus E_r, respectively.

6.3.4. NanoTest 600 Indentation System

Depth-sensing indentation (DSI) experiments were performed by using a NanoTest 600 system. This system was manufactured by Micro Materials, Wrexham UK. A

schematic view of the NanoTest 600 system is shown in Fig. 6.4. Precise DC motors with displacement resolution of 17.3 nm in X, Y, and Z directions are used to manipulate the sample stage. A high-resolution microscope is utilized to define the exact positions of the indents in a sample with the help of a microscope monitor. A calibration process is needed before starting the test for “focal plane” and “measurement plane”. The “focal plane” is the plane parallel to the Y-Z plane of the sample holder, wherein the sample’s surface is in focus at the highest magnification. When the sample is changed, it is brought to the focal plane before starting an indentation test. The “measurement plane” is the plane parallel to the X-Z plane of the sample holder, wherein the sample’s surface is approximately 50 µm from the indenter tip (Fig. 6.5).

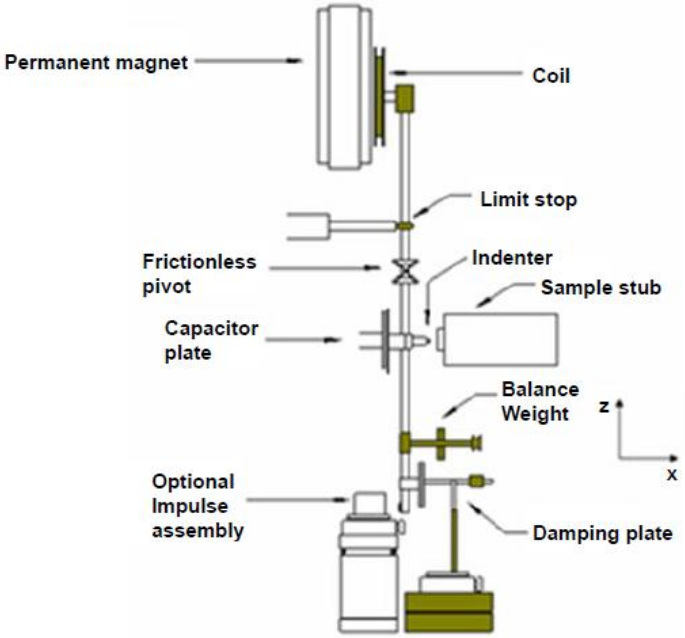

Figure 6.4: Schematic illustration of NanoTest 600 indentation system [17]

A light-weight pendulum with an indenter that can rotate on a frictionless pivot constitutes the nanohead with a load range of 0.1-500 mN and resolution of 0.1 µN. The pendulum column is made from a ceramic that is stiff enough to sustain the maximum load of 500 mN with negligible deflection. A coil is assembled to the pendulum head. When the current is applied to the coil, it is attracted towards a permanent magnet, resulting in the indenter motion towards the sample surface. The indenter displacement is measured by means of a parallel plate capacitor,

where one of the plates is attached to the indenter holder. Consequently, when the load is applied and the indenter starts to penetrate the sample's surface, capacitance is changed and the displacement is measured by a capacitance bridge. The latter is located close to the measuring capacitor to minimize the unwanted capacitance effects. A weight necessary to counter-balance the coil's and indenter's masses is attached below the capacitance plates. The maximum outward movement of the indenter as well as the operating orientation of the pendulum is defined by the limit stop when the load is applied. It can be adjusted manually with a micrometer. A balance weights movable along both the horizontal and vertical axes is used to adjust the equilibrium position of the pendulum at zero load current. The governing parameters of the DSI experiments are the maximum load, loading rate, dwell period, and unloading rate.

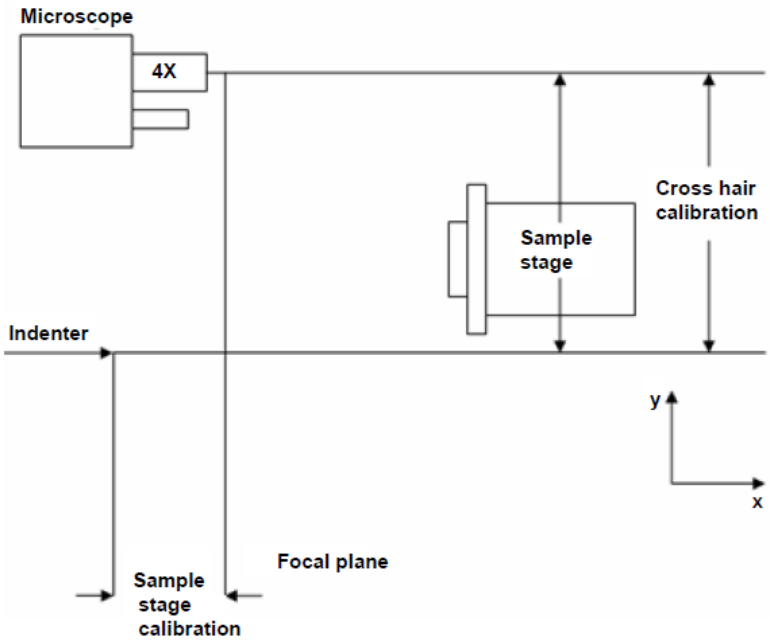

Figure 6.5: Plan view of NanoTest 600 indentation system [17]

6.3.5. Specimen Preparation

The specimen preparation and storage protocol are the same as those for the uniaxial tension tests discussed earlier in Section 5.2.2. Four identical specimens with dimensions of 5 mm × 3 mm × 15 mm were used for optical microscopy and nanoindentation experiments. After cutting the optical and nanoindentation specimens from the posterior cortex using the milling machine, they were ground

using a series of grinding papers Standard ANSI grit, 240, 600, 1200, and then polished with cloth of 1 μm grits so that the topology of the osteonal cortical bone could be observed with optical microscopy.

6.3.6. Experimental Procedure

The nanoindentation tests were performed with the Nano-test 600 indentation system at room temperature of 23.3°C and relative humidity of 31.7%. A spherical diamond tip with a radius of 25 μm with a low-load head for 0.1-500 mN was employed, and the maximum measurement depth when the system is set at full sensitivity was approx. 1.5 μm. NanoTest (NT2) materials testing platform was used to calibrate, set the control parameters, and allow monitoring and analyzing the experimental data. The specimen, the transverse-radial section of the mid-diaphysis of a bovine femoral cortical bone, was glued horizontally to a holder and gently firmed in front of the indenter tip. The microscope accompanied with the indenter tip allowed precise positioning of the indenter at the required position to test either osteons or the interstitial matrix.

Nanoindentation tests were performed for four identical cortical bone specimens cut from the posterior cortex position in the transverse-radial plane at maximum loads of 5 mN, 10 mN, 20 mN and 50 mN, with each specimen being tested under one loading condition. The specimen tested under a maximum load of 10 mN was also employed to investigate the effect of loading rate on the elastic-plastic behaviour with three different rates of 0.5 mN/s, 1 mN/s and 2 mN/s; the rest of the specimens were tested at loading rate of 0.5 mN/s. For each specimen, two indents with 100 μm separating distance were performed within three osteons and three interstitial matrix positions. For each indent, ten loading-unloading cycles were performed to construct the flow stress-flow strain curve, with each cycle constituting a point on the curve. For all loading conditions and rates, to investigate the effect of holding time, each indent was performed twice with dwell times of 0 s and 120 s. The tests were performed in a load-control regime.

A view of the NanoTest 600 indentation system and the experimental arrangement of the bovine cortical bone's indentation test are shown in Figs. 6.6 and 6.7, respectively.

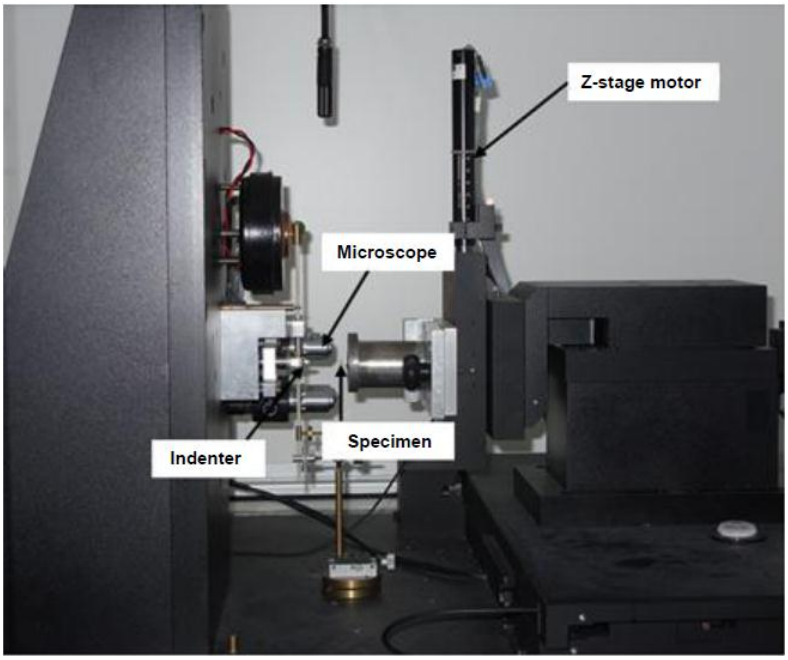

Figure 6.6: NanoTest 600 indentation system

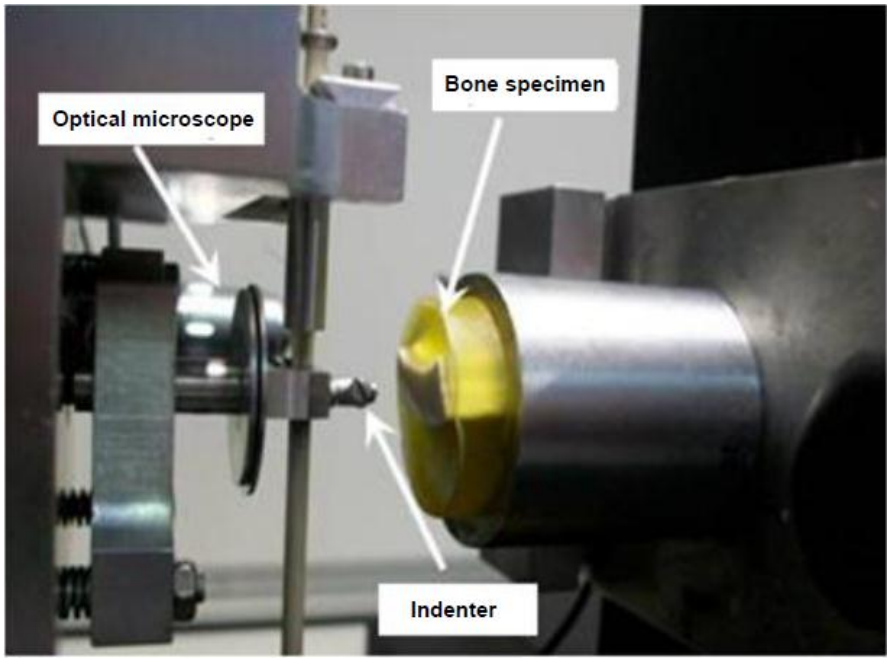

Figure 6.7: Experimental arrangements for nanoindentation test of bovine femoral cortical bone tissue

6.4. Bone as Composite Material

Several authors have attempted to mathematically model bone as a composite material to derive certain mechanical properties. These include the rule of mixture approaches based on Voigt and Reuss hypotheses. It was assumed that bone has two or more phases (e.g. collagen and mineral or soft and hard tissue) [177-179]. These phases contribute to a mechanical property P that is directly proportional to the volume fraction f that they occupy. Most commonly P is the elastic modulus. Such a model can be simplified to consist of alternating blocks of two phases. These two blocks can be arranged so that they can have either the same strain or the same stress. The former follows the Voigt model; the latter follows the Reuss model [18]. In the Voigt model, see Fig. 6.8a, the two blocks are loaded with equal strain; whereas in Reuss model, see Fig. 6.8b, they are loaded with equal stress.

In the Voigt model, the composite property is given by [18]

$$P_c = P_1 f_1 + P_2 f_2 , \qquad (6-17)$$

where the subscripts 1 and 2 refer to two components of the composite property P_c.

In the Reuss model, the composite property is described by [18]

$$P_c = \frac{P_1 P_2}{P_1(1-f_1)+P_2(1-f_2)} , \qquad (6-18)$$

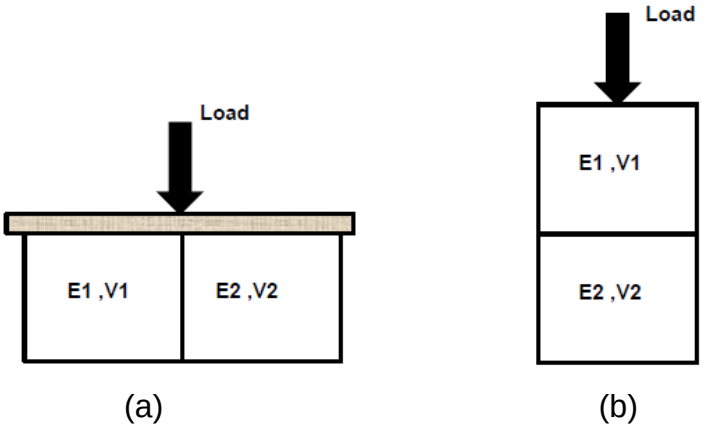

Figure 6.8: Models for composite material formed by two phases; (a) Voigt model; (b) Reuss model (after [18])

In the past few decades, several approaches were proposed using these two approaches to mathematically model and analyse composite materials (see [180] and the references therein). In fact, using reliable rules based on these approaches can help to overcome the complexity accompanying the use of experimental tests and numerical models that demand a significant effort. Therefore, a simple solution can be obtained using the classical rule of mixture. The effective material properties obtained using the rule of mixture is assumed to be independent of the geometry, the loading condition and the boundary conditions [181].

In this study, the rule of mixture named after Voigt will be used to calculate the effective elastic modulus of cortical bone specimens cut from posterior cortex positions based on nanoindentation and topological measurements using the following equation:

$$E_c = E_o A_o + E_m A_m , \qquad (6-19)$$

where E_c is the effective macroscopic elastic modulus, E_o and E_m are the microscopic elastic moduli for osteons and interstitial matrix, respectively. A_o and A_m represent the area fraction of osteons and interstitial matrix, respectively.

6.5. Results and Discussion

6.5.1. Microscopy Analysis

Several light-microscopy pictures of a radial-transverse section of the bovine cortical bone were captured; sample pictures are shown in Fig. 6.2. Various geometrical parameters were extracted from those pictures: diameters of the osteons and Haversian canals, cement line thickness, and diameters of voids. All the pictures have identical dimensions of 700 µm × 525 µm (width × thickness). The statistical analysis for those pictures exhibited an osteons volumetric fraction of approx. 60% and a porosity ratio between 1.6% and 5.3%. The average thickness of cement lines was about 5 µm. All the parameters were measured from those pictures using digital image analysis software, IMAGE-PRO EXPRESS. The observations obtained from that study were statistically analysed to be fitted to one of the well-known distributions that describe the random phenomena. It was found that random distribution of the osteon diameters can be fitted with the hypersecant

distribution curve described by the values of continuous scale μ and location parameter ϑ 35.3 and 99.9, respectively, see Fig. 6.9a. On the other hand, Dagum (4P) curve revealed a good fit for diameters of Haversian canal and can be defined by k = 1.52, α = 2.7, ψ = 12.9, and γ = 3.3, see Fig. 6.9b. The average diameters of osteon fibre and Haversian canal were 99.89 µm and 23.1 µm, respectively.

The probability density function of the hypersecant distribution is as follows:

$$f(x) = \frac{\operatorname{sech}\left(\frac{\pi(x-\mu)}{2\vartheta}\right)}{2\vartheta}. \qquad (6-20)$$

The probability density function of Dagum (4P) distribution is as follows:

$$f(x) = \frac{\alpha k \left(\frac{x-\gamma}{\psi}\right)^{\alpha k-1}}{\beta\left(1+\left(\frac{x-\alpha}{\psi}\right)^{\alpha}\right)^{k+1}}. \qquad (6-21)$$

where k and α are continuous shape parameters, and ψ and γ are continuous scale and location parameters.

These distributions along with the properties measured using nanoindentation technique underpin the microscale finite-element model to investigate deformation and fracture of the cortical bone tissue at microstructural level. Implementation of statistical realizations based on these distributions to build the geometry of the microscale finite-element model will be discussed in details in the next chapters.

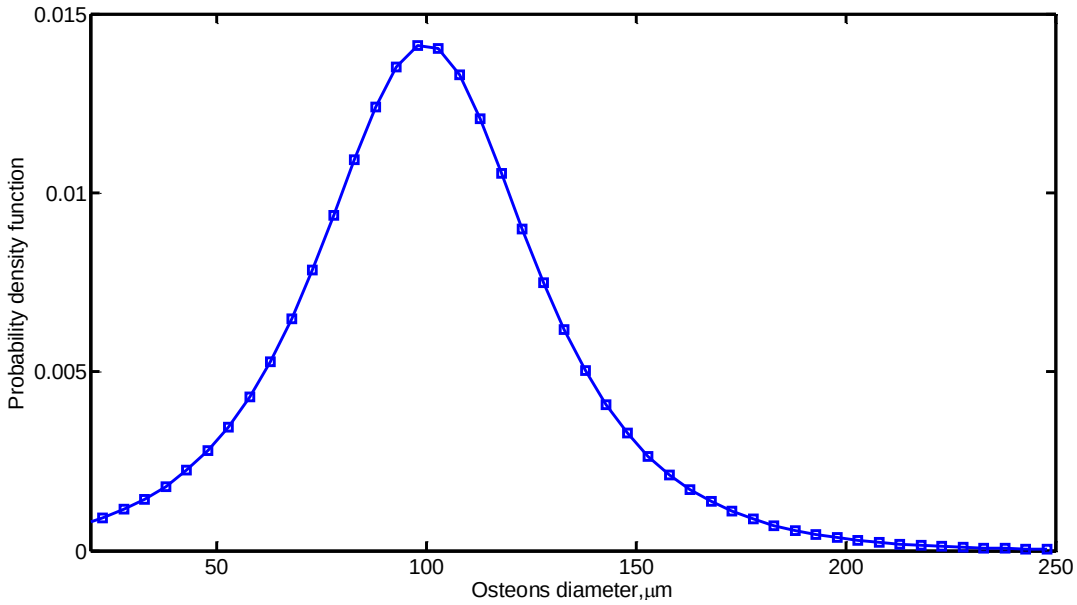

(a)

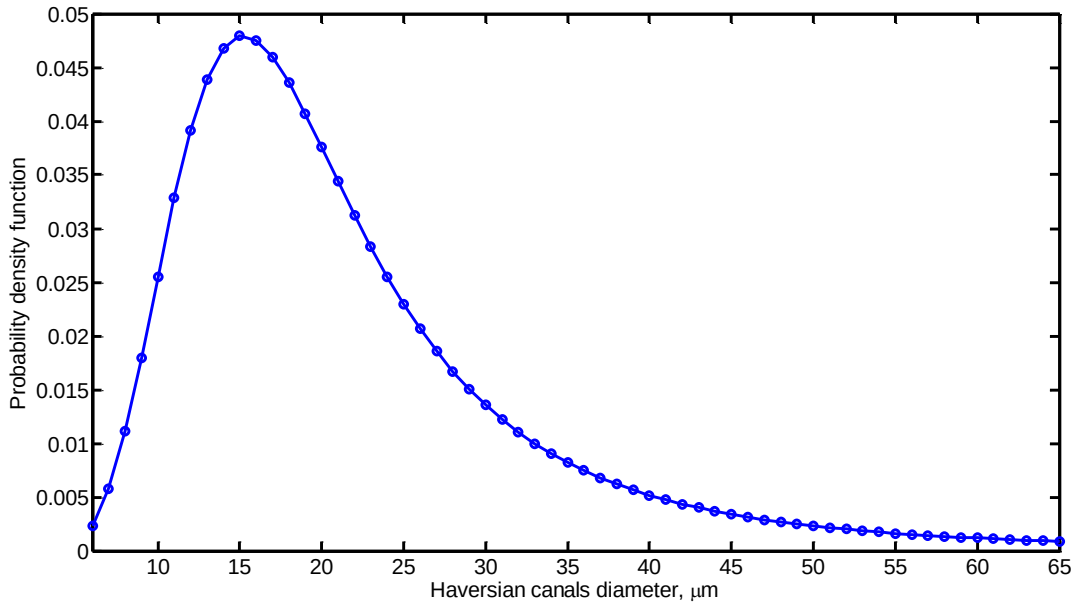

(b)

Figure 6.9: (a) Experimental and hypersecant distribution of osteons diameters; (b) Dagum (4P) distribution of Haversian canals diameters

6.5.2. Nanoindentation Tests Results

Recently, the nanoindentation technique has been applied to biological tissues including a bone tissue [173]. Measuring the mechanical properties of cortical bone at the lamellar level is important for developing theoretical micromechanical models and finite-element schemes along with gaining better understanding of bone's fracture mechanisms. Since many of the features of interest in cortical bone are at microscopic level, its intrinsic mechanical properties at that level can be probed directly by nanoindentation technique. A load-displacement curve for nanoindentation test shows that as the load increases, the indenter sinks in the material causing elastic-plastic deformation. On the other hand, when unloading the indenter, the material recovers mainly elastically. Using this technique, the elastic modulus, post-yield behaviour and hardness of cortical bone tissue were characterized as discussed in the next sections.

Elastic Modulus and Hardness

The nanoindenter with a spherical tip with radius of 25 μm made imprints on the bone specimens' surface, clearly visible under a light microscope (see Fig. 6.10). The shape of indents is nearly spherical, demonstrating that a nanoindenter could easily make small indents within desired microstructural features of cortical bone tissues such as osteons and interstitial bone. No cracks were found around the spherical imprints.

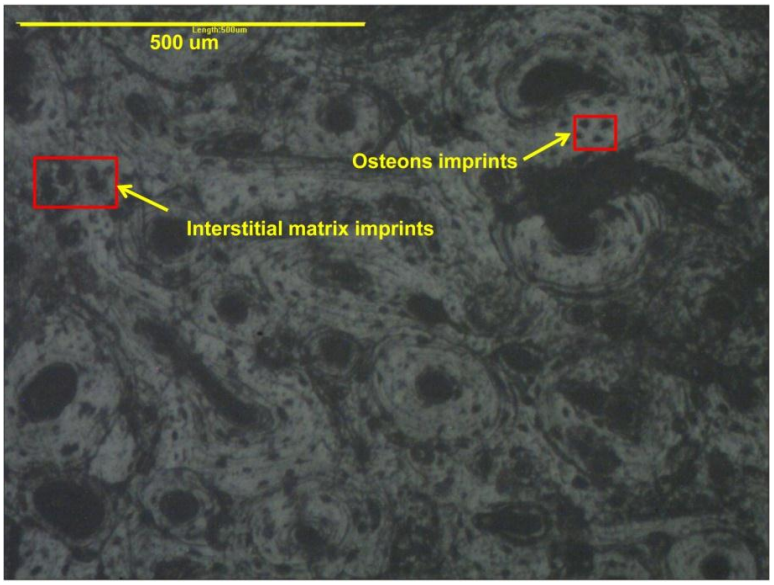

Figure 6.10: Spherical indents in osteons of cortical bone's specimen

The basic response acquired with the depth-indentation system is a load-displacement curve representing the loading-unloading history of the sample. The typical cyclic load-displacement (depth) curves for osteons and interstitial matrix obtained in the indentation tests at maximum load of 20 mN, loading-unloading rate of 0.5 mN/s and two time delays – 0 s and120 s – are shown in Fig. 6.11.

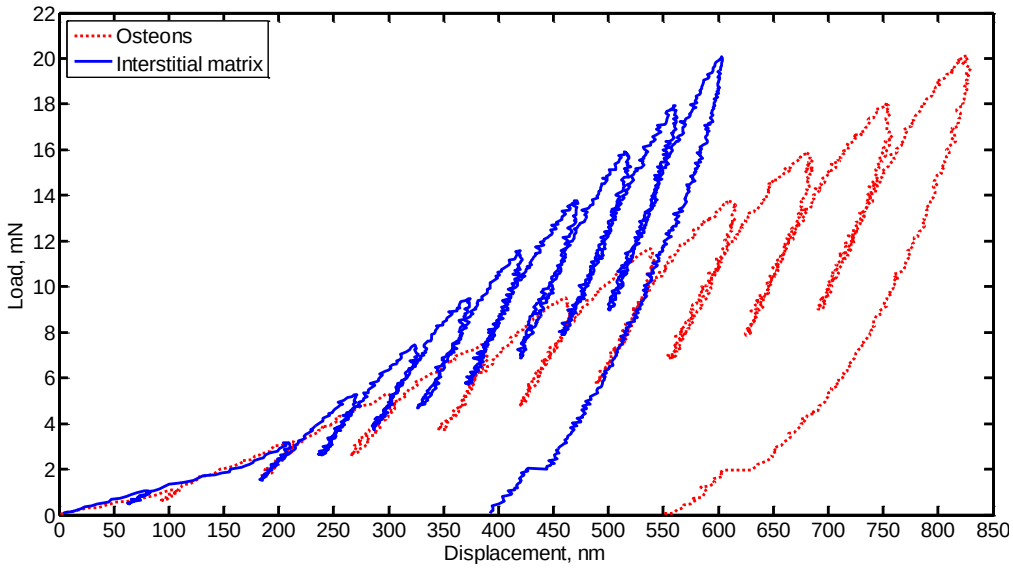

(a)

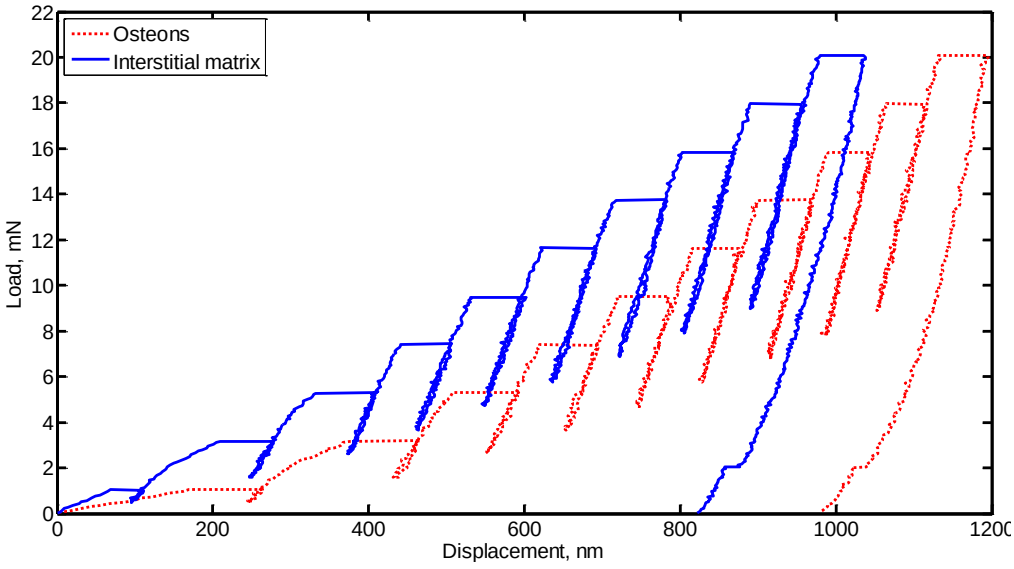

(b)

Figure 6.11: Typical cyclic load-displacement curves from nanoindentaion experiments for osteons and interstitial matrix (maximum load 20 mN, loading rate 0.5 mN/s) for dwell time = 0 s (a) and dwell time = 120 s (b)

The load-control method used showed a different indentation depth for osteons and interstitial matrix at the same indentation load. For instance, a maximum load of 20 mN corresponded to depths of 823.3 nm and 1194 nm for osteons at the last cycle, while they were 602.5 nm and 1038 nm at the same load in the interstitial matrix for time delays of 0 s and 120 s, respectively. It was the case for all the performed cycles indicating that stiffness of interstitial matrix exceeded that of osteons. Moreover, for the time delay of 120 s, both osteons and interstitial matrix demonstrated higher depths when compared to those acquired at the time delay of 0 s indicating a viscoelastic nature of the cortical bone tissue that was addressed in details in the previous chapter.

Using both the experimental data acquired and the theoretical method described in Sections 6.3.1 and 6.3.3, mechanical properties such as elastic modulus can be obtained using Eq. 6-12, and hardness using Eq. 6-11. For the elastic moduli calculations a Poisson's ratio of 0.42 was used for the microstructural feature of cortical bone tissue based on the Poisson's ratios' measurements for specimens cut from posterior cortex (Section 5.5.2). Figure 6.12a shows the effect of loading-unloading rate on the elastic modulus values of osteons and interstitial matrix measured with different time delays – 0 s and 120 s. Generally, the values of elastic modulus values were higher for interstitial matrix compared to osteons for all the loading-unloading rates, 0.5 mN/s, 1 mN/s and 2 mN/s, and for the time delays, 0 s and 120 s. The fact that bone is in a continuous remodelling process consisting in a succession of resorption and formation processes that lead to heterogeneity of bone material, and the correlation between the mineral content and elastic modulus underpin the difference between elastic properties of the osteon and interstitial matrix [164, 182]. Values of the elastic modulus for osteons showed lower levels of variation compared to those for interstitial matrix for all loading rates. Again, the variance in the elastic modulus values was likely related to mineral, collagen and noncollagenous protein composition [170]. In addition, there may have been other sources of variance including subsurface porosity, subsurface lacunae, and surface irregularities [170].

The elastic moduli increased with the increase in the loading rate for both osteons and interstitial matrix for the time delays of 0 s and 120 s. For the time delay 0 s, the moduli measured for osteons were 12.98$\pm$1.08 GPa, 13.05$\pm$0.81 GPa and

13.48±1.1 GPa while those for interstitial matrix were 14.29±1.72 GPa, 14.30±1.65 GPa and 14.90±1.5 GPa for loading-unloading rates of 0.5 mN/s, 1 mN/s and 2 mN/s, respectively. On the other hand, for time delay of 120 s, they were 7.68±0.53 GPa, 8.89±1.06 GPa and 11.90±1.03 GPa for osteons and 9.5±0.05 GPa, 9.63±0.77 GPa and 13.22±1.71 GPa for interstitial matrix for loading-unloading rates of 0.5 mN/s, 1 mN/s and 2 mN/s, respectively. Based on these results, it can be noticed that for time delay of 0 s, no significant difference was found between elastic moduli neither for osteons nor for interstitial matrix at the studied loading rates. However, for the time delay of 120 s, there were no significant differences between the values of elastic modulus for loading rates of 0.5 mN/s and 1 mN/s, whereas a significant difference was found between values measured at these rates and 2 mN/s for both osteons and interstitial matrix. For the maximum – indentation – load study, the elastic moduli for interstitial matrix were higher than those of osteons at the same indentation load for both time delays. For the time delay of 0 s, the elastic moduli increased with the maximum-load increase for loads of 5 mN and 10 mN, while the values were approximately the same for loads of 20 mN and 50 mN for both osteons and interstitial matrix. Interestingly enough that only a slight difference was found between the elastic-modulus values for time delays 0 s and 120 s for a maximum load of 50 mN. It can be noticed here that as the indentation load increases as, in turn, the indentation depth, the values of elastic modulus converge. This can be linked to the surface polishing artifact and inaccurate area estimation for shallow indents. The depth-sensitivity findings are in line with a similar study by Hoffler *et al*. [170].

The average elastic properties in our experiment were comparable to data in the literature, elastic moduli in the range from 2 to 45.8 GPa were reported for different animal species including bovine bone [183], and in the range from 13.4 GPa to 24.2 GPa for bovine bone osteons [182]. However, the obtained elastic-modulus data were sometimes lower compared to some of those available in the literature because they have used sharper indentation tip, such as Berkovich or a cube corner. In the current study, spherical indentation tip was used to obtain the elastic-plastic behaviour of cortical bone constituents that yielded higher indentation area, which, in turn, led to lower the values of elastic moduli and hardness. However, the effective elastic modulus based on Eq. 6-19 and microscopic analysis was

calculated to be 13.14 GPa and 12.73 GPa at load of 50 mN and loading rate of 0.5 mN/s for time delay of 0 s and 120 s, respectively, which is in agreement with the obtained elastic modulus value for specimens cut from posterior cortex – 12.53 GPa (Table 5.1).

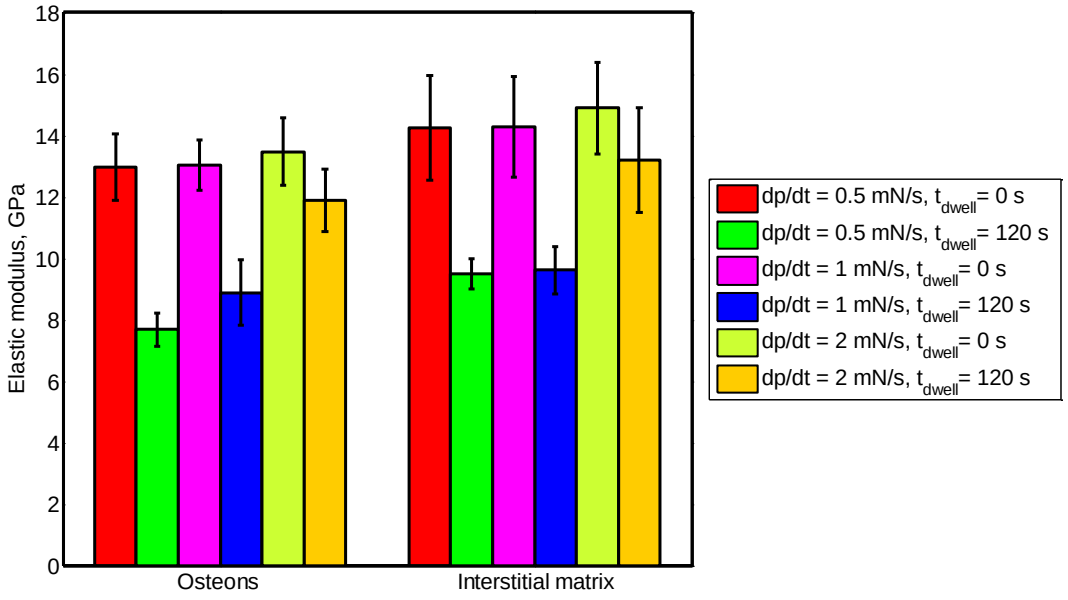

(a)

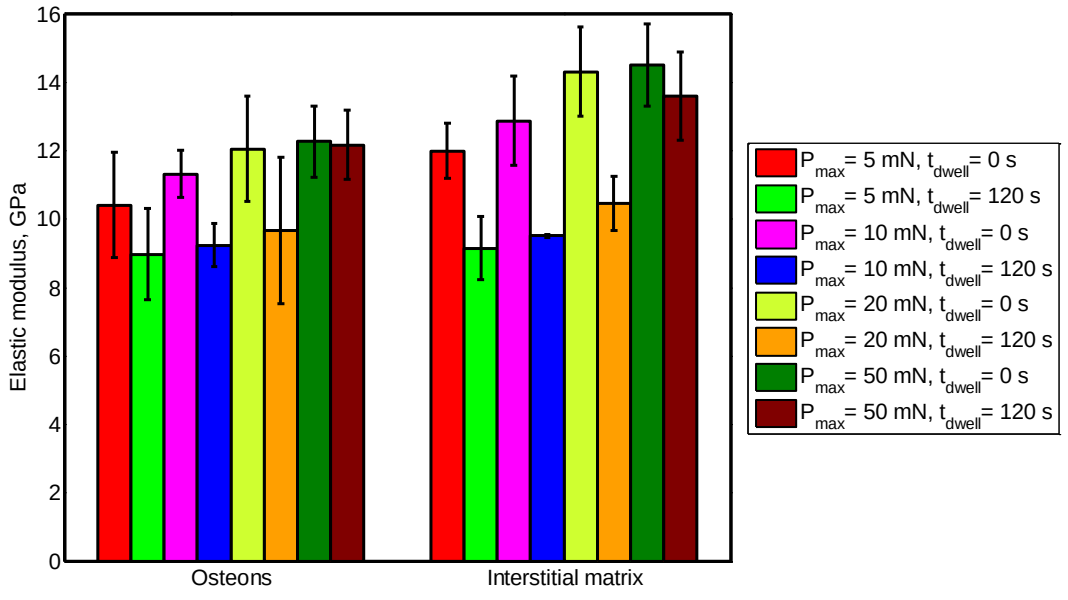

(b)

Figure 6.12: Elastic modulus for osteons and interstitial matrix: (a) effect of loading-unloading rate and dwell time at maximum load 10 mN; (b) effect of maximum applied load and dwell time at loading-unloading rate 0.5 mN/s

The average hardness values were 0.398±0.008 GPa, 0.421±0.019 GPa, 0.435±0.03 GPa and 0.518±0.064 GPa for osteons and 0.618±0.012 GPa, 0.622±0.015 GPa, 0.634±0.094 GPa and 0.765±0.048 GPa for interstitial bone tissue for maximum loads of 5 mN, 10 mN, 20 mN and 50 mN, respectively. As expected, these values are slightly lower than those obtained using a sharper notch due to the larger area accompanied indentations with the spherical tip that led to lower hardness values. A hardness values were reported in literature of 0.578±0.052 GPa for osteons and 0.818± 0.049 GPa for interstitial matrix obtained for bovine cortical bone at a maximum load of 20 mN using Berkovich indenter [183]. However, in order to quantify the elastic-plastic behaviour of cortical bone tissue at microstructural scale, a spherical tip had to be used to obtain a smooth transition from elastic to plastic behaviour.

Flow stress and flow strain

Ten-cycle indentation tests were performed for both the osteonal area and interstitial matrix, with flow stresses and strains were calculated for each cycle using the obtained experimental data together with Eqs. 6-13 and 6-14. As an example, the calculated flow stress-flow strain curves for osteons and interstitial matrix at loading-unloading rate of 0.5 mN/s and time delay of 120 s are demonstrated in Fig. 6.13.

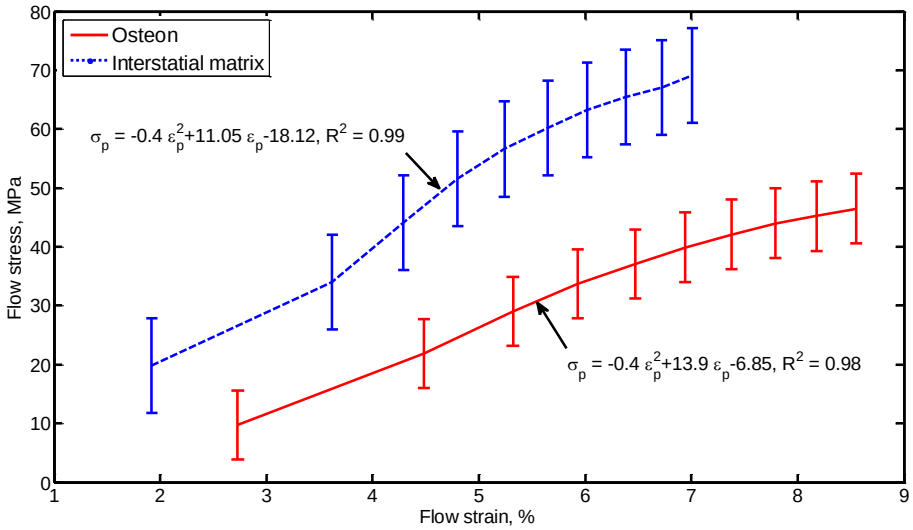

Figure 6.13: Flow stress-flow strain graphs for osteons and interstitial matrix (maximum load 50 mN; loading-unloading rate 0.5 mN/s; dwell time 120 s). Error bars show standard deviation

Since the nanoindentation technique leads to elastic-plastic deformation, using cyclic loading with spherical indenter enabled us to resolve elastic and plastic responses. Accordingly, each point on these curves is the result of one complete cycle of loading-unloading indentation test. Then, the quadratic regression was used with high correlation factors to fit the experimental data for both constituents (Fig. 6.13). It was found that not only the elastic modulus and hardness values of the interstitial matrix were higher than those of osteons, but also the flow stresses required to achieve the same flow strains were higher. Obviously, it is well documented in literature that a bone mineral content plays a major role in bone strength, and a collagen component plays a role in plastic deformation [184]. In addition, in another study, it was shown that collagen maturity is a strong predictor of a cortical bone's plastic behaviour at microstructural level [164]. In fact, the interstitial matrix is the remaining part of the remodelling process; hence, its age is greater than that of osteons. In this sense, its collagen component is more mature and plastic as indicated in Fig. 6.13.

In investigating the loading-unloading effect on the post-yield behaviour, it was found that cortical bone's microstructural features (osteons and interstitial matrix) are strain-rate sensitive as apparent from comparing the respective flow stress–flow strain curves for different loading rates (Fig. 6.14). The higher the loading rate, the higher the values of flow stresses at the same flow strains. These results indicate that cortical bone at the microstructural level possesses time-dependent elastic-plastic behaviour demonstrated by the effect of loading rate on the elastic modulus values as shown in Fig. 6.12 and on the plastic response as shown in Fig. 6.14. Flow stress-flow strain graphs are higher for higher strain rates; moreover, the response indicates a hardening effect for both osteons and interstitial matrix. It is worth noticing also that for higher strain rates, the material started to yield at lower flow strain for both osteons and matrix.

Indents in all the series gave the same behaviour with some slight changes in the values of the flow stresses and strains. Most probably, the changes in those values were due to local variations in properties linked to collagen maturity, surface porosity, subsurface lacunae, or irregularities that remain after polishing [170].

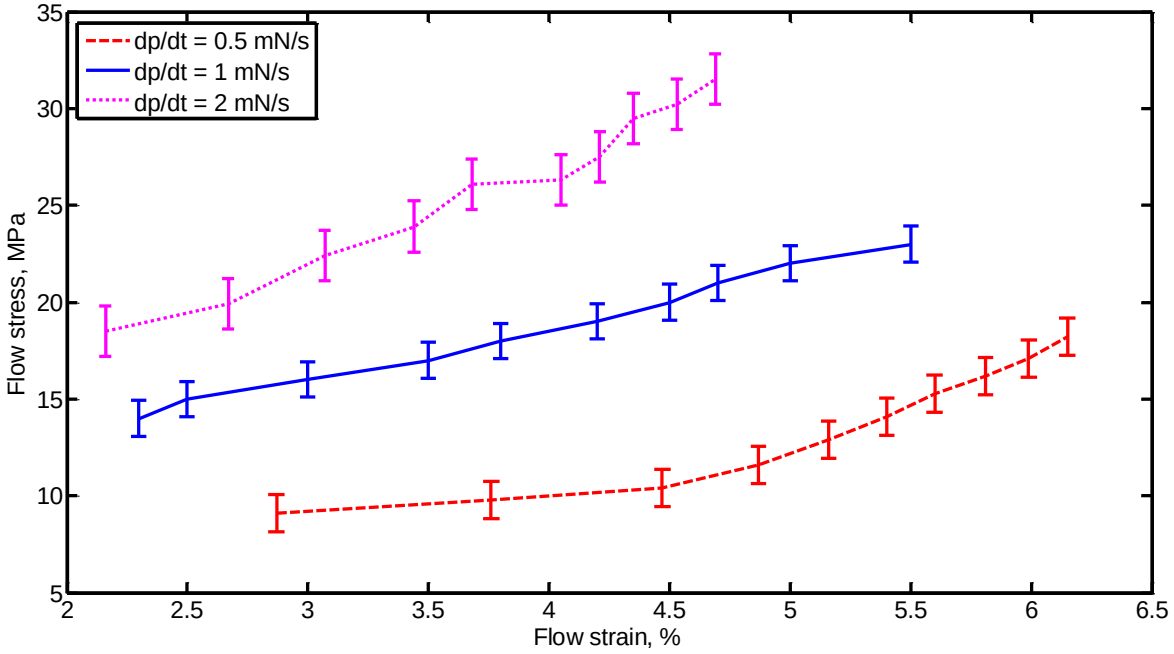

(a)

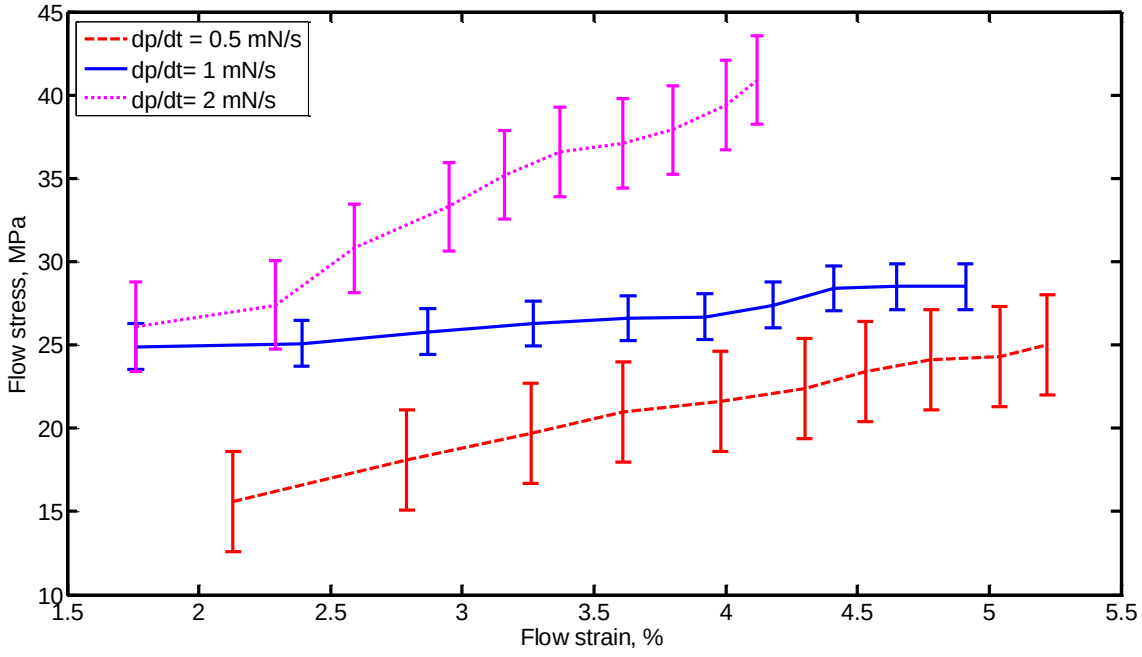

(b)

Figure 6.14: Effect of loading-unloading rate on flow stress-flow strain graphs (maximum load 10 mN; dwell time 120 s): (a) osteons; (b) interstitial matrix. Error bars show standard deviation

When using nanoindentation to measure mechanical properties of the cortical bone tissue, significant effects on the results due viscoelasticity may arise, since Oliver and Pharr method [16], described in Section 6.3.1, assumes a purely plastic behaviour during unloading. One method to reduce the error due to viscosity effects in the Oliver-Pharr analysis is increasing the time delay before unloading [185]. In the current study, elastic moduli obtained at maximum load of 50 mN, loading-unloading rate of 0.5 mN/s and time delay of 120 s along with topology information produced effective modulus value closer to those obtained in the uniaxial tension test of posterior cortex specimens. Hence, the effect of the time delay was considered for the post-yield behaviour as shown in Fig. 6.15. A significant difference was found between the flow stress-flow strain behaviours obtained based on a time delay of 0 s and 120 s for both osteons and interstitial matrix. Obviously, the use of the higher time delay produced higher values of flow strain due to the creep effect but required lower levels flow stress. Also, the harder material – interstitial matrix – exhibited a more pronounced change in the gradient of flow stress as flow strain increased. Both constituents showed a gradual work hardening under the indenter as the load is increased in every subsequent cycle. This means that plastic deformation started to occur beneath the indenter surface but it was constrained by the surrounding elastic material at the beginning, then the plastic region extended to the surface of the specimen and continued to grow. It was suggested in another study that most of the bone's toughness takes place after yielding, in which energy depends on both strength and ductility, i.e., a degree of permanent deformation of bone [186]. Obviously, two different constituents exhibited different behaviours; the interstitial matrix demonstrated higher post-yield toughness – measured as the area under the flow stress-flow strain curve – than osteons; this was the case for different loading rates. The constituents showed a quadratic hardening, with magnitudes and slopes for osteons being different than those for the interstitial matrix. Because of the hierarchical organizations of a cortical bone tissue, it is believed that different toughening mechanisms at the microstructural level could be responsible for higher toughness of interstitial matrix.

It suggested that global viscoelasticty of cortical bone is defined by viscoelastic properties of its constituents at the microstructural level. The next stage of our research will be devoted to quantification of this link.

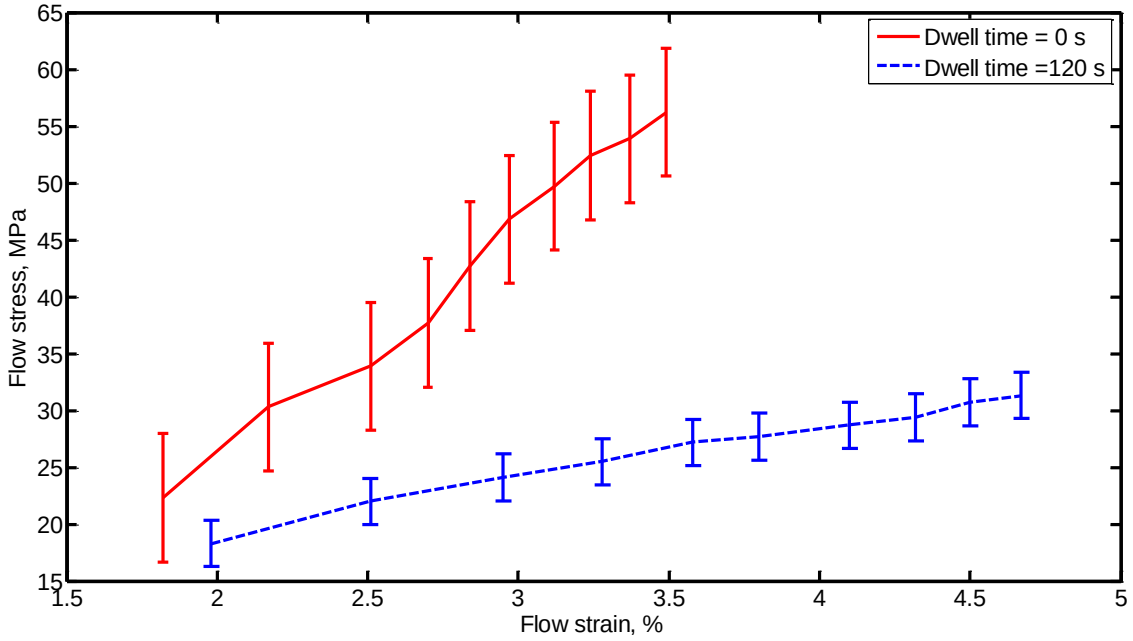

(a)

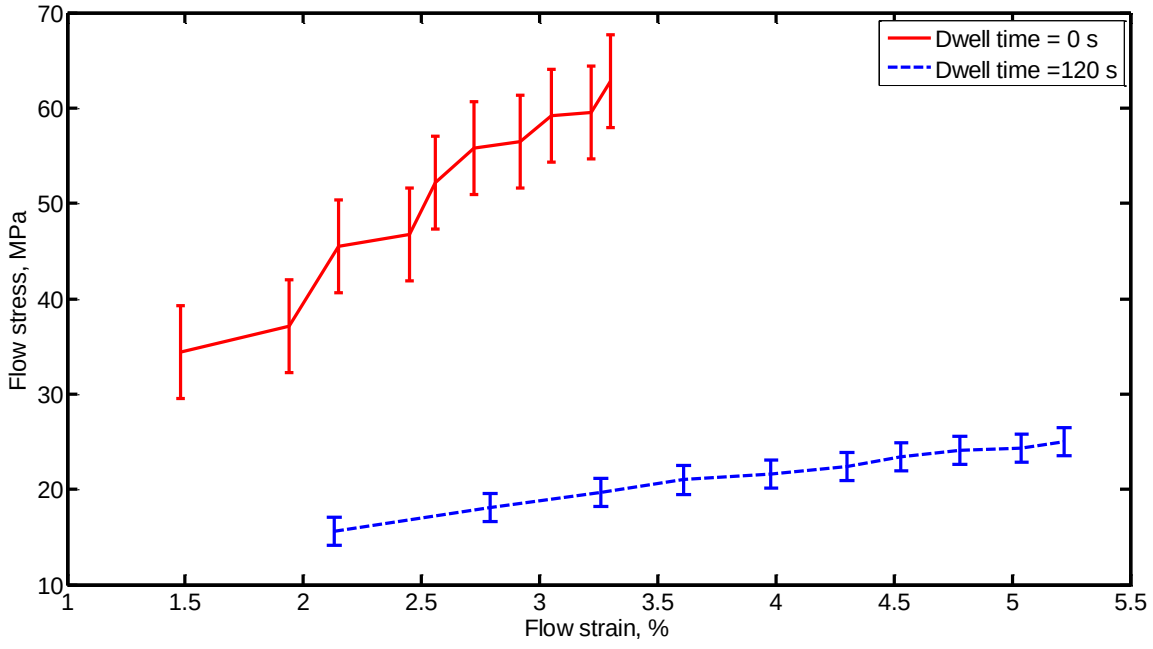

(b)

Figure 6.15: Effect of dwell time on flow stress-flow strain graphs (maximum load 10 mN; loading-unloading rate 0.5 mN/s): (a) osteons; (b) interstitial matrix. Error bars show standard deviation

6.6. Conclusions

In this study a spherical nanoindentation tests were performed to study a mechanical behaviour of microstructural constituents of cortical bone tissue - osteons and interstitial matrix - in order to quantify their elastic properties, hardness and post-yield behaviour. Also, the topological analysis of a transverse-radial section cut from the posterior cortex position was performed to obtain a statistical data to construct microscale finite-element models.

The following conclusions were drawn:

- The random distribution of diameters of osteons and the Haversian canals were fitted with the hypersecant and Dagum (4P) distribution curves, respectively. These curves underpin the development of microscale finite-element models based on several statistical realizations.
- The nanoindentation results demonstrated higher stiffness values for interstitial matrix compared to those of the osteons. The difference is related to the heterogeneity of cortical bone due to continuous remodelling processes that result in gradient in the mineral content.
- Cortical bone's microstructural constituents (osteons and interstitial matrix) exhibited the time-dependent elastic-plastic behaviour. The nanoindentation results obtained at the maximum load of 50 mN, loading rate of 0.5 mN/s and delay time of 120 s along with the use of the rule of mixture produced an effective elastic modulus consistent with the results of uniaxial tension tests of the cortical bone tissue for the same cortex position.
- The stiffer post-yield behaviour of interstitial matrix compared to osteons reflects the relationship between the post-yield behaviour and collagen maturity.
- The viscoelasticity effect on the nanoindentation results was reduced by using the time-delay method.
- The obtained elastic-plastic behaviour of cortical bone tissue's microstructural constituents can now be implemented in finite-element models to study microstructural processes of deformation and fracture.

7. Chapter 7

Characterisation of Dynamic Properties of Cortical Bone Tissue

7.1. Introduction

Bone is the principal structural component of a skeleton: it assists the load-bearing framework of a living body. Both healthy and unhealthy bones are susceptible to fracture as a result of low- or high-energy traumas. High-energy traumas are usually linked to car or cycling accidents, while low-energy traumas often occur in contact sports. In both cases, traumas are caused by dynamic loading. Factors such as mass, material properties and geometry of bone as well as the magnitude and orientation of applied loads affect its response to such loading. Bones are fractured when they are exposed to severe loads that generate stresses exceeding its ultimate strength. Thus, a fracture event occurs initially at the material level that eventually affects the load-carrying capacity of the whole bone at its structural level [22]. Despite the fact that cortical bone's impact resistance is essential for activities such as jumping and running as well as protecting internal organs from impact (as in the case of skull and ribs), less attention has been paid to quantifying its impact properties [187]. Still, numerous previous studies have been devoted to analysis of quasi-static mechanical properties and resistance to fracture of the cortical bone tissue. For instance, Augat and Schorlemmer [188] demonstrated the role of structural properties of cortical bone and its microstructure in its competence. Various experimental studies investigating the effect of structural properties of cortical bone and its mechanical properties have been also conducted [53, 184]. Although they dealt with acquisition of the respective data at different levels of bone's hierarchical structure – macroscopic and microscopic – using different methodological approaches, only quasi-static loading was employed. From a perspective of fracture mechanics, a review of the structure and properties of bone focusing on mechanical and deformation behaviour at different length scales was introduced by Launey *et al*. [189]. In another study, Nalla *et al*. [190] analysed the nature of local cracking events that preceded catastrophic fracture of human cortical

bone and their relation to the microstructure. Again, those investigations were mainly based on a quasi-static loading regime. Regarding dynamic properties of this tissue, only few studies paid attention to them. For instance, both dynamic and static material properties of a human femur were investigated using, respectively, a split Hopkinson bar technique and tests with a universal testing machine [191]. The average dynamic Young's modulus of 19.9 GPa was found to be 23% greater than that for static loading - 16.2 GPa. In terms of bone impact characteristics, only preliminary data are available [192], with a Charpy impact test used to measure the energy absorbed by strips cut from proximal femur. In other experiments, Lee *et al*. [187] tested non-mineralized and mineralized materials, such as cortical bone utilizing a drop-weight test to investigate its impact strength along with impact damage. In a similar study, longitudinal human cortical specimens were tested in a tensile-impact tester at a strain rate of 133 s^{-1} [193]. A marked non-linearity was observed in the stress-strain behaviour, including plastic deformation and strain-hardening effects. The mean tensile-impact strength and impact energy were 126.3 ± 33.1 MPa and 18.79 ± 7.36 kJ/m^2, respectively. Obviously, few authors approached the matter, but investigating and relating behaviours of specimens cut from several cortex positions and linking them to bone's microstructure are still lacking. Also, those behaviours play an important role in validating numerical studies of the dynamic behaviour of a cortical bone tissue (discussed in the next chapters). In the previous chapters, the cortical bone's mechanical properties were quantified and analyzed under a quasi-static loading regime at macro- and microscale levels. In the current chapter, its dynamic properties are measured and analyzed using Izod and tensile-impact tests. They are performed on notched bone specimens of bovine femur to measure its fracture behaviour for different cortex positions.

7.2. Izod Tests

An amount of energy absorbed during a suddenly applied force can be quantified with impact tests of materials; the required data about deformation and failure of materials during high-strain-rate loading cannot be determined using quasi-static fracture tests. Impact testing is usually performed with Charpy, Izod or tensile-impact test machines. An Izod test system incorporates a swinging pendulum

(hammer) that impacts a notched specimen fixed in a cantilever-beam position with the notch facing the hammer [187].

7.2.1. Test Principle and Experimental Equipment

In this study, the Resil Impactor is used to conduct resilience tests, in order to determine impact fragility characteristics of the cortical bone tissue (Fig. 7.1a). The device is used to conduct the most widely test methods called *Izod*, *Charpy* and *tensile-impact* test. The difference between these three methods is in the way of gripping the specimen and application of load. In the current study, only Izod and tensile-impact tests are performed. In the former, the specimen is supported as embedded beam (cantilever-bending mode) and is broken by a single oscillation of the pendulum, whereas in the latter, the specimen is loaded in tensile mode; one end of the specimen is clamped in the instrument's vice and another end is attached to a movable clamping element (crosshead) [19]. The measuring method is based on determining the amount of energy needed to break a specimen under specific conditions, such as specimen location, notch shape and speed of the hammer. As the maximum potential energy is related to the weight of the hammer and the drop height, the latter is a function of the starting angle; the energy absorbed by the specimen can be determined by measuring the hammer rise angle after impact (Fig. 7.1b) [19]:

$$E = mgl\,(\cos\alpha_o - \cos\alpha_r) \qquad (7-1)$$

where m and l are the mass and length of the hammer; respectively; g is the gravitational acceleration; α_o and α_r are the starting angle and the angle of rise, respectively.

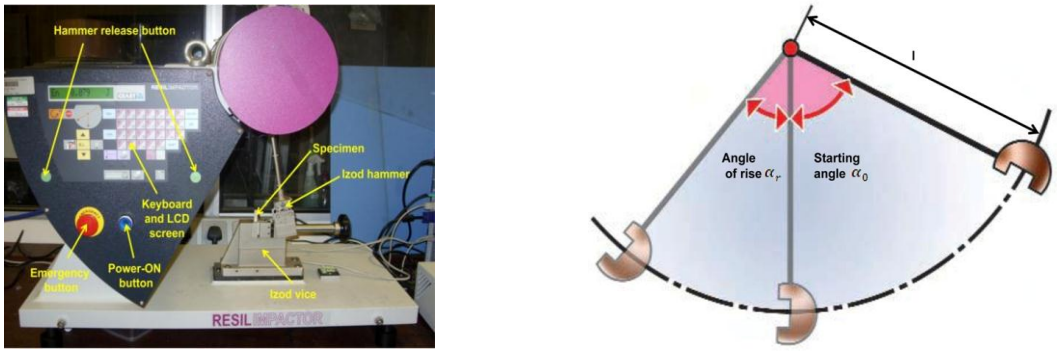

(a) (b)

Figure 7.1: (a) Resil Impactor (Izod test configuration); (b) theory of measurements

Conventionally, resilience can be evaluated by preparing specimens with a specific geometry and employing a pendulum machine to break them. The absorbed energy by the specimen is recorded and divided by the resisting cross-sectional area of the specimen yielding resilience (J/m^2 or kJ/m^2). The absorbed energy by the specimen during fracture consists of three different components:

1. Energy required to initiate fracture;
2. Energy required to propagate fracture;
3. Energy consumed to separate the pieces of the specimen.

The traditional technical solution of absorbed-energy measurements is to use a swinging pendulum together with a device to record its angular position. Recent technological developments led to a more sophisticated solution – the so-called *instrumented test* that involves a direct detection of the impact force. The instrumented test allowed studying the dynamic behaviour of tested specimens. It is based on detection of force using suitable sensors including strain gauges or piezoelectric load cells applied to the striker or the vice. Even though the entire impact event takes place in milliseconds, the instrumented tests enable capturing complete a force-time curve and provide enough information to calculate deformation and, in turn, resilience [19]. The Resil Impactor, used in the current work, is an example of the instrumented-test system. The used system is equipped with a pneumatic brake, and the range of energy is from 1 to 25 J. It is provided with two devices: pneumatic actuator applied to the hammer brake that permits automatic braking of the hammer after impact and another pneumatic device to release the hammer (Fig. 7.1a). The instrumented hammer is connected to data acquisition system (DAS 8000) and personal computer. DAS 8000 is a high-speed data acquisition system designed to record data during fast events, such as impact test (Fig. 7.2).

Figure 7.2: Data acquisition system (DAS8000) [19]

DAS 8000 consists of a modular structure housing the CPU board (8 bit microprocessor), CPU power supply board, display power supply board and LCD graphic display. Eight independent acquisition boards can be equipped in the main CPU board. Each one can be attributed to one signal channel with separate system of acquisition (2 MHz A/D converters) and a memory able to store up to 8000 point acquired [19]. There are two types of acquisition boards available according to the signal coming from different types of sensors, such as strain-gauges, piezoelectric, and load-cell. The signal of variable intensity coming from the sensor is sampled by DAS 8000 then it is sensed through USB port to the DAS8WIN Extended Version©CEAST program on the personal computer [19]. The sampled signal is processed through the program, and the resulted graphical data is obtained.

7.2.2. Specimen Preparation

The specimen preparation and storage protocol are the same as those for the uniaxial tension tests discussed earlier in Section 5.2.2. Since our previous studies of mechanical properties of this tissue demonstrated their variability, a transversal cross-section is divided into four main parts (see Fig. 7.3a) anterior, posterior, medial and lateral. In total thirty-two specimens were cut from these four different cortex positions using a milling machine along the bone axis. Eight specimens were used for each position to ensure reproducibility of the experimental results. All the specimens had the same dimensions: 50 mm $\times$ 8 mm $\times$ 4 mm (length $\times$ width $\times$ thickness), see Fig. 7.3b. A 300 µm-deep notch was created perpendicular to the bone axis and along the tangential axis direction in one-half of the specimens using a razor; the notch in the second half was 600 µm. After cutting the specimens, they were ground using a series of grinding papers Standard ANSI grit: 240, 600, and 1200 to make sure that the surface is clean, without any scratches or irregularities. Specimens were stored at room temperature in a 0.9% saline solution until tested.

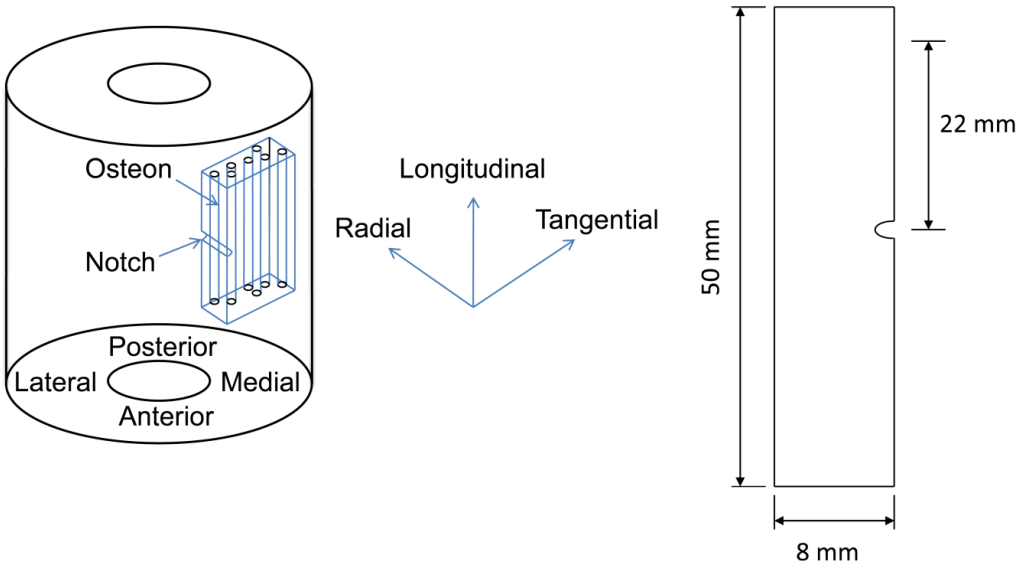

(a) (b)

Figure 7.3: (a) Cortical bone with axes and direction of specimen cutting; (b) Izod test specimen

7.2.3. Experimental Procedure

In the current study, dynamic impact tests were carried out using the CEAST Resil Impactor. In the tests, the bottom half of the specimen was fixed firmly in the machine vice, and a knife-edge wedge was used to define the notch position (Fig. 7.4). The upper half of the specimen was struck by a pendulum hammer with a controlled level of energy. The distance between the notch and the position of hammer strike was standard - 22 mm. In this study, a calibrated hammer with a mass of 0.6746 kg and 0.3268 m long was used. The maximum nominal hammer energy of 2 J corresponds to the initial position of 150° resulting in an impact velocity of 3.46 m/s. The level of initial energy can be varied by changing the initial angle of the hammer. Two levels of energy were used for each specimen in this study - 0.02 J (non-destructive) and 0.5 J (destructive); they correspond to initial angles of 10° and 58°, respectively. A piezoelectric force transducer was fixed rigidly to the hammer to capture the impact-force signal. When the pendulum is released from the pre-defined angle, its impact with the specimen generates a change in electrical resistance of the piezoelectric sensor that is captured by the data acquisition system – DAS 8000 – connected to the impactor. The measured

signal is registered with a sampling frequency of 833 kHz; a 1 kHz filter is used to reduce the noise. The magnitudes of force F and time can be downloaded to a computer; other parameters such as velocity V displacement d and absorbed energy $\bar{E}$ can be calculated using the following relationships:

$$V_i = V_{i-1} - \Delta t \left(\frac{F_{i-1}+F_i}{2m}\right) - g, \qquad (7-2)$$

$$d_i = d_{i-1} + \frac{\Delta t}{2}(V_{i-1} + V_i), \qquad (7-3)$$

$$\bar{E}_i = \bar{E}_{i-1} + \frac{\Delta t}{2}[(FV)_{i-1} + (FV)_i]. \qquad (7-4)$$

where the index i relates to the current time step and $i-1$ to the previous measurement, with a time difference of Δt; g is the gravitational acceleration; F is the impact force.

The ANOVA test was used for the statistical analysis of the obtained results. It allows testing for differences in the means of different groups. ANOVA tests the null hypothesis that mean values of all the groups are equal. It produces a p-value that is called *level of significance*. A p-value of 0.05 (5%) is generally regarded as sufficiently small to reject the null hypothesis, and it is called the significance level of the test [194].

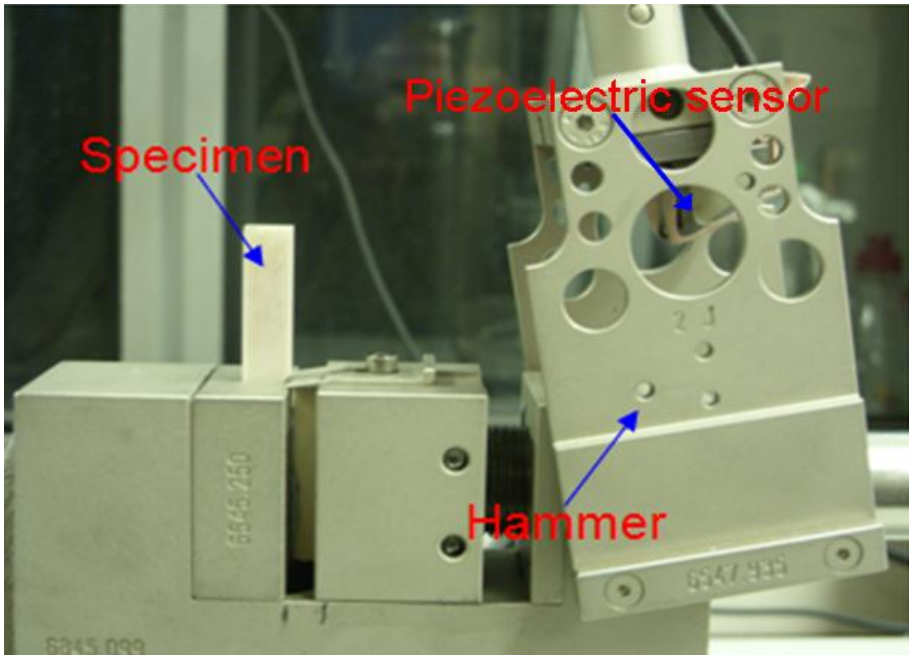

Figure 7.4: Izod test set-up

7.3. Micro-Computed Tomography

A non-destructive characterization technique – X-ray micro-computed tomography (μXCT) – was employed to visualize a three-dimensional microstructure of Izod test specimens before and after a non-destructive impact test. The specimens were scanned using a HMXS μXCT system to investigate any damage at the microstructural level. The setup of X-ray power was adjusted to 138 kV and 75 μA for the tests to maximize the signal-to-noise ratio. Transmitted X-rays resulted in a voxel size in the reconstructed three-dimensional image of 7 μm. After scanning the notched part of the specimen the studied volume was reconstructed using the CT-Pro2 software. Then, the reconstructed volumetric data was post-processed using the VG studio Max 2 software.

7.4. Tensile-Impact Tests

Trauma associated with low- and/or high-energy activities often involves fracture of long bones. Despite the fact that these fractures most probably occur due to impulse loading, relatively small data are available about the impact behaviour and properties of cortical bone [195]. Like any brittle material, bone is weak in tension [148]; therefore, investigating tensile-impact tolerance of cortical bone is essential. Characterization of the tensile-impact properties of cortical bone tissue is described in the next sections.

7.4.1. Experimental Equipment

As mentioned, the Resil Impactor, described in Section 7.2.1, can be configured to perform different impact tests, such as Izod, Charpy and tensile-impact tests. This can be achieved by interchanging the hammer and the vice to fit with the performed test. The system with the tensile-impact configuration is shown in Fig. 7.5. In this configuration the specimen is supported at one end by an instrumented vice and the other end is struck by a pneumatically controlled hammer resulting in a uniaxial dynamic loading regime. In the current work, a calibrated hammer with mass of 0.951 kg and nominal length of 0.2297 m was used. The hammer can generate energy of up to 4J and at a speed of 2.9 m/s that is corresponding to an initial angle of 150° to the striking position. The instrumented vice shown in Fig. 7.6 consists of a piezoelectric load-cell rigidly fixed between the specimen clamping bracket and the

rigid part of the vice. Also, a calibrated traction movable terminal is joined to the free specimen end by two steel plates joined by bolts (Fig. 7.6). The energy level can be changed by changing the initial angular position of the hammer. The effect of aerodynamic effects and friction can be accounted by performing a pre-test with no specimen involved and then subtracting the obtained value from the measured one.

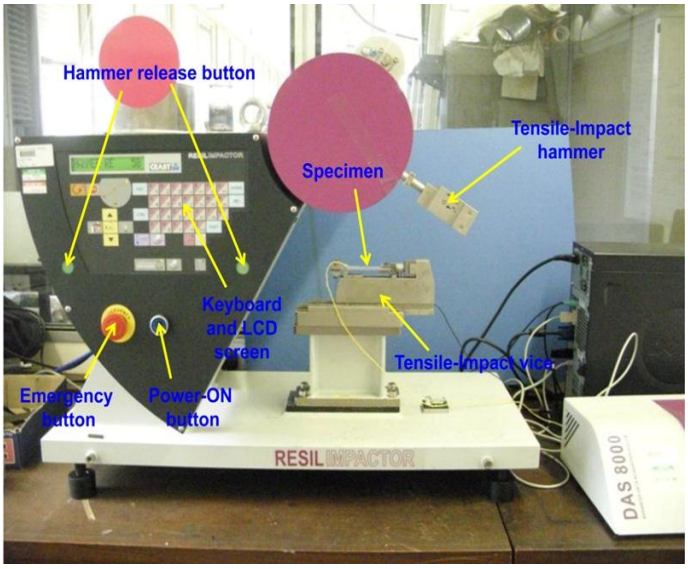

Figure 7.5: Resil Impactor (tensile-impact test configuration)

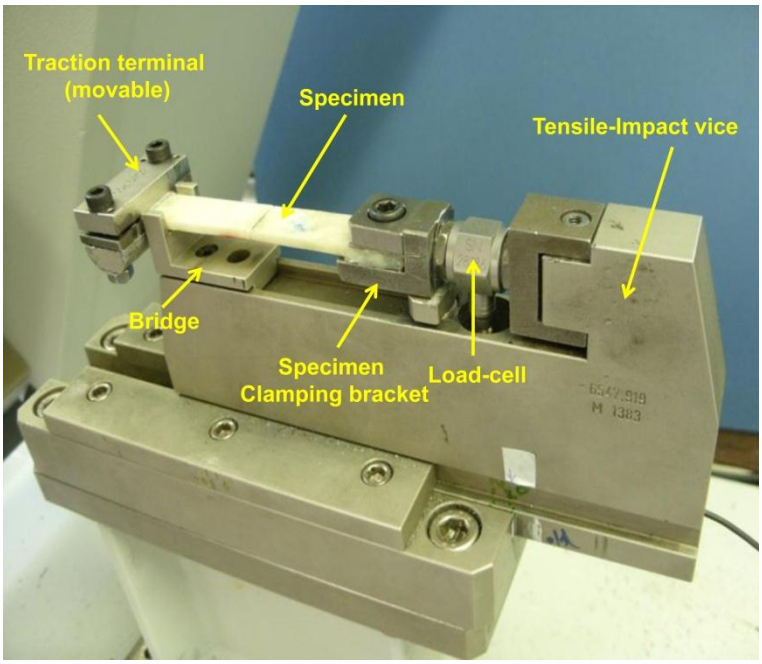

Figure 7.6: Tensile-impact test set-up

7.4.2. Specimen Preparation

The specimen preparation and storage protocols are the same as those for the uniaxial tension tests discussed earlier in Section 5.2.2. To account for the mechanical properties' variability caused by bone's microstructure, specimens from four main parts (see Fig. 7.3a) – anterior, posterior, medial and lateral – were tested. Thirty-two specimens were cut along the bone axis from these four different cortex positions using a milling machine. Eight specimens were used for each position to ensure reproducibility of experimental results. The specimen's dimensions and shape are shown in Fig. 7.7. The fixed end of the specimen was drilled with a 6 mm drill-tip to be attached to the specimen clamping bracket hole with a screw; its free end was shaped to fit into the groove of the traction terminal (Fig. 7.7). In order to avoid specimen's fracture at these two positions due to introduced stress concentrations, metal parts (end tabs) were manufactured and glued to both sides of the specimen using Araldite 2024 that is appropriate for impact loading applications. In addition, two notches were generated on both sides of the specimen using an automatic drilling system with 600 μm routing-tip; they were cut at very high speed of 30,000 rpm to ensure smooth notch surfaces. After preparation, specimens were stored at room temperature in a 0.9% saline solution until tested.

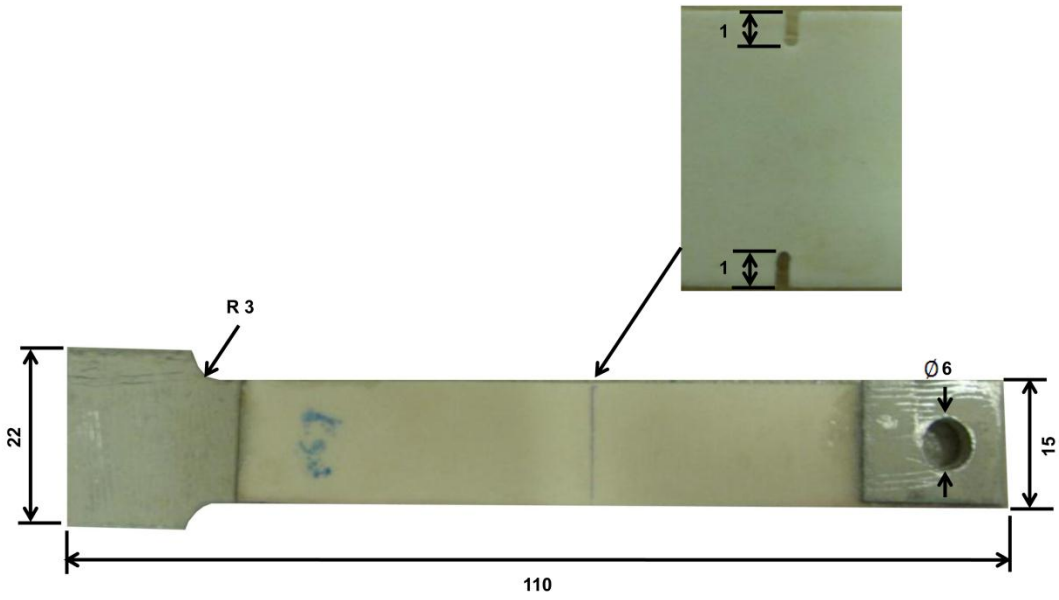

Figure 7.7: Dimensions and shape of specimens with notches for tensile-impact tests; specimen thickness 3 mm. Dimensions in mm

7.4.3. Experimental Procedure

The tensile-impact tests were carried out using the CEAST Resil Impactor. In the tests, one end of the specimen was fixed to the specimen clamping bracket using a 6 mm diameter screw and the free end was assembled with the traction terminal using steel plates and screws as shown in Fig. 7.6. The traction terminal was struck by a pendulum hammer with a controlled level of energy. The energy level of 3 J with impact velocity of 2.53 m/s was used for each specimen in this study that corresponds to the initial angle of 115°. A piezoelectric force transducer was fixed rigidly to the vice to capture the impact-force signal. The signal was sampled by the data acquisition system – DAS 8000 – and processed with the DAS8WIN Extended Version©CEAST program on the personal computer. The magnitudes of velocity, displacement, and absorbed energy can be calculated using the same as equations for the Izod test (Eqs. 7-2 – 7-4).

7.5. Results and Discussion

7.5.1. Izod Tests

A proper treatment of bones and prevention of their fracture can be supported by in-depth understanding of deformation and fracture behaviour of the bone tissue in both quasi-static and dynamic events at various length scales. *In-vivo*, cracks can travel through and break a bone, when it is exposed to spontaneous, or fatigue loading. However, it is unusual for a bone to fail when it is loaded in quasi-static loading, which is the case with specimens tested *in-vitro* [196]. The aim of this part of the study was to investigate experimentally the variability of fracture force and impact strength of specimens cut from four different cortex positions of bovine cortical bone along the femur axis and their link to the microstructure.

The fracture behaviour of bone is closely linked to its underlying hierarchical structure; therefore, the measured fracture parameters depend on the length scale, at which they are measured. Moreover, in order to correctly assess the cracking and fracture behaviour of bone, the crack direction should be clinically relevant, i.e. cracks propagating in the transverse direction and involving realistic flaw sizes [21]. Accordingly, in this part of the study, two groups of specimens were tested: the first group consisted of specimens with a 300 μm notch and the second group with a

600 μm notch. For all the specimens, the notch was generated perpendicular to the osteons, see Fig. 7.3. The chosen notch sizes were below or equal to 600 μm according to the physiologically pertained flaw size reported by Koester *et al*. [21]. As our quasi-static tests on cortical bone demonstrated and as it is well-known from the literature, cortical bone's properties vary from one cortex position to another due to variation in both composition and microstructure. Hence, its fracture force and absorbed energy were studied for four different cortex positions; see Figs. 2.5 and 7.3, using two energy levels – non-destructive and destructive. In the impact Izod test, the axial stresses are non-uniformly distributed in a transverse section. Hence, a fracture force parameter is used in place of a fracture stress.

For the specimens subjected to the low energy level – 0.02 J – for both initial notch depths (300 μm or 600 μm), the average recovered energy was approx. 0.016 J for the four cortex positions. The statistical results at that energy level showed no significant difference for specimens from different cortex positions with initial notch depths of 300 μm (p = 0.774) or 600 μm (p = 0.565). The reason for this is a nearly perfectly elastic response of material at a low level of energy (Fig. 7.8). No damage or plasticity mechanisms were activated as proved by the symmetry of the force-time curve and was also confirmed by a micro-computed tomography study (discussed later).

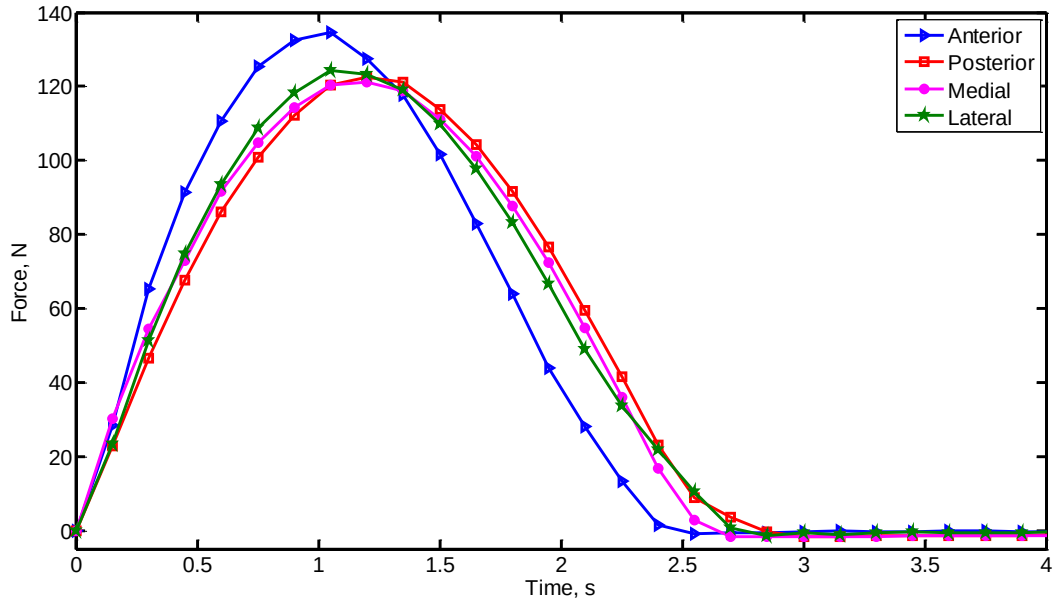

Figure 7.8: Evolution of contact force in impact loading (notch size 300 μm) and energy level of 0.02 J

For the higher energy level – 0.5 J – the experimentally measured mean values of fracture force of different cortex positions are shown in Fig. 7.9. Here, each data set represents the mean value for four specimens and the error bars are the standard deviation (SD) of the measurements. It is seen from Fig. 7.9 that fracture force of all the cortex positions is lower for specimens with 600 μm initial notch depth compared to those with 300 μm notch, though the difference for medial and lateral specimens of different notch depths is small - 7% and 4.3%, respectively. Anterior specimens showed the highest fracture force for both notch magnitudes. The medial and posterior positions were characterized by the lowest fracture force values for the initial notches of 300 μm and 600 μm, respectively. The specimens with deeper notches demonstrated lower variability of the obtained data for fracture force. From statistical point of view, based on the use of a one way ANOVA procedure [194], the values of the fracture force express no significant difference for the cortex positions for specimens with 300 μm notches ($p = 0.067$), whereas an increase in the notch depth to 600 μm caused a significant difference ($p = 0.011$). Since the threshold of physiologically pertinent flaw sizes is 600 μm (according to [21]), it means that the diaphysis part of the bovine femur cortical bone has a low variability of the fracture force in the case of the absence of initial damage/faults. For the destructive energy level, Figure 7.10 shows a comparison for data obtained for these positions for 300 μm- and 600 μm-notched specimens; the initial energy level used in those tests was 0.5 J. The impact strength was measured as the absorbed impact energy divided by the un-notched cross-sectional area of the specimen. The obtained results show that, for the same applied energy level and cortex position, the notch size has a negative effect on impact strength of the cortical bone tissue. In general - apart from the medial cortex position with nearly the same average impact strength for both notch sizes - specimens notched with 300 μm required higher energy per unit area to fail compared to those with a 600 μm notch. Statistically, the average impact strength required to produce fracture appears to be higher at the lateral position, with different magnitudes for different notch sizes. However, considering the spread of the mean impact energy for all cortex positions and notch depths, it is apparent that it is within the interval from 6 kJ/m^2 to 12 kJ/m^2.

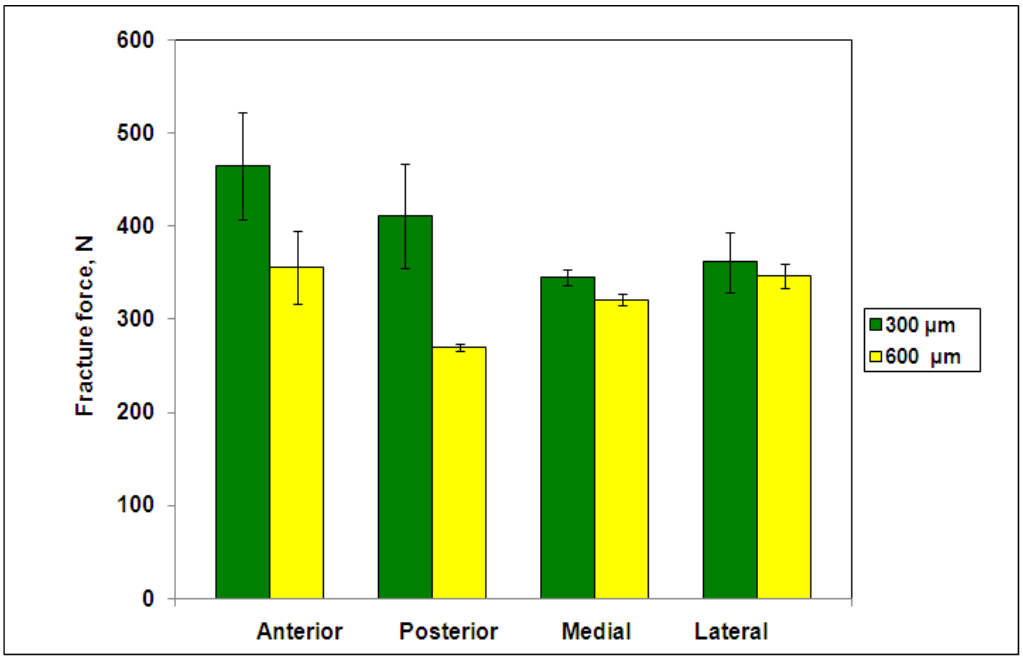

Figure 7.9: Fracture force of cortical bone specimens from different cortex positions for destructive impact for two different notch depths (error bars represent SD)

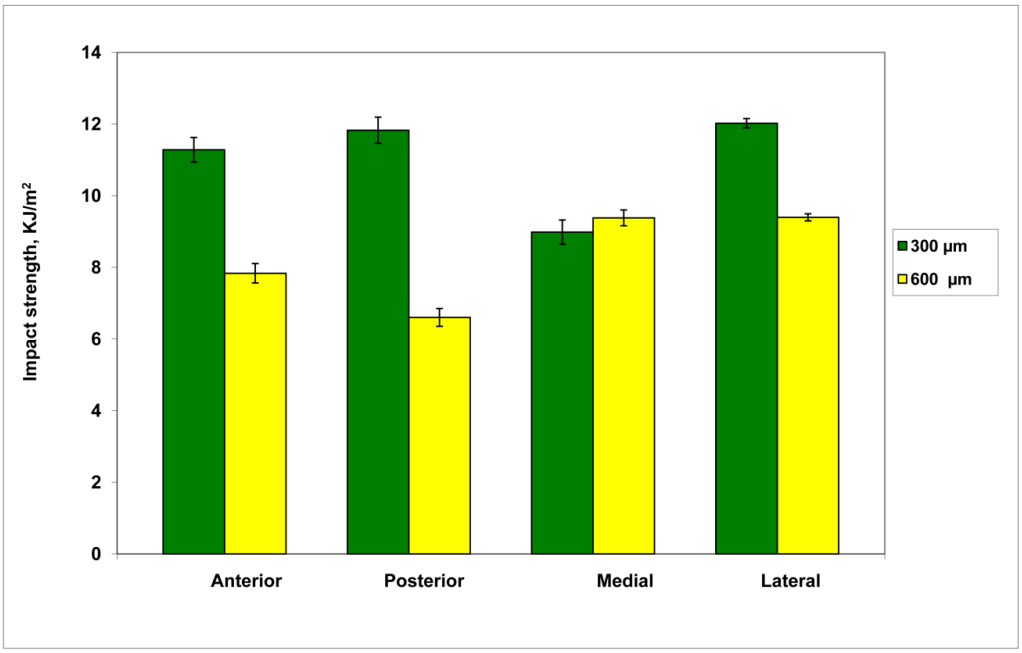

Figure 7.10: Impact strength of longitudinal cortical bone specimens for different cortex positions and two different notch sizes

The statistical analysis for cortex positions revealed no significant difference in the mean impact strength for both notch depths for 300 μm (p = 0.862) and for 600 μm (p = 0.354). Also, checking the combined effect of both factors – cortex position and notch depth – on the mean impact strength no significant difference was demonstrated (p = 0.642). Based on these results, bovine femur seems to have nearly uniform impact strength. The values obtained for the impact strength are in a good agreement with other studies in the literature; for instance, using a four-point-bending setup, bovine cortical bone was found to have an impact strength in the range of approximately 6 kJ/m^2 to 24 kJ/m^2 [197]. In a separate study, the impact strength of bovine cortical bone was found to be 10 kJ/m^2 in drop-weight tests [187]. The obtained impact-strength results of our study agree well with those in the literature, even based on different techniques. Also, these results are consistent with a study on human cortical femur bone that reported an approximately uniform distribution of the relative fracture energy in the diaphysis part [192]. A study of a section of the tested femora with optical microscopy demonstrated a different microstructure – osteonal and primary bone – for various cortex positions (Fig. 5.7). Such microstructural changes are among the reasons for variability of fracture force and type of fracture surfaces (Fig. 7.11); they also affect the fracture energy but its spatial difference was not significant. Most likely, there are different toughening mechanisms for osteonal and primary bones, but the average effect of those mechanisms are nearly the same. Existence of different toughening mechanisms can be also confirmed by the variability of the fracture surfaces of specimens cut from different cortex positions (Fig. 7.11). Despite cracks in all the specimens starting at the notch due to the stress concentration, their paths vary for specimens cut from different cortex position. However, similar crack paths were found for specimens cut from the same cortex. The stress state across the width and depth of the specimen along with the underlying microstructure defines the crack propagation scenario. Obviously, from the beam theory, when a bone specimen was strained due to the impact load, a bending type of stress distribution was generated; its maximum value is in the plane of the notch. It consists of a tension zone (ahead of the crack tip up to the neutral axis) and a compression one (from the neutral axis to the opposite side). In addition, a shear stress was generated due to the impact force; it is nearly distributed uniformly between the

position of impact and the notch location. A combination of these stresses yields a complex stress state that leads to complex fracture behaviour.

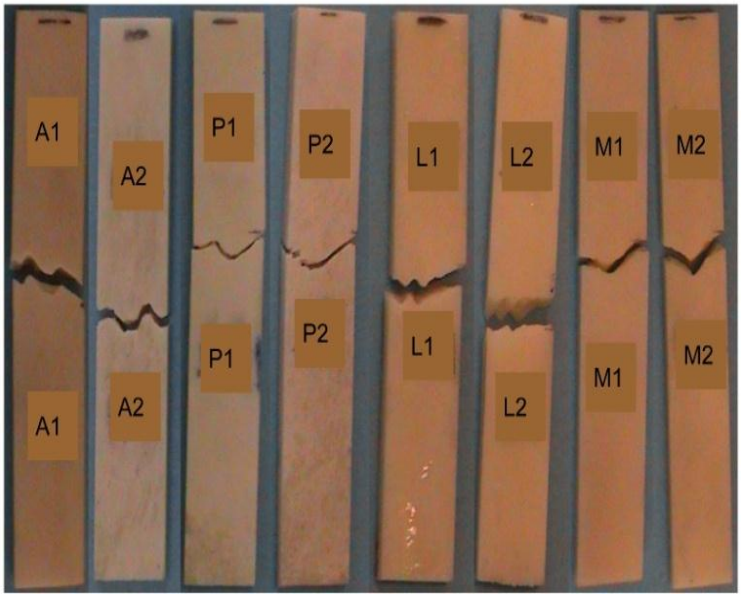

Figure 7.11: Fractured longitudinal cortical bone Izod specimens for different cortex positions and notch size of 300 μm. A, P, M and L stand for anterior, posterior, medial and lateral, respectively. 1 and 2 stand for specimen's number

Due to the complex stress state, fracture modes I and II are dominant between the notch root and the neutral axis of the specimen, whereas between the latter and the opposite side of the specimen, compression stress accompanied with Mode II constitutes complex failure behaviour. To get an understanding of this complexity as well as the contribution of the microstructure on the crack route, the fracture surfaces of selected bone specimens were examined using scanning electron microscopy at two different magnifications – 50X and 200X (Fig. 7.12). It is shown that for the tensile side – ahead of the notch – the fracture surface is rougher than that of the opposite side. A head of the notch, there are signs for partial pullouts of osteons (Figs. 7.12a and c) due to the weak interface – cement lines – between them and the interstitial matrix. On the other hand, the smooth surface of the opposite side indicates the dominance of shearing of the surface rather than pulling it out (Figs. 7.12b and d). It can be inferred that within the tension side of the specimen, predominantly a cleavage type of fracture occurred with a rough texture originated at the notch root tip, whereas for the compression side of the specimen, failure occurred along planes of low shear strength.

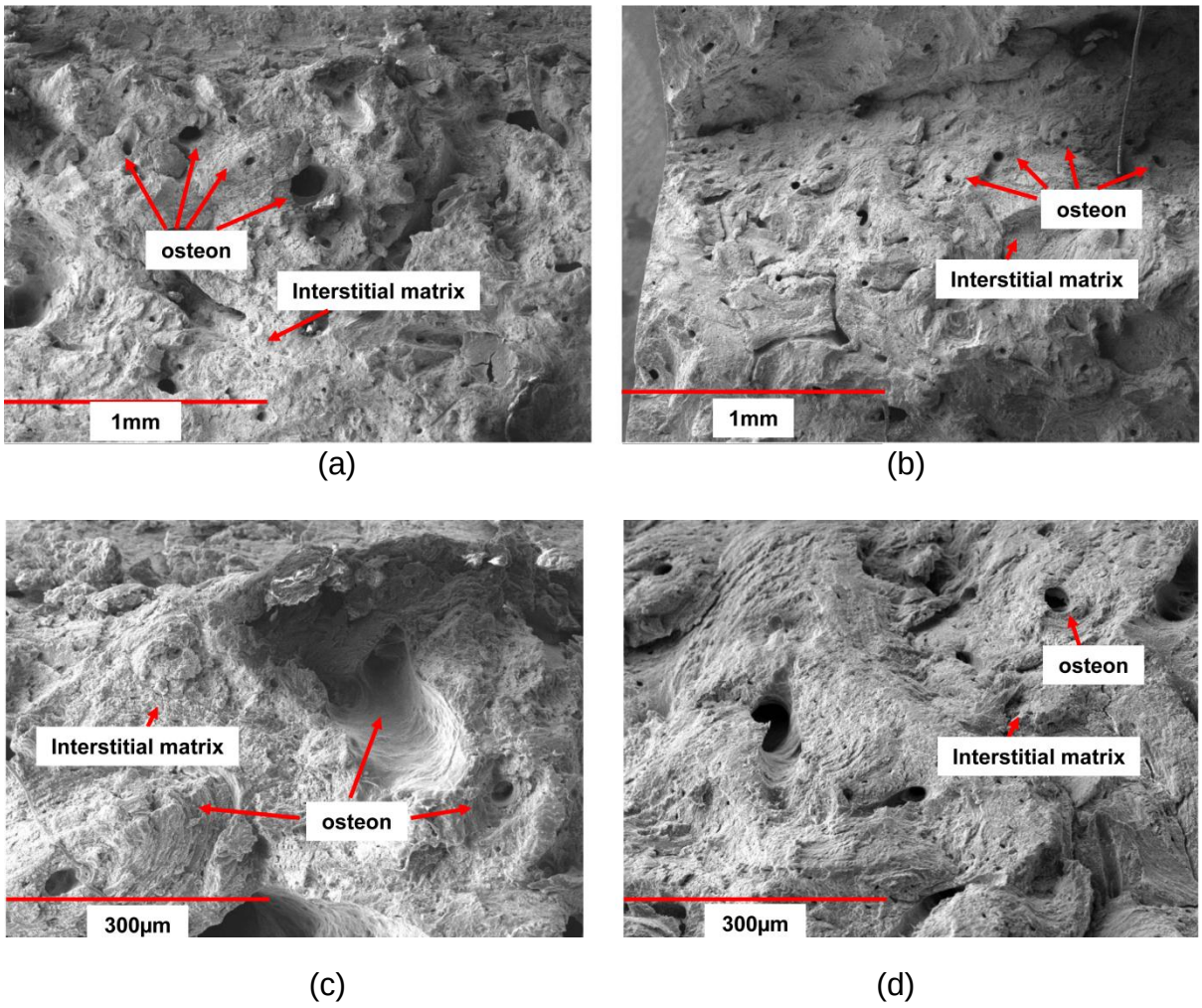

Figure 7.12: Scanning electron micrographs of fracture surfaces of Izod test's posterior specimens: (a) tension side [50X]; (b) compression side [50X]; (c) tension side [200X]; (d) compression side [200X]

In summary, the experimental results of this part of the study can play an important role in laying the foundation for development of numerical models implementing dynamic analysis of the diaphysis part of the femur. Using the obtained experimental properties based on the study of only one quadrant of the femur diaphysis's sufficient for numerical simulations (discussed in the following chapters). Additionally, those results are also a better indicator of bone fracture resistance as they are close to fall mechanics (impact injury) as also concluded in another study [192].

7.5.2. Micro-Computed Tomography

A destructive Izod test obviously initiates various damage and fracture mechanisms, complicating comparability of data on dynamic properties' of cortical bone. Though low-energy non-destructive impacts have caused no visible external damage to specimens or crack initiation in them, the extent of microscopic changes, e.g. in a form of microcracks etc, should be analysed.

Three-dimensional images of an anterior longitudinal bovine cortical bone specimen obtained with X-ray computed tomography before and after the non-destructive impact test are shown in Fig. 7.13. Analysis of the microstructural features of the specimen demonstrated that the impact at that energy level did not cause any internal damage in the vicinity of the notch and its other parts. This is also confirmed by a nearly symmetric shape of the force-time curves of the specimens, see Fig. 7.8. During the high impact energy test, the specimens were fragmented and it was not possible to obtain the micro XCT images after the test.

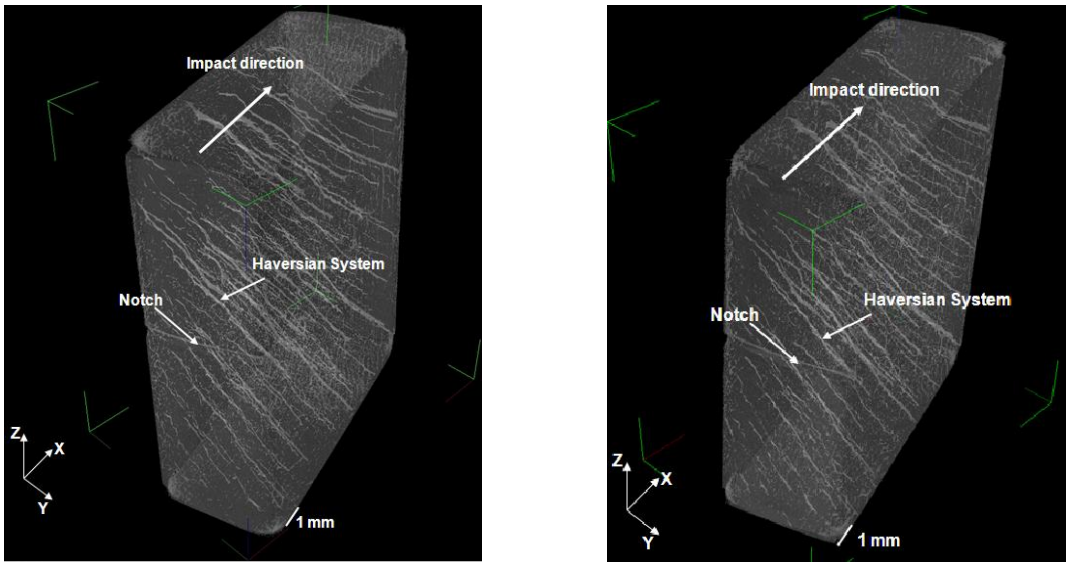

(a) (b)

Figure 7.13: Micro X-ray computed tomography of Izod test specimen before (a) and after (b) non-destructive impact

7.5.3. Tensile-Impact Tests

In this part of the study, an instrumented impact tester was used to record the force-time signal history generated when a cortical bone specimen was exposed to a

tensile impulse load. Using Eqs. 7-2 – 7-4, it was possible to calculate also the velocity, displacement and absorbed energy during the impact event. Compared to transverse-impact tests, longitudinal-impact tests can provide data about the ultimate stress of cortical bone. In the transverse-impact loading regime, the stress distribution is not uniform across the specimen's width; therefore, it was not possible to calculate the ultimate stress based on the measured force-time signal history and the cross-sectional area. Thus, transverse-impact loading provides the impact strength of cortical bone, yet it fails to yield the ultimate stress. Hence, tensile-impact tests offer solutions for the shortcomings of Izod tests.

In the present study, the pendulum velocity was reduced slightly due to the energy lost in the specimen breaking and tossing the broken parts away during longitudinal-impact loading regime; therefore, it was reasonable to assume a constant velocity during the impact event. Thus, the strain rate based on the impact velocity (2.53 m/s) and the specimen geometry was 28.6 s^{-1}. In fracture scenarios, bone often is exposed to high-strain rates. Even though a strain rate depends on particular circumstances of the fracture scenario, Hansen *et al*. [198] suggested a magnitude of strain rate in the order of 25 s^{-1} as a rough upper bound relevant to bone failures during traumatic events.

The aim of these tests was to examine the fracture behaviour of cortical bone tissue; therefore, notches on both sides of specimens were introduced as shown in Fig. 7.7. Obviously, notches serve as stress concentrators and result in a localized increase in stresses ahead of the notch that lead to fracture. For the used notch and specimen dimensions, the stress concentration factor – the ratio of the highest stress to the nominal stress – is 3.7. The average values of the nominal stresses were 56.16$\pm$5.2 MPa, 22.41$\pm$2.6 MPa, 52.69$\pm$4.32 MPa and 52.11$\pm$3.91 MPa for specimens cut from anterior, posterior, medial and lateral cortex positions, respectively (Fig. 7.14). These stresses were calculated based on the peak value of the impact force and the cross-sectional area of the ligament between the two side notches of the specimen (Fig. 7.7). Interestingly enough, all the specimens were broken with cracks starting and propagating from the notch during the impact tests; this indicates that, during the impact event, the notches magnified the nominal stresses and, in turn, nominal strains at the notch tip that led to crack initiation and propagation within the specimens. It is worth mentioning that the ratios of the

average quasi-static and dynamic ultimate stresses measured in this work were 2.2, 2.7, 2.1 and 2.1 for four cortex positions, respectively. Hence, the notches provided values of concentrated stresses higher than the quasi-static ultimate stresses; therefore, it offered a good chance for cracks to initiate and grow. A similar range for dynamic rapture stress – 33 MPa ≤ $\sigma_{rapture}$≤ 50 MPa – was reported in literature [157]. It was also found that notched specimens tested in tensile-impact required significantly less impact energy for fracture and exhibited reduced levels of ultimate stress and strain compared to those in un-notched ones [195]. The comparison of un-notched and notched specimen behaviours suggested that bone is highly susceptible to the stress concentrations and confirms that a large amount of the impact energy consumed in initiating the crack and the subsequent crack propagations requires a small part of the total fracture energy [195]. In this study, values of tensile-impact strength (absorbed energy per unit area) of specimens cut from anterior, posterior, medial and lateral were 10.04±2.21 kJ/m^2, 6.61±1.61 kJ/m^2, 8.33±2.51 kJ/m^2 and 8.1±2.62 kJ/m^2, respectively (Fig. 7.15). It was obvious that bone specimens with lamellar microstructure sustained higher energy to failure compared to specimens containing secondary osteons. Specimens cut from anterior cortex with lamellar structure required the highest absorbed energy to rapture; while those cut from posterior entailed the lowest (Fig. 5.7). On the other hand, lateral and medial specimens needed approximately the same levels of absorbed fracture energy. In this study, microstructural investigations exhibited variations not only between specimens from different cortex positions but also between specimens cut from the same cortex but from different animals. This indicates partially the slight variations between the impact strength values obtained for two different loading conditions in this study: Izod and tensile-impact (Figs. 7.10 and 7.15). Obviously, the obtained impact strength values for both loading regimes are within the domain reported in the literature (6 kJ/m^2 to 24 kJ/m^2 [197]); however, specimens used in both tests were collected from the same source but different animals. Another study investigated, from another point of view, the effect of the microstructure on the maximum stress and the impact strength of human and bovine bone were examined in terms of the percentage area of secondary osteons [199]. A strong negative correlation and linear regression equations were found between the maximum

stress and impact strength and the percentage areas of secondary osteons, respectively. Those findings are in line with the results obtained in this study.

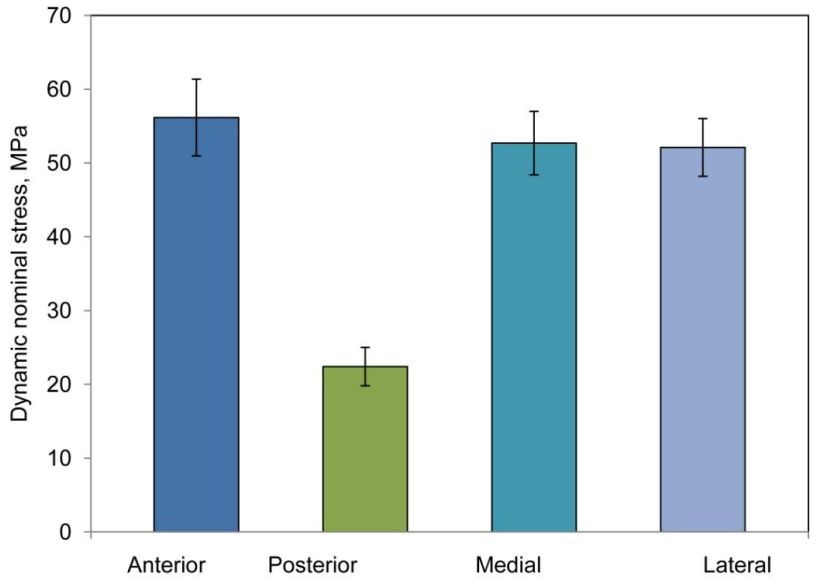

Figure 7.14: Dynamic nominal stress for destructive impact of cortical bone specimens from different cortex positions (error bars represent SD)

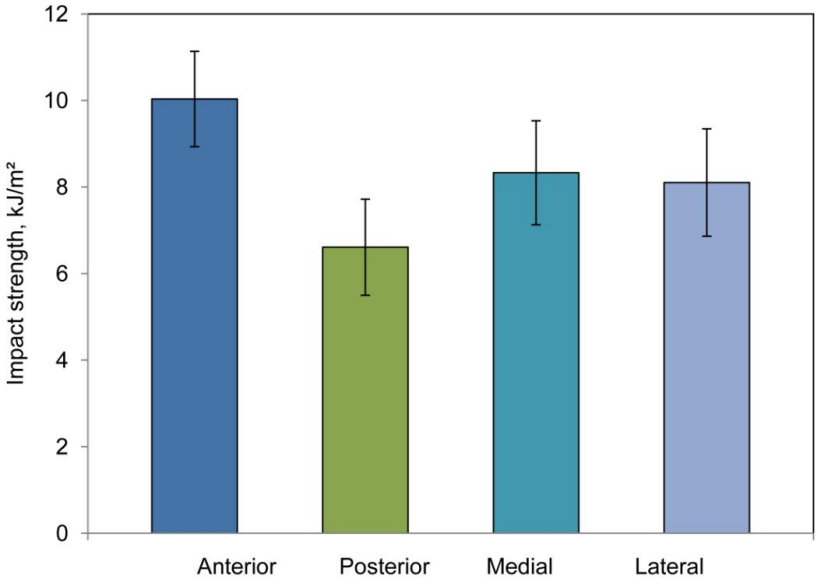

Figure 7.15: Impact strength of longitudinal cortical bone specimens for different cortex positions (error bars represent SD)

It was observed here that specimens cut from posterior cortex required the lowest energy to fail compared to specimens cut from other cortices. As mentioned before, posterior cortex contains a higher fraction of secondary osteons compared to other cortices, as reported by Currey [62]. There are two explanations to the negative

correlation between impact strength and the area fraction of Haversian bone: (1) Haversian bone has a higher relative cavity area, and (2) it is less mineralized than primary (lamellar) bone. Unless the total cavity area is not large, the first effect is not so important. In another study, a significant positive correlation was found between the area of the secondary osteons and the area of cavity space [199]. This indicates that a higher fraction of osteons implies a higher fraction of cavity space, and hence, less bone to resist the applied load. Also, Haversian bone exhibits reduced strength and absorbed energy because its mineral content is lower compared to the surrounding bone matrix and primary osteons. Several studies showed that primary osteons have a higher mineral content (5% to 20 %) compared to secondary osteons and the mineralization of osteons is 4% lower than interstitial matrix [200, 201]. Though this variation is small, but Currey [44] and Vose and Kubala [202] reported appreciable changes in strength caused by a small change in mineral content. In addition, it was found that well-mineralized compact bone specimens failed catastrophically when tested at high strain rates, with damage being confined mostly to the vicinity of the fracture surfaces [203]. Another possible reason for the weakness of specimens with high fraction of secondary osteons could be the interface between osteons and interstitial matrix that facilitate crack propagation and failure.

In order to determine the nature of the fracture process and to relate the fracture-surface topography to the causes and the basic mechanisms of fracture, the fracture surfaces of the tensile-impact specimens were examined. Figure 7.16 shows fracture profiles of some tensile-impact specimens. Macroscopically, brittle fracture was the general feature for most of the specimens and, as shown in Fig. 7.16, the fracture surfaces started at notch but followed paths that were not always normal to the loading direction. These observations suggested that failure occurred along planes of low shear strength. Figure 7.17 shows microscopic images for the tensile-impact fracture surface of specimen contains secondary osteons at different magnifications (50X and 200X) using scanning electron microscopy (SEM). Typically, a rough texture was observed with evidence of partial pullout of osteons due to a weak interface between osteons and interstitial matrix (Fig. 7.17b). Cracks started predominantly at notch and followed paths of lowest shear strength; however, some of the natural faults in the cortical bone, such as Volkmann's canal,

Haversian canal, canaliculi and resorption cavities might also have affected the crack paths. These features are considered as stress concentrators that might play an important role in the initiation and propagation of secondary cracks accompanying the main-crack. Moreover, they can stop or deviate a propagating crack.

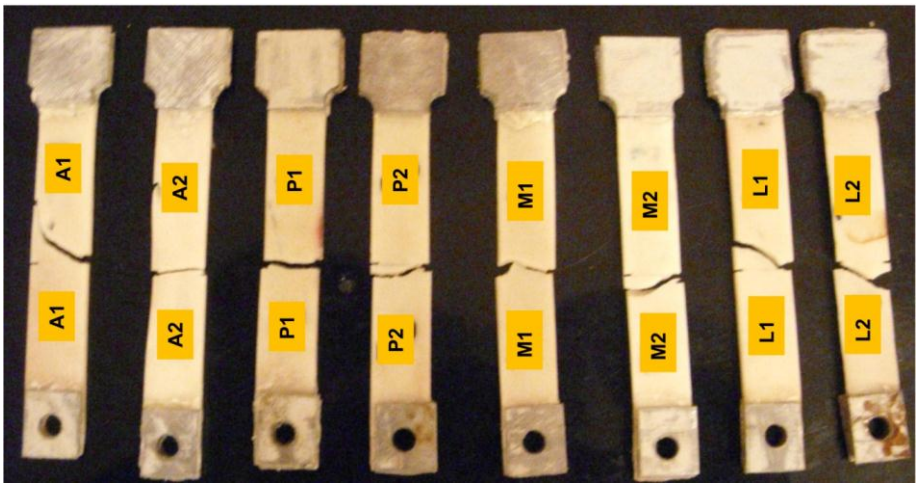

Figure 7.16: Fractured longitudinal cortical bone tensile-impact specimens for different cortex positions. A, P, M and L stand for anterior, posterior, medial and lateral, respectively. 1 and 2 stand for specimen's number

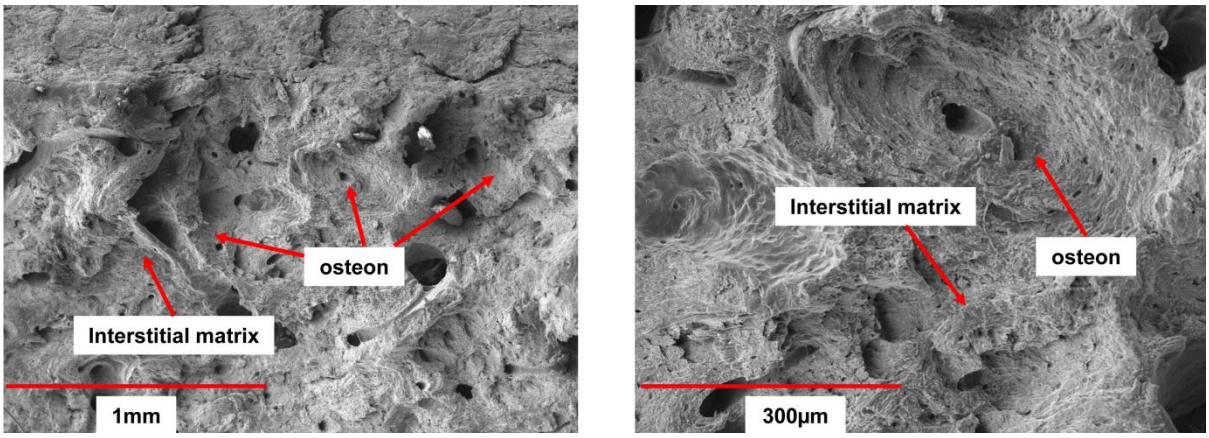

(a) (b)

Figure 7.17: Scanning electron micrographs of fracture surfaces of tensile-impact test posterior specimen; 50X (a) and 200X (b)

The dependence of the quasi-static and dynamic properties of the cortical bone tissue on its microstructure highlights the necessity not only to numerically model cortical bone macroscopically but also microscopically to investigate its fracture. Those numerical models are discussed in the following chapters.

7.6. Conclusions

Experimental tests with two different loading regimes (Izod and tensile-impct) were performed to study the transient dynamic behaviour of cortical bone tissue under scenarios of bending and tension. The variability of its fracture force and absorbed energy for different cortex positions and notch depths was studied using Izod impact and tensile-impact tests. For both tests, fractographic analysis of bone fracture surfaces was performed and helped to expand our understanding of bone fracture. It also emphasized the important role of micromechanics in fracture of bone. Based on the obtained results the following conclusions can be formulated:

- The bovine femoral cortical bone tissue has a nearly uniform character of recovered and fracture energy for different cortex positions and is not sensitive to the notch depth within the physiological pertinent range.
- The studied tissue demonstrated a low variability of the fracture force for specimens with the notch depths of less than 600 μm.
- Impacts with a low energy level of 0.02 J do not activate any damage or plasticity mechanisms in the bovine femoral cortical bone tissue.
- Impact with a higher energy level of 0.5 J showed a negative correlation between both fracture force and impact strength and notch size.
- Variations in the underlying microstructure for different spatial specimens explained the variability of fracture force and impact strength of bending and tension loading regimes.
- Cleavage fracture ahead of the notch and shear failure away from the notch were dominant in Izod test specimens.
- Side notches magnified the nominal stress and strain and led to failure in tensile-impact tests.
- Specimens with lamellar microstructure sustained higher absorbed energy and fracture forces compared to those for secondary-osteons microstructure.
- A higher fraction of cavity area, over mineralization and weak interface between osteons and interstitial matrix are possible reasons for weakness of Haversian bone during impact tests.
- Cracks followed paths of lower shear strength and were affected by underlying microstructure in tensile-impact tests.

- Fractographic studies of fracture surfaces of the studied cortical bone tissue highlights the need for both macro- and micro-scopic numerical models to study its fracture.

8. Chapter 8

Microscale Finite-Element Modelling of Cortical Bone Tissue

8.1. Introduction

Bone fractures have significant health, economic and social consequences. To plan prevention therapies and treatment strategies, scientific knowledge of bone fracture mechanisms is needed [204]. A failure process in a cortical bone tissue is affected by several factors, such as bone mineral density (bone loss), microstructural changes, variations in its material properties and accumulation of microcracks [13, 205]. Factors such as porosity, mineralization, orientation, diameters and spacing of collagen fibres and other aspects of histological structure strongly affect mechanical properties; they have effect on crack initiation and growth [206]. The effect of bone quantity on its mechanical behaviour and structural integrity was established previously [207, 208]; however, more in-depth investigations of the contributory effects of microstructure, material properties, and microcrack propagation are still required [205, 209]. An improved understanding of bone's resistance to crack initiation and propagation can help in assessing bone-fracture risk [210]. It is well-known that damage occurs in both trabecular and cortical bones due to daily-activity loading regime [211]. Microdamage can be repaired by remodelling process; however, if the bone's repair mechanism is deficient, fragility fractures may result due to minor trauma, especially in ageing bone [212]. Experimentally, both the damage location and morphology in the form of linear microcracks were characterised [213]. Also, a relationship between the crack length and propagation in compact bone tested in cyclic fatigue under four-point bending was investigated [212]. It was found that if linear microcracks possess enough energy or the repairing system is deficient, they can propagate and lead to fracture.

Structurally, bone is a complex hierarchical composite. Histologically, bovine cortical bone is characterised as primary and secondary. During bone growth, primary bone is established on existing bone surfaces, such as circumferential lamellar bone underneath the perisosteal surface [212]. Blood vessels are surrounded by

concentric lamellae known as primary osteons. Primary osteons are smaller, shorter, fewer in numbers and have no cement lines as compared to compact bone's secondary osteons [214]. The latter result from absorption and replacement of old bone by new lamellar bone through remodelling process. Their shapes are round to ellipsoidal in radial-transverse cross-sections of cortical bones, and they form basic building blocks of the cortical bone tissue [212]. Their diameters vary between 100 and 400 μm and can be between 1 and 2 mm in length [215]. Each osteon comprises several lamellae surrounding a central Haversian canal and bounded by a so called *cement line* that separates one osteon from another and from the surrounding interstitial bone. The material properties of this weak thin amorphous interface – cement line – are not fully established yet [137]. Secondary compact bone can be considered as composite material [13, 209]. In such a composite, osteons represent its fibres and interstitial bone its matrix.

Few finite-element (FE) models have been developed to investigate the effect of microstructural constituents on the deformation and fracture behaviour of a cortical bone tissue. Prendergast and Huiskes [137] modelled numerically an osteon to investigate the relationship between damage formation and local strain to ascertain that microdamage changes the local strain field in the bone microstructure. Dong *et al*. [138] used a generalized self-consistent method to estimate the effective elastic moduli of a fibre-reinforced composite, and the model was considered useful to examine the dependence of the elastic properties of cortical bone on its porosity. In another study, Budyn and Hoc [143] introduced a multi-scale method for modelling multiple crack growth in a cortical bone tissue under tension using X-FEM. In another attempt, a microscale finite-element model of the osteonal cortical bone tissue was developed by Raeisi Najafi et al. [141] to evaluate the interaction between osteons and microcracks. To the best of the author's knowledge, none of those studies have studied the elastic-plastic deformation of cortical bone tissue under uniaxial tension loading nor investigated the effect of cement lines through comparative study.

The study of the effect of cement lines on microcrack propagation paths and on the macroscale behaviour as well as relating it to that of a homogenised material and a composite model of the osteonal cortical bone tissue without cement lines can promote our understanding of their role in inhibiting bone fracture. To achieve this, a

2D microscale finite-element models are suggested to investigate the effect of microstructural constituents, particularly cement lines, on fracture scenarios and the global macroscopic mechanical behaviour. This study focuses on the failure and elastic-plastic deformation processes of a microstructural osteonal cell of cortical bone tissue using X-FEM implemented into the finite-element code Abaqus 6.10.

8.2. Microscale Finite-Element Models

8.2.1. Model Geometry

A microstructural cell of secondary osteonal cortical bone is simulated using three models: homogeneous, three-phase composite and four-phase composite. At microscale four different constituents are considered: osteons, interstitial bone, cement lines and Haversian canals. Osteons are considered as fibres since they are approximately circular; interstitial bone is considered a matrix as it fills the gaps between the osteons. Each osteon is surrounded by a thin layer – cement line – and contains a canal, see Fig. 8.1c. The four-phase model accounts all the microstructural types, while the three-phase composite model neglects the effect of cement lines. In this model, a constitutive behaviour of interstitial bone was assigned also to the cement-line regions. Several light-microscopy images for a radial-transverse section of the bovine cortical bone were captured from its posterior position; a sample picture is shown in Figs. 8.1a and 6.2. Those images were used to quantify geometrical parameters of the Haversian-system: diameters of osteons and Haversian canals and thicknesses of cement lines. All the images have identical dimensions of 0.7 mm × 0.525 mm (width × height). The statistical analysis for those images produced an osteons volumetric fraction of approx. 60% and a porosity ratio between 1.6% and 5.3%. The average width of the cement lines was between 1 and 5 μm. In the developed model, the area, directly reflecting microscale information, was embedded into the region with homogenised properties of the cortical bone making the dimensions of the entire model 0.9 mm × 0.725 mm × 0.3 mm (width × height × thickness). This homogenised area enabled the application of uniform external deformation and reaction forces at both sides of the cell. All the parameters were measured from those images using the digital image analysis software, Image-Pro Express [216]. The data obtained from that analysis

were statistically analysed to be fitted to one of the well-known distributions describing the random phenomena (Section 6.5.1).

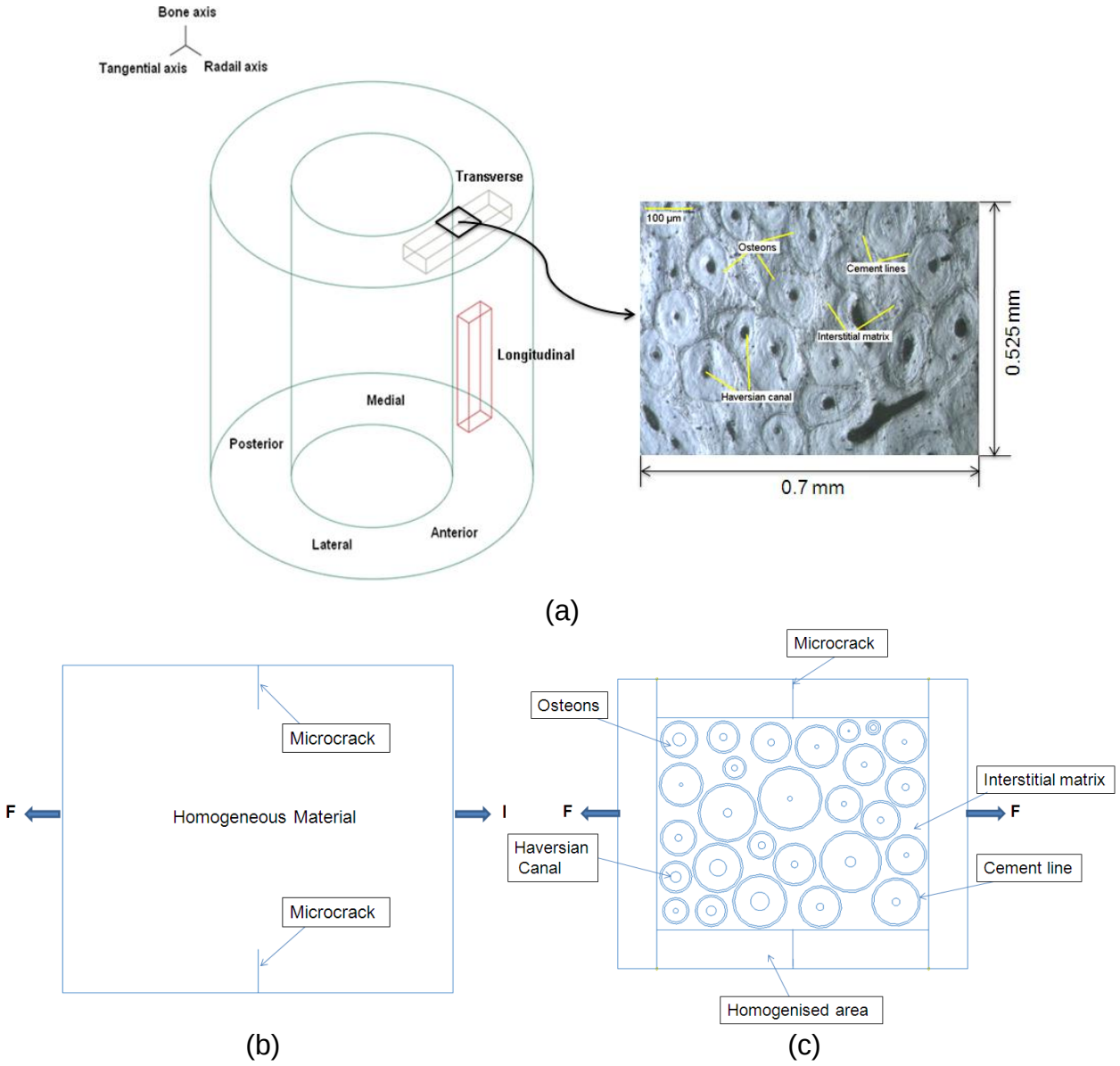

Figure 8.1: (a) Light-microscopy micrograph and its position in transverse-radial cross-section of osteonal bovine cortical bone tissue; (b) schematic illustration of homogeneous model; (c) schematic illustration of microstructured model

The average diameters of osteon fibres and Haversian canals were 99.89 µm and 23.1 µm, respectively. The random microstructure of the model, Fig. 8.1c, was established using MATLAB [217]. Using a developed script, the positions and diameters of osteons were chosen randomly based on the hypersecant distribution curve until they filled 60% of an area with the same dimensions as micrographs.

Then, the Dagum (4P) distribution curve was used to choose randomly the Haversian canal diameters until their total area was within the range 1.6-5.3%. The random positions, diameters of osteons and Haversian canals were then used as an input to Abaqus 6.10 [9].

8.2.2. Material Properties

The material properties of microstructural constituents and homogenised properties of osteonal cortical bone were obtained experimentally as discussed in chapters 5 and 6. All the data were measured for fresh bovine diaphysis femora. Regarding the homogenised material properties, the data was based on our experimental measurements (Section 5.5.1). Also, the elastic-plastic data for osteons and interstitial bone were obtained using the nanoindentation technique (Section 6.5.2). As shown by Lakes and Saha [161], cement lines have isotropic viscoelastic behaviour due to their specific chemical composition. Therefore, their elastic properties differ from those of the osteons that they encircle. In this study, the elastic properties of cement lines were taken 25% lower than those for osteons following Budyn and Hoc [143]. Osteons, interstitial bone and cement lines were chosen to be isotropic in this model. The Poisson's ratio of the constituents and the homogenised area were chosen based on the literature data [143, 218]. Tables 8.1 and 8.2 summarise the elastic-plastic and fracture material properties used in our numerical simulations.

Table 8.1: Elastic properties, and strain energy-release rate of microscopic features and homogenised material of osteonal cortical bone tissue in transverse direction

Material	Elastic modulus (GPa)	Poisson's ratio	Stress Intensity Factor (MPa/$\sqrt{m}$)
Homogenised material	12.73	0.42	0.514
Osteons	12.16	0.17 [143]	0.55 [122]
Interstitial matrix	13.58	0.153 [143]	0.46 [122]
Cement lines	6.85 [143]	0.49 [218]	0.23 [122, 219]

Table 8.2: Plastic properties of microscopic features and homogenised material of osteonal cortical bone tissue in transverse direction

#	Osteons		Interstitial matrix		Homogenized material	
	Strain %	Stress (MPa)	Strain %	Stress (MPa)	Strain %	Stress (MPa)
1	0	9.7	0	19.8	0	14.75
2	1.75	21.9	1.70	34.0	1.73	27.95
3	2.59	29.0	2.37	44.1	2.48	36.55
4	3.20	33.7	2.88	51.5	3.04	42.60
5	3.74	37.1	3.32	56.6	3.53	46.85
6	4.21	39.9	3.73	60.2	3.97	50.05
7	4.65	42.1	4.10	63.3	4.38	52.70
8	5.06	44.0	4.46	65.5	4.76	54.75
9	5.45	45.2	4.80	67.1	5.13	56.15
10	5.82	46.5	5.09	69.1	5.46	57.80

8.2.3. Elastic-Plastic Deformation of Cortical Bone's Microstructure

For all three models, the geometrical attributes used to study the fracture process were also employed to investigate the elastic-plastic deformation process. All the boundary conditions were retained. The material definitions were changed to implement the elastic-plastic behaviour of the microstructural constituents and homogenised area of osteonal cortical bone as given in Table 8.1 and 8.2.

8.2.4. X-FEM-Based Cohesive Behaviour and Fracture Properties

In this study, an X-FEM-based cohesive segment for a crack propagation analysis was used to simulate crack initiation and propagation for both homogeneous and microstructural models. The formulae and laws that govern the behaviour in this approach are similar to those used for cohesive elements, based on a traction-separation constitutive behaviour. The similarity comes from the use of the linear-elastic traction-separation model, damage initiation and damage evolution criteria [9]. The initial stage of the traction-separation model assumes a linear-elastic behaviour followed by damage initiation and evolution. Both elastic stiffness and the

traction-separation behaviour are sufficiently defined by elastic properties attributed to the material in an enriched region. For all the models in this study, all elements were chosen as an enriched region. On the other hand, damage modelling allows the simulation of the degradation stage and eventual failure of an enriched element [9]. The failure in many biological materials is described based on an elastic damage-based criterion [143] that in human cortical bone is governed by the strain-based criterion [190]. In these models, the onset of fracture is based on the critical maximum principal strain. A value of 0.4% was chosen to initiate the cracks in the homogenised material as well as in all the microstructural constituents [220]. In a similar model, it was shown that cracks can be initiated perpendicular to the maximum principal stress direction, mode I in tension [143], therefore, an initial microcrack of length 100 μm was placed at the middle of upper and lower boundaries of the modelled area perpendicular to the loading (tensile) direction, see Figs. 8.1b and c. Once the initiation criterion is met, cracks start to grow obeying the damage evolution law that describes the rate, at which the cohesive stiffness degrades [9]. Evolution of damage in our models was defined based on the energy required for failure (fracture energy) after the initiation of damage. The stress intensity factor for the homogenised material is based on data by Nalla *et al*. [221], and those for osteons and interstitial bone were defined using guidance from [122]. A ratio $k_m/k_{cl} = 2$, where k_m and k_{cl} are stress intensity factors of matrix (interstitial bone) and cement line, respectively, was utilized to obtain the latter factor based on [219]. Table 8.1 summarizes the fracture energies used for homogenised and microstructural constituents. All the models were stretched under deformation-control loading. A 1% strain was applied to the right-hand side of the area in *x*-direction; while the left-hand side was kept in place by constraining it in *x*-direction, with only the middle point being also constrained in *y*-direction, see Figs. 8.1b and c.

8.2.5. Mesh Convergence

In our FE simulations, a convergence study was performed using different element sizes and a maximum principal strain as the convergence criterion. The criterion is based on the maximum value of the maximum principal strain distribution within the model. It is a current limitation of the X-FEM formulation in Abaqus 6.10 [9] to use

only the first-order solid continuum elements. Therefore, 4-node bilinear plain-strain quadrilateral CPE4R elements were used. Figure 8.2 shows variation of the value of maximum principal strain with element sizes. When the element size was smaller than 0.002 mm, the model overestimated the maximum principal strain values. On the other hand, when the element size was in the range between 0.002 mm and 0.004 mm, the value of the maximum principal strain was nearly the same. The latter value started to increase again when the element size was greater than 0.004 mm. Hence, for the current simulations, the element size of 0.003 mm was used in the development of the microstructured models.

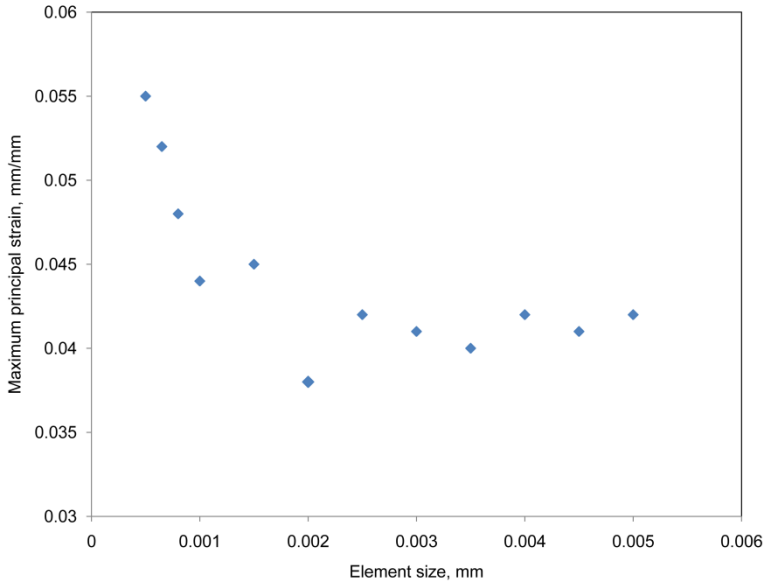

Figure 8.2: Mesh convergence study demonstrates maximum principal stress variation with different element size of four-phase composite FEM

8.3. Results and Discussion

To validate the microscale finite-element models against an experimental data, elastic-plastic material definitions were introduced for the osteons, interstitial matrix and homogenized area. Cracks were not included in the verification simulations. The global stress-strain behaviours were obtained for the studied models by using a kinematic constraint equation between a reference point to which the load is applied and an edge of the homogenized area. In that method, nodes of the homogenized area's edge remained on the straight line parallel to the initial state during the deformation period to maintain material continuity. The stress-strain behaviours obtained from finite-element simulations were compared to those obtained for the

specimens cut from the posterior cortex in the transverse direction. A comparison of the finite-element models' stress-strain behaviours and that of the experimental data is shown in Fig. 8.3. All the three models based on elastic-plastic data demonstrated the same behaviour along with the experimental one up to a strain of 0.05%. Then, models with implemented microstructure started to affect the stress-strain behaviour similar to that observed in the experiment up to 0.3%. On the other hand, the behaviour of the model based on the homogenized material of osteons and interstitial matrix deviated from that of the experimental immediately when yielding started. It exhibited a higher stress-strain curve than that of the experiment. It is obvious that the model based on cement lines shows behaviour closest to reality compared to others.

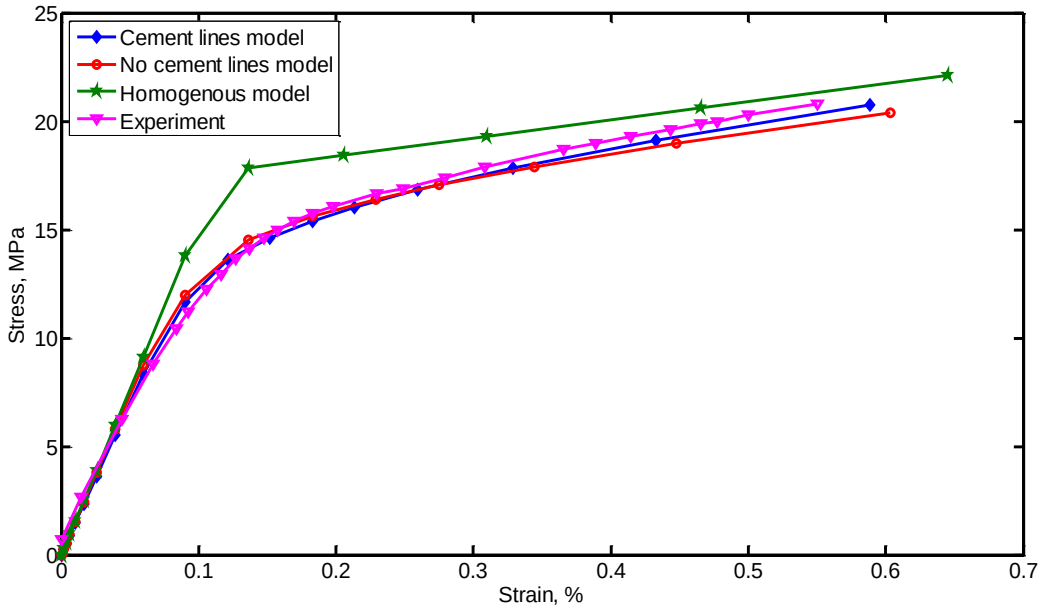

Figure 8.3: Stress-strain behaviours of three studied models compared to experimental data

Fields of calculated Von Mises plastic zones are shown in Fig. 8.4 for a transverse loading regime. These distributions are shown at an applied strain of 0.58%. For models with and without cement lines, the finite-element simulations showed that the critical localized plastic zones started at the interface between osteons and interstitial matrix. On the other hand, the homogenized material model showed a uniform distribution of Von Mises stress with σ_e = 18.56 MPa at the same applied strain. Obviously, for the models with and without cement lines, the areas of interstitial matrix exhibit higher stresses than those in osteons and the homogenized area. It was also observed that Von Mises stress is higher for two osteons

separated by a smaller distance. On the contrary, when the cement lines are implemented, the highest stress values were confined to the area of cement lines. This indicates that cement lines play a prominent role in isolating the osteons from the interstitial matrix; they appear as critical elements in the protection of bone against fracture. The results for models with the elastic-plastic material formulation underpin those simulating the fracture behaviour of cortical bone (Models A, B and C) as discussed below. They all demonstrate the paramount role of cement lines in the fracture process of the cortical bone tissue at the microscale. In addition, the simulation results comply with experimental observations on the effect of the cement lines as osteonal barriers [212].

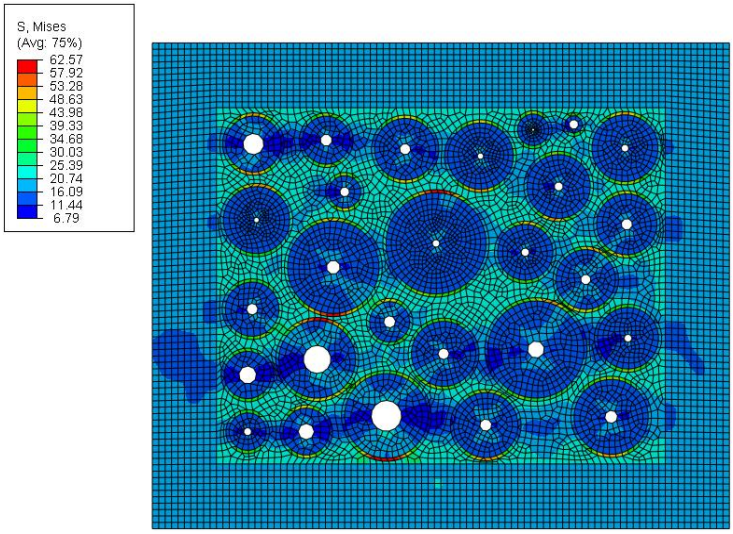

(a)

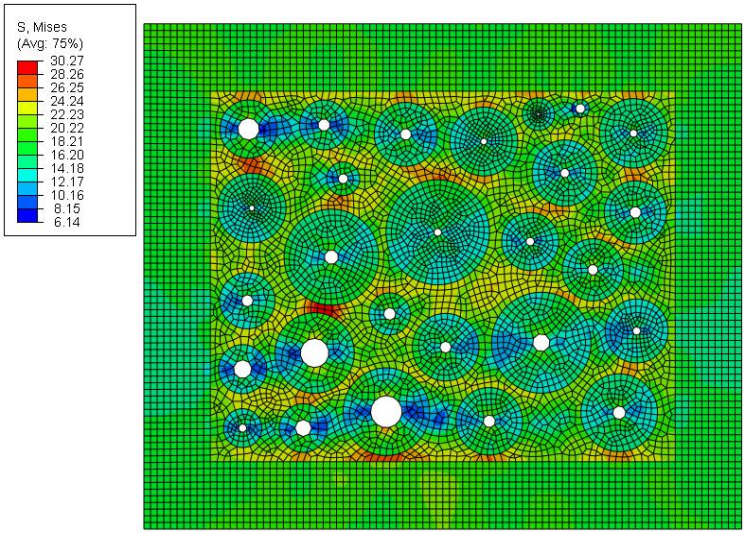

(b)

Figure 8.4: Von Mises stress distributions for models with cement lines (a) and without cement lines (b) for strain 0.58%. Tension is in horizontal direction

By implementing the X-FEM technique, the validated models were employed to investigate the fracture behaviour of the cortical bone tissue at microscale. Three different finite-element models – homogeneous (Model A), three-phase (Model B) and four-phase composite (Model C) – were developed to investigate the effect of microstructual features of the osteonal cortical bone tissue, particularly cement lines, on its global behaviour and crack propagation paths in it [222]. A quasi-static analysis of those models showed obvious differences between their global stress–strain behaviours, see Fig. 8.5. The macroscopic elastic moduli for all the models were approximately the same as apparent for the obtained curves below $\varepsilon = 0.2\%$; the crack initiation and propagation changed their global response. It is most obvious for the homogenised material (Model A) demonstrating significant damage-induced effective softening. In contrast, Model C is characterised by the highest applied stress and applied strain for the microcracks to start growing, while Model B is between those two – see Table 8.3. Model C required 17.5% higher applied stress for microcracks to start growing, while Model B required 16.9%. Two microstructural models are much closer to each other. Although the criterion used for crack initiation was the same for all the models, heterogeneity of different topologies resulted in different distributions of stresses and strains that, in turn, led to different required applied stresses to advance the microcracks.

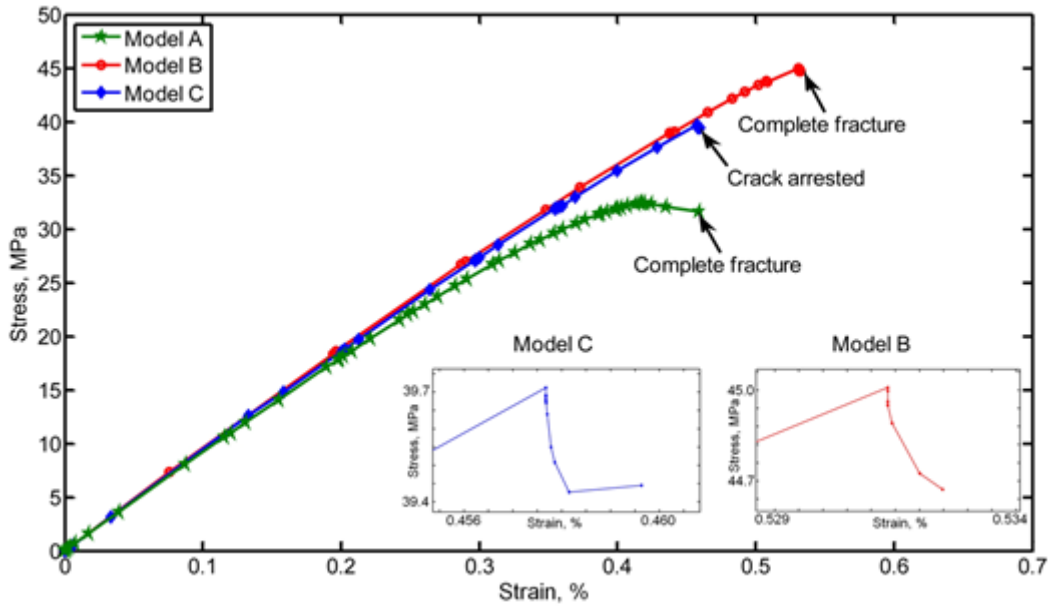

Figure 8.5: Stress-strain behaviour of three studied models under tension

Table 8.3: Crack initiation conditions of three different models

Model	Crack initiation conditions			
	Applied force (N)	Applied stress (MPa)	Applied strain (%)	Applied deformation (mm)
Model A (homogeneous)	2.38	10.60	0.115	0.0010
Model B (without cement lines)	2.87	12.77	0.133	0.0012
Model C (with cement lines)	2.89	12.85	0.136	0.0013

These results are also supported by Fig. 8.6 that shows that at the same level of deformation microcracks in Model A grew quicker compared to those in microstructured models. Also, there was a significant difference between the microcracks total length at the point of fracture. It was also noticed that without cement lines (Model B) the osteons tend to transfer more deformation to the matrix than in Model C; this can explain higher hardening that was also reported in other simulations by Budyn and Hoc [143]. The homogenised model (Model A) had the lowest fracture stress and strain while Model B had the highest values, see Fig. 8.5 and Table 8.4. The behaviour in Model C was somewhere between that of other models. Its final state was not a percolation in the cell but rather an arrest of the microcracks either at a void or a cement line. In this model, due to the current limitations of the X-FEM, the upper crack was unable to propagate any further to show the final crack path along with its final global stress–strain behaviour. The post-fracture behaviour of Models B and C are shown in insets in Fig. 8.5. Obviously, as the modelled cell was not fully damaged in Model C, its global mechanical response started to harden again after its microcracks were stopped, with the remaining undamaged material between two microcracks responding elastically. On the other hand, at the fracture point in Model B, its behaviour softened before a final cell failure. These results indicate the direct effect of the microstructural heterogeneity on the global behaviour of the cortical bone tissue.

The final stage of Model C is consistent with our experimental results for the posterior-transversal direction. Model B required the magnitudes of applied stress and strain 27.5% and 21.5% higher, respectively, than those in Model A to achieve a cell percolation.

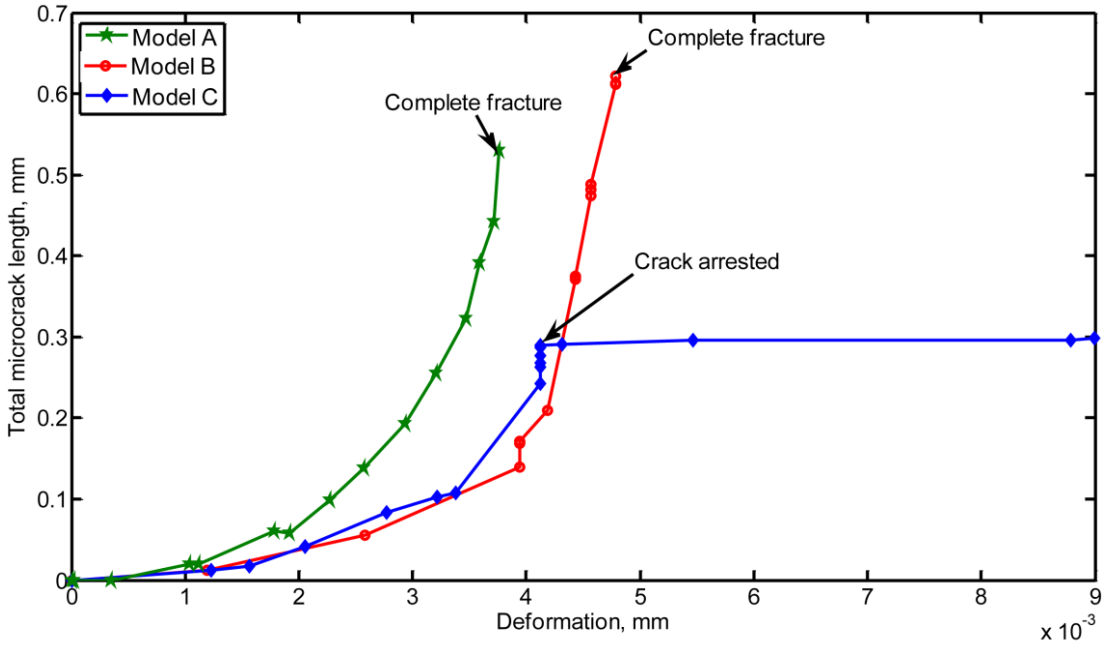

Figure 8.6: Evolution of total crack length with deformation in three studied models under tension

Table 8.4: Levels of applied force, stress, strain and deformation at point of complete fracture for three models (crack is arrested in Model C)

Model	Fracture conditions			
	Applied force (N)	**Applied stress (MPa)**	**Applied strain (%)**	**Applied deformation (mm)**
Model A (homogeneous)	7.29	32.42	0.418	0.0038
Model B (without cement lines)	10.06	44.69	0.533	0.0048
Model C (with cement lines)	8.88	39.44	0.459	0.0041

In another way to quantify the distinctions between the models, the total length of microcrack propagation was measured and the respective deformation recorded at each time increment; the relationship between them is shown in Fig. 8.6. An obvious difference between the total crack lengths at the same deformation level was observed for the models. In the homogenised material (Model A) the microcracks did not find any obstacles to propagate and meet midway in a path normal to the applied load. This was not the case for two other models. The microcracks of microstructural models grew in the same fashion up to a deformation of 0.0035 mm; this also can be seen in Fig. 8.7. As the cement line arrested the microcrack in Model C, the total length of microcracks remained unchanged as the deformation evolved. Therefore, this relationship highlights the role of the cement line to inhibit microcracks. Also, the cement lines played an important role and forced the upper microcrack to change its path between two osteons, while in their absence the distribution of maximum principal stress changed resulting in kinks, see Figs. 8.8 and 8.9. The total length of microcracks was longer in Model B; moreover, they extended until a complete fracture of the cell, providing information about the full failure behaviour. The simulation results of Model C show two different paths: the upper microcrack went straight away between two osteons and split the one ahead until being arrested by its Haversian canal, see Fig. 8.8a. Obviously, the path of the upper microcrack was affected by osteons; this is consistent with simulation results in [141]. On the other hand, the lower microcrack deviated towards an osteon and tried to split it but the cement line arrested the microcrack. It is worth noting that the length of the lower microcrack when it hit the cement line was 175 μm; this is consistent with an experimental study that investigated short microcracks and showed that microcracks of intermediate length (100-300 μm) were deflected as they hit the cement lines [212].

At the final stage of simulations, the upper and lower microcracks managed to split both Models A and B into halves, see Fig. 8.7b while they were arrested in Model C (see Fig. 8.7a). The final crack path in the homogenised model was exactly perpendicular to the loading direction. The effect of cement lines can also be noticed in the character of distributions of maximum principal stress (see Figs. 8.8 and 8.9); the presence or absence of cement lines gave completely different distributions resulting in different microcrack paths through the cell, since

microcracks are guided by the normal to the maximum principal stress. The microscopic stresses showed sudden changes over regions of Haversian canals and cement lines that controlled the microcrack propagation process.

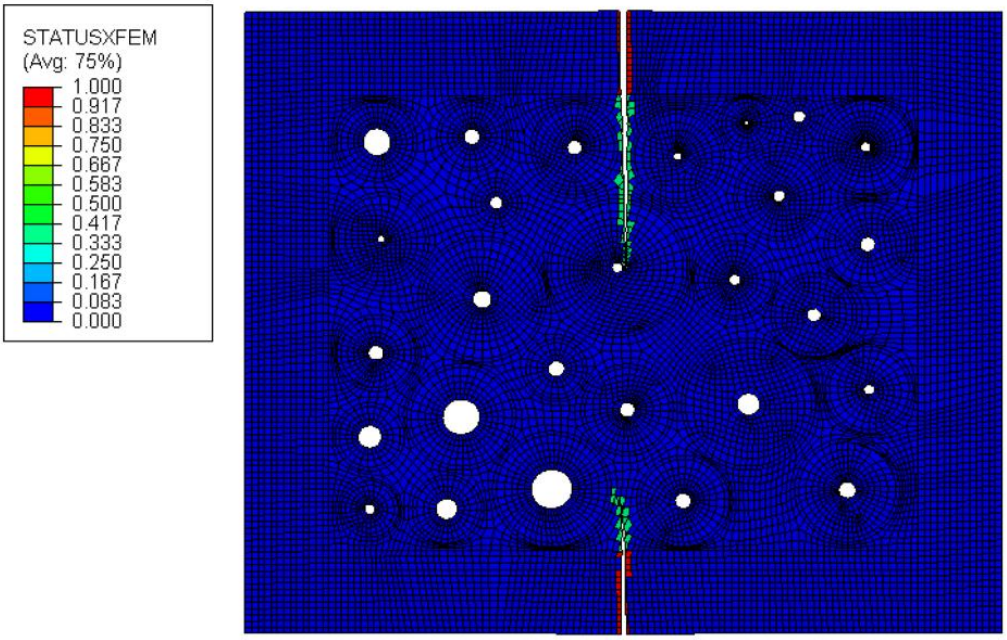

(a)

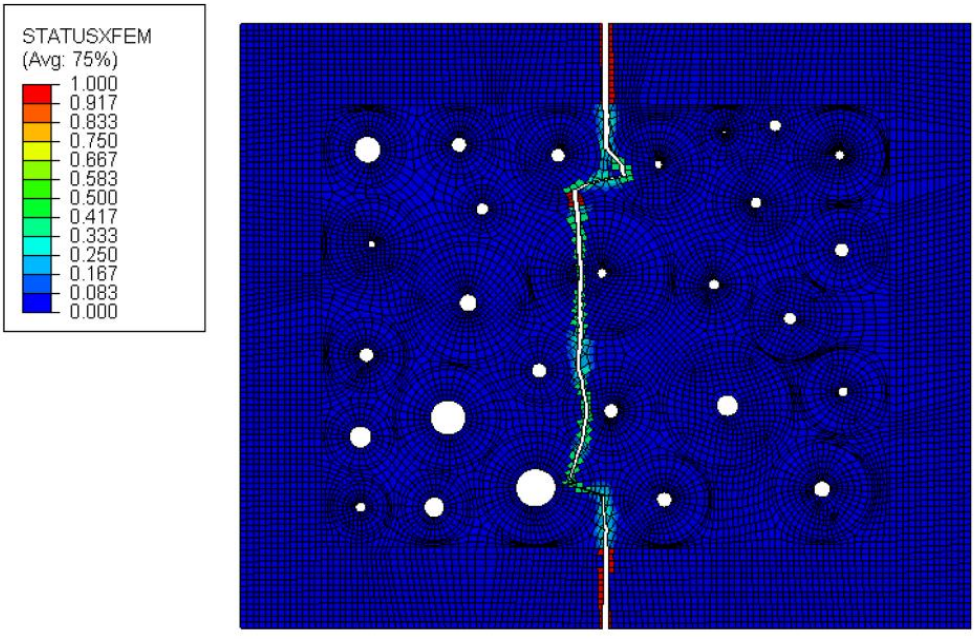

(b)

Figure 8.7: Final crack propagation paths for Models C (a) and B (b) of osteonal cortical bone tissue. Tension is in the horizontal direction

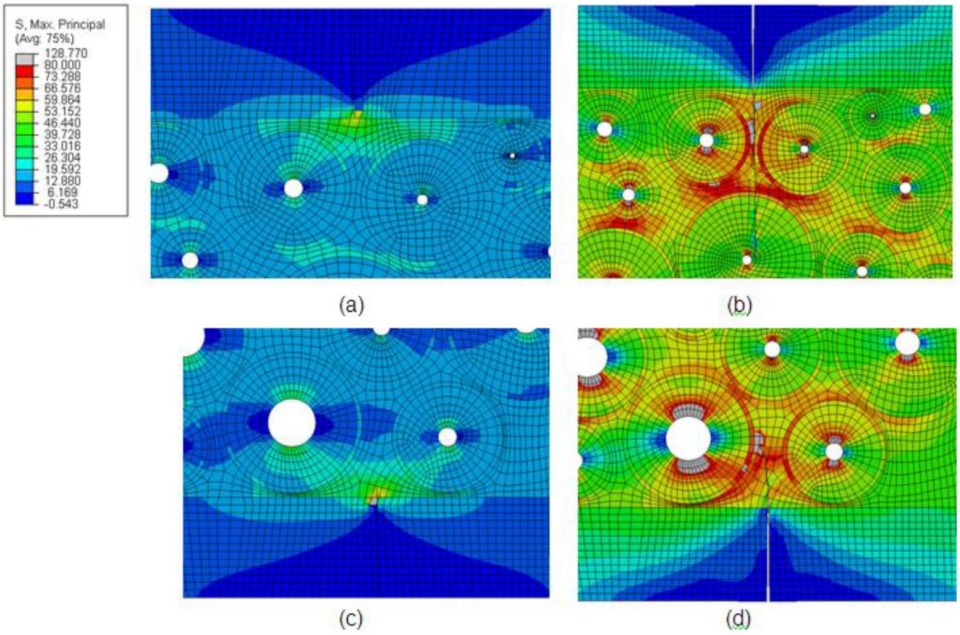

Figure 8.8: Distributions of maximum principal stress in vicinity of upper (a) and lower (c) microcracks at crack initiation increment, and for increment of arrest of upper microckack by void (b) and arrest of lower microcrack at cement line (d) in Model C of osteonal cortical bone tissue

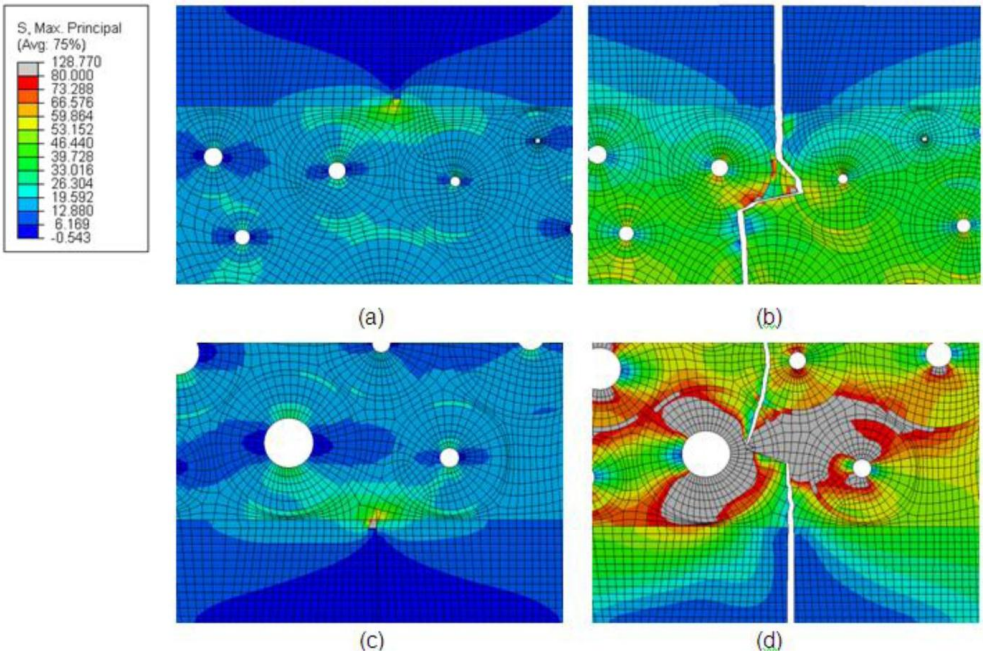

Figure 8.9: Distributions of maximum principal stress in vicinity of upper (a) and lower (c) microcracks at crack initiation increment and for increment of complete fracture for upper microckack (b) and lower microcrack (d) in Model B of osteonal cortical bone tissue

Hence, there is an effect of cement lines on the crack paths according to our study along with two other similar studies [141, 143]. However, it was reported in an experimental study that when the crack plane is perpendicular to the osteon's axis, the underlying microstructure has a much stronger influence on the crack path [221]. In that case, it was observed that crack initiation and initial crack growth did not follow a path normal to the maximum tensile stress, but rather in the osteon's direction. It was concluded that cement lines can provide a weak path for the crack propagation [221].

8.4. Conclusions

Three different finite-element models were developed and implemented to study the effect of cement lines on microcracks growth trajectories and the global behaviour of osteonal cortical bone tissue. These features were studied with a four-phase composite model (Model C), directly incorporating cement lines. The obtained results were compared to those of two other models: a three-phase composite model without cement lines (Model B) and a model of a homogenised material (Model A). Based on the results obtained from numerical simulations the following conclusions can be formulated:

- Dissimilar global stress–strain behaviours were observed in the studied models; the homogeneous material in Model A started to soften immediately after a crack started to propagate, while the implementation of a heterogeneous material in Models B and C resulted in a non-softening behaviour.
- Presence of cement lines demanded higher levels of stresses and strains for the growth of microcracks.
- A significant difference between the total microcrack lengths at the fracture point was observed for the homogeneous model and the microstructural ones.
- The homogeneous model had the lowest final fracture stress and strain; Model B had the highest values, while the cement lines arrested the crack propagation in Model C.

- The relationship between the total length of microcracks and deformation highlights the role of the cement lines to inhibition of fracture at microscale level.
- The Haversian microstructure affects the distribution of maximum principal stress that, in its turn, influences the microcracks' propagation trajectories.
- Cement lines play a prominent role in isolating osteons from the interstitial matrix; they appear as critical elements in protection of bone against fracture.

9. Chapter 9

Finite-Element Analysis of Impact Loading of Cortical Bone Tissue

9.1. Introduction

Usual reasons for bone's fracture are falls, high-energy trauma during sports, and engagement in transportation or industrial accidents. The stresses imposed on a bone during such activities do not necessarily have a relation to those produced during daily activities, such as running or jumping [62]. Obviously, the generated stresses during an impact can be far higher than those produced during normal daily activities and, hence, lead to bone fracture. In order to plan prevention therapies and treatment strategies, scientific knowledge of bone fracture mechanisms and behaviour is paramount. Even though, in principle, studying bone's deformation and fracture behaviour is of immense benefit, but it is not possible to engage volunteers in *in-vivo* investigations. Moreover, though *in-vitro* experiments provide large amounts of qualitative and quantitative data, still, FEM can enhance our understanding of processes in bones and offer solutions for, many challenges of experimentation. Using reliable FE models, the time and cost of experimentation can be reduced or eliminated. Alongside with the latter benefit, using FE models, bone specimens cut from different species can be investigated when their material data are available. Additionally, specimens of healthy or diseased, young or aged, mineralised, partially mineralised or demineralised bone can also be analysed. In this light, developing adequate numerical models capable of predicting and describing the bone's deformation and fracture behaviour in the impact loading regime can provide a detailed study of reasons for, and ways to, prevent bone fracture.

Often, *in-vivo* bone fracture is initiated and promoted by cracks; therefore, fracture mechanics is used as an important tool to assess its strength and fracture toughness and to improve diagnoses and treatment of bone fractures [132]. Up to now, Linear-Elastic Fracture Mechanics (LEFM) was mostly used to assess the

toughness of cortical bone tissue; it yields a single-valued fracture parameter – the critical stress intensity factor or the critical strain energy release rate [223, 224]. Due to complex composition and microstructure of the cortical bone tissue, it has several toughening mechanisms, such as diffuse microcracking, crack deflection, and fibre bridging [225-228]. The inadequacy of LEFM theory application to describe cortical bone tissue fracture was raised due to observed resistance-curve (R-curve) behaviour [10, 108]. As a numerical endeavour to model bone fracture, cohesive zone models were used to analyse the initiation and propagation of cracks in cortical bone [10, 229, 230]. Another method in a recent study [11] demonstrated the adequacy of a Double-Cantilever Beam (DCB) test for determining fracture toughness under pure mode-I loading of cortical bone by implementing a new data-reduction scheme based on specimen compliance.

Still, analysis of the actual crack initiation and growth was hard to achieve using the mentioned approaches in simulations due to the well-known fact that the crack path has to be defined well in advance. With a new Extended Finite-Element Method (X-FEM), crack initiation and propagation can be modelled more easily. Thus, the aim of this part of the study was to develop and validate numerical models using X-FEM for analysis of the deformation and fracture behaviour of cortical bone tissue exposed to impact loading regimes of Izod and tensile-impact setups. In this chapter, Extended Finite-Element Method implemented into the commercial finite-element software Abaqus 6.10 was used to simulate the crack initiation and growth for specimens of cortical bone exposed to impact loading. Three different models were developed for the Izod testing setup including notched cortical-bone specimens to simulate the deformation and fracture behaviours of cortical bone tissue: two-dimensional (2D) impact, three-dimensional (3D) impact and 3D quasi-static models. On the other hand, for the longitudinal tensile-impulsive and quasi-static loading regime, three different 3D impact models were developed to simulate the fracture and deformation behaviour of cortical bone tissue. The data obtained in the experimental part of this study was used to define the materials' parameters and to verify the numerical models. It is worth mentioning here that bone is a viscoelastic material (as discussed in chapter 5); therefore, this type of mechanical behaviour is considered when dealing with dynamic events, such as impact.

9.2. Numerical Models of Izod Impact Test

In this part of the simulations, three finite-element models (FEM) were developed: Model A, Model B, and Model C. Model A is a 2D X-FEM model used to simulate the fracture of cortical bone exposed to impact loading in the Izod-test setup. Model B is a 3D formulation of Model A, whereas Model C is a 3D X-FEM model for quasi-static fracture analysis. The impact tests were simulated with the finite-element software Abaqus 6.10/Implicit using Models A and B to verify the applicability of the X-FEM to analyse the failure behaviour of the cortical bone tissue under impact-loading conditions. In addition, Model C was developed to elucidate fracture development in the cortical bone tissue under different loading conditions. A full description of the Model A and Model B can be found in our published work [231, 232].

9.2.1. Model Geometry and Boundary Conditions

In Model A, the impact Izod test was simulated with the Abaqus/Implicit finite-element software using a 2D formulation. The real geometry and masses of the hammer and specimen with 300 μm notchs were used in simulations (see Fig. 9.1). The following model assumptions were made: (1) plain-strain conditions of the specimen; (2) homogeneous and isotropic material properties for both the specimen and the hammer; (3) frictionless contact between the hammer and the specimen. Before employing Model A to analyse the fracture behaviour of the bone specimen using X-FEM, a special emphasis was put on analysis of the effect of the type of material's mechanical model – without using X-FEM at this stage – on results of simulations. The specimen was presented as made of an elastic, elastic-plastic or viscoelastic material, while the hammer was modelled using an elastic material model due to its significantly higher stiffness. A node on the proximal part of the hammer shown as "pivot" in Fig. 9.1b was constrained in x and y directions and set free to rotate around *z*-axis to simulate its centre of rotation. In simulations, the initial position of the hammer was close to the specimen; its angular velocity of 5.33 rad/s corresponded to an initial angle of 58° (initial energy of 0.5 J). The specimen's support was modelled as rigid; all the degrees of freedom of the specimen's bottom part were constrained (see Figs. 9.1b and 9.1c). In Model B, 3D geometry and real

masses of the hammer and specimen with a 300 μm notch were used (see Fig. 9.2).

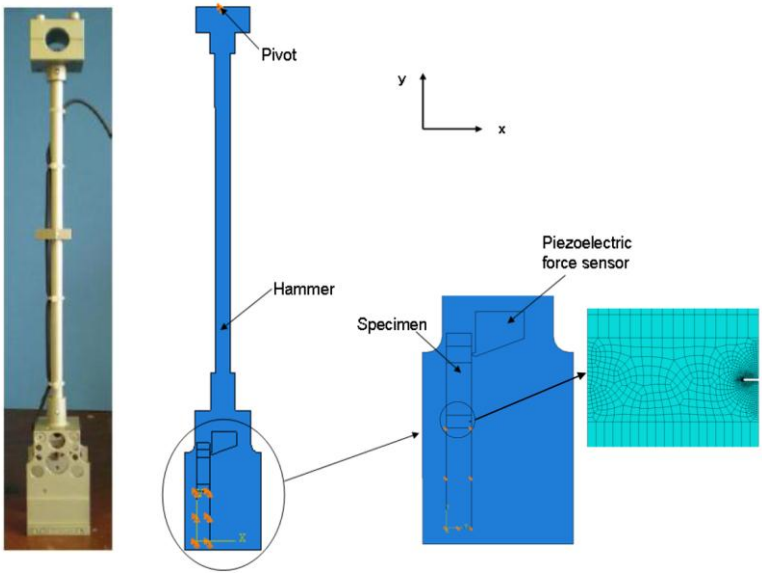

(a) (b) (c)

Figure 9.1: (a) Real hammer; (b) Model A; (c) hammer-specimen interaction and mesh around the notch

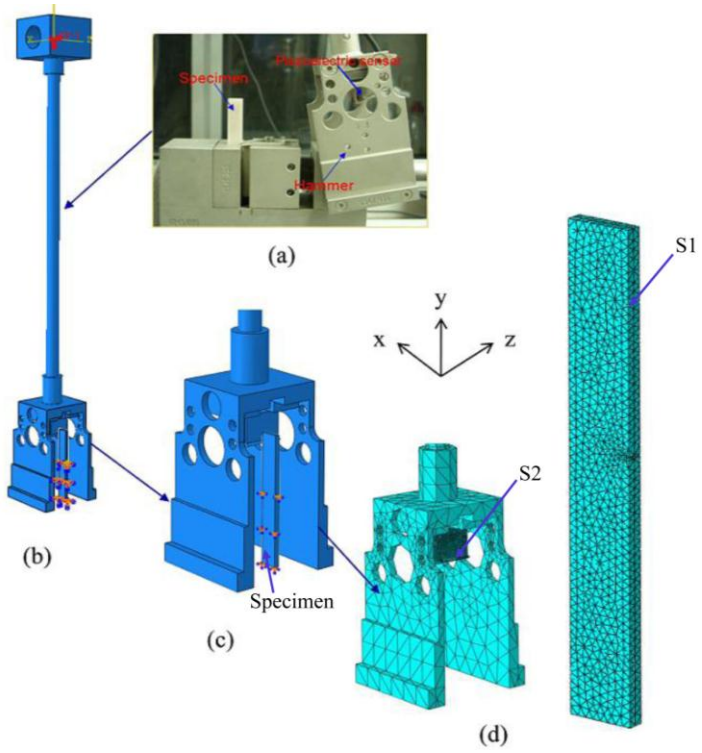

Figure 9.2: (a) Setup of Izod test; (b) Model B; (c) hammer-specimen interaction; (d) meshing of hammer and specimen (specimen is shown larger)

In Abaqus 6.10, a kinematic coupling constraint is used to transmit rotation to a structure while permitting a radial motion. Hence, this feature was employed to constrain the hammer from radial or translational movements except around one axis only; it is z-axis in this case (Fig. 9.2). To get the exact movement of the hammer as it happens in real tests, all the nodes of the inner cylinder's surface of the upper block of the hammer were kinematically coupled to a reference point at the middle of that cylinder, then the reference point was restrained to translate along x, y, and z and to rotate around x or y axes (Fig. 9.2b). The reference point was only free to rotate around z-axis. Using Abaqus/CAE, two sets were defined: the reference point (set1) and the inner surface (set2). The following equation was used to define the coupling between those sets:

$$ur_1 - ur_2 = 0, \qquad (9-1)$$

where ur_1 and ur_2 are the rotational degrees of freedom for set1 and set2, respectively.

On the other hand, two surfaces were chosen to define a surface-to-surface contact between the specimen and the hammer. These surfaces are shown as S1 and S2 in Fig. 9.2d. The master surface was chosen to be S2 with S1 chosen to be the slave one. The mesh of the master surface was adjusted to be finer than that of the slave surface. A finite sliding with frictionless tangential behaviour formulation was chosen between the two surfaces. The hammer's initial condition with an angular velocity of 5.33 rad/s and the specimen boundary conditions are the same as in Model A.

To compare the force-time history data of experiments and simulations, the force due to contact pressure between the piezoelectric force sensor and counterpart of the specimen elements was recorded in the history output of the finite-element software Abaqus/Implicit. Also, the status of the X-FEM that shows the crack path was used as an output along with the distributions of stress and strain components and their principal values. In order to compare the fracture behaviour of the cortical bone specimen under quasi-static and impact loading, Model C (Fig. 9.3) was developed. It consists of a cantilever-beam specimen of cortical bone with the same geometry, mesh and material properties as in Model B. In Model C, the hammer was excluded from the analysis and instead a displacement-controlled load of 2 mm

was applied at the same position of the hammer-specimen interaction, see Fig. 9.3b.

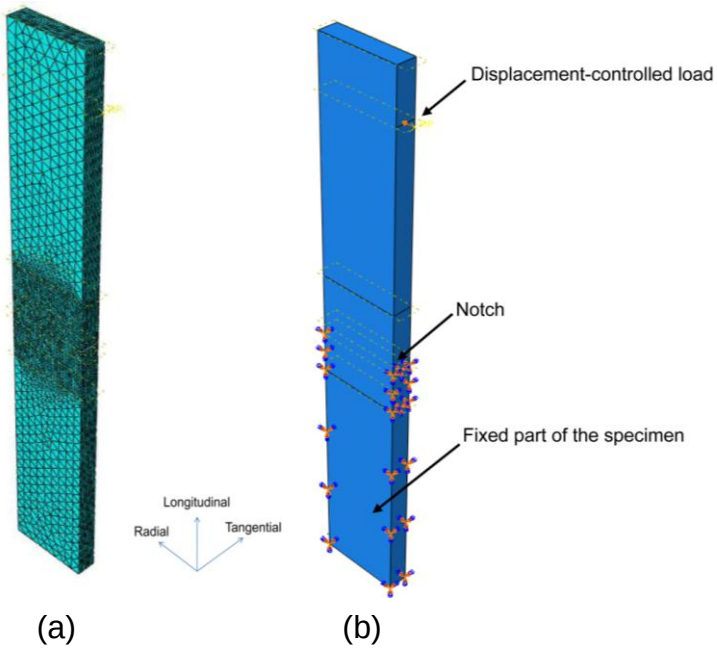

Figure 9.3: (a) Meshed 3D quasi-static specimen; (b) applied displacement and boundary conditions of 3D quasi-static model (Model C)

9.2.2. Material Properties

The Resil Impactor's hammer used in this study is made of carbon steel. Its elastic material properties are given in Table 9.1. These data were obtained from direct contact with the manufacturer.

Table 9.1: Elastic Material properties of Resil Impactor's hammer

Part	Material	Elastic modulus (GPa)	Poisson's ratio	Density (kg/m^3)
Hammer	Carbon steel	210	0.3	7850

For bone tissue, before starting the numerical analysis, two important conclusions of the previous parts of the study were recalled: (1) experimental Izod impact tests demonstrated that the studied bovine femoral cortical bone tissue had a nearly uniform character of fracture energy for different cortex positions and was not sensitive to the notch depth within the physiological pertinent range (see chapter 7);

(2) quasi-static tests provided a low level of anisotropy (between 1.2 and 2) compared to traditional composites (see chapter 5). Hence, in this light, it is reasonable to consider only specimens cut from anterior longitudinal cortex position when dealing with fracture – for Models A, B and C – and to approximate its material properties as isotropic.

The elastic, plastic and viscoelastic data of cortical bone tissue were quantified in the experimental part of this study (see chapter 5). The average elastic modulus and Poisson's ratio of anterior longitudinal specimens are given in Table 5.1 and 5.2, respectively. The average true plastic stress – plastic strain behaviour of the latter specimens is given in Table 9.2.

Table 9.2: True plastic stress-strain values of anterior longitudinal cortical bone tissue specimen

Plastic strain (mm/mm)	Plastic stress (MPa)
0	105.20
0.019	109.95
0.094	124.19
0.165	135.23
0.222	144.00
0.351	165.43
0.439	182.49
0.488	191.89
0.525	200.38
0.565	209.32

The density of the cortical bone tissue was measured as 1860 kg/m^3. The viscous behaviour of bones was introduced into the finite-element models A and B in terms of the Prony series expansion of the dimensionless relaxation modulus as

discussed in chapter 3. These material's constants are the shear relaxation modulus ratios e_i, bulk relaxation ratios k_i and relaxation time τ. They are provided in Table 5.3 for all cortex positions, but only those for specimens cut from the anterior position were used. Only linear-elastic material model was used for Model C for quasi-static loading.

In these simulations, the X-FEM-based cohesive segments method was used to simulate crack initiation and propagation along an arbitrary, solution-dependent path in the balk material, since the crack path is independent from the boundaries of the elements in the mesh. In Models A, B and C, the enrichment area was chosen as the bone specimen. For Models A and C, the crack was introduced as a plane with dimensions of 300 μm $\times$ 4 mm to reproduce the notch depth and the specimen thickness of real experiments, respectively. On the other hand, it was introduced as a 300 μm-long line to represent the notch depth for Model B.

In general, damage modelling allows simulation of crack initiation and eventual failure of an enriched area in the solution domain. The initial response is linear, while the failure mechanism consists of a damage initiation criterion and a damage propagation law. Damage initiation was defined based on the maximum principal strain of 0.25% [220, 233]. When damage initiation criterion is met, damage propagation law starts to take place. In this study, damage evolution was defined in terms of fracture energy (per unit area) and linear softening was chosen. The mixed-mode behaviour was chosen and the fracture energies for fracture modes were introduced into X-FEM. The fracture toughness values were 1374 N/m, 4710 N/m and 4016 N/m for Mode I, Mode II and Mode III, respectively [117].

9.2.3. Mesh Convergence

A high-degree mesh refinement technique is normally used to increase the accuracy of simulations when accompanied with high stress gradients. A local refinement of the respective region and a smooth transition between refined and coarse elements is the basis of the technique that allows avoiding excessive computational requirements. However, this technique is reasonable when the studied model does not include geometrical singularities. In the current model, due to the implementation of the side notch, stress raiser, the history of the force-time signal is used as the criterion of convergence. For Model A, the linear quadrilateral

(CPE4R) and triangular (CPE3) elements were used to mesh the finite-element structure; it is the current limitations of the X-FEM in Abaqus 6.10 to use only linear elements. To verify the model against the experimental data, the force due to contact pressure between the piezoelectric force sensor and counterpart of the specimen elements was requested in the history output of the finite-element software Abaqus 6.10/Implicit. For Models B and C, linear tetrahedron (C3D4) elements were used for both specimen and hammer; it is currently the only element type that can be used for 3D X-FEM analysis. The mesh sensitivity study (Fig. 9.4) was performed with changing only the specimen's element size and an element size of 2.5 μm was used for all three models.

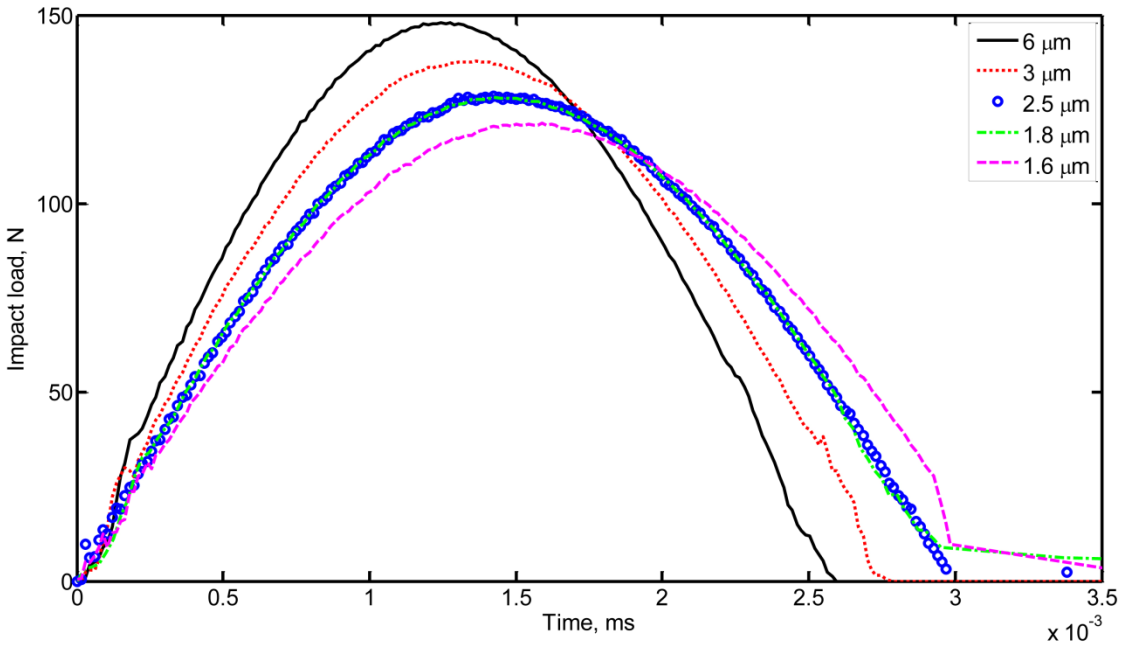

Figure 9.4: Force-time history using different element sizes for 2D Izod test using low level of energy – 0.02 J

9.3. Numerical Models of Tensile Impact Test

The development of numerical model of tensile-impact tests is aimed at understanding the crack growth behaviour within a cortical bone specimen under such impact loading condition. An advanced finite-element technique, X-FEM, implemented into the standard finite-element software Abaqus 6.10, was employed to achieve this goal. The finite-element model was developed for a single impact supposing that the failure of the cortical bone tissue is related to the maximum load during applied impulsive loading. Three different 3D models were developed for the

Tensile-impact setup: Model D, Model E, and Model F. In Model D, due to the complexity accompanied with the model's geometry, boundary conditions and dynamic loading regime, the elastic-plastic data of a specimen manufactured from aluminium alloy was assigned to the specimen to verify the 3D tensile-impact model without using X-FEM. Model E is nearly the same as Model D but with two differences: (1) cortical-bone viscoelastic parameters were assigned to the specimen; (2) X-FEM definition was implemented. Material properties were measured in the current study for both the aluminium alloy and bone tissue (discussed below). In addition, Model F was developed to expose the fracture development in the cortical bone tissue under quasi-static loading conditions. In the following sections, a detailed description of the steps used to develop the tensile-impact test models is introduced.

9.3.1. Model Geometry

For Models D and E, the tensile-impact model is composed of five basic elements: (1) hammer; (2) specimen; (3) traction terminal; (4) bridge; (5) tensile-impact vice (Fig. 9.5). The dimensions of real hammer were measured, and its 3D representation was developed using Abaqus/CAE. By direct contact with the manufacturer of the Resil Impactor, it was brought to our attention that the hammer rod (Fig. 9.5) is a hollow cylindrical part with external and internal diameters of 14 mm and 12 mm, respectively. The rest of the hammer parts are solid. Also, by using the Abaqus/CAE, the specimen with its 3D dimensions, shown in Fig. 7.7, was built. While both the real 3D dimensions of the traction terminal and the bridge were measured and their 3D representation was made using Abaqus/CAE, only a small 3D part of the tensile-impact vice was modelled and its remaining fixed part was represented by complete-constraint boundary conditions. The real photographs of the basic components of the model are shown in Figs. 7.5 and 7.6., while their 3D representation is given in Fig. 9.5.

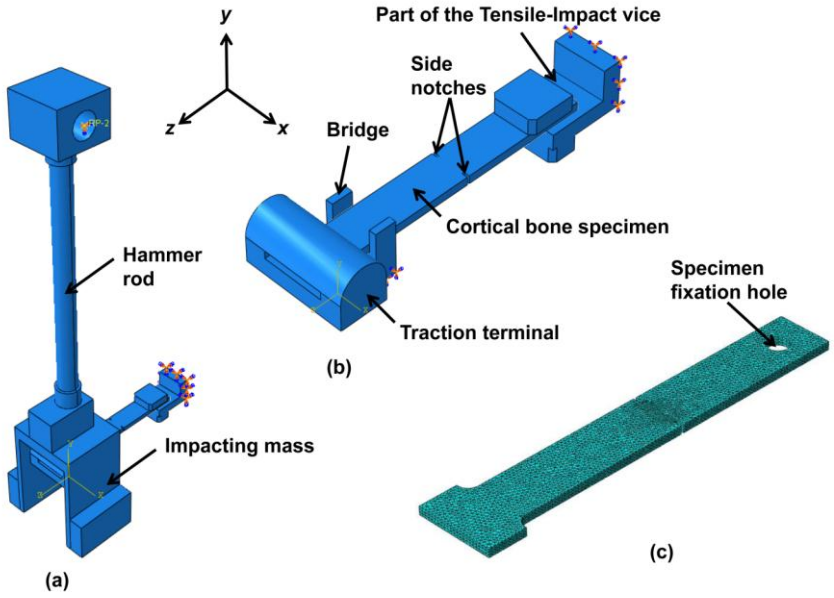

Figure 9.5: (a) Model of a hammer-specimen interaction; (b) Model of specimen, bridge, part of tensile-impact vice and traction terminal; (c) meshing of specimen

In order to compare the fracture behaviour of the cortical bone specimen under quasi-static and impact loading, Model F was developed. It consists of the tensile-impact specimen of cortical bone with the same geometry, mesh and material properties as Model E. In Model F, the hammer was excluded from the analysis and, instead, a displacement-controlled load of 2 mm was applied at the position of hammer-specimen interaction.

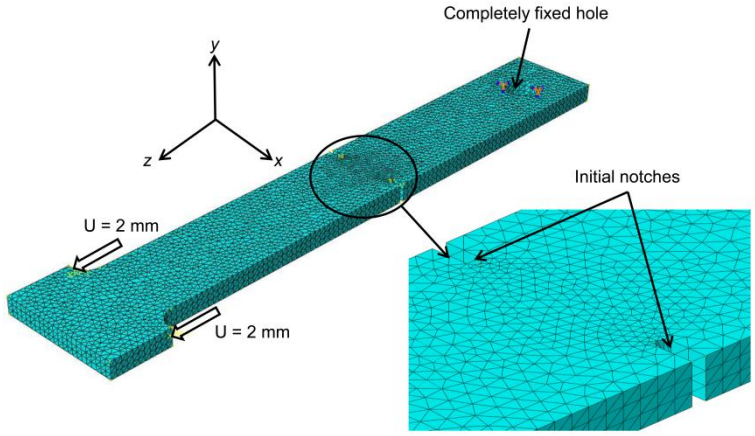

Figure 9.6: Meshed 3D quasi-static specimen with applied displacement and boundary conditions in Model F

9.3.2. Material Properties

For Models D and E, the material properties of the tensile-impact hammer, used in the current model, were the same as the ones used in the Izod-test models, see Table 9.1. There are three different material models used for the specimen in the tensile-impact FE models: (1) aluminium alloy material in Model D; (2) viscoelastic cortical bone material in Model E; (3) linear-elastic cortical bone material in Model F. The density, elastic modulus and Poisson's ratio of the aluminium alloy are 2650.4 kg/m^3, 67.1 GPa and 0.3, respectively, while its plastic behaviour is given in Table 9.3. Elastic and viscoelastic data of cortical bone tissue were the same as those described in Section 9.2.2. Model D was used to verify the results of the experimental against the experimental results, while Models E and F were used to simulate the crack evolution in the bone specimen using X-FEM technique under impact and quasi-static loading, respectively.

Table 9.3: True plastic stress-strain values of aluminium alloy specimen used in Model D

Plastic strain (mm/mm)	Plastic stress (MPa)
0	167.98
0.0014	197.59
0.0054	211.59
0.0114	223.43
0.0176	233.30
0.0239	241.94
0.0304	249.62
0.0369	256.22
0.0437	262.02
0.0504	267.07
0.0573	271.51
0.0641	275.39
0.0709	278.78
0.0778	281.82
0.0818	283.39

9.3.3. Boundary Conditions

For Models D and E, a kinematic coupling constraint was applied to allow the hammer to rotate around a specific axis (x-axis in the model) and to avoid linear movement (Fig. 9.5). Hence, to emulate the movement of the real hammer, all the nodes of the inner cylinder's surface of the upper block of the hammer were kinematically coupled to a reference point at the middle of that cylinder, then the reference point was restrained to translate along *x*, *y*, and *z* and to rotate around *x*-axis (Fig. 9.5a). The reference point was only free to rotate around *x*-axis. Equation 9-1 was used to define the kinematic coupling between the reference point and the inner cylindrical surface of the hammer's upper block. On the other hand, to model the contact between the model's parts, the general contact algorithm implemented into Abaqus 6.10 was employed. All-inclusive surface was used to define the contact domain; it automatically defines the contact pairs and includes all element-based surface facets [9]. A finite sliding with a frictionless tangential behaviour formulation was chosen between the surfaces in contact. To reduce the computation time, the hammer was assembled very close to the specimen as an initial position in simulations. A linear velocity of 2.53 m/s – along *z*-axis – corresponding to the initial angle of 115° (initial energy of 3 J) was applied to the hammer. The bridge and the tensile-impact vice were fully constrained at their bottom and back surfaces, respectively, as shown in Fig. 9.5b. To compare the force-time history data of experiment and simulations, the force due to contact pressure between the inner surfaces of the specimen fixation hole (see Fig. 9.5c) and the elements of the vice fixation pin was recorded in the history output of the finite-element software Abaqus/Implicit. Only for Model E, the status of the X-FEM that shows the crack path was used as an output along with the distributions of stress and strain components and their principal values. On the other hand, for Model F, all the degrees of freedom of the internal surface of the hole at the end of the specimen were restrained, while a displacement of 2 mm was applied to the specimen-hammer interaction position, see Fig. 9.6.

9.3.4. Mesh Convergence

In Model D, due to the implementation of the two side notches, stress raisers, the history of the force-time signal is used as the criterion of convergence. Linear

tetrahedron (C3D4) elements were used both for specimen and hammer; it is currently the only element type that can be used for 3D X-FEM analysis. In addition, this element type was chosen as the final mesh used in Models E and F. The mesh convergence study, as shown in Fig. 9.7, exhibited that when the element size was reduced from 2.5 mm to 1.6 mm, slight changes in the results were observed. An element size of 1.8 mm was chosen for the current model. The mesh-sensitivity study was performed with changing only the specimen's element size and by using the aluminium alloy's material model.

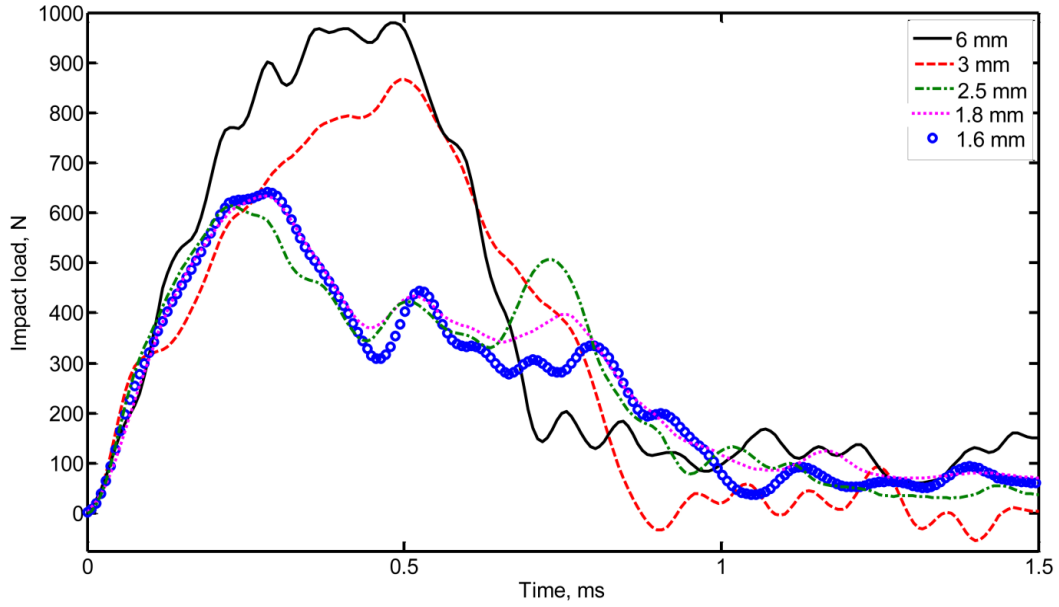

Figure 9.7: Force-time history for different element sizes (aluminium-alloy specimen)

9.4. Results and Discussion

9.4.1. Numerical Models of Izod Tests

Based on the experimental results that showed a nearly uniform character of recovered and fracture energy for different cortex positions and notch depths (see chapter 7), it was possible to introduce numerical models of bone only for one notch depth and using properties of one of the four cortex positions. In this numerical study, material data for the anterior part that required the highest fracture force before fracture was chosen to be implemented into the numerical model. For Model A, several sets of simulations for different material models were performed to analyze their effect on results for the hammer-specimen interaction. A comparison

between the experimental data and the results of finite-element simulations for energy level of 0.5 J is shown in Fig. 9.8. The obtained results are presented for three different anterior cortical bone material models: linear-elastic, elastic-plastic and viscoelastic. The effect of the type of material model was studied based on our quasi-static tensile test results for the cortical bone tissue that demonstrated elastic-plastic behaviour for a fixed strain rate and sensitivity to strain rate as well as the time-dependent character. Consequently, an elastic-plastic cortical-bone material model (see Table 9.2) was initially implemented to ascertain its validity to capture the cortical bone behaviour under impact test. Comparing the results of that model with the obtained experimental data, it was noticed that it underestimated the force magnitude – by 46.7% for its maximum magnitude, indicating its inability to capture correctly the response of the cortical bone tissue under impact load. Moreover, the calculated force peak leads the experimental peak by 0.16 ms (i.e. some 37%). Then, results of simulations based on the linear-elastic material model were analysed. The introduction of that type of material's behaviour resulted in lower underestimation of the level of force (39.2% lower for the maximum value). Also, similar to elastic-plastic material model, its force peak value leads the experimental peak by 0.16 ms, see Fig. 9.8. At that point of the analysis, the viscoelastic material model, based on our experimental results (see Table 5.3) was employed; it provided a good agreement with the observed experimental data for the period of interaction between the hammer and specimen in the Izod test. Divergence of numerical and experimental results after the vertical dashed line in Fig. 9.8, representing the time when the specimen started to fracture, is naturally explained: at this stage of simulations the models did not employ any fracture criterion that can introduce the specimen's failure behaviour. So, the part of the force-time curve after the peak force exhibits recovery of the stored energy in the specimen, as the hammer was retracted backwards. Thus, the viscoelastic model is capable to present correctly the behaviour of anterior cortical bone under impact loading until the onset of the specimen's fracture.

When the initial angle was adjusted for low-level impact energy – 0.02 J – the numerical simulations also resulted in three different behaviours for the three different material models as shown in Fig. 9.9. Here, both linear-elastic and elastic-plastic constitutive models resulted in almost identical behaviours due to a low-level

of mechanical excitation. The models based on those two types of material's behaviour underestimated the experimentally obtained peak force magnitude by 8% and 38.5%, respectively, for the lower and upper bounds of the band of experimental data, see Fig. 9.9. The peak force in the viscoelastic model lies within that band confirming once more the adequacy of the viscoelastic model to simulate the behaviour of cortical bone tissue under impact loading. Employment of the viscoelastic finite-element model led to a shorter contact time compared to that obtained in simulations with other formulations; it was comparable with the experimentally obtained contact time that was in the range of 1.0 - 1.2 ms.

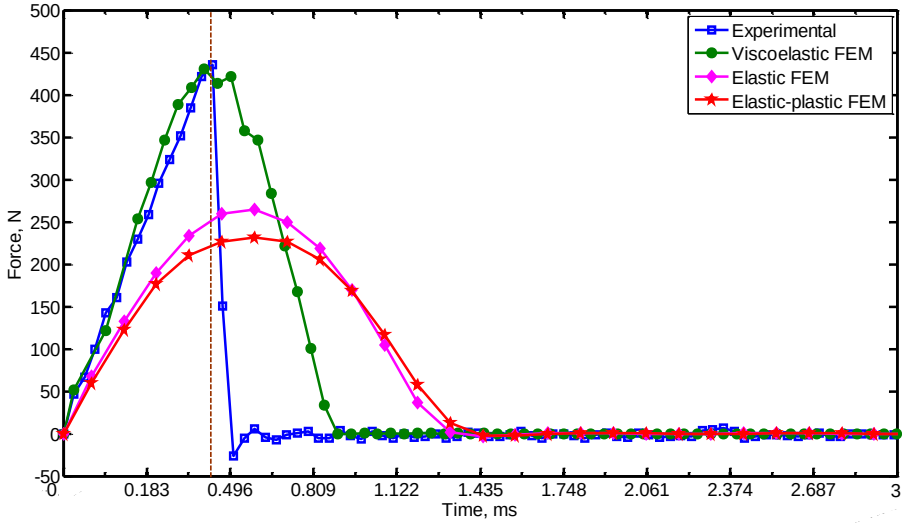

Figure 9.8: Comparison of experimental and FEM results for anterior cortex position for higher energy level of 0.5 J

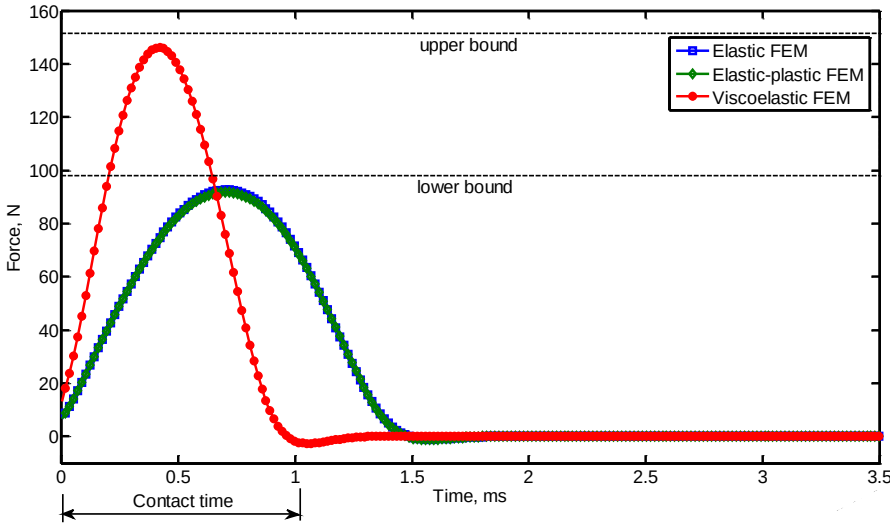

Figure 9.9: FEM results for anterior cortex position for lower energy level of 0.02 J (horizontal dashed lines represent bounds for experimentally measured values of maximum load)

The next step of our study was to analyse the effect of the constitutive model on the character of evolution of stresses and strains in the bone specimen exposed to dynamic loading. Distributions of the maximum principal stress in the vicinity of the notch tip obtained in the finite-element simulations for impact energy of 0.5 J for three different material models at the force's peak times (t = 0.43 ms for viscoelastic model and t = 0.59 ms for both linear-elastic and elastic-plastic models) are shown in Fig. 9.10. It was noticed that both linear-elastic and elastic-plastic models demonstrated a similar character of stress distribution, though with different magnitudes. In contrast, the viscoelastic model had a considerably different character of distribution, with an area of higher stresses occupying a significantly larger part of the specimen. For all the models, the highest maximum principal stress magnitude located at the notch's root, starting to decline ahead of the notch and forming nearly symmetric contours in the direct vicinity of the tip. Here, the finite-element models demonstrated the role of the notch as a stress raiser.

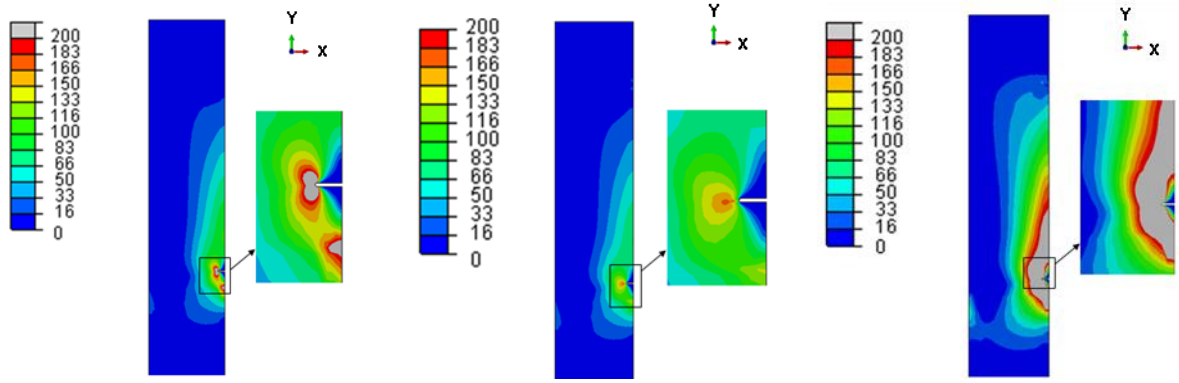

Figure 9.10: Distribution of maximum principal stress (in MPa) for linear-elastic FEM (a) elastic-plastic FEM (b) and viscoelastic FEM (c) at peak force time (t = 0.43 ms for viscoelastic model and t = 0.59 ms for both linear-elastic and elastic-plastic models) for higher energy level of 0.5 J

As discussed above, the linear-elastic and elastic-plastic constitutive models underestimated the maximum force magnitudes. Obviously, the magnitudes of stresses would differ respectively. All the three models produced a very high level of stresses near the notch tip, exceeding the strength of bone. Such high principal stress would cause crack initiation not accounted by the models.

The distributions of maximum principal strain for three constitutive models of anterior cortical bone at the force's peak time (t = 0.43 ms for viscoelastic model and t = 0.59 ms for both linear-elastic and elastic-plastic models) are presented in Fig. 9.11. Various material formulations produced different numerical results: the linear-elastic material model had the lowest maximum principal strain levels, while the elastic-plastic had the highest. Obviously, all three distributions have some common features, e.g. strain concentration near the notch tip. Since the attained level of stresses in that area exceeded the yield limit, the plastic formulation resulted in higher principal strain values ahead of the notch. Although the viscoelastic model had the highest principal stress value at the notch's root, its maximum principal strain was lower than that of the elastic-plastic model. This can be naturally explained by a short duration of high stresses insufficient for generation of a considerable magnitude of the viscous component of strain. Let's also note that the local shapes and magnitudes of maximum principal strain vary for different material models. In the elastic-plastic model, the area exceeded the yield limit was large and evolving ahead of the notch tip, while it was nearly symmetric and small around the notch tip for both linear-elastic and viscoelastic models.

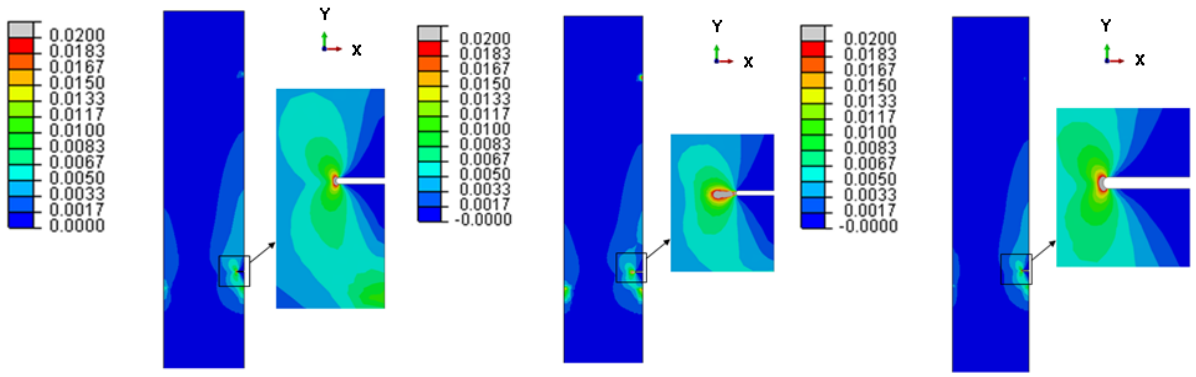

Figure 9.11: Distribution of maximum principal strain for linear-elastic FEM (a) elastic-plastic FEM (b) and viscoelastic FEM (c) at peak force time (t = 0.43 ms for viscoelastic model and t = 0.59 ms for both linear-elastic and elastic-plastic models) for higher energy level of 0.5 J

In this part of simulations, the applicability of three different material formulations for Model A, was examined using transient finite-element simulations to investigate the behaviour of cortical bone tissue under impact loading. The simulation results for

the viscoelastic constitutive material model showed good agreement with the experimental data. The force's peak magnitude and time as well as the character of force evolution in experiments and simulations were similar. Hence, these results show the ability of the finite-element model to capture and predict the processes occurring during impact loading before fracture, and highlight the profound role of viscoelasticity of bone in dynamic events such as impact.

Now, a crack-propagation path using X-FEM implementation can be employed to study whether Models A, B and C can capture correctly the main feature of the real crack's growth process, and to emphasize the adequacy of the advanced approach to reproduce the crack path in cortical bone exposed to dynamic loading. Below, results of simulations with Models A, B and C – using X-FEM – of the fracture behaviour of cortical bone tissue under impact and quasi-static loading are presented in comparison with experimental data. The contact-force profile obtained in our Izod tests of cortical-bone specimens was used to validate the developed finite-element Models A and B. A comparison of the experimental results with simulation ones (Fig. 9.12) demonstrates that Model A reproduces transient fracture behaviour of the cortical bone tissue. However, Model B, though showing a good agreement both with Model A and the experimental results until its termination point, results in an unrealistic fracture scenario afterwards as will be discussed below. The dynamic nature of the imposed load induced the oscillations in the response for both Model B and experimental data. Some deviations from the experimental results can be linked to different factors that are not incorporated into the current stage of model development. Among them are a complex hierarchical structure, anisotropy, and heterogeneity of the cortical bone tissue contributing to its fracture behaviour. As a consequence of composition and microstructure, there are several experimentally observed toughening mechanisms in the fracture process of cortical bone tissue, such as diffuse microcracking, crack deflection and fibre bridging [225, 226, 228] that can affect propagation of the crack.

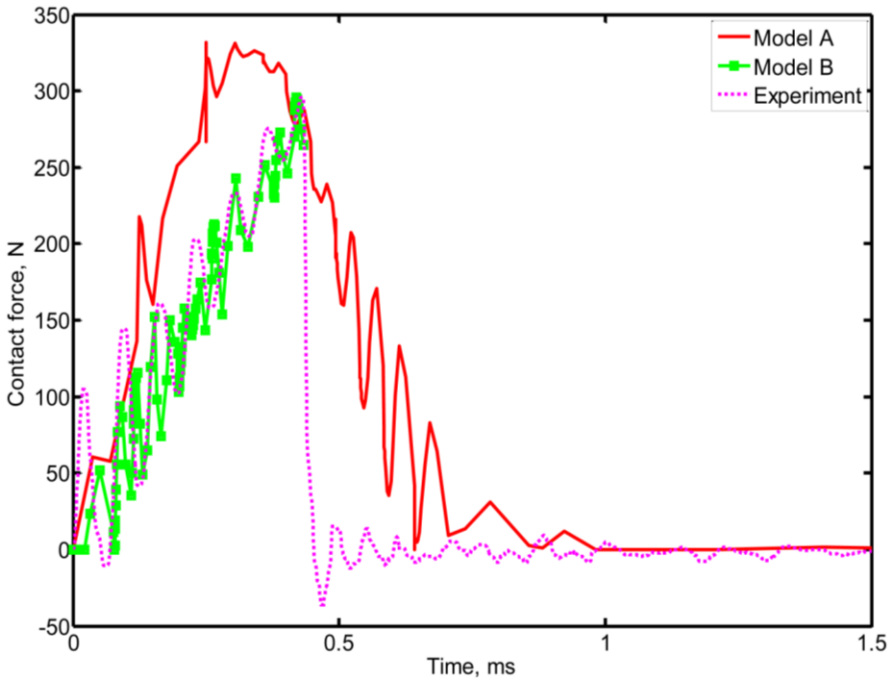

Figure 9.12: Comparison of evolution of contact force in impact loading (notch size 300 μm)

It was also noticed that the cortical bone specimen failed in tests catastrophically in a brittle manner as soon as the maximum force was reached; it is presented by a nearly vertical line in Fig. 9.12 after the peak. In the simulation results of Model A, see Fig. 9.13, specimen's fracture is represented in terms of a normalized crack length ($L_{cr}/(W - L_{notch})$) against time. It was calculated as the length of the crack (L_{cr}) divided by the un-notched width ($W - L_{notch}$) measured on the specimen's surface. At the beginning, the crack started to evolve slowly up to approximately 10% of this width at t = 0.2 ms, then grew steeply up to the moment of contact force's peak (331.3 N at t = 0.36 ms), at which only 30% of the specimen failed. However, even when the force started to decline; it was still high enough to propagate the crack. The crack growth accelerated after the maximum force position up to the specimen's failure point, with the crack spending only 0.28 ms to reach the opposite side of the specimen. Obviously, at the moment of complete failure of the specimen the contact force vanished. For Model A, the STATUSXFEM output - available in Abaqus 6.10 - shows the crack evolution during the course of analysis. This parameter varies over the range between 0 and 1; when it equals to 0 there is no damage, and in the case of complete failure, it

equals to 1. Figure 9.14 shows the evolution of the crack originating from the notch and propagating across the width of the specimen towards the opposite side.

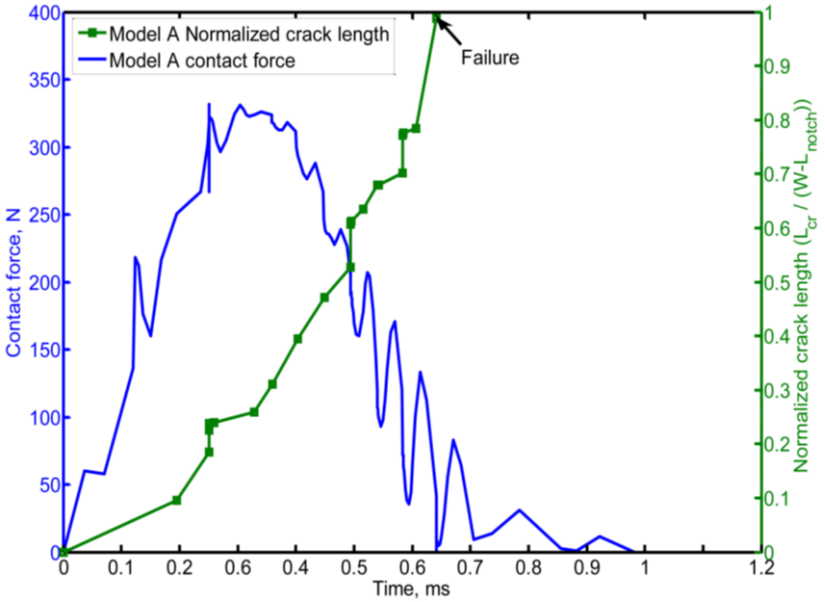

Figure 9.13: Evolution of contact force and normalized crack length in Model A (notch size 300 μm)

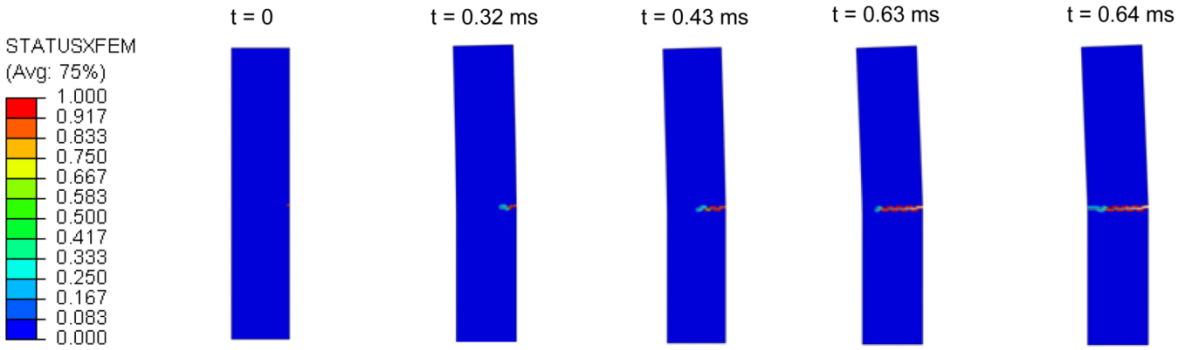

Figure 9.14: Crack evolution at different time increments (Model A)

It was noticed that the crack started to propagate immediately along an inclined plane, with the notch root indicating the mixed-mode fracture behaviour (Mode I and Mode II). That was followed by a small horizontal crack path. These changes in the crack path direction correspond to kinks in the first part of the contact force-time curve up to the contact-force's peak, see Fig. 9.13. Obviously, from the point of view of the beam theory, the studied cantilever beam is exposed to two types of stresses: normal stress (bending) and transverse shear stress. In these models, the beam's span-to-width ratio is 2.2; so the transverse shear stresses should be significant. It was found that the shear stress level was comparable to that of normal ones (Figs. 9.15 and 9.16). Also, a transverse distribution of shear stress is parabolic across the

width of the cantilever and uniform from the position of specimen-hammer interaction up to the notch location, see Fig. 9.15. This stress state causes Mode-II fracture. On the other hand, normal stress S_{22} in y-direction causes Mode-I fracture behaviour. Therefore, immediately after the impact takes place and at the notch root, only Mode-I fracture took place due to vanishing (or very small) shear stresses. At the neutral plane of the cantilever, where the shear stress has its peak while the bending stress vanishes, Mode II dominates fracture. The opposite side of the beam was under compression, with shear stress vanishing. Thus, between the notch side and the opposite side and the neutral plane, both Modes I and II took place. When the crack started to propagate, it caused stresses redistribution that resulted in a complex crack path; this can be seen in Fig. 9.17.

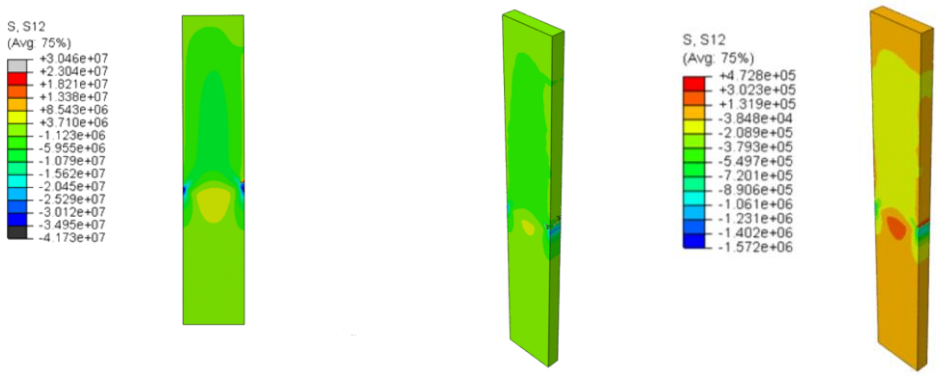

Figure 9.15: Distribution of shear stresses S_{12} in Model A (a), Model B (b) and Model C (c); t = 0.6 ms

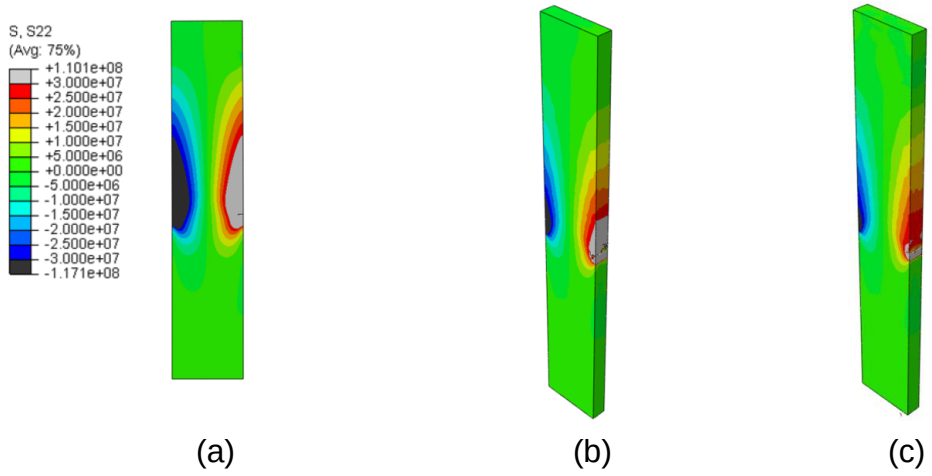

Figure 9.16: Distribution of normal stresses S_{22} in Model A (a), Model B (b) and Model C (c); t = 0.6 ms

While both Models A and C showed one main crack that originated from the notch and propagated in the depth and width of the specimen towards the opposite face (Figs. 9.17a and c), Model B demonstrated a band of random short cracks around the notched area of the specimen with no major crack percolating the specimen. In this model, due to the impact load suddenly applied to the specimen, elastic stress waves were generated, propagating in different directions in the specimen, activating all fracture modes and initiating multiple cracks. As elastic waves keep moving and reflecting in a complex way inside the specimen, a band of damaged zone was formed instead of a single crack, demonstrating limitations of the current 3D X-FEM routine of Abaqus 6.10 with respect to dynamic cracking problems (Fig. 9.17b). On the other hand, in Model C, a single crack propagated from the root of the notch to the opposite side of the specimen. That crack path was similar to that observed in the experiment, see Fig. 9.17d. Still, the effect of underlying microstructure, such as weak interfaces – cement lines – between osteons and the interstitial matrix that can deflect the crack [228], can be responsible for some deviations from the solution obtained with an isotropic homogeneous formulation.

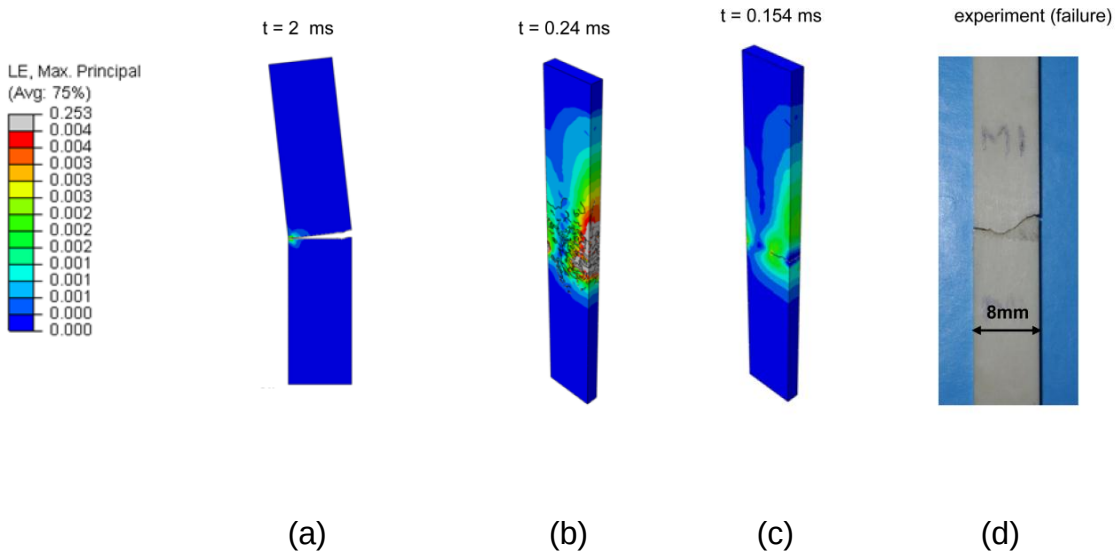

Figure 9.17: Distributions of maximum principal strain in Model A (a), Model B (b) and Model C (c). (d) Final crack path in Izod-test specimen

Damage initiation and evolution behaviours for Models A and C are shown in Fig. 9.18. In this figure, the linear component of displacement in x-direction at the contact position is obtained from Abaqus and used as an external parameter for the

axis of abscissas. Apparently, damage started immediately as the beam was subjected to the load. In addition, at the same deformation level the crack length in Model C was larger than that in Model A. It is worth recalling that a linear elastic material model was assigned to the quasi-static model (Model C), whereas a viscoelastic material model was used in the impact models (Models A and B). Hence, different behaviours could be due to activated relaxation mechanisms that assisted to dampen some of the applied energy of the hammer and resulted in differences between two results. However, at the beginning (up to a displacement level of 0.15 mm) both cases are close; at this stage both models still behave elastically. Apparently, the current 3D X-FEM routine in Abaqus 6.10 causes some convergence problems even in quasi-static formulations: simulations with Model C terminated before the crack reached the opposite side (at the normalized length of about 0.75 (Fig. 9.18). Model A did not demonstrate such a problem. Analysis of a through-thickness variation in crack length for Model C, demonstrated that its front had a non-uniform character (Fig. 9.19), changing with displacement. Due to a stress state varying across the thickness, the crack propagated with a different rate at various positions along its front.

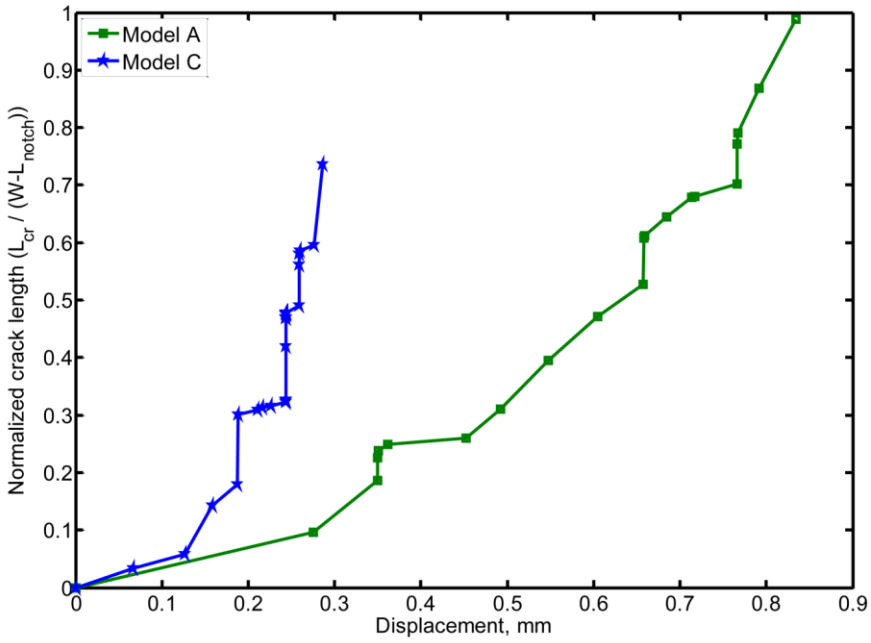

Figure 9.18: Evolutions of crack length for Models A and C

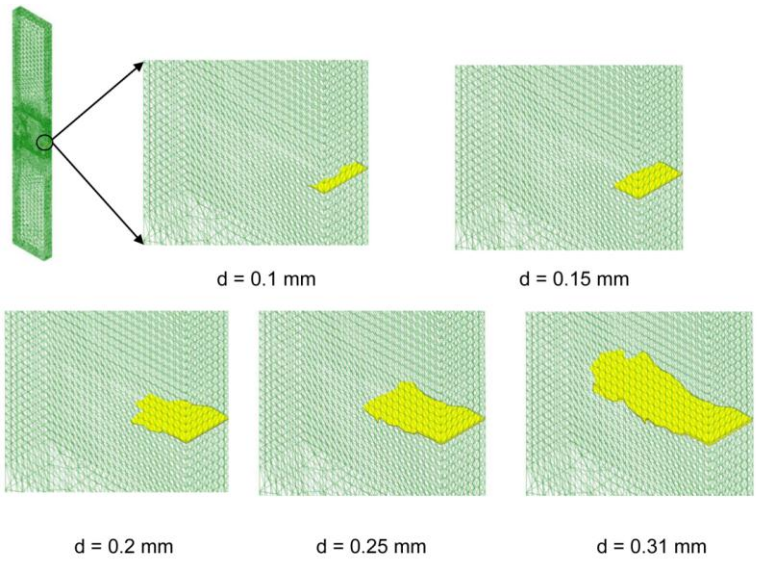

Figure 9.19: Crack length variation along its front in Model C

A direct measurement of crack length as function of time and/or deformation is not available in Abaqus 6.10; therefore, various images at different time increments were taken and measured using Image Pro-Express software [216]. The crack growth rate for Model A was obtained by differentiation of the curve-fit equation for the crack length; Figure 9.20 shows both parameters as a function of time. Since the crack length has a quadratic curve-fit equation, the crack growth rate shows a linear increase with time. At t = 0 the specimen was exposed to a sudden impact with the hammer with initial velocity of 1.74 m/s, causing an initial crack propagating rate of 2.054 m/s. This rate has evolved during the fracture process to reach 19.5 m/s at the final percolation of the specimen.

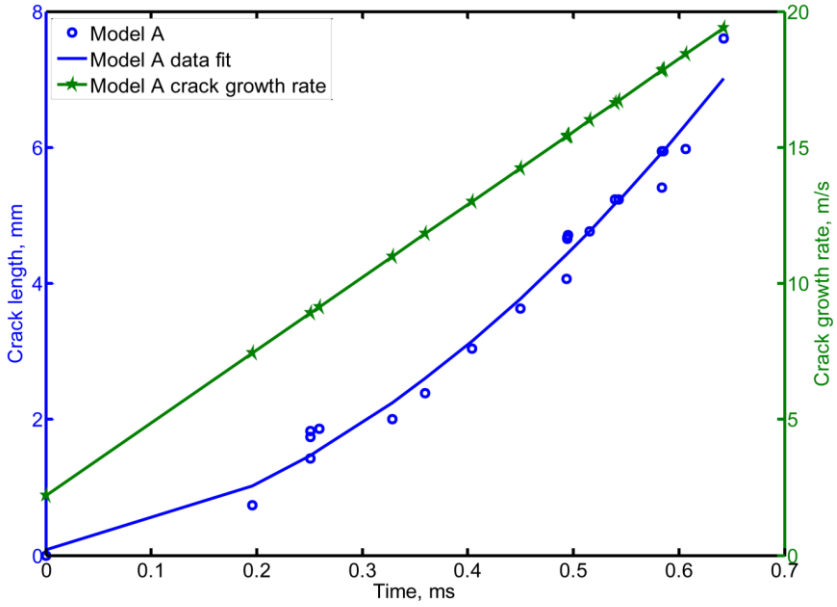

Figure 9.20: Evolution of crack length and crack growth rate in Model A

It is obvious that to study a bone *in-vivo*, embedded in a composite system of muscles and ligaments, it is necessary to develop larger models, directly incorporating other tissues. Still, the developed approach is important for elucidating the main deformation and failure mechanisms in bones exposed to dynamic loading.

9.4.2. Tensile-Impact Numerical Model

In this section, simulation results of three different 3D models are presented: Models D, E and F. Model D aimed at verifying the developed 3D tensile-impact model using aluminium-alloy material. Based on this verified model, the cortical-bone material along with employing the X-FEM tool were implemented into Model E to investigate the deformation and fracture behaviour of this tissue under impact loading conditions. On the other hand, Model F was developed on the basis of the 3D quasi-static, cortical bone material and X-FEM implementation to compare its behaviour with the dynamic one – Model E.

For Model D, the predicted and experimental impact-force profiles were used as the basis of the model verification. A comparison of the experimental and simulation results (Fig. 9.21) demonstrates that Model D reproduces the transient response of the aluminium alloy.

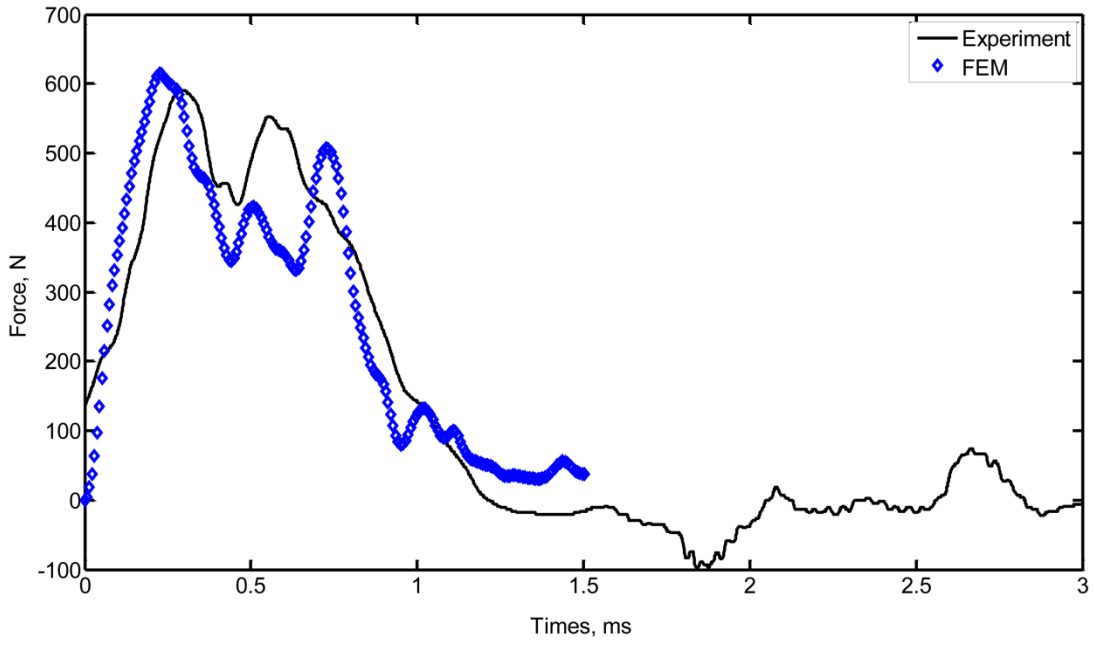

Figure 9.21: Comparison of evolution of contact force in tensile-impact loading using aluminium-alloy material model without X-FEM – Model D

In Model D, the simulations time was set to 1.5 ms to reproduce only the specimen-hammer interaction. During that period, the model emulated the experiment in terms of the trend, force amplitude and contact time with insignificant errors. Due to the dynamic nature of the imposed load along with plasticity of the aluminium alloy, both the model and the experiment revealed some oscillations in the response. Part of these oscillations could also be due to the vertical movement (*y*-axis) between the impacting mass of the hammer and traction terminal (Fig. 9.5). The next step of the simulations was to use the verified model to study the transient deformation and fracture behaviour of the cortical bone tissue using X-FEM. For Model E, Figure 9.22 shows a comparison between the predicted and experimental impact force-time profiles for cortical bone tissue under impact loading. Still, the response exhibits some oscillations due to the dynamic nature of imposed loading and the movement between the impacting elements.

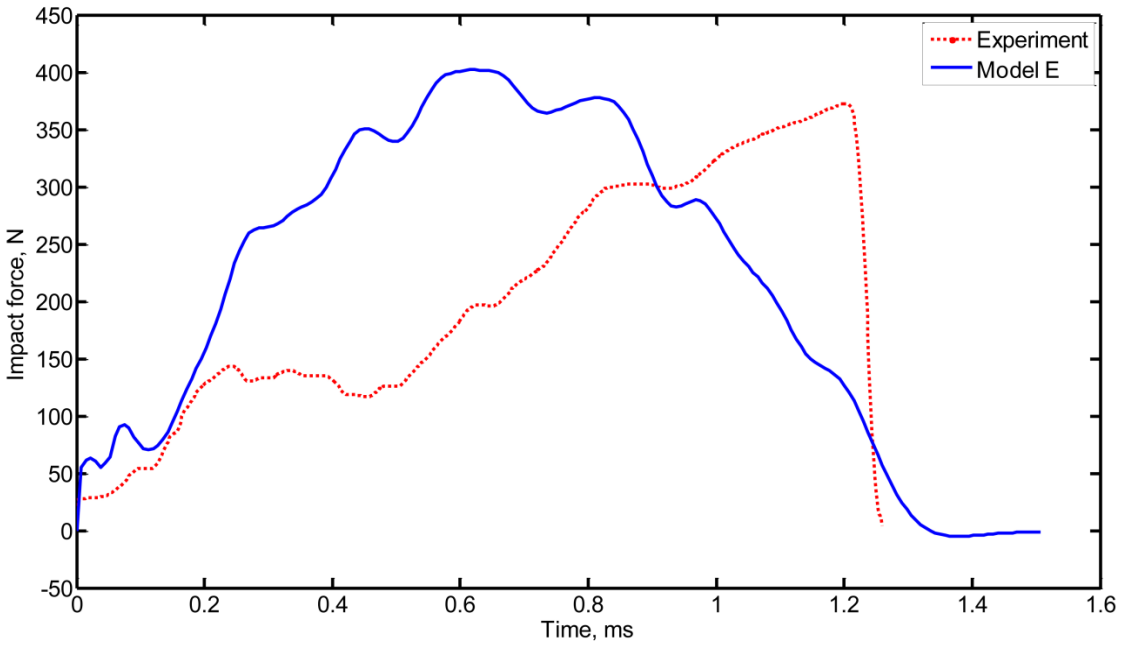

Figure 9.22: Comparison of evolution of impact force for Model E and experiment

In Figure 9.22, it can be observed that the predicted response is approximately symmetric with no sudden decrease in the impact force amplitude as in the experiment that indicates the specimen's failure. In general, it is obvious that there is a deviation between the predicted impact force profile of the model and the experimental one. Having verified the model based on the impact loading using a standard material, the reason for this variation can be linked to the fracture behaviour using the X-FEM technique. In order to expose the reasons behind this

deviation, the final crack path within the bone specimen was investigated. By examining the crack path, a band of random short cracks around the side notches was observed with no main crack penetrating the specimen (Fig. 9.23). This indicates that the specimen did not fail and the crack propagation criterion was not activated, but the existence of several short cracks is a clear evidence of the crack initiation criterion was met. This situation needs additional investigations.

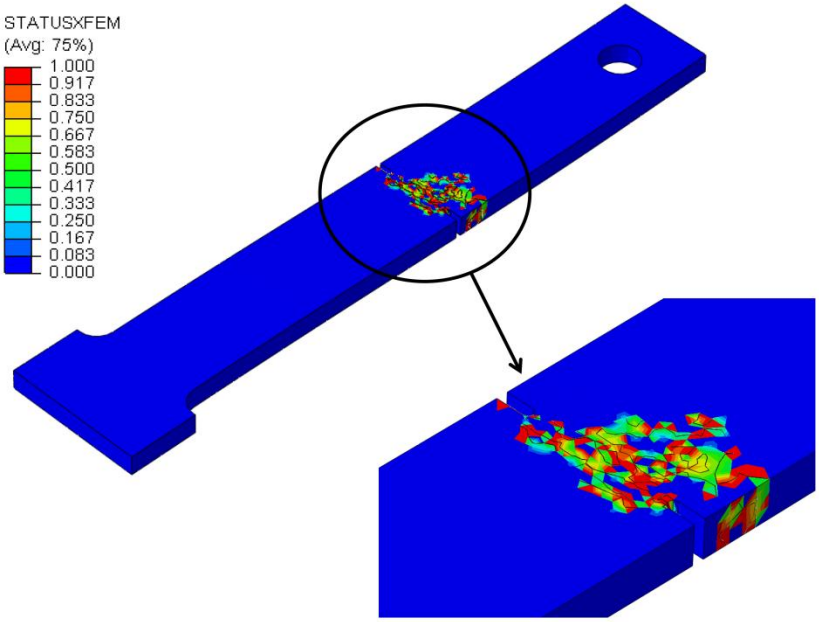

Figure 9.23: X-FEM status for cortical bone specimen during tensile-impact loading. When STATUSXFEM = 1 for complete element failure; no failure for STATUSXFEM = 0

Hence, the distributions of the maximum principal stress within the bone specimen at different moments were inspected (Fig. 9.24). Generally, it was observed from these distributions over several time increments that due to the sudden imposing of the load, elastic stress-waves were generated and propagated in different directions in the specimen, and those stress waves produced accompanied strain waves. Figure 9.25 shows the distributions of the maximum principal strain in the bone specimen. The interaction between the randomly moving stress waves within the specimen generated a maximum principal strain that was able to activate the crack initiation together with the side notches that worked as stress raiser. This is apparent in Figs. 9.24 and 9.25 at t = 0.016 ms, when the first stress wave arrived near the side notches, activating the crack initiation criterion and generating short cracks. Also, it can be observed from these figures that the stress and strain waves

kept moving forward and backward in the specimen activating more cracks every time they passed by the side notches.

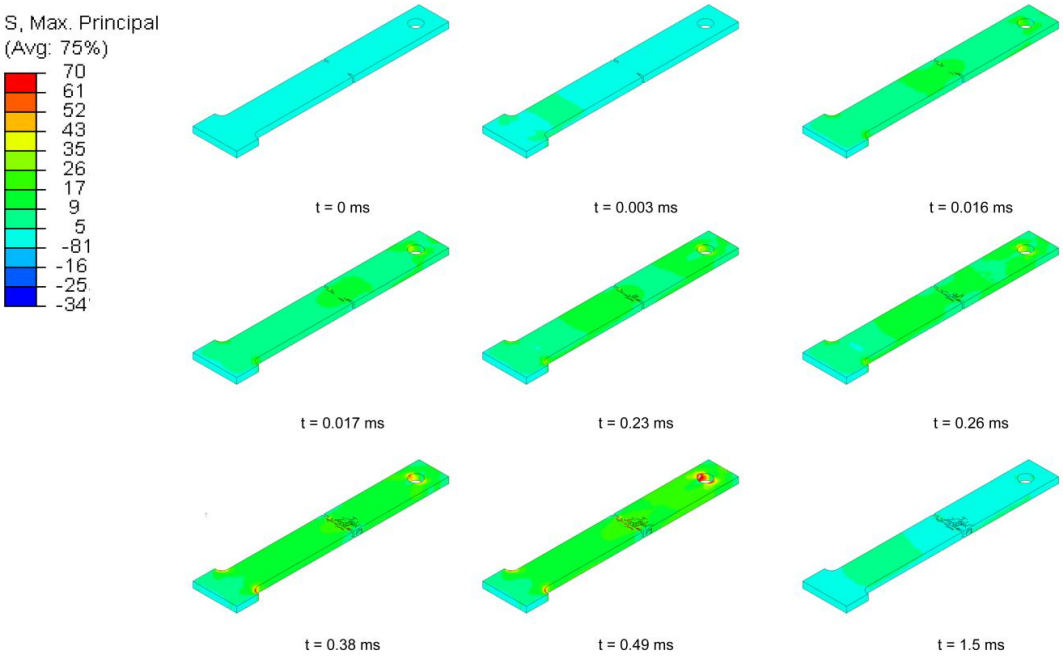

Figure 9.24: Maximum principal stress distribution at different time increments (Model E); stress units in MPa

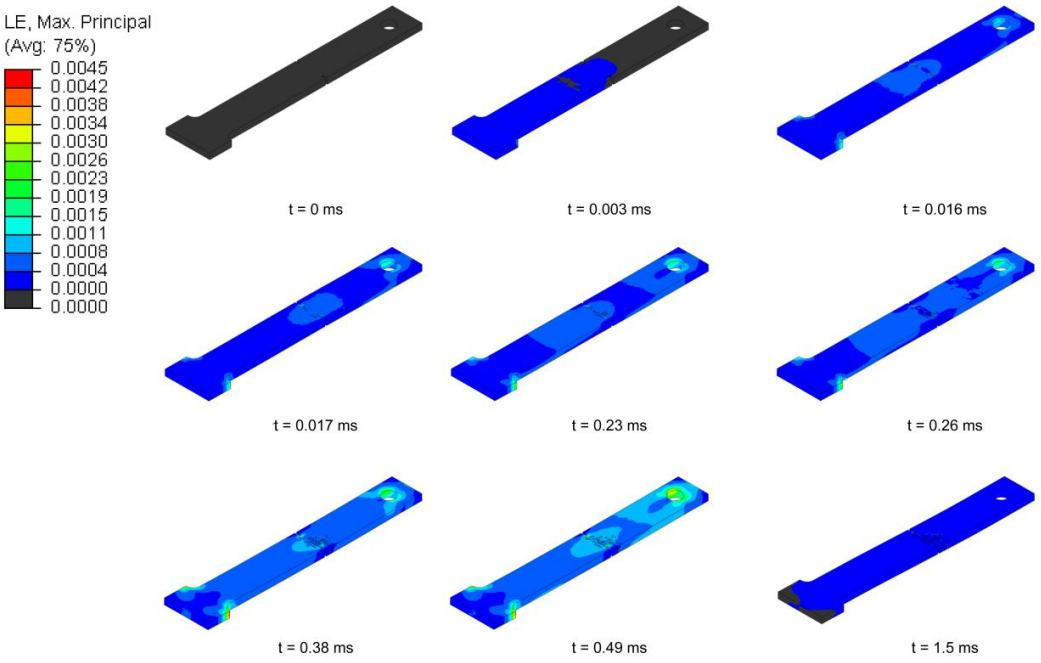

Figure 9.25: Maximum principal strain distribution at different time increments (Model E)

At this point, to gain a better understanding of the fracture behaviour of the cortical bone tissue under various loading conditions, a 3D quasi-static model (Model F) was introduced. The simulation results exhibited a single crack propagating from one side notch to another in the specimen (Fig. 9.26). By imposing a quasi-static load on the same specimen, the crack smoothly started to propagate without any random short cracks formed. By investigating the 3D transparent view of the cracked specimen, it was observed that the through-thickness crack length changed non-uniformly with the displacement. This is due to a stress state varying across the thickness; the crack propagated with a different rate at various positions along its front.

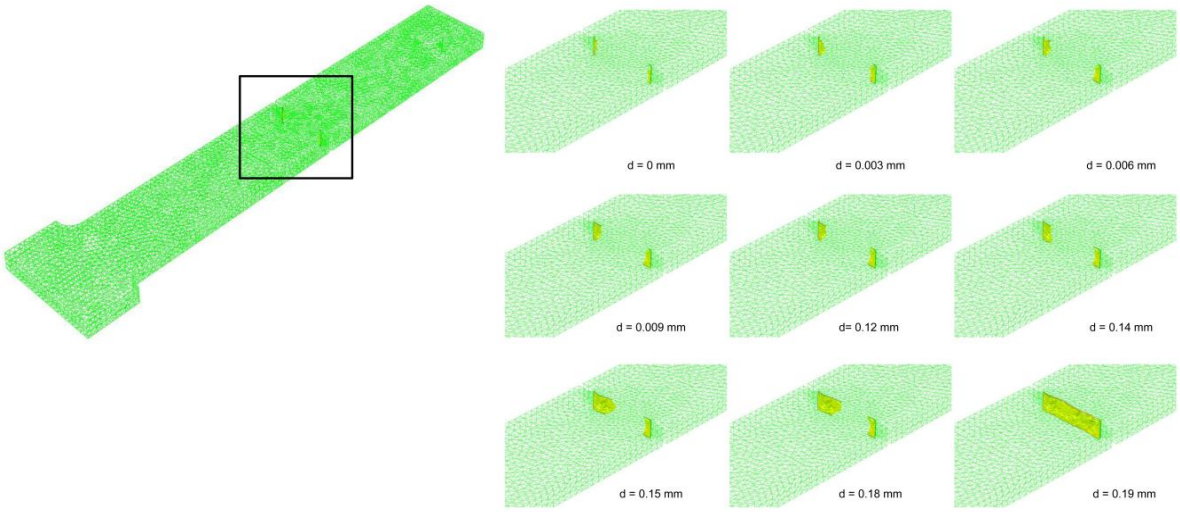

Figure 9.26: Crack length variation along its front in Model F

9.5. Conclusions

Though instrumented impact tests provide useful experimental data, such as impact strength and fracture force, they cannot offer other important results, such as stress and strain distributions, crack length variation with deformation or distinction between ranges of material model behaviours; finite-element simulations can provide such data and more information about the process. Therefore, various finite-element models were developed for Izod and tensile-impact tests setups to study the transient dynamic and quasi-static behaviours of cortical bone tissue. At first, by employing the Izod test setup, three different 2D impact models were used to examine the applicability of different constitutive material models for analysis of

the behaviour of cortical bone tissue under impact loading. The obtained simulation results demonstrated that the viscoelastic constitutive material predicts successfully the behaviour of bovine femoral cortical bone under impact loading. Linear-elastic and elastic-plastic constitutive material models underestimate the response of bone specimens to impact loading. Thus, a combination of viscoelastic constitutive material model and X-FEM approach was used to analyse the onset of cracking and crack propagation under dynamic loading conditions. Following the results of the 2D impact Izod finite-element approach, a 3D formulation of the impact Izod test was developed in addition to a 3D quasi-static model. Crack initiation and growth under quasi-static and impact loading of the cortical bone tissue were studied using 3D numerical simulations. Finally, for the tensile-impact test setup, three different models were developed to validate the 3D dynamic model and to study the crack initiation and propagation scenarios under impact and quasi-static loading regimes.

Based on the obtained results from the numerical studies for the Izod test setup the following conclusions can be formulated:

- The obtained numerical results were quite close to the experimental ones, and the numerical models have the capability to reproduce the failure of cortical bone tissue under both impact and quasi-static loading.
- The finite-element results provide more detailed information than the experimental tests and helped to gain a better understanding of the fracture behaviour of cortical bone tissue.
- An elastic-plastic cortical bone material model underestimated the force magnitude – by 46.7% for its maximum magnitude; also, the calculated force peak led the experimental peak by 0.16 ms (i.e. some 37%). Similarly, the results of simulations based on linear-elastic material model underestimated the level of force (39.2% lower for the maximum value), and, similar to the elastic-plastic material model, its force peak value led the experimental peak by 0.16 ms. Those results indicate that both linear-elastic and elastic-plastic material models are incapable to correctly capture the response of the cortical bone tissue under impact load.

- The viscoelastic material model provided a good agreement with the observed experimental data for the period of interaction between the hammer and specimen in the Izod test.
- Finite-element simulations demonstrated that the magnitude of the highest maximum principal stress located at the notch's root, starting to decline ahead of the notch and forming nearly symmetric contours in the direct vicinity of the tip. This affirms the role of the notch as a stress raiser.
- Numerical simulations showed that the bone tissue's fracture behaviour was reasonably well predicted using the 2D formulation in terms of the contact force profile and the crack path, while the 3D formulation exhibited unrealistic fracture scenario: formation of a damage band with multiple cracks across the specimen's width and thickness around the notch.
- The dynamic nature of the imposed load induced oscillations in the response for both numerical and experimental data.
- Distributions of normal and shear stress revealed that Modes I and II took place within the Izod test specimen. Also, when the crack started to propagate, it caused stresses redistribution resulting in a complex crack path.
- While both models of 2D impact Izod test and 3D quasi-static loading showed one main crack that originated from the notch and propagated in the depth and width of the specimen towards the opposite face, the model of 3D impact Izod test demonstrated a band of random short cracks around the notched area of the specimen with no major crack percolating the specimen. This was pertained to the elastic stress waves generated that propagated in different directions in the specimen and activated all fracture modes, initiating multiple cracks. As elastic waves kept moving, reflecting in a complex way inside the specimen, a band of damaged zone was formed instead of a single crack, demonstrating limitations of the current 3D X-FEM routine of Abaqus 6.10 with respect to dynamic cracking problems.
- For the 2D impact Izod model, the crack length has a quadratic curve-fit equation; the crack growth rate shows a linear increase with time.

Based on the obtained results from the numerical studies for the tensile-impact test setup the following conclusions can be formulated:

- The 3D tensile-impact finite-element model for the aluminium-alloy material predicted closely the experimental behaviour and showed that the model had the capability to reproduce the impact transient behaviour under tensile-impact loading conditions.
- This finite-element model demonstrated a band of random short cracks around the side notches of the specimen with no major crack percolating the specimen. With more investigations using the maximum principal stress and strain distributions at several time increments, it was observed that elastic stress waves were generated and propagated in different directions in the specimen. The interaction between the randomly moving stress waves within the specimen produced a maximum principal strain that was able to activate the crack initiation process near the side notches that worked as stress raisers. A damaged zone was formed instead of a single crack, demonstrating once more the limitations of the current 3D X-FEM routine of Abaqus 6.10 with respect to dynamic cracking problems. More evidence was introduced by investigating the 3D quasi-static model of bone that showed one single crack from one side notch to another.

10. Chapter 10

Conclusions and Future Work

10.1. Conclusions

The skeletal system is made up of individual bones and the connective tissue that joins them. Bone is the principal structural component of a skeleton: it assists the load-bearing framework of a living body. Unfortunately, bone can bear only certain levels of loading and it fails when loaded beyond those levels. Bone fracture is an internationally known problem with immense social and economic consequences. Over the last few decades, with bone fractures attracting many researchers and a body of research into its deformation and fracture being available in literature, still, the mechanisms behind bone fracture have not been entirely understood. In fact, some actions can prevent such fracture but it cannot be fully avoided. However, we still need to comprehend bone failure to be able to deal with it. The roots of the bone- fracture problem were explored and a conclusion was made that the majority of bone fractures were mainly due to impact loading accompanied with different circumstances. Such circumstances could be unavoidable in someone's life, such as sports injuries, traumatic falls and involvement in car crash. And, no matter whether the bone is young or old, healthy or diseased; it fails, when it is exposed to impact loading that generates stresses beyond its strength. Obviously, a fracture event occurs initially at the material level that eventually affects the load-carrying capacity of the whole bone at its structural level [22]. In this sense, the current study was mainly aimed at studying the deformation and fracture behaviours of a cortical bone tissue under impact loading. This aim was achieved by conducting a critical literature review followed by experimental and numerical studies. Several types of experiments were performed in order to quantify mechanical properties of the cortical bone tissue at macro- and micro-scale levels and under quasi-static and dynamic loading regimes for different cortex positions. Those experiments were carried out for two purposes: (1) to characterise its mechanical properties in order to develop finite-element models to simulate the deformation and fracture of cortical bone tissue at different length scales and loading circumstances; (2) to investigate

the link between its mechanical properties and different cortex positions with various microstructures. Based on the results of those experiments, a number of finite-element models were developed in order to analyse deformation and fracture of cortical bone using X-FEM. Among those models are (i) 2D FE models used to simulate its fracture and deformation at microscale level under quasi-static tensile loading, (ii) 2D and 3D FE models for analysis of its fracture and deformation at macroscale level for the Izod impact test setup, and (iii) 3D FE model used to simulate fracture and deformation at macroscale level under tensile-impact loading conditions. The developed models provided high-quality results, and most, importantly, they adequately reflected the experimental data. Following the objectives of this study (see chapter 1), the PhD research has brought the results described below.

10.1.1. Experimentation

Macroscale Mechanical Properties

Direct measurements of the macroscopic mechanical properties of cortical bone tissue were performed in order to analyse its spatial variability and to develop finite-element models capable of reproducing experimental results obtained under quasi-static and dynamic loading conditions. The undertaken experimental studies include the characterisation of elastic–plastic behaviour as well as viscoelastic properties using creep tests for different cortex positions. The experiments resulted in the following conclusions:

- Microstructural features of the cortical bone tissue play an important role in its elastic-plastic behaviour. In general, bone specimens with lamellar microstructure (e.g. anterior, medial and lateral specimens) maintained higher properties compared to those containing secondary osteons (e.g. posterior specimens).
- Uniaxial tension tests revealed an inelastic behaviour for specimens cut from different cortex positions along the bone axis and perpendicular to it. Also, for all cortex positions and directions, a bi-linear hardening behaviour after yielding was shown with different failure strains ranging between 0.71% and 1.18%.

- The average values of the elastic modulus for all cortex positions measured along the bone axis were in the range of 12 – 21 GPa. On the other hand, the average values of respective parameter measured perpendicular to the bone axis were in the range of 10 – 14 GPa. All the obtained data are within the range for cortical bone tissue's moduli, accepted in the literature, suggested as 6-24 GPa in [61, 153].
- Low anisotropy ratios were observed for the longitudinal and transverse directions of the bovine cortical bone tissue with magnitudes ranging between 1.2 and 2; the anterior specimens had the ratios close to those of lateral ones, while the medial position was closer to the posterior one in this respect.
- Specimens cut from anterior, medial and lateral demonstrated similar pre- and post-yield properties, such as elastic modulus, stress at fracture and strain at fracture, while posterior specimens were weaker. The distribution of voids and defects in the specimen, such as Haversian canals, canaliculi, resorption cavities led to variation in both stress and strain values at failure.
- Different values of the Poisson's ratios obtained for different cortex positions are linked to its underlying microstructure. The difference between the Poisson's ratios for specimens cut from anterior, medial and lateral in the longitudinal direction was small, while it was negligible in the transverse direction. For all cortex positions and directions, the Poisson's ratios in the range between 0.26 and 0.55 were found.
- The bovine cortical bone tissue in the longitudinal directions started to creep when the stress level greater than 45 MPa was applied. Mechanisms, such as viscous motion of cement lines, boundaries between lamellae and osteons, and fluid flow in porous media can contribute to cortical bone viscoelasticity.
- In the stress range of 45 MPa to 60 MPa, the cortical bone tissue demonstrated linear-viscoelastic behaviour; therefore, its response can be represented by mechanical models that include a number of springs and dashpots. These mechanical models can be represented mathematically by the Prony series. When comparing the isochronous curves and parameters

of the Prony series for different cortex positions, insignificant difference was found.

Microscale Mechanical Properties

In order to develop finite-element models to analyse the deformation and failure behaviours of the cortical bone tissue at its microstructural level, it was crucial to quantify the elastic-plastic behaviour of its microscopic features. A spherical nanoindentation tests were performed to study the mechanical behaviour of microstructural constituents of the cortical bone tissue – osteons and interstitial matrix. Also, topological analysis of a transverse-radial section cut from the posterior cortex position was performed to obtain statistical data to develop microstructured finite-element models. The performed tests resulted in the following observations:

- The nanoindentation results demonstrated higher stiffness values for the interstitial matrix compared to those of the osteons. The difference is related to the heterogeneous nature of cortical bone due to continuous remodelling processes that result in a gradient in the mineral content.
- Nanoindentation results obtained at a maximum load of 50 mN, loading rate of 0.5 mN/s and delay time of 120 s produced, employing the rule of mixture, an effective elastic modulus consistent with results of the uniaxial tension test for the same cortex position.
- The osteons and interstitial matrix demonstrated higher indentation depths indicating the viscoelastic nature of the cortical bone tissue at the microscopic level when the indenter was hold for 120 s.
- Elastic moduli increased with the increase in the loading rate for both osteons and interstitial matrix for the time delays of 0 s and 120 s.
- Values of the elastic modulus were higher for the interstitial matrix compared to the osteons for all the loading-unloading rates, 0.5 mN/s, 1 mN/s and 2 mN/s, and for the time delays, 0 s and 120 s.
- A higher post-yield behaviour of the interstitial matrix compared to that of the osteons reflects the relationship between the post-yield behaviour and collagen maturity.

- The effect of viscoelasticity on the nanoindentation results was reduced by using the time-delay method.
- The obtained elastic-plastic behaviour of the cortical bone tissue's microstructural constituents was fed into the developed finite-element models to study microstructural processes of deformation and fracture.
- The random distribution of diameters of osteons and Haversian canals was fitted with the hypersecant and Dagum (4P) distribution curves, respectively. Those curves underpin the development of microscale finite-element models.

Dynamic Mechanical Properties

In order to investigate the variability of transient dynamic behaviours of longitudinal cortical bone specimens, experimental tests were performed with two different loading regimes using Izod and tensile-impact setups. Two central parameters were studied: fracture force and absorbed energy (impact strength). Also, a fractographic study of bone fracture surfaces was carried out in order to gain adequate knowledge of its fracture mechanisms. Based on the obtained results the following conclusions can be formulated:

- The bovine femoral cortical bone tissue has a nearly uniform character of recovered and fracture energy for different cortex positions and is not sensitive to the notch depth within the physiological pertinent range.
- The studied tissue demonstrated a low variability of the fracture force for specimens with the notch depths of less than 600 μm.
- Impacts with a low-energy level of 0.02 J did not activate any damage or plasticity mechanisms in the bovine femoral cortical bone tissue.
- In the case of low-energy impacts, some 80% of the impact energy was recovered by specimens cut from different cortex positions.
- Impact with a higher energy level of 0.5 J showed a negative correlation between both of fracture force and impact strength and the notch size.
- The average impact strength required to produce fracture using the Izod-test setup for all cortex positions and notch depths was within the interval from 6 kJ/m^2 to 12 kJ/m^2.

- Variations in the underlying microstructure with different spatial positions explained the variability of fracture force and impact strength of bending and tension loading regimes.
- Cleavage-type fracture ahead of the notch and shear failure away from it were dominant in Izod-test specimens.
- Side notches amplified the nominal stress and strain and led to failure in tensile-impact tests.
- Specimens with lamellar microstructure sustained higher levels of absorbed energy and fracture forces compared to those with secondary osteons.
- A higher fraction of cavity area, over mineralization and a weak interface between osteons and interstitial matrix are possible reasons for weakness of Haversian bone in impact tests.
- The specimens in the tensile-impact setup were exposed to a strain rate of 28.6 s^{-1}, which is relevant to bone failure during traumatic events.
- Cracks in specimens followed paths of lower shear strength and were affected by underlying microstructure in Tensile-impact tests.
- The ratios between the average quasi-static and dynamic ultimate stresses measured were 2.2, 2.7, 2.1 and 2.1 for specimens cut from anterior, posterior, medial and lateral cortex positions, respectively.
- The average impact strength required to produce fracture using the tensile-impact setup for all cortex positions and notch depths was within the interval from 5 kJ/m^2 to 12.25 kJ/m^2.
- Fractographic studies of fracture surfaces of the cortical bone tissue highlighted the necessity of both macro- and microscopic numerical models to study its fracture micromechanics.
- The crucial role of micromechanics to understand fracture of bone was emphasized.

10.1.2. Simulations

Microscale Finite-Element Models

Following the emphasis of fractographic studies of the central role of micromechanics to comprehend the fracture phenomenon of cortical bone tissue,

three different finite-element models were developed and implemented to study the effect of cement lines on microcracks growth trajectories and the global behaviour of the osteonal cortical bone tissue. These features were studied with a four-phase composite model directly incorporating cement lines. The obtained results were compared to those of two other models: a three-phase composite model without cement line and a model of a homogenised material. Based on the results obtained in numerical simulations the following conclusions can be formulated:

- Dissimilar global stress–strain behaviours were observed in the studied models, the homogeneous material-based model revealed softening immediately after a crack started to propagate, while the implementation of a heterogeneous material in the three- and four-phase composite material models resulted in a non-softening behaviour.
- An account for cement lines in the model demanded higher levels of stress and strain for growth of microcracks.
- The final state of the four-phase composite model was not a percolation in the cell but rather arrest of the microcracks either at a void or a cement line.
- A significant difference between the total microcrack lengths at the fracture point was observed for the homogeneous model and the microstructural ones.
- The homogeneous model had the lowest final fracture stress and strain; the three-phase composite model had the highest values, while the cement lines arrested the crack propagation in the four-phase composite model.
- The relationship between the total length of microcracks and deformation highlights the role of the cement lines to inhibition of the fracture at microscale level.
- The Haversian microstructure affected the distribution of maximum principal stress that, in its turn, influenced propagation trajectories of microcracks.
- Cement lines played a prominent role in isolating the osteons from the interstitial matrix; they appeared as critical elements in the protection of bone against fracture.
- The microstructured finite-element models – three- and four-phase composite – reproduced the experimental stress-strain behaviour more adequately compared to the homogeneous-based model.

Izod Tests Numerical Models

Important results can be obtained using the finite-element simulations, such as distributions of stresses and strains, variation of crack length with deformation and distinction between several material behaviours. In this part of the study, various finite-element models were formulated for the Izod-test setup to investigate dynamic and quasi-static behaviours of the cortical bone. Three different models were developed to examine the behaviour of different constitutive models, to study the dynamic and quasi-static behaviours of cortical bone. Those models employed the Izod-test setup and included 2D and 3D finite-element formulations. At first, three 2D models were used to examine different constitutive formulations for the bone material to analyse the behaviour of the cortical bone tissue under impact loading conditions. The obtained simulation results demonstrated that the viscoelastic constitutive material formulation predicted successfully the behaviour of bovine femoral cortical bone under impact loading. Linear-elastic and elastic-plastic constitutive material models underestimated the response of bone specimens to impact loading. Accordingly, the viscoelastic constitutive material model was used to analyse the crack initiation and growth in the cortical bone specimen under impact loading with the 3D Izod-test finite-element model. Following the 3D formulation of the impact Izod test, a 3D quasi-static model was developed, with which crack initiation and propagation of the cortical bone tissue were studied. Based on the obtained results from the numerical studies the following conclusions can be formulated:

- More detailed information about the fracture and deformation processes was obtained using the finite-element simulations and enhanced a better understanding of the processes. Additionally, simulation results were quite close to the experimental ones, and the finite-element models had the capability to reproduce the failure process of cortical bone specimen under impact.
- The cortical bone's elastic-plastic and linear-elastic material formulations underestimated the force magnitude – by 46.7% and 39.2% for its maximum magnitude, respectively. Hence, both linear-elastic and elastic-plastic material models were incapable to correctly capture the response of the

cortical bone tissue under impact load. On the contrary, the cortical bone's viscoelastic material formulation provided a good agreement with the observed experimental data for the period of interaction between the hammer and specimen in the Izod test.

- Numerical simulations with the 2D finite-element Izod test model reproduced the deformation and fracture processes, while the 3D formulation exhibited an unrealistic fracture scenario: formation of a damage band with multiple cracks across the specimen's width and thickness around the notch area. Obviously, the impact loading generated elastic stress waves that propagated in different directions in the specimen and activated multiple fracture modes, and led to initiate multiple cracks. Hence, the band of damaged zone was formed instead of a single crack demonstrating limitations of the current 3D X-FEM routine of Abaqus 6.10 with respect to dynamic cracking problems.
- Finite-element simulations demonstrated oscillations in response to the imposed dynamic load and affirmed the role of the notch as a stress raiser.
- A Complex fracture process including Modes I and II took place in the Izod test specimen in response to the dynamic loading condition with a crack growth resulting in stresses redistribution.
- While the crack length demonstrated a quadratic curve-fit equation, the crack growth rate showed a linear increase with time for the 2D impact Izod model.

Tensile-Impact Numerical Model

Similar to the instrumented Izod tests, instrumented tensile-impact tests provide valuable information about the dynamic behaviour of cortical bone tissue including the impact force-time history, fracture force, and impact strength. In addition, without introducing notches within the specimens, the dynamic stress-strain behaviour can be obtained. Therefore, finite-element analysis employing the advanced technique such as X-FEM can provide wealth of additional information that can expand the knowledge about deformation and fracture of the cortical bone tissue. In this light, three different 3D models were developed to validate the dynamic-based model and to investigate the fracture and deformation behaviours of

cortical bone tissue under various loading condition. The performed tests resulted in the following observations:

- The tensile-impact finite-element model based on the aluminium-alloy material closely predicted the dynamic behaviour of the tensile-impact experiment and revealed its capability to reproduce the transient impact behaviour.
- A band of random short cracks were produced in dynamic loading around the side notches with no partial or complete failure of the specimen. Elastic stress waves along with the current limitations of the X-FEM technique of Abaqus 6.10 were the main reasons for the predicted behaviour.
- The 3D quasi-static model exhibited one single crack growing from one side notch to another; it underpins the interpretations of the dynamic model's response.

10.2. Future Work

During the course of the current study, several challenges were overtaken, yet there are some further research aims at can still be achieved in order to expand the recent study. In the next sections, some future investigations are suggested for experimentation and simulations.

10.2.1. Experimentation

- Further research is still required to examine the behaviour of cortical bone specimens cut from different species and at different ages and health conditions.
- Due to the central role of the microstructure in both quasi-static and dynamic behaviours of the bone tissue, it will be useful to investigate quantitatively the correlation between the behaviour of young and aged, or healthy and diseased specimens and the underlying microstructures.
- In this study, the behaviours of cortical bone only were examined; it will be beneficial to test specimens from trabecular bones as well.

- More experiments can be conducted using Izod and tensile-impact setups to study the effect of age, disease, notch sizes and energy levels with expanded ranges.
- Experiments can be performed to quantify the size effect on the mechanical and fracture properties using special grips for the uniaxial tension machine.
- Distinction between various creep mechanisms at low- and high-stress levels can be identified through a programme of experiments of cortical bone tissue.
- More in-depth investigations of the fracture mechanisms under impact loading for whole bone segments, such as femur, tibia or fibula can be experimentally quantified.

10.2.2. Simulations

- Comparisons between young, aged, healthy and diseased bone cut from different species can be based on simulations using the developed microstructured finite-element models.
- Due to the paramount effect of the underlying microstructure of the cortical bone tissue, its 3D rendered volumes based on micro-CT scans can be incorporated into the 3D Izod and tensile-impact finite-element models to get an in-depth understanding about their role during crack growth process.
- Specimens cut from different healthy species, such as human bones, and from diseased bones, such as osteoporotic or cancerous bone can be examined using the developed models in the current study.
- In the future, with the improvements of the X-FEM approach incorporated into Abaqus finite-element software, it will be useful to improve the models using higher-order elements.
- Hopefully, in the future, the challenge encountered with the X-FEM and resulted in a damaged area instead of one main crack when dealing with impact loading can be investigated with new versions of Abaqus with improved X-FEM algorithms.
- Simulations of fracture and deformation of full bone segments, such as femur can be performed under various loading conditions.

- Finite-element models based on more natural fracture scenarios, e.g. traumatic falls can be developed based on the experimental part of the current study.
- Finite-element models for artificial hip and knee designs with the aid of the experimental and numerical results of the current study are also encouraged.

References

1. Nagaraja, S., *Microstructural Stresses and Strains Associated with Trabecular Bone Microdamage*, in *George W. Woodruff School of Mechanical Engineering*. 2006, PhD thesis, Georgia Institute of Technology: USA.
2. Hing, K., *Bone Repair in the Twenty-First Century: Biology, Chemistry or Engineering.* Philos. Transact. A. Math. Phys. Eng. Sci., 2004. **362**: p. 2821-2850.
3. Kessel, R.G., Kardon, R. H., *Tissues and Organs: A Text Atlas of Scanning Electron Microscopy*. 1979, W. H. Freeman & Co. Ltd.
4. Lakes, R., *Materials with Structural Hierarchy.* Nature, 1993. **361**: p. 511-515.
5. Van der Vegt, A.K., *From Polymers to Plastics*. 2002, Netherlands: DUP Blue Print, 2628 CA Delft, The Netherlands, 2006.
6. Tschoegl, N.W., *The Phenomenological Theory of Linear Viscoelastic Behavior*. 1989, Springer, Verlag, Heidelberg.
7. Ritchie, R.O., Kinney, J.H., Kruzic, J.J., Nalla, R.K., *A Fracture Mechanics and Mechanistic Approach to the Failure of Cortical Bone.* Fatigue Fract. Eng. M., 2005. **28**: p. 345-371.
8. Millins, L.P., Bruzzi, M.S., McHugh, P.E., *Measurement of the Microstructural Fracture Toughness of Cortical Bone using Indentation Fracture.* J. Biomech., 2007. **40**: p. 3285-3288.
9. Abaqus, *Theory manual – Version 6.10 Edition.* Providence, RI, USA, 2010.
10. Ural, A., Vashishth, D., *Cohesive Finite-Element Modelling of Age-Related Toughness Loss in Human Cortical Bone* J. Biomech., 2006. **39**: p. 2974-2982.
11. Morias, J.j.L., de Moura, M.F.S.F., Pereira, F.A.M., Xavier, J., Dourado, N., Dias, M.I.R., Azevedo, J.M.T., *The Double Cantilever Beam Test Applied to Mode I Fracture Characterization of Cortical Bone Tissue.* J. Mech. Behav. Biomed. Mater., 2010. **3**(6): p. 446-453.
12. Liu, X., Qin, X., Du, Z., *Bone Fracture Analysis Using the Extended Finite Element Method (XFEM) with Abaqus*. *The 34th Annual Meeting of the American Society of Biomechanics*. 2010. Brown University.
13. Hogan, H.A., *Micromechanics Modelling of Haversian Cortical Bone Properties.* J. Biomech., 1992. **25**(5): p. 549-556.
14. Budyn, E., Henry, L., Hoc, T., *Multiple Crack Growth Failure in Cortical Bone under Tension by the Extended Finite Element Method*. *III European Conference on Computational Mechanics Solids, Structures and Coupled Problems in Engineering*. 2006. Lisbon, Portugal.

15. User Manual Guide, *Instron MicroTester (5848), User's Guide, Instron Corporation.* 2001.
16. Oliver, W.C., Pharr, G.M., *An Improved Technique for Determining Hardness and Elastic Modulus using Load and Displacement Sensing Indentation Experiments.* J. Mat. Res., 1992. **7**(6): p. 1564-1583.
17. Micro Materials Ltd, *NanoTest On-line Help File Version 1.0 and NanoTest Manual Version 3.0. Unit 3, The Byre, Wrexham Technology Park, Wrexham, LL13 7YP, United Kingdom.* 2004.
18. Martin, R.B., Burr, D.B., Sharkey, N.A., *Skeletal Tissue Mechanics*. 1998, New York: Springer
19. Resil Impactor - Operation and Maintenance Instructions, M.E.R., CEAST S.P.A., Via Airauda, 10-12 10044 PIANEZZA (TO) - ITALY, 2002.
20. Reilly, D.T., Burstein, A.H., *The Mechanical Properties of Cortical Bone.* J. Bone Joint Surg., 1974. **56-A**: p. 1001-1022.
21. Koester, K.J., Ager III, J.W., Ritchie, R.O., *The True Toughness of Human Cortical Bone Measured with Realistically Short Cracks.* Nature, 2008. **7**: p. 672-677.
22. Cullinane, D.M., Einhorn, T.A., *Biomechanics of Bone*, in *Principles of Bone Biology*, B. J.P., Raisz, L.G., Rodan, A.R., Editors. 2002, Academic Press: San Diego.
23. Jee, W.S.S., *Integrated Bone Tissue Physiology: Anatomy and Physiology*, in *Bone Mechanics Handbook*, C. S., Cowin, Editor. 2001, CRC Press LLC: Boca Raton, FL.
24. Mow, V.C., Hayes, W. C., *Basic Orthopaedic Biomechanics*. 1997: Lippincott-Raven.
25. Jepsen, K.J., Goldstein, S.A., Kuhn, J.L., Schaffler, M.B., Bonadio, J., *Type-I Collagen Mutation Compromises the Post-Yield Behaviour of Mov13 Long Bone.* J. Orthop. Res., 1996. **14**(3): p. 493-499.
26. Wang, X., Bank, R.A., Tekoppele, J.M, Agrawal, C.M., *The Role of Collagen in Determining Bone Mechanical Properties.* J. Orthop. Res., 2001. **19**(6): p. 1021-1026.
27. Nyman, J.S., Roy, A., Shen, X., Acuna, R.L., Tyler, J.H., Wanga, X., *The Influence of Water Removal on the Strength and Toughness of Cortical Bone.* J. Biomech., 2006. **39**(5): p. 931-938.
28. Smith, J.W., Walmsely, R., *Factors Affecting the Elasticity of Bone.* J. Anat., 1959. **93**: p. 503-523.
29. Bronner, F., Worrell, R.V., *Orthopaedics: Principles of Basic and Clinical Science*. 1999: CRC Press.
30. Frost, H.M., *Bone "Mass" and the "Mechanostat": A Proposal.* Anat. Rec., 1987. **219**: p. 1-9.

31. Frost, H.M., *The Mechanostat: A Proposed Pathogenic Mechanism of Osteoporoses and the Bone Mass Effects of Mechanical and Nonmechanical Agents.* Bone Miner., 1987. **2**: p. 73-85.
32. Frost, H.M., *Vital Biomechanics: Proposed General Concepts for Skeletal Adaptations to Mechanical Usage.* Calcif. Tissue Int., 1988. **42**: p. 145-156.
33. Parsamian, G.P., *Damage Mechanics of Human Cortical Bone*, in *College of Engineering and Mineral Resources*. 2001, PhD thesis, West Virginia University: USA.
34. Gibson, L.J., Ashby, M.F., *Cellular Solids: Structure and Properties*. 2nd ed. 1999, Cambridge: Cambridge University Press.
35. Rho, J.Y., Kuhn-Spearing, L., Zioupos, P., *Mechanical Properties and the Hierarchical Structure of Bone.* Med. Eng. Phys., 1998. **20**: p. 91-102.
36. Currey, J.D., *The Mechanical Adaptations of Bones*. 1984, Princton, NJ: Princeton University Press.
37. Boyde, A., *Electron Microscopy of the Mineralizing Front.* Metab. Bone Dis. Relat. Res., 1980 **2S**: p. 61-67.
38. Ascenzi, A., Bonucci, E., Ripatomi, A., Roveri, N., *X-Ray Diffraction and Electron Microscope Study of Osteons during Calcification.* Calc. Tiss. Res., 1978. **25**: p. 133-143.
39. Enlow, D.H., *The Bone of Reptiles*, in *Biology of the Reptilia*, C. Gans, Editor. 1969, Academic Press: New York. p. 45-80.
40. Ascenzi, A., Bonucci, E., Bocciarelli, D.S., *An Electron Microscope Study on Primary Periosteal Bone.* J. Ultrastr. Res., 1967. **18**: p. 605-618.
41. Burr, D.B., Martin, R.B., Schaffler, M.B., Radin, E.L., *Bone Remodeling in Response to in-vivo Fatigue Microdamage.* J. Biomech., 1985. **18**: p. 189-200.
42. Bundy, K.J., *Composite Material Models for Bone*, in *Bone Mechanics*, Cowin, S.C., Editor. 1989, CRC Press: Boca Raton, FL. p. 197-210.
43. Crolet, J.M., Aoubiza, B., Meunier, A., *Compact Bone: Numerical Simulation of Mechanical Characteristics.* J. Biomech., 1993. **26**: p. 677-687.
44. Currey, J.D., *The Relationship Between the Stiffness and the Mineral Content of the Bone.* J. Biomech., 1969. **2**: p. 477-480.
45. Katz, J.L., Meunier, A., *The Elastic Anisotropy of Bone.* J. Biomech., 1987. **20**: p. 1063-1070.
46. Katz, J.L., *Hierarchical Modeling of Compact Haversian Bone as a Fibre Reinforced Material*, in *Advances In Bioengineering*, Smith, C.R., Mates, R.E., Editors. 1976, American Society of Mechanical Engineers: New York.

47. Lucchinetti, E., *Composite Models of Bone Properties*, in *Bone Mechanics Handbook*, Cowin, S.C., Editor. 2001, CRC Press LLC: Boca Raton, FL.
48. Curry, J.D., *The Mechanical Properties of Bone.* Clin. Orthop. Relat. Res., 1970. **73**: p. 209-231.
49. Ashman, R.B., Cowin, S.C., Van Burskirk, W.C., Rice, J.C., *A Continuous Wave Technique for the Measurement of Elastic Properties of Cortical Bone.* J. Biomech., 1984. **17**: p. 349-361.
50. Hasegawa, K., Turner, C.H., Burr, D.B., *Contribution of Collagen and Mineral to the Elastic Anisotropy of Bone.* Calc. Tissue Int., 1994. **55**: p. 381-386.
51. Sasaki, N., Matsushima, N., Ikawa, T., Yamamura, H., Fukuda, A., *Orientation of Bone Mineral and its Role in the Anisotropic Mechanical Properties of Bone-Transverse Anisotropy* J. Biomech., 1989. **22**: p. 157-164.
52. Wang, X., Athanasiou, K.A., Agrawal, C.M., Contribution *of Collagen to Bone Mechanical Properties*. *17th Southern Biomedical Engineering Conference* 1998., P. 112, San Antonio.
53. Zioupos, P., Currey, J.D., Hamer, A.J., *The Role of Collagen in the Declining Mechanical Properties of Aging Human Cortical Bone.* J. Biomed. Mater. Res., 1999. **45**: p. 108-116.
54. Hulsen, C., *Specifisches Gewicht, Elasticitat und Festigkeit des Knochengewebes.* Bulletin of Laboratory Biology St. Petersburg, 1898. **1**: p. 7-37.
55. Currey, J.D., *The Mechanical Consequences of Variation in the Mineral Content of Bone.* J. Biomech., 1969. **2**: p. 1-11.
56. Kimura, H., *Tension Test upon the Compact Substance in the Long Bones of Cattle Extremities.* J. Kioto Pref. Med. Univ., 1952. **51**: p. 365-372.
57. Sweeney, A., Byers, R., Kroon, R., *Mechanical Characteristics of Bone and its Constituents*. *ASME Human Factors Conference*. ASME Publ. No. 65 WZ/HUF-7, 1965, New York: American Society of Mechanical Engineers.
58. Mcelhaney, J., Fogle, J., Byars, E., Weaver, G., *Effect of Embalming on the Mechanical Properties of Beef Bone.* J. Appl. Physiol., 1964. **19**: p. 1234-1236.
59. Mcelhaney, J.H. *Dynamic Response of Biological Materials*. *ASME Human Factors Conference*. ASME Publ. No 65 WZ/HUF-9, 1965, New York: American Society of Mechanical Engineers
60. Simkin, A., Robin, G., *The Mechanical Testing of Bone in Bending.* J. Biomech., 1973. **6**: p. 31-39.
61. Burstein, A.H., Currey, J.D., Frankel, V.H., Reilly, D.T., *The Ultimate Properties of Bone Tissue: The Effects of Yielding.* J. Biomech., 1972. **5**: p. 34-44.

62. Currey, J.D., *Differences in the Tensile Strength of Bone of Different Histological Types.* J. Anat., 1959. **93**: p. 87-95.

63. Ko, R., *The Tension Test upon the Compact Substance of the Long Bones of Human Extremities.* J. Kyoto Pref. Med. Univ., 1953. **53**: p. 503-525.

64. Lang, S.B., *Ultrasonic Method for Measuring Elastic Coefficients of Bone and Results on Fresh and Dried Bovine Bone.* IEEE Trans. Biomed. Eng., 1970. **17**(2): p. 101-105.

65. Van Buskirk, W.C., Ashman, R.B., *The Elastic Moduli of Bone, in Mechanical Properties of Bone*. *Joint ASME-ASCE Applied Mechanics, Fluids Engineering and Bioengineering Conference*. 1981. Boulder, CO.

66. Yaszemski, M.J., Payne, R.G., Hayes, W.C., Langer, R., Mikos, A.G., *Evaluation of Bone Transplantation: Molecular, Cellular, and Tissue Strategies to Engineer Human Bone.* Biomater., 1996. **17**: p. 175-185.

67. Cameron, G.B., *A Finite Element and Experimental Investigation of the Femoral Component Mechanics in a Total Hip Arthroplasty*, in T*he Centre of Build Environment and Engineering Research, School of Engineering Systems*. 2005, PhD thesis, Queensland University of Technology: Australia.

68. Athanasiou, K.A., Zhu, C.F., Lanctot, M.S., Agrawal, C.M., Wang, X., *Fundamentals of Biomechanics in Tissue Engineering of Bone.* Tissue Eng., 2000. **6**: p. 361-381.

69. Rho, J.Y., *An Ultrasound Method for Measuring the Elastic Properties of Human Tibial Cortical and Cancellous Bone.* Ultrasonics 1996. **34**: p. 777-783.

70. Pithioux, M., Lasaygues, P., Chabrand, P., *An Alternative Ultrasonic Method for Measuring the Elastic Properties of Cortical Bone.* J. Biomech., 2002. **35**: p. 961-968.

71. Yamashita, J., Furman, B.R., Rawls, H.R., Wang, X.D., Agrawal, C.M., *The Use of Dynamic Mechanical Analysis to Assess the Viscoelastic Properties of Human Cortical Bone.* J. Biomed. Mater. Res., 2001. **58**(1): p. 47-53.

72. Yamashita, J., Furman, B.R., Rawls, H.R., Wang, X.D., Agrawal, C.M., *Collagen and Bone Viscoelasticity: A Dynamic Mechanical Analysis.* J. Biomed. Mater. Res., 2002. **63**: p. 31-36.

73. Lakes, R., *Viscoelastic Properties of Cortical Bone*, in *Bone Mechanics Handbook*, S.C. Cowin, Editor. 2001, CRC Press LLC: Boca Raton, FL.

74. Abramowitch, S.D., *An Evaluation of the Non-Linear Viscoleastic Properties of the Healing Medial Collateral Ligament*, *School of Engineering*. 1998, PhD thesis, University of Pittsburgh: Pittsburgh.

75. Rauber, A.A., *Elasticitat und Festigkeit der Knochen*. Anatomisch-Physiologische Studie. 1876, Engelmann: Leipzig.

76. Smith, R., Keiper, D., *Dynamic Measurement of Viscoelastic Properties of Bone.* Am J. Med. Elec. , 1965. **4**: p. 156-160.

77. Sedlin, E.D., *A Rheologic Model for Cortical Bone.* Acta Orthop. Scand., 1965. **Suppl. 83**: p. 77.

78. Knets, I.V., Vilks, Y.K . *Creep of Compact Human Bony Tissue under Tension.* Polymer Mech., 1975. **11**: p. 543-547.

79. Lakes, R.S., Katz, J. L., *Interrelationships among the Viscoelastic Functions for Anisotropic Solids: Application to Calcified Tissues and Related Systems.* J. Biomech., 1974. **7**: p. 259-270.

80. Lakes, R.S., *Viscoelastic Properties of Wet Cortical Bone-I Torsional and Biaxial Studies.* J. Biomech., 1979. **12**: p. 657-678.

81. Lakes, R.S., *Viseoelastic Properties of Wet Cortical Bone-II. Relaxation Mechanisms.* J. Biomech., 1979. **12**: p. 679-687.

82. Lakes, R.S., *Viseoelastic Properties of Wet Cortical Bone-III. A Non-Linear Constitutive Equation.* J. Biomech., 1979. **12**: p. 689-698.

83. Nomura, S., Hiltner, A., Lando, J. B., Baer, E., *Interaction of Water with Native Collagen.* Biopolymers, 1977. **16**: p. 231-246.

84. Sedlin, E.D., Hirsch, C., *Factors Affecting the Determination of the Physical Properties of Femoral Cortical Bone.* Acta Orthop. Scand., 1966. **37**(1): p. 29-48.

85. Lakes, R.S., Katz, J. L., Sternstein, S.S., *Viseoelastic Properties of Wet Cortical Bone-I: Torsional and Biaxial Studies.* J. Biomech., 1979. **12**: p. 657-678.

86. Sasaki, N., Enyo, A., *Viscoelastic Properties of Bone as a Function of Water Content.* J. Biomech., 1995. **28**(7): p. 809-815.

87. Bowman, S.M., Gibson, L.J., Hayes, W.C., McMahon, T.A., *Results from Demineralized Bone Creep Tests Suggest That Collagen is Responsible for the Creep Behaviour of Bone.* J. Biomech. Eng., 1999. **121**(253-258).

88. Fois, M., Lamure, A., Fauran, M.J., Lacabanne, C., *Study of Human Cortical Bone and Demineralized Human Cortical Bone Viscoelasticity.* J. Appl. Polym. Sci., 2001. **79**: p. 2527-2533.

89. Rimnac, C.M., Petko, A.A., Santner, T.J., Wright, T.M., *The Effect of Temperature, Stress and Microstructure on the Creep of Compact Bovine Bone.* J. Biomech., 1993. **26**(3): p. 219-228.

90. Iyo, T., Maki, Y., Sasaki, N., Nakata, M., *Anisotropic viscoelastic Properties of Cortical Bone.* J. Biomech., 2004. **37**: p. 1433-1437.

91. Fondrk, M., Bahniuk, E., Davy., D.T., Michales, C., *Some Viscoelastic Characteristics of Bovine Bone and Human Bone.* J. Biomech., 1988. **21**(8): p. 623-630.

92. Cotton, J.R., Zioupos, P., Winwood, K., Taylor, M., *Analysis of Creep Strain During Tensile Fatigue of Cortical Bone.* J. Biomech., 2003. **36**: p. 943-949.

93. Cotton, J.R., Winwood, K., Zioupos, P., Taylor, M., *Damage Rate is a Predictor of Fatigue Life and Creep Strain Rate in Tensile Fatigue of Human Cortical Bone Samples.* J Biomech. Eng., 2005. **127**(2): p. 213-219.

94. Tanabe, Y., Tanaka, S., Sakamoto, M., Hara, T., Takahashi, H., Koga,Y. , *Influence of Loading Rate on Anisotropy of Compact Bone.* J. Phys. IV, 1991. **1**: p. C3-305-C3-310.

95. Lakes, R.S., Katz, J.L., *Viscoelastic Properties of Wet Cortical Bone-II: Relaxation Mechanisms.* J. Biomech., 1979. **12**(9): p. 679-687.

96. Won, J., Karl, J.J, Dwight, T.D., *The Effect of Recovery Time and Test Conditions on Viscoelastic Measures of Tensile Damage in Cortical Bone.* J. Biomech., 2007. **40**(12): p. 2731-2737.

97. Wetton, R.E., Marsh, R.D.L., Van-de-Velde, J.G., *Theory and Applications of Dynamic Mechanical Thermal Analysis.* Thermochimica Acta, 1991. **175**(1): p. 1-11.

98. Wang, T., Feng, Z., *Dynamic Mechanical Properties of Cortical Bone: the Effect of Mineral Content.* Mater. Lett., 2005. **59**: p. 2277-2280.

99. Schaller, R., Barrault, S., Zysset, Ph., *Mechanical Spectroscopy of Bovine Compact Bone.* Mater. sci. Eng. A, 2004. **370**(1-2): p. 569-574.

100. Yener, N.Y., Gregory, T.C., Turner, A.S., Clifford, M. L., David, P.F., *Apparent Viscoelastic Anisotropy as Measured from Non-destructive Oscillatory Tests Can Reflect the Presence of a Flaw in Cortical Bone.* J. Biomed. Mater. Res., 2004. **69A**: p. 124–130.

101. Morgan, E.F., Barnes, G.L., Einhorn, T.A., *The Bone Organ System: Form and Function*, in *Osteoporosis*, Marcus, R., Feldman, D., Kelsey, J., Editors. 2008, Elsevier: San Diego, CA. p. 3-4.

102. Ramaswamy, R., *Correlating Mechanical Properties of Cancellous Bone in the Rat with Various Density Measures*, PhD thesis, *Texas A&M College of Engineering*. 2003, Texas A&M University: Texas.

103. Pan, J., Han, X., Niu, W., Cameron, R. E., *A Model for Biodegradation of Composite Materials Made of Polyesters and Tricalcium Phosphates.* Biomater., 2011. **32**(9): p. 2248-2255.

104. Athanasiou, K.A., Zhu, C.F., Lanctot, M.S., Agrawal, C.M., Wang, X., *Fundamentals of Biomechanics in Tissue Engineering of Bone.* Tissue Eng., 2000. **6**(4): p. 361-381.

105. Bonfield, W., Li, C.H., *Deformation and Fracture of Bone.* J. Appl. Phys., 1966. **37**: p. 869-875.

106. Behiri, J.C., Bonfield, W., *Orientation Dependence of the Fracture Mechanics of Cortical Bone.* J. Biomech., 1989. **22**: p. 863-872.

107. Wang, X., Shen, X., Li, X. Agrawal, C.M., *Age-Related Changes in the Collagen Network and Toughness of Bone.* Bone, 2002. **31**: p. 1-7.

108. Lucksanambool, P., Higgs, W.A.J., Higgs, R.J. E.D., Swain, M.W., *Fracture Toughness of Bovine Bone: Influence of Orientation and Storage Media.* Biomater., 2001. **22**: p. 3127-3132.

109. Knott, J.F., *Fundamentals of Fracture Mechanics*. 1973: Wiley.

110. Melvin, J.W., Evans, F.G., *Crack Propagation in Bone.,* ASME Biomaterials Symposium AMD, 1973. **2**.

111. Wright, T.M., Hayes, W.C., *Fracture Mechanics Parameters for Compact Bone- Effect of Density and Specimen Thickness.* J. Biomech., 1977. **10**: p. 419-430.

112. Bonfield, W., Grynpas, M.D., Young, R.J., *Crack Velocity and the Fracture of Bone.* J. Biomech., 1978. **11**: p. 473-479.

113. Wang, X., Argawal, C.M., *Fracture Toughness of Bone Using a Compact Sandwich Specimen: Effects of Sampling Sites and Crack Orientations.* J. Bimed. Res., 1996. **33**: p. 13-21.

114. Robertson, D.M., Robertson, D., Barrett, C.R., *Fracture Toughness, Critical Crack Length and Plastic Zone Size in Bone.* J. Biomech., 1978. **11**: p. 359-364.

115. Bonfield, W., Datta, P.K., *Fracture Toughness of Compact Bone* J. Bimed. Res., 1976. **9**: p. 131-134.

116. Yan, J., Mecholsky, J., Clifton, K.B., *How Tough is Bone? Application of Elastic-Plastic Fracture Mechanics to Bone.* Bone, 2007. **40**: p. 479-484.

117. Feng, Z., Rho, J., Han, S., Ziv, I., *Orienation and Loading Condition Dependence of Fracture Toughness in Cortical Bone.* Mater. Sci. Eng. C, 2000. **C11**: p. 41-46.

118. Palmqvist, S., *Occurrence of Crack Formation during Vickers Indentation as a Measure of Toughness of Hard Materials.* Arch. Eisenhuettenwes., 1962. **33**: p. 629-633.

119. Evans, A.G., Lawn, B.R., Marshall, D.B., *Elastic/plastic Indentation Damage in Ceramics: the Median/Radial Crack System.* J. Am. Ceram. Soc., 1980. **63**: p. 574-581.

120. Hassan, R., Caputo, A.A., Bunshah, R.F., *Fracture Toughness of Human Enamel.* J. Dent. Res., 1981. **60**: p. 820-827.

121. Yan, J., Clifton, K.B., Mecholsky, J., John, J., Reep, R. L., *Fracture Toughness of Manatee Rib and Bovine Femur using a Chevron-Notched Beam Test.* J. Biomech., 2006. **39**: p. 1066-1074.

122. Mullins, L.P., Sassi, V., McHugh, P.E., Bruzzi, M.S., *Differences in the Crack Resistance of Interstitial, Osteonal and Trabecular Bone Tissue.* Ann. Biomed. Eng., 2009. **37**(12): p. 2574-2582.

123. Fan, Z.F., Swadener, J.G., Muir, P., Smith, P.A., Harris, G.F. *Tissue Fracture Toughness of Bone Measured by Microindentation*. *52nd Annual Meeting of the Orthopaedic Research Society*. 2006. Chicago, IL.

124. Ota, T., Yamamoto, I, Morita, R., *Fracture Simulation of the Femoral Bone using the Finite-Element Method: How a Fracture Initiates and Proceeds.* J. Bone Miner. Metab., 1999. **17**(2): p. 108-112.

125. Dolbow, J., Nadeau, J.C., *On the Use of Effective Properties for the Fracture Analysis of Microstructured Materials* Eng. Fract. Mech., 2002. **69**: p. 1607-1634.

126. Yazid, A., Abdelkader, N., Abdelmadjid, H., *A State-of-the-Art Review of the X-FEM for Computational Fracture Mechanics.* Appl. Math. Model., 2009. **33**: p. 4269-4282.

127. Belytschko, T., Black, T., *Elastic Crack Growth in Finite-Elements with Minimal Remeshing,* Int. J. Numer. Methods Eng., 1999. **45**: p. 601-620.

128. Melenk, J.M., Babuska, I., *The Partition of Unity Finite Element Method: Basic Theory and Applications.* Comput. Methods Appl. Mech. Eng., 1996. **139**: p. 289-314.

129. Oshita, F., Omori, K., Nakahira, Y., Miki, K., *Development of a Finite Element Model of the Human Body*. *7th International LS-DYNA Users Conference*. May 19-21, 2002. Dearborn, Michigan.

130. Chawla, A., Mukherjee, S., Mohan, D., Parihar, A., *Validation of Lower Extremity Model in THUMS 155*. *International IRCOBI Conference on the Biomechanics of Impact*. September 22-24, 2004. Indian Institute of Technology, India.

131. Aoubiza, B., Crolet, J.M., Meunier, A., *On the Mechanical Characterization of Compact Bone Structure Using the Homogenization Theory.* J. Biomech., 1996. **29**(12): p. 1539-1547.

132. Wang, X., Puram, S., *The Toughness of Cortical Bone and its Relationship with Age.* Ann. Biomed. Eng., 2004. **32**: p. 123-135.

133. Ural, A., Vashishth, D., *Anisotropy of Age-Related Toughness Loss in Human Cortical Bone: A Finite Element Study.* J. Biomech., 2007. **40**: p. 1606-1614.

134. An, B., Liu, Y., Arola, D., Zhang, D., *Fracture Toughening Mechanism of Cortical Bone: An Experimental and Numerical Approach.* J. Mech. Behav. Biomed. Mater., 2011: **4**(7): p. 983-992.

135. Ural, A., Zioupos, P., Buchanan, D., Vashishth, D., *The Effect of Strain Rate on Fracture Toughness of Human Cortical Bone: A Finite-Element Study.* J. Mech. Behav. Biomed. Mater., 2011: **4**(7): p. 1021-1032.

136. Grasa, J., Bea, J.A., Doblare, M., *A Probabilistic Extended Finite Element Approach: Application to the Prediction of Bone Crack Propagation.* Key Eng. Mat., 2007. **348-349**: p. 77-80.

137. Prendergast, P.J., Huiskes R., *Microdamage and Osteocyte-Lacuna Strain in Bone: A Microstructural Finite Element Analysis.* J. Biomech. Eng., 1996. **118**: p. 240-246.

138. Dong, X.N., Zhang, X., Huang, Y.Y., Guo, X. E., *A Generalized Self-Consistent Estimate for the Effective Elastic Moduli of Fiber-Reinforced Composite Materials with Multiple Transversely Isotropic Inclusions.* Int. J. Mech. Sci., 2005. **47**(6): p. 922-940.

139. Mullins, L.P., McGarry, J.P., Bruzzi, M.S., McHugh, P.E., *Micromechanical Modelling of Cortical Bone.* Comput. Methods Biomech. Biomed. Eng., 2007. **10**(3): p. 159-169.

140. Racila, M., Crolet, J. M., *Nano and Macro Structure of Cortical Bone: Numerical Investigations.* Mech. Adv. Mater. Struc., 2007. **14**: p. 655-663.

141. Raeisi Najafi, A., Arshi, A.R., Eslami, M.R., Fariborz, S., Moeinzadeh, M.H., *Micromechanics Fracture in Osteonal Cortical Bone: A Study of the Interactions Between Microcrack Propagation, Microstructure and the Material Properties.* J. Biomech., 2007. **40**: p. 2788-2795.

142. Huang, J., Rapoff, A.J., Haftka, R.T., *Attracting Cracks for Arrestment in Bone-Like Composites.* Mater. Design, 2006. **27**(6): p. 461-469.

143. Budyn, E., Hoc, T., *Multi-Scale Modelling of Human Cortical Bone: Aging and Fracture Studies.* Mater. Res. Soc. Symp. Proc., 2007. **16**: p. 215-238.

144. Hamed, E., Lee, Y., Jasiuk, I., *Multiscale Modeling of Elastic Properties of Cortical Bone.* Acta Mech., 2010. **213**: p. 131-154.

145. Weiner, S., Traub, W., Wagner, H.D., *Lamellar Bone: Structure-Function Relations.* J. Struct. Biol., 1999. **126**(3): p. 241-255.

146. Lakshmanan, S., Bodi, A., Raum, K., *Assessment of Anisotropic Tissue Elasticity of Cortical Bone from High-Resolution, Angular Acoustic Measurements.* IEEE Trans. Ultrason. Ferroelectr. Freq. Control, 2007. **54**(8): p. 1560-1570.

147. Pietruszczak, S., Gdela, K., Webber,C.E., Inglis, C.E, *On the Assessment of Brittle–Elastic Cortical Bone Fracture in the Distal Radius.* Eng. Fract. Mech., 2007. **74**: p. 1917-1927.

148. Evans, F.G., *Stress and Strain in Bones*. 1957, Illinois: Springfield, Thomas.

149. Evans, F.G., Lebow, M., *Regional Differences in Some of the Physical Properties of the Human Femur.* J. Apple. Physiol., 1951. **3**: p. 563-572.

150. Cowin, S.C., *Mechanics of Materials*, in *Bone Mechanics Handbook*, S.C. Cowin, Editor. 2001, CRC Press LLC: Florida

151. Saito, S., *Die Verteilung von Dichte, Druck-und Zugfestigkeit im Menslichen Femurschaft.* Anat. Anz. Jena., 1983. **154**: p. 365-376.

152. Abdel-Wahab, A.A., Alam, K., Silberschmidt, V.V., *Analysis of anisotropic viscoelastoplastic properties of cortical bone tissues.* J. Mech. Behav. Biomed. Mater., 2011. **4**(5): p. 807-820.

153. Reilly, D.T., Burstein, A.H., *The Elastic and Ultimate Properties of Compact Bone Tissue.* J. Biomech., 1975. **8**(6): p. 393-405.

154. Edward, G.X., *Mechanical Properties of Cortical Bone and Cancellous Bone Tissue*, in *Bone Mechanics Handbook*, S.C. Cowin, Editor. 2001, CRC Press LLC: Florida

155. Raftopoulos, D., Katsamanis, E., Saul, F., Liu, W., Saddemi, S., *An Intermediate Loading Rate Technique for the Determination of Mechanical Properties of Human Femoral Cortical Bone.* J. Biomech. Eng., 1993. **15**: p. 60-66.

156. Ferreira, F., Vaz M.A., Simoes J.A., *Mechanical Properties of Bovine Cortical Bone at High Strain Rate.* Mater. Charact., 2005. **57**: p. 71-79.

157. Pithioux, M., Subit, D., Chabrand, P., *Comparison of Compact Bone Failure under Two Different Loading Rates: Experimental and Modelling Approaches.* Med. Eng. Phys., 2004. **26**(8): p. 647-653.

158. Wolff, J., *The Law of Bone Remodeling*. 1986, Berlin Heidelberg New York: Springer (translation of the German 1892 edition).

159. Sasaki, N., Nakayama, Y., Yoshikawa, M., Enyo, A., *Stress Relaxation Function of Bone and Bone Collagen.* J. Biomech., 1993. **26**: p. 1369-1376.

160. Katz, J.L., *Anisotropy of Young's Modulus of Bone.* Nature, 1980. **283**: p. 106-107.

161. Lakes, R.S., Saha, S., *Cement Line Motion in Bone.* Science, 1979. **204**: p. 501-503.

162. Garner, E., Lakes, R., Lee, T., Swan, C., Brand, R., *Viscoelastic Dissipation in Compact Bone: Implications for Stress-Induced Fluid Flow in Bone.* Trans ASME. J. Biomech. Eng., 2000. **122**: p. 166–172.

163. Joo, W., *Cross-Modal Effects of Damage on Mechanical Behavior of Human Cortical Bone*. 2006, PhD thesis, Case Western Reserve University: Cleveland.

164. Bala, Y., Depalle, B., Douillard, T., Meille, S., Clément, P., Follet, H., Chevalier, J., Boivin, G., *Respective Roles of Organic and Mineral Components of Human Cortical Bone Matrix in Micromechanical Behavior: An Instrumented Indentation Study.* J. Mech. Behav. Biomed. Mater., 2011. **4**(7): p. 1473–1482.

165. Turner, C.H., Burr, D.B., *Experimental Techniques for Bone Mechanics*, in *Bone Mechanics Handbook*, S.C. Cowin, Editor. 2001, CRC Press LLC: Boca Raton, FL.

166. Doerner, M.F., Nix, W.D., A *Method for Interprenting the Data from Depth-sensing Indentation Instrument.* J. Mater. Res., 1986. **1**(4): p. 601-609.

167. Rho, J.Y., Tsui, T.Y., Pharr, G.M., *Elastic Properties of Human Cortical and Trabecular Lamellar Bone Measured by Nanoindentation.* Biomater., 1997. **18**: p. 1325-1330.

168. Ko, C.C., Douglas, W.H., Cheng, Y-S, *Intrinsic Mechanical Competence of Cortical and Trabecular Bone Measured by Nanoindentation and Microindentation Probes.* Adv. Bioeng. ASME, 1995. **BED-29**(415-416).

169. Rho, J.Y., Ashman, R.B., Turner, C.H., *Young's Modulus of Trabecular and Cortical Bone Material: Ultrasonic and Microtensile Measurements.* J. Biomech., 1993. **26**(2): p. 111-119.

170. Hoffler, C.E., Guo, X.E., Zysset, P.K., Goldstein, S.A., *An Application of Nanoindentation Technique to Measure Bone Tissue Lamellae Properties.* J. Biomech. Eng., 2005. **127**(7): p. 1046-1053.

171. Turner, C.H., Rho, J., Takano, Y., Tsui, T.Y., Pharr, G.M., *The Elastic Properties of Trabecular and Cortical Bone Tissues are Similar: Results from Two Microscopic Measurement Techniques.* J. Biomech., 1999. **32**(4): p. 437-441.

172. Hengsberger, S., Enstroem, J., Peyrin, F., Zysset, P., *How is the Indentation Modulus of Bone Tissue Related to its Macroscopic Elastic Response? A Validation Study.* J. Biomech., 2003. **36**(10): p. 1503-1509.

173. Zysset, P.K., Guo, X.E., Hoffler, C.E., Moore, K.E., Goldstein, S.A., *Elastic Modulus and Hardness of Cortical and Trabecular Bone Lamellae Measured by Nanoindentation in the Human Femur.* J. Biomech., 1999. **32**(10): p. 1005-1012.

174. Orías, A., *The Relationship Between the Mechanical Anisotropy of Human Cortical Bone Tissue and its Microstructure*, PhD thesis, *Graduate School*. 2005, University of Notre Dame in Notre Dame: Indiana, USA.

175. Sneddon, I.N., *The Relation between Load and Penetration in the Axisymmetric Boussinesq Problem for a Punch of Arbitrary Profile.* Int. J. Eng. Sci., 1965. **3**: p. 47-57.

176. Zihiqiang, C., Zhang, X., *Nanoindentation Stress-Strain Curves of Plasma-Enhanced Chemical Vapor Deposited Silicon Oxide Thin Films.* Thin Solid Films, 2008. **516**: p. 1941-1951.

177. Currey, J.D., *Three Analogies to Explain the Mechanical Properties of Bone.* Biorh., 1964. **2**: p. 1-10.

178. Katz, J.L., *Hard Tissue as a Composite Material. I. Bounds on the Elastic Behaviour* J. Biomech., 1971. **4**: p. 455-473.

179. Bonfield, W., Liu, C.H., *Anisotropy of Non-elastic Flow in Bone* J. Appl. Phys., 1967. **38**: p. 2450.

180. Hashin, Z., *Analysis of Composite Materials - A Survey.* Appl. Mech. Rev., 1983. **50**: p. 481–505.

181. Alam, K., *Experimental and Numerical Analysis of Conventional and Ultrasonically -Assisted Cutting of Bone*, 2009, PhD thesis, *Wolfson School of Mechanical and Manufacturing Engineering*, Loughborough University: UK.

182. Hoc, T., Henry, L., Verdier, M., Aubry, D., Sedel, L., Meunier, A., *Effect of Microstructure on the Mechanical Properties of Haversian Cortical Bone.* Bone, 2006. **38**: p. 466-474.

183. Thurner, P.J., *Atomic force microscopy and indentation force measurement of bone.* Wiley Interdisciplinary Reviews: Nanomedicine and Nanobiotechnology, 2009. **1**(6): p. 624-649.

184. Curry, J.D., *Role of Collagen and other Organics in the Mechanical Properties of Bone.* Osteoporosis Int., 2003. **14**: p. S29-S36.

185. Rho, J.Y., Pharr, G.M., *Effects of Drying on the Mechanical Properties of Bovine Femur Measured by Nanoindentation.* J. Mater. Sci. Mater. Med., 1999. **10** p. 485-488.

186. Nyman, J.S., Roy, A, Tyler, J.H., Acuna, R.L., Gayle, H.J., Wang, X., *Age-Related Factors Affecting the Postyield Energy Dissipation of Human Cortical Bone.* J. Orthop. Res., 2007. **25**(5): p. 646-655.

187. Lee, S., Novitskaya, E.E., Reynante, B., Vasquez, J., Urbaniak, R., Takahashi, T., Woolley, E., Tombolato, L., Chen, Po-Yu, McKittrick, J., *Impact testing of structural biological materials.* Mat. Sci. Eng. C, 2011. **31**(4): p. 730-739.

188. Augat, P., Schorlemmer, S., *The Role of Cortical Bone and its Microstructure in Bone Strength.* Age Ageing, 2006. **35-s2**: p. ii27-ii31.

189. Launey, M.E., Buehler, M.J., Ritchie, R.O., *On the Mechanistic Origins of Toughness in Bone.* Ann. Rev. Mater. Res., 2010. **40**: p. 25-53.

190. Nalla, R.K., Stolken, J.S., Kinney, J.H., Ritchie, R.O., *Fracture in Human Cortical Bone: Local Fracture Criteria and Toughening Mechanisms.* J. Biomech., 2005. **38** p. 1517–1525.

191. Katsamanis, F., Raftopoulos, D. D. , *Determination of Mechanical Properties of Human Femoral Cortical Bone by the Hopkinson Bar Stress Technique.* J. Biomech., 1990. **23**(11): p. 1173-1184.

192. Panagiotopoulos, E., Kostopoulos, V, Tsantzalis, S, Fortis, A P, Doulalas, A., *Impact Energy Absorption by Specimens from the Upper End of the Human Femur.* Injury 2005. **36**(5): p. 613-617.

193. Saha, S., Hayes, W. C., *Tensile Impact Properties of Human Compact Bone.* J. Biomech. , 1976. **9**(4): p. 243-251.

194. PASW Statistics 18, R.V.Ó.S., Inc., 2009, Chicago, IL).

195. Saha, S., Hayes, W. C. , *Instrumented Tensile-impact Tests of Bone.* Exp. Mech., 1974. **14**(2): p. 473-478.

196. Currey, J.D., Bear, K., Zioupos, P., *The Effect of Ageing and Changes in Mineral Content in Degrading the Toughness of Human Femora.* J. Biomech., 1996. **29**(2): p. 257-260.

197. Reilly, G.C., Currey, J. D., *The Effect of Damage and Microcracking on the Impact Strength of Bone.* J. Biomech., 2000. **33**: p. 337-343.

198. Hansen, U., Zioupos, P., Simpson, R., Curry, J., Hynd, D., *The Effect of Strain Rate on the Mechanical Properties of Human Cortical Bone.* J Biomech. Eng., 2008. **130**(1): p. 011011.

199. Saha, S., Hayes, W. C., *Relations between Tensile Impact Properties and Microstructure of Compact Bone* Calc. Tiss. Res., 1977. **24**: p. 65-72.

200. Amprino, R., Engstrom, A., *Studies on X-ray Absorption and Diffraction of Bone Tissue* Acta Anat. , 1952. **15**: p. 1-22.

201. Strandh, J., *Microchemical Studies on Single Haversian Systems. II. Methodological Considerations with Special Reference to Ca/P Ratio in Microscopic Bone Structures* Exp. Cell. Res., 1960. **21**: p. 406.

202. Vose, G.P., Kubala, A.L., *Bone Strength - Its Relations to X-ray Determined Ash Content* Hum. Biol., 1959. **31**: p. 262-270.

203. Behiri, J.C., Bonfield, W., *Fracture Mechanics of Bone - The Effects of Density, Specimen Thickness, and Crack Velocity on Longitudinal Fracture.* J. Biomech., 1984. **17**: p. 25-34.

204. Ferreira, F., Vaz, M.A., Simoes, J.A., *Mechanical Properties of Bovine Cortical Bone at High Strain Rate.* Mater. Charact., 2006. **57**: p. 71-79.

205. Wang, X.D., Masilamani, N.S., Mabrey, J.D., Alder, M.E., Agrawal, C.M., *Changes in the Fracture Toughness of Bone May Not Be Reflected in its Mineral Density, Porosity, and Tensile Properties.* Bone, 1998. **23**(1): p. 67-72.

206. Martin, R.B., Burr, D.B., *Structure, Function, and Adaptation of Compact Bone*. 1989, New York: Raven Press.

207. Bevill, G., Eswaran, S.K., Gupta, A., Papadopoulos, P., Keaveny, T.M., *Influence of Bone Volume Fraction and Architecture on Computed Large-Deformation Failure Mechanisms in Human Trabecular Bone.* Bone. 2006. **39**: p. 1218–1225.

208. Morgan, E.F., Bayraktar, H.H., Keaveny, T.M., *Trabecular Bone Modulus-Density Relationships Depend on Anatomic Site.* J. Biomech., 2003. **36** p. 897-904.

209. Guo, X.R., Liang, L.C., Goldstein, S.A., *Micromechanics of Osteonal Cortical Bone Fracture.* J. Biomech. Eng., 1998. **120**(1): p. 112-117.

210. Mullins, L.P., Sassi, V., McHugh, P.E., Bruzzi, M.S., *Differences in the Crack Resistance of Interstitial, Osteonal and Trabecular Bone Tissue.* Ann. Biomed. Eng., 2009. **37** (12): p. 2574–2582.

211. Zioupos, P., *Accumulation of in-vivo Fatigue Microdamage and its Relation to Biomechanical Properties in Ageing Human Cortical Bone.* J. Microsc. , 2001. **201** (2): p. 270–278.

212. Mohsin, S., O'Brien, F.J., Lee, T.C., *Osteonal Crack Barriers in Ovine Compact Bone.* J. Anat., 2006. **208** (1): p. 81–89.

213. Boyce, H.M., Fyhire, D.P., Glotkowski, M.C., Radin, E.L., Schaffler, M.B., *Damage Type and Strain Mode Associations in Human Compact Bone Bending Fatigue.* J. Orthop. Res., 1998. **16** (3): p. 322–329.

214. Atkinson, P.J., Hallsworth, A.S., *The Spatial Structure Bone*, in *Progress in Anatomy*, R.J. Harrison, Navaratum, V., Editors. 1982, Cambridge University Press: Cambridge. p. 179–199.

215. Mohsin, S., Taylor, D., Lee, T.C., *Three-dimensional Reconstruction of Haversian systems in Ovine Compact Bone.* Eur. J. Morphol. , 2002. **40** p. 309–315.

216. Express, V.I.-P., *Version Media Cybernetics.* 2005.

217. MATLAB7, *The MathWorks.* 2007a.

218. Sabelman, E.E., Koran, P., Diep, N., Lineaweaver, W.C., *Collagen/Hyaluronic Acid Matrices for Connective Tissue Repair*. *First Smith & Nephew International Symposium: Advances in Tissues Engineering and Biomaterials*. 20–23 July, 1997. York, UK.

219. Yeni, Y.N., Norman, T.L., *A Formulation of the Influence of Osteons on the Fracture Toughness of Cortical Bone in Longitudinal Crack Growth* <http://www.asbweb.org/conferences/1990s/1999/ACROBAT/024.PDF>, 1999. Date: 20.06.2011.

220. Bayraktar, H.H., Morgan, E.F., Niebur, G.L., Morris, G.E., Wong, E.K., Keaveny, T.M., *Comparison of the Elastic and Yield Properties of Human Femoral Trabecular and Cortical Bone Tissue.* J. Biomech. , 2004. **37**: p. 27–35.

221. Nalla, R.K., Kinney, J.H., Ritchie, R.O., *Mechanistic Fracture Criteria for the Failure of Human Cortical Bone.* Nature 2003. **2**: p. 164–168.

222. Abdel-Wahab, A.A., Maligno, A.R., Silberschmidt, V.V., *Microscale Modelling of Bovine Cortical Bone Fracture: Analysis of Crack Propagation and Micro-structure Using X-FEM.* Comp. Mater. Sci., 2011 **doi:10.1016/j.commatsci.2011.01.02**.

223. Norman T.L., N., S.V., Burr, D.B., *Resistance to Crack Growth in Human Cortical Bone is Greater in Shear than in Tension.* J. Biomech., 1996. **29**: p. 1023-1031.

224. Norman, T.L., Vashishth, D., Burr, D.B., *Fracture Toughness of Human Bone under Tension.* J. Biomech., 1995. **28**: p. 309-320.

225. Zioupos, P., *Recent Developments in the Study of Failure of Solid Biomaterials and Bone: Fracture and Prefracture Toughness.* Mater. Sci. Eng. C, 1998. **6**: p. 33-40.

226. Vashishth, D., Tanner, K.E., Bonfield, W., *Contribution, Development and Morphology of Microcracking in Cortical Bone during Crack Propagation.* J. Biomech., 2000. **33**: p. 1169-1174.

227. Yeni, Y.N., Norman, T.L., *Calculation of Porosity and Osteonal Cement Line Effects on the Effective Fracture Toughness of Cortical Bone in Longitudinal Crack Growth.* J. Biomed. Mater. Res. B Appl. Biomater. , 2000. **51**: p. 504-509.

228. Nalla, R.K., Kruzic, J.J., Ritchie, R.O., *On the Origin of the Toughness of Mineralized Tissue: Microcracking or Crack Bridging?* Bone 2004. **34**: p. 790-798.

229. Yang, Q.D., Cox, B.N., Nalla, R.K., Ritchie, R.O., *Re-evaluating the Toughness of Human Cortical Bone.* Bone. 2006. **38**: p. 878–887.

230. Cox, B.N., Yang, Q., *Cohesive Zone Models of Localization and Fracture in Bone.* Eng. Fract. Mech., 2007. **74**: p. 1079-1092.

231. Abdel-Wahab, A.A., Maligno, A.R., Silberschmidt, V.V., *Dynamic Properties of Cortical Bone Tissue: Izod Tests and Numerical Study.* Comp. Mater. Con., 2010. **19**(3): p. 217-238.

232. Abdel-Wahab, A.A., Silberschmidt, V.V., *Numerical Modelling of Impact Fracture of Cortical Bone Tissue Using X-FEM.* J. Theor. Appl. Mech., 2011 (**In Press)**.

233. Pattin, C.A., Calet, W.E., Carter, D.R., *Cyclic Mechanical Property Degradation During Fatigue Loading of Cortical Bone* J. Biomech., 1996. **29**: p. 69-79.